Measuring Physical Properties at the Surface of a Comet Nucleus

by

Andrew Jonathan Ball

December 1997

A thesis submitted for the degree of Doctor of Philosophy

Unit for Space Sciences and Astrophysics
University of Kent
Canterbury, UK

Acknowledgements

First of all I would like to thank my principal co-workers, Dr. Norbert Kömle of the Institut für Weltraumforschung, Graz, and Matt Whyndham of University College London's Mullard Space Science Laboratory, Holmbury St. Mary. I enjoyed working in Graz– a total of eight weeks– and appreciate the welcome I received from Norbert, his family and colleagues. Thanks are of course due to the Austrian Academy of Sciences for funding my stays there, and to Masara Dziruni and Günter Kargl with whom I also worked.

At MSSL Matt Whyndham (backed by Dr. Alan Smith) has provided much-needed assistance on the experimental front over the past three years, working with me on the densitometer as it evolved as well as all aspects of the experiments presented here. Dr. Ann Chadwick at UKC guided us safely though the radiation protection procedures, and led us to obtain the ^{137}Cs source from Bristol at no cost. The CdTe detector used in the attenuation experiments was kindly lent to us for evaluation by Eurorad, Strasbourg.

I would also like to thank Prof. Tilman Spohn and Dr. Karsten Seiferlin at the Institut für Planetologie, Münster for their support and skilful management of *MUPUS* along the way. It has been a pleasure to work with the international *MUPUS* team.

I would like to thank those at UKC who have contributed to our *MUPUS* activities, in particular Mark Leese, Harjinder Jolly and Malcolm Wright, as well as the University's Research Fund which helped us through the early stages of preparing and submitting the proposal. More recently, James Garry and Dr. Martin Towner have been very helpful in developing our penetrometry research activities. Dr. Chris Solomon of the Applied Optics group introduced me to both Compton scattering and Matlab, as well as being there to discuss the details of my work on backscatter densitometry and Monte Carlo simulation.

Andy Salmon of the Midlands Spaceflight Society provided me with useful information on some of the more obscure aspects of the Soviet / Russian space programme. Maxim Jacobson at the Moscow Aviation Institute has also been helpful in this respect.

The Space Education Trust enabled me to attend the 1996 Summer Session of the International Space University in Vienna– thanks are due to my many ISU friends around the world and to Mrs. Sue Bayford, Executive Secretary of the SET. I would also like to thank the ERASMUS scheme for funding my travel to Austria that year.

The Particle Physics and Astronomy Research Council gave me their support in the form of a three-year quota award, as well as financial assistance for attendance at the

Alpbach Summer School in 1995 and the European Geophysical Society conference in Vienna, 1997.

My supervisor, Dr. John Zarnecki, has provided friendly encouragement and advice throughout. Without John I would not have had the opportunity to work with the *MUPUS* team or test my map-reading skills on the motorways of France, Belgium, the Netherlands and Germany.

Thanks are due to my fellow students in and around Room 164 for their comradeship during my time here– in particular Emma Taylor, Jon Marchant and Nick Shrine for sharing the ups and downs of the writing-up process, whether that be in the project room, Possums Bistro, Woody's or simply slumped happily on the sofa after a large meal. I would also like to thank Nick Shrine for the sterling help he has always provided with our computer systems– I'm not sure how we'd have coped otherwise. Sarah Dunkin and the restaurants around UCL have also been very supportive.

My family have of course supported and encouraged me all the way.

Abstract

The European Space Agency's cornerstone mission *Rosetta* is due for launch in January 2003. It will perform a rendezvous with comet 46P/Wirtanen beyond 3 AU and, following an initial mapping phase, deploy a lander to a selected site on the nucleus surface. The *Rosetta Lander* will provide unprecedented access to cometary material. Some of the most uncertain characteristics of the nucleus material are physical properties such as its density, the structure of the surface layers and its mechanical strength.

MUPUS (Multi-Purpose Sensors for Surface and Sub-Surface Science) is one of the experiment packages selected for the Lander payload which will address certain physical properties and their evolution with time. This thesis focuses on the *in situ* measurement of the density of the surface layers by a radiation densitometer incorporated into the *MUPUS* thermal probe, and on the penetrometry measurements to be performed by an accelerometer mounted in the Lander's anchoring harpoon.

A concept for incorporation of a gamma ray attenuation densitometer into the thermal probe is presented and explored. A ^{137}Cs radioisotope source will be mounted near the tip of the probe and semiconductor radiation detectors situated at the top of the probe will monitor the transmitted count rate during probe insertion, as the intervening material attenuates the radiation. Preliminary experiments to evaluate cadmium telluride (CdTe) detectors for this purpose are presented, as well as results from a specially-developed Monte Carlo computer code designed to model the absorption and scattering of photons in bulk material.

Also presented is a control algorithm to dynamically re-budget the integration time and depth resolution of the instrument as it is inserted by the hammering mechanism. This is required due to: a) the wide range of possible densities the instrument may encounter, b) the variation vs. depth of required integration time, and c) the limited time in which the measurement must be performed. For lower than nominal densities, integration time may be wasted when it could be used to improve the accuracy and depth resolution. For higher densities the integration time at particular depths may not be sufficient to obtain acceptable accuracy; in this case some depth resolution could be sacrificed to improve the accuracy. The proposed algorithm uses the density measured at each point to update the time budget and depth resolution for the remaining stages of penetration.

Although the use of the gamma ray backscatter type of densitometer was eventually rejected in favour of the aforementioned attenuation technique, investigation of the backscatter technique resulted in an extension to the Single Scattering Model– an analytic approximation of its operation. This extended model adds to our understanding of these devices' response to spatial inhomogeneity.

Calculations show that anchoring of the Lander is necessary to avoid possible ejection from the nucleus by gas drag in the case of a landing in an active area. The use of the Lander's anchoring harpoon to perform penetrometry measurements is reported, including the results of preliminary experiments and techniques for analysing the accelerometry data. It is shown that layers with distinctly different strengths may be identified, and that the mean deviatoric stress– a strength parameter– may be constrained to within a factor of about 2.2. This would be a significant improvement on current estimates, which vary by several orders of magnitude.

Together with other investigations on the *Rosetta* mission the densitometry and penetrometry measurements will serve to constrain models of the physical state and evolution of the cometary material found at the landing site. In particular both instruments are sensitive to near-surface layering, which may be expected from theoretical models of cometary activity.

Table of Contents

List of Acronyms

ACC	Accelerometer
ACC-E	Accelerometer External
ANC-M	Anchor Penetrometer
ANC-T	Anchor Temperature Sensor
APXS	Alpha-Proton-X-Ray Spectrometer
CASSE	Comet Acoustic and Seismic Sounding Experiment
CBD	Compton Backscatter Densitometer
CIT	California Institute of Technology
ÇIVA	Comet Nucleus Infrared and Visible Analyser
CNES	Centre National d'Etudes Spatiales
CNRS	Centre National de la Recherche Scientifique
CNSR	Comet Nucleus Sample Return
CONSERT	Comet Nucleus Sounding Experiment by Radio wave Transmission
CONTOUR	Comet Nucleus Tour
COSAC	Cometary Sampling and Composition Experiment
CPPP	Champollion Physical Properties Package
CRAF	Comet Rendezvous and Asteroid Flyby
CZT	Cadmium Zinc Telluride
DIDSY	Dust Impact Detection System
DIM	Dust Impact Monitor
DLR	Deutsche Forschungsanstalt für Luft- und Raumfahrt
DS2	Deep Space 2
DS4	Deep Space 4
ECDR	ESA Critical Design Review
ESA	European Space Agency
FFT	Fast Fourier Transform
IAS	Institut d'Astrophysique Spatiale
IDL	Interactive Data Language
IfP	Institut für Planetologie
IKI (ИКИ)	Space Research Institute (Институт Космических Исследований)
IWF	Institut für Weltraumforschung
JPL	Jet Propulsion Laboratory
KOSI	Kometen Simulation

LAL (ДАС)	Long-term Automated Lander (Долгоживущую Автономную Станцию)
MDS	Microbalance Deposition Sensor
MODULUS	Method of Determining and Understanding Light Elements from Unequivocal Stable Isotope Compositions
MPG	Max-Planck-Gesellschaft
MPI	Max-Planck-Institut
MSSL	Mullard Space Science Laboratory
MUPUS	Multi-Purpose Sensors for Surface and Sub-Surface Science
NASA	National Aeronautics and Space Administration
NEAR	Near-Earth Asteroid Rendezvous
ODS	Optical Deposition Sensor
PEN	Penetrator
PEN-CBD	Penetrator Densitometer
PEN-M	Penetrator Penetrometer
PEN-THC	Penetrator Thermal Conductivity Probe
PEN-TP	Penetrator Temperature Sensors
PI	Principal Investigator
PP	Permittivity Probe
PROP-F (ПРОП-Ф)	Mobile Robot for the Evaluation of the Surface of Phobos (Подвижной Робот Оценки Поверхности - Фобос)
PROP-M (ПРОП-М)	Mobile Robot for the Evaluation of the Surface of Mars (Подвижной Робот Оценки Поверхности - Марс)
PS	Pressure Sensor
RAZREZ (РАЗРЕЗ)	Penetrator with temperature sensors and accelerometer on the LAL
ROMAP	RoLand Magnetic Field Investigation and Plasma Monitor
RTG	Radioisotope Thermoelectric Generator
SESAME	Surface Electrical, Seismic and Acoustic Monitoring Experiments
SRC	Space Research Centre
SSM	Single Scattering Model
SSP	Surface Science Package
SuSI	Suite of Spike Instruments
TM	Thermal Mapper
UCL	University College London
UKC	University of Kent at Canterbury
USSA	Unit for Space Sciences and Astrophysics

1 Introduction

ESA's international *Rosetta* mission to comet 46P/Wirtanen (ESA, 1993; Verdant and Schwehm, 1998) provides the first chance to perform an extended *in situ* analysis of a comet nucleus. Due for launch in January 2003, the mission will rendezvous with the comet beyond 3 AU from the Sun in August 2012. After an initial reconnaissance phase by the Orbiter, a landing site will be chosen and the *Rosetta Lander* deployed towards the surface of the nucleus (*Rosetta Lander* ECDR, 1997). After landing, a number of experimental investigations will be carried out by the Lander's science payload. The Unit for Space Sciences and Astrophysics of the University of Kent is a founding member of one of the instrument teams, *MUPUS*, which aims to investigate the physical properties of the cometary material at and just below the surface (*MUPUS* Proposal, 1995). This chapter introduces the reader to comet nucleus material, some of the reasons why it is worthy of investigation, and outlines the history of *Rosetta*, the *Rosetta Lander* and *MUPUS* in particular. An overview of this thesis in the context of cometary science is then presented.

1.1 Comet Nucleus Material

The nuclei of comets have for many years been cited as likely repositories for primordial material left over from the formation of the Solar System (Huebner, 1990). Why should we expect to find such primitive material in comet nuclei? There are three main reasons (*MUPUS* Proposal, 1995): –

- their formation in the cold environment of the solar nebula;
- their storage at low temperatures for most of the history of the Solar System; and
- their small size which strongly inhibits differentiation and endogenic processing.

The activity of cometary nuclei brings these bodies to the attention of astronomers and, indeed, the general public. However this activity caused by the higher solar flux in the inner Solar System is the main influence thought to modify the remaining material relative to its pristine state. By measuring basic physical properties and their evolution with time *MUPUS* will help us understand how the material near the surface changes with time, in response to thermally induced processes such as the sublimation of volatiles. The surface of the nucleus is the most important interface in the structure of an active comet. Better knowledge of the energy balance across this surface will lead to increased understanding of cometary activity and evolution. This will enable a more confident assessment of the

degree to which the material analysed by the *Rosetta Lander* is representative of primordial comet nucleus material.

The study of cometary nuclei also provides information useful to the understanding of

1. the formation of planetesimals,
2. the early history of the Solar System,
3. the evolution of planets through cometary impacts and
4. the possible origin of life on Earth due to the influx of comets.

Another reason why we might wish to examine cometary nuclei is the potential threat that Earth-crossing comets pose to our planet. In order to defend ourselves against a catastrophic impact we first need to know the nature of the threat– what sort of body has to be dealt with? Secondly, a number of possible methods of defence may require detailed knowledge of the physical properties of the nucleus material, such as its density, strength and mechanism of activity. Applying a sufficient impulse to the nucleus to divert its orbit requires the nucleus mass to be known. Destroying the nucleus requires knowledge of its strength, while artificially inducing a jet of activity on the nucleus requires knowledge of how activity may be initiated and sustained.

Cometary material is thought to be porous and of low density– a result of its probable formation by low velocity aggregation of fluffy grains in the solar nebula (Donn, 1990). It is composed of many different chemical and mineralogical components. These include refractory minerals, organic compounds and ices of volatile compounds such as H_2O and CO. Cometary nuclei were described by Whipple (1950, 1951) as ‘dirty snowballs’. Much of the complexity of cometary activity and nucleus evolution arises from the porosity of the material and the ways in which the many constituent species behave and interact as the nucleus approaches the Sun. This complexity is reflected in the difficulty with which the nucleus' physical state, chemistry and mineralogy can be analysed remotely from Earth or even by spacecraft flyby. Ejection of material by cometary activity is associated with significant physical differentiation and chemical change, such that the nucleus may not be ‘reconstructed’ from this material, merely constrained.

Primitive interplanetary dust grains can be collected by aircraft in the Earth’s upper atmosphere (e.g., Love *et al.*, 1994)– many of these are of a fluffy structure that suggests they originate from porous, undifferentiated bodies. However the volatile components originally present in the comet have of course already been lost through sublimation.

1.1.1 Past, present and future investigations of cometary material

As the field of cometary science progresses, new techniques are being applied. In addition to the continued advances in ground-based astronomy, many new Earth-orbiting observatories have become available at a range of wavelengths. The exploration of the outer planets has moved from the flyby era of the *Pioneers* and *Voyagers* to the orbiter / entry probe era of *Galileo* and *Cassini/Huygens*. In the same way, cometary exploration has moved from flybys (of Giacobini-Zinner (1985), Halley (1986) and Grigg-Skjellerup (1992)) to the *Rosetta* rendezvous and landing mission and NASA's *Stardust* Discovery mission (flyby and coma dust sample collection of Wild 2 in January 2004, returning to Earth in January 2006).

Further cometary missions are planned as part of NASA's New Millennium and Discovery programmes, though in these cases technology demonstration will be a much stronger driver in their design. *Deep Space 4* (*DS4*) is a comet nucleus sample return mission derived from the *Champollion* lander concept conceived for *Rosetta*. It will rendezvous with comet Tempel 1 in May 2005 and return a sample to Earth in May 2010, two years before the arrival of *Rosetta* at comet Wirtanen. In effect the *DS4* mission has 'spun off' from *Rosetta*, and some have questioned both the wisdom of this (should NASA have stayed on board the *Rosetta* mission?) and the validity of *Rosetta* given that it appears to be pre-empted by *DS4*. The issues are complex but one could argue that while *DS4* will demonstrate key technologies and return a small sample to Earth, *Rosetta* will be better equipped to perform a comprehensive *in situ* analysis and set of remote sensing observations over an extended period.

In October 1997 NASA selected another Discovery mission to be targeted at cometary nuclei. CONTOUR (Comet Nucleus Tour) will visit at least three comets to obtain images of the nuclei and analyse the dust and gas flowing from them. CONTOUR is due for launch in July 2002 and will perform comet flybys in November 2003 (Encke), June 2006 (Schwassmann-Wachmann-3) and August 2008 (d'Arrest).

Since the Halley encounters there has also been increased activity in the laboratory using cometary analogue materials. In particular the series of KOSI (Kometen Simulation) experiments from 1987 $\rightarrow$ 1993 contributed greatly to our understanding of the physical processes involved in the modification of cometary material (see *Geophys. Res. Lett.* **18**(2), 1991 for several KOSI-related papers).

From an astronomical perspective, three major events have pushed cometary science forward in recent years. In July 1994 the fragments of comet Shoemaker-Levy 9 impacted

Jupiter's atmosphere. 1996 and 1997 saw the spectacular apparitions of comets Hyukatake and Hale-Bopp. These three events occurred at a time when an unprecedented array of observational tools had become available on Earth, in Earth orbit and in interplanetary space. While there remains much analysis and interpretation to be performed on the data obtained during these three events it is already clear that the knowledge obtained will prove useful in the next phase of the exploration of comets by spacecraft. The Shoemaker-Levy 9 impact in particular provided more information on cometary nuclei. Certainly the main qualitative conclusion is that nuclei are delicate and easily disrupted, suggesting both low density and porosity.

Many questions remain about the physical nature of cometary material. These are summarised in subsection 2.1.4 (page 41).

1.2 History of the Rosetta Mission

In May 1985 ESA's Solar System Working Group made an initial recommendation for a 'Mission to the Primitive Bodies of the Solar System' as a cornerstone of the new *Horizon 2000* science programme (ESA SP-1070, 1984). Short-period comets were selected as candidates for the mission's primary target. Known briefly as the Comet Nucleus Sample Return (CNSR) mission, it had by 1987 been renamed *Rosetta*. This name was chosen to reflect the hypothesis that primordial material found in comets could be the 'Rosetta Stone' to help our understanding of the formation of the whole Solar System.

By the end of 1985 a joint ESA / NASA Science Definition Team had been formed to define in detail the mission's scientific objectives, NASA being envisaged as a partner for ESA on the mission. Planning began in earnest after the *Giotto* spacecraft's pioneering encounter with comet Halley in March 1986, which provided an important 'first look' at the type of body *Rosetta* was due to visit.

An ESA workshop was held at the University of Kent (the home of *Giotto's* Dust Impact Detection System DIDSY) from 15 to 17 July 1986 to bring together the cometary community to look forward to the next European cometary space mission. The proceedings were published as ESA SP-249 (1986).

The report of the Science Definition Team was published in 1987 (ESA SCI(87)3). Work on the sample return mission scenario continued (see Atzei *et al.* (1989) for an overview), producing a Mission and System Definition Document (ESA SP-1125) in June 1991. This outlined the type of spacecraft and mission architecture that would be required. A large commitment from NASA was envisaged in the form of a carrier spacecraft derived

from the Mariner Mark-II bus. This would carry the landing stage to the comet, lifting off from the surface after about 15 days of sampling operations, to bring about 10 kg of cometary material back to Earth in an Earth Return Capsule. Figure 1.1 shows the spacecraft configuration as it would appear during on-comet operations, while Figure 1.2 shows an earlier artist's impression of the carrier lifting off for the return journey to Earth.

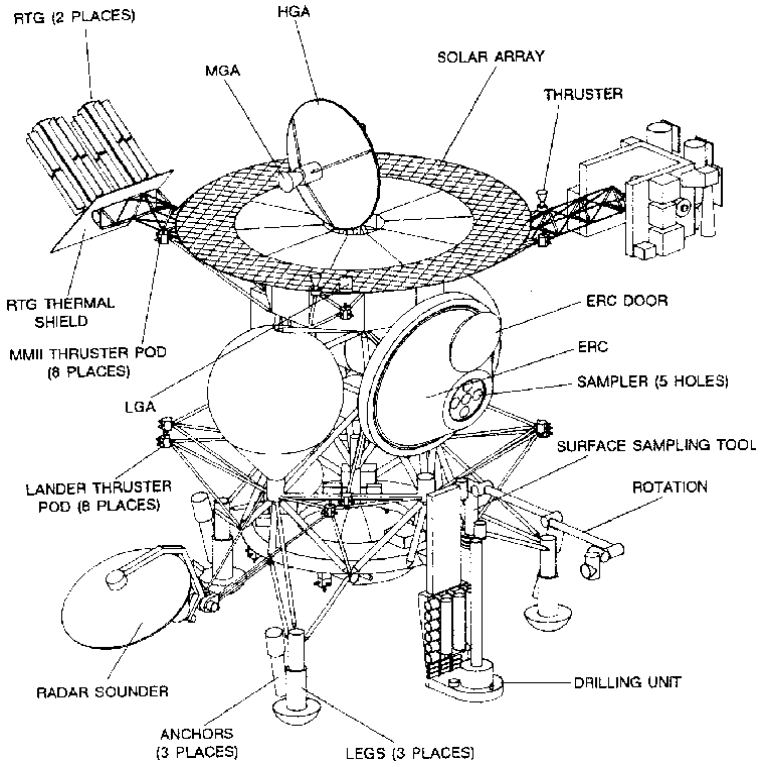

Figure 1.1. The configuration of the *Rosetta* CNSR (Comet Nucleus Sample Return) spacecraft during on-comet operations (from ESA SP-1125, 1991). The three main components are a carrier derived from the Mariner Mark-II bus; a lander section for *in situ* measurements and sample collection, and an Earth Return Capsule which would be brought back to Earth by the carrier and perform a re-entry.

Much attention was paid to the procedure for sampling the comet material and its storage for the journey to Earth. In particular there was concern over the degree to which the material would be changed by the sample-return process. Physical, mechanical and even chemical changes may have been unavoidable, reducing the scientific value of the sample once it had reached the terrestrial laboratory. However a significant advantage of the CNSR concept is that the sample analysis is not restricted by the payload capabilities of a single spacecraft. Techniques can be applied that are not yet possible in space, and the analysis can take advantage of new technology developed both during and after the mission.

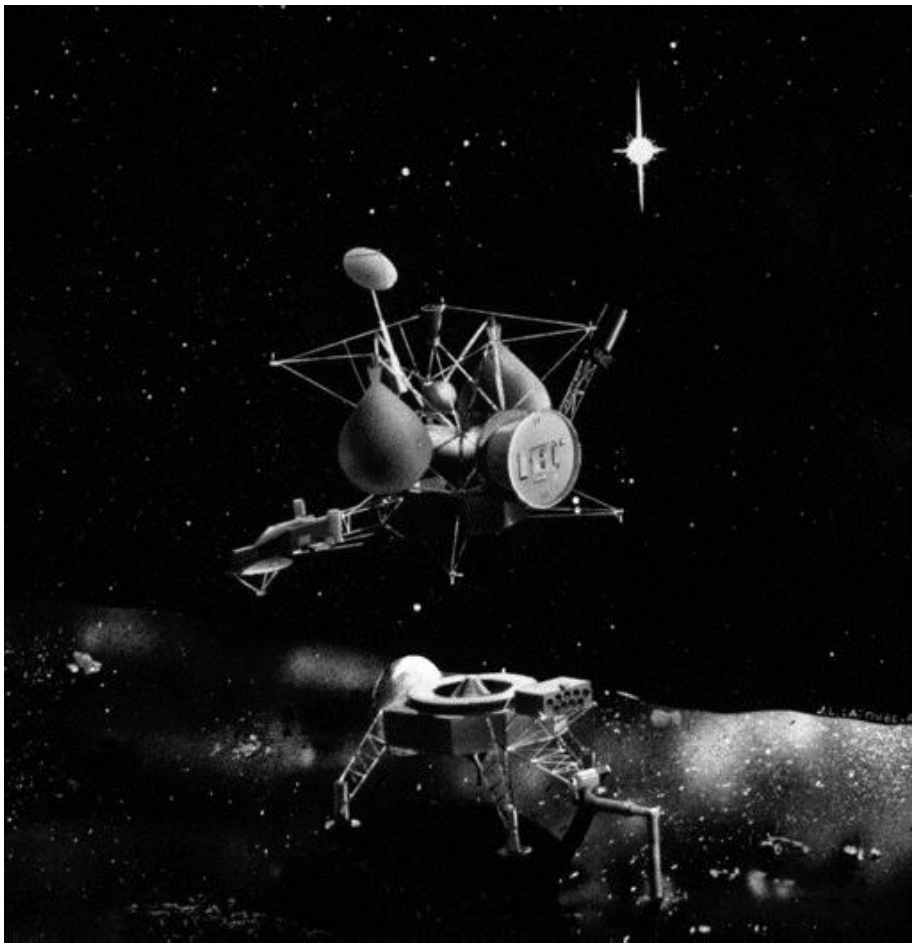

Figure 1.2. Artist's impression of the *Rosetta* CNSR concept (ESA, *circa* 1989). The carrier part of the spacecraft is shown departing for Earth with the sample return capsule.

The goals and requirements of the *Rosetta* CNSR were described as follows (ESA SCI(87)3, 1987; ESA SP-1125, 1991): –

A returned comet sample should preserve such fundamental properties as:

- the chemical and isotopic composition of the individual molecular species of the volatile compounds
- the chemical, isotopic and structural state of the individual phases and crystals constituting higher temperature condensates and aggregates
- the molecular structure and isotopic composition of complex carbon compounds and their aggregates.

To acquire cometary samples which will permit the investigation of the above listed properties, the *Rosetta* mission must:

- rendezvous with an active and relatively fresh comet,
- characterise the surface of the nucleus as active and inactive regions and allow high-resolution imaging and in situ characterisation of the sample site (e.g. temperature),
- acquire three classes of samples: (1) which preserves stratigraphy to a depth of at least 1 m, preferably 3 m, (2) containing all volatile components, sealed to prevent any loss of such volatiles and (3) surface samples intended to provide a large amount of possible less volatile components for analysis,
- store the samples until their return to Earth at a temperature at the most equal to the ambient temperature at the sampling site, but in any case below 160 K and
- distribute cometary samples for study to scientists in dedicated appropriately equipped and staffed laboratories.

Early in 1992, however, financial and programmatic difficulties within NASA (related to its own ill-fated *CRAF* (Comet Rendezvous and Asteroid Flyby) mission proposal) prompted a re-examination of the original sample return concept, with a need to show that the mission could be achieved by European technology alone. As a result, *Rosetta* was re-oriented as a comet rendezvous and *in situ* analysis mission. A new System Definition Study (December 1993) was carried out to define the new mission. An ESA Study Report (ESA SCI(93)7) was produced. This re-examined the scientific objectives and model payload as well as outlining the new mission architecture, thus superseding the previous publications. The *Rosetta* 'comet rendezvous' concept involves a main orbiter spacecraft which will carry both a payload for remote sensing of the nucleus and *in situ* measurements of the dust, gas and plasma environment, and a 75 kg lander to be deployed towards the surface. Rendezvous with the target comet will occur at just over 3 AU heliocentric distance and the primary mission will last until perihelion a year or so later. A computer-generated image of the Orbiter is shown in Figure 1.3. A major difference between this design and the CNSR concept is the use of solar arrays rather than RTGs. The Orbiter will not actually descend to the surface with the Lander (as was the case for the CNSR scenario). Rather, it will stay in orbit around the nucleus and perform a much more extensive remote sensing investigation from rendezvous until perihelion.

Figure 1.3. ESA Visulab computerised image of the *Rosetta* Orbiter (from Visulab web site at www.estec.esa.nl/vislab.html, 1996). The spacecraft bus is derived from a communications satellite.

The scientific objectives of this mission are as follows, reproduced from a paper giving a general overview of *Rosetta* (Schwehm and Hechler, 1994):

- Global characterisation of the nucleus, determination of dynamic properties, surface morphology and composition.
- Chemical, mineralogical and isotopic compositions of volatiles and refractories in a cometary nucleus.
- Physical properties and interrelation of volatiles and refractories in a cometary nucleus.
- Study the development of cometary activity and the processes in the surface layer of the nucleus and in the inner coma (dust-gas interaction).
- Origin of comets; relationship between cometary and interstellar material; and implications for the origin of the Solar System.

During the cruise phase *Rosetta* will encounter asteroids Mimistrobell (September 2006) and Rodari (May 2008). An additional mission goal (Verdant and Schwehm, 1998) is their global characterisation, including the determination of dynamic properties, surface morphology and composition.

Compared with the *Rosetta* CNSR these mission objectives are expressed much more clearly in terms of cometary science. This is perhaps a more satisfactory approach, helping to develop a more carefully focussed mission. For CNSR the resulting mission may have been more directly concerned with satisfying the sample return requirements than achieving a set of scientific objectives.

Reviewing the plans for the original CNSR mission scenario it becomes clear how restricted the possibilities for *in situ* investigations would have been. With only 15 days of surface operations there would have been little or no chance to observe the onset and gradual increase of activity, either at the surface or from cometary orbit. Surface operations would have focussed on the gathering of samples and the characterisation of their context, rather than examination of the undisturbed 'living' material. Certainly it would have been difficult to perform a satisfactory investigation of the physics of cometary activity. Such activity is clearly the most distinctive feature of comets and results from physical properties which are difficult to preserve in a returned sample, including porosity, thermal properties and distribution of volatile phases. The prospects for studying cometary activity more fully have improved since the transition from the CNSR scenario to a rendezvous and landing mission. The longer orbital phase will also allow better global characterisation of the nucleus and its evolution as it approaches the Sun.

An Announcement of Opportunity for the *Rosetta* Orbiter science payload was finally released on 1 March 1995, with a deadline of 1 August 1995. The two lander consortia had already (October / November 1994) made preliminary proposals to ESA (see section 1.3). Following preliminary selection of the Orbiter and Lander payloads in the autumn of 1995 there followed a year-long confirmation phase, during which technical feasibility had to be demonstrated and spacecraft interfaces defined in more detail. The industrial contract was issued to Dornier in March 1997, with completion of the definition phase and start of the main development phase due at the end of 1998. The confirmed Orbiter payload is shown in Table 1.1.

Table 1.1. Confirmed science payload of the *Rosetta* Orbiter.

Instrument	**Description**	
OSIRIS	Optical, Spectroscopic and Infrared Remote Imaging System	
GIADA	Grain Impact Analyser and Dust Accumulator	
ALICE	UV Spectrometer	
VIRTIS	Visible and Infrared Thermal Imaging Spectrometer (visible / infrared mapping spectrometer)	
MIRO	Microwave Spectrometer	
ROSINA	Ion and Neutral Mass Spectrometer	
MODULUS	Isotopic Composition Analyser	
COSIMA	Cometary Secondary Ion Mass Analyser	
MIDAS	Microdust Analyser and Sampler (atomic force microscope)	
RPC	*Rosetta* Plasma Consortium:	
	LAP	Langmuir Probe
	IES	Ion and Electron Sensor
	MAG	Fluxgate Magnetometer
	ICA	Ion Composition Analyser
	MIP	Mutual Impedance Probe
CONSERT	Comet Nucleus Sounding Experiment by Radio wave Transmission (Nucleus Tomography)	
RSI	Radio Science Investigation	

1.3 History of the Rosetta Lander

Until the *Rosetta* mission relatively little effort had been applied to the problem of performing a rendezvous with a comet and deploying a lander to its surface. Among the challenges presented by such a mission scenario are the following: –

- Very low surface gravity (risk of rebound on landing and ejection by reaction forces during mechanical operations)
- Wide variations in temperature across the surface (dependent on nucleus rotation state and topography)
- Wide variations in temperature on both diurnal and orbital timescales
- Cometary activity may eject the Lander from the surface (see section 7.2, page 117) and cause problems for attitude and orbital control of the Orbiter (Oria and Bowling, 1995).
- Cometary dust may inhibit solar cells, optics and mechanisms.
- Uncertain size, mass and rotation state until after arrival of the spacecraft at the comet
- Uncertain surface topography until completion of the mapping phase
- Uncertain surface strength (Lander may penetrate too deep into the surface if the material is softer than expected)

Kührt *et al.* (1997) published a detailed study of the physical risks of landing on a cometary nucleus. The Wirtanen Nucleus Reference Model (Möhlmann, 1996) is a useful survey of the current state of knowledge of key physical parameters, many of which are only very loosely constrained.

The original *Rosetta* CNSR concept involved a large lander attached to the carrier vehicle, as shown in Figure 1.1. Since the reorientation of *Rosetta* to a comet rendezvous the surface mission has changed from being a major component of the spacecraft system (provided by ESA) to the status of a large PI-led instrument mounted on the Orbiter. As a result the design of the landers was left to such PI-led consortia. The 1993 System Definition Study carried out for ESA by industry presented three alternative concepts for a lander, based on three possible landing techniques. Penetrators were also considered– in particular the design for NASA's *CRAF* proposal (see Figure 1.4) was cited as adaptable for *Rosetta*.

The only previous attempt to land on a minor body was made by the Soviet Union's *Phobos 1* and *Phobos 2* missions to the Martian moon in 1988. Both spacecraft carried a Long-Term Automated Lander (*LAL*), while *Phobos 2* also carried a 'Hopper', called *PROP-F*. *Phobos 1* failed before reaching Mars, while *Phobos 2* was lost in Martian orbit before either lander could be deployed. Figure 1.5 shows the *PROP-F* while Figure 1.15 and Figure 1.16 (pages 24 and 25) show the *LAL*.

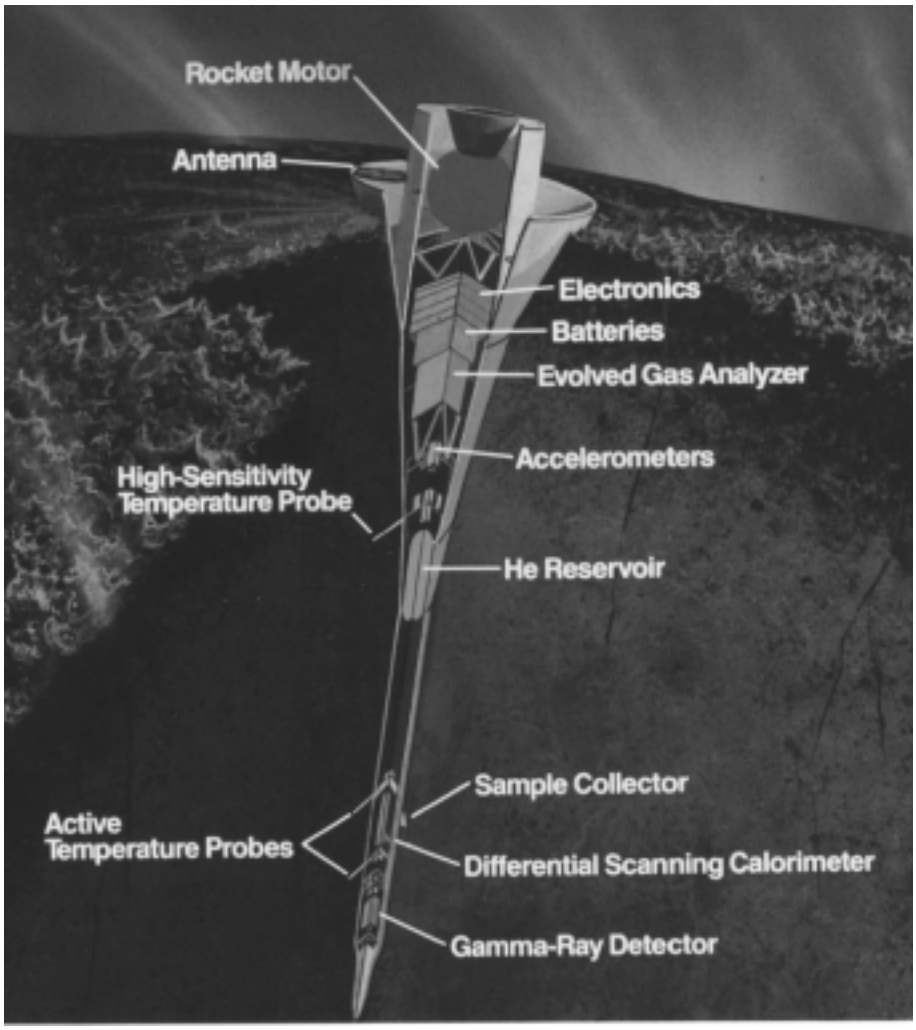

Figure 1.4. Artist's impression of the *CRAF* penetrator (NASA, 1987). It would have been 1.5 m in length and propelled by the rocket motor into the cometary surface at 40 ms^{-1}.

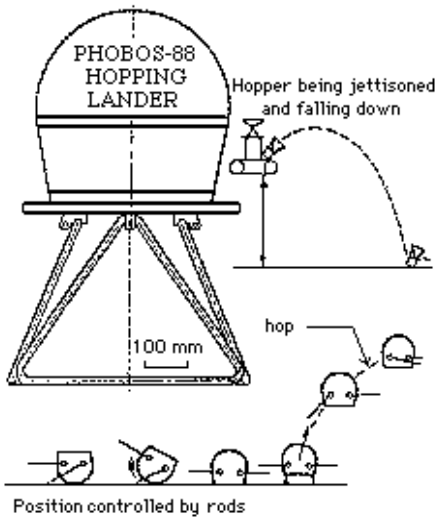

Figure 1.5. Diagram of the *PROP-F* Phobos 2 'Hopper' taken from the *Space Educators' Handbook* web site (http://tommy.jsc.nasa.gov/~woodfill/SPACEED/SEHHTML/).

Figure 1.6 shows the *Rosetta* System Definition Study concept of a probe using the passive touchdown technique, where the impacts would be damped by crushable material. Due to the low gravity the probe would bounce several times before finally coming to rest. This concept is similar in some ways to that used for the *PROP-F*.

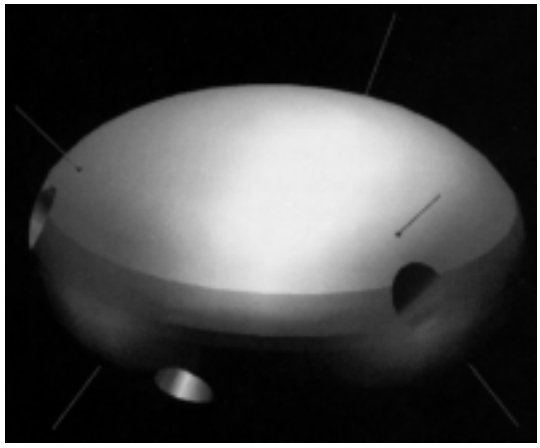

Figure 1.6. Probe concept with passive impact damping, from the System Definition Study, December 1993.

To avoid rebounds the lander could be equipped with a small hold-down thruster to be fired on touchdown. Damping material is only required on the underside and the landing can be performed with greater precision. However, this method is less suitable at higher landing velocities than the passive technique. Figure 1.7 shows this concept– of the three landers in the System Definition Study this is the one showing most similarity to the subsequent *Champollion, RoLand* and *Rosetta Lander* designs. Hold-down thrusters were also to be used on the *Phobos LALs*.

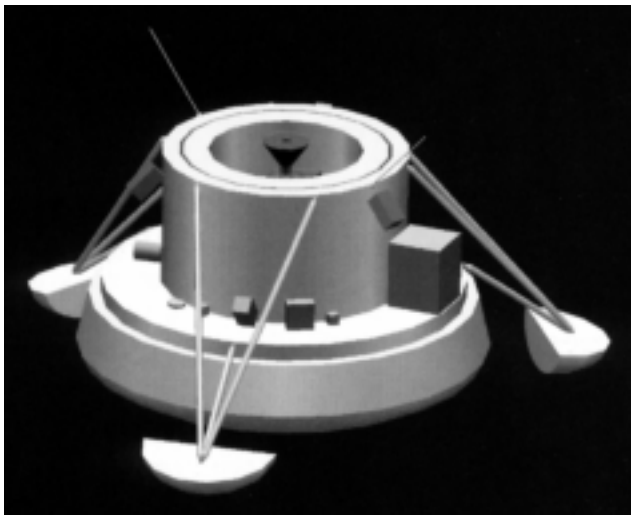

Figure 1.7. Probe concept with active landing, from the System Definition Study, December 1993.

A combined active and passive landing technique is shown in Figure 1.8. In the case of a large comet (and hence high impact speed), the lander would stay folded and follow the same landing scenario as the passive lander. Opening of the three petals would then ensure its correct orientation– a technique reminiscent of the Soviet / Russian small stations used on the Moon and Mars. For low impact speeds the three petals would be deployed prior to landing to act as landing legs in a similar way to the active lander. In this case the hold-down thruster would be used on touchdown.

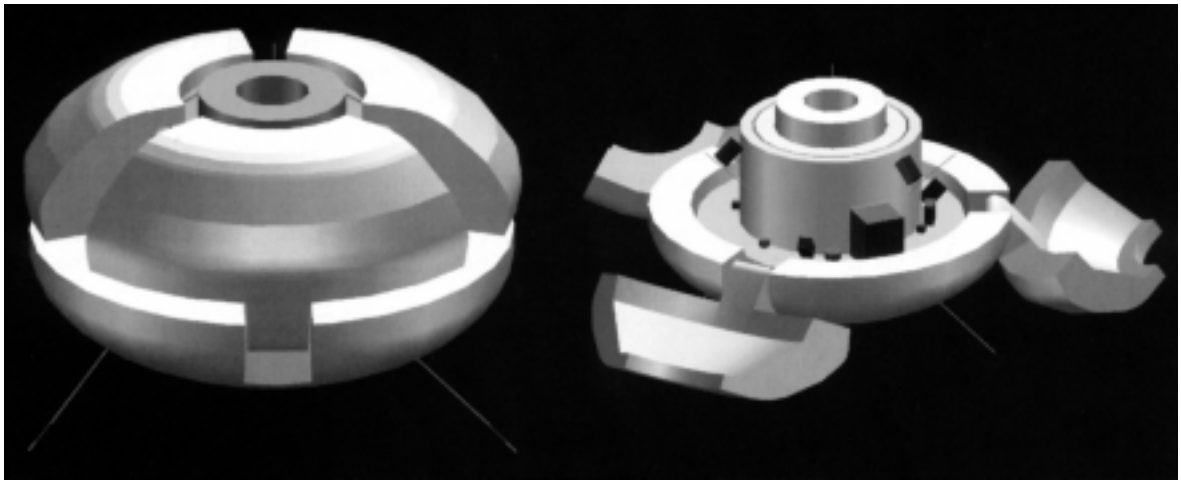

Figure 1.8. Probe concept with combined active and passive landing, from the System Definition Study, December 1993.

In 1993 or early 1994 ESA called for preliminary proposals for 45 kg landers, on the basis that two of these could be accommodated on the Orbiter. Two consortia were formed, one based on a CNES / NASA JPL partnership, the other a German-led consortium centred on the Max-Planck-Gesellschaft (MPG) and the DLR (Deutsche Forschungsanstalt für Luft- und Raumfahrt). An early concept for *Champollion*, the CNES / NASA lander, is shown in Figure 1.9. Crushable feet are used for impact damping and anchoring is achieved by three anchoring spikes at the end of deployable arms. A sampling drill is mounted centrally.

The early design for *RoLand* from autumn 1994 is shown in Figure 1.10. The main body is covered almost entirely with solar cells, and a central hold-down thruster is used. In comparison with *Champollion* the landing gear allows the main body to stand off from the surface. It would appear that this solution causes less disruption to the material under the lander.

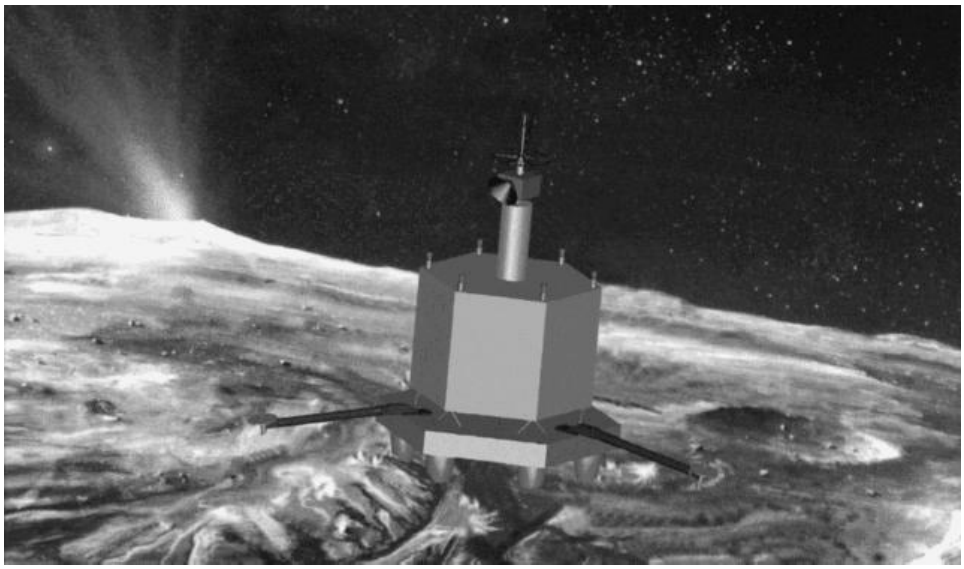

Figure 1.9. Montage of the *Champollion* lander concept on the cometary surface, early 1995 (downloaded from the former *Champollion* web site at NASA JPL).

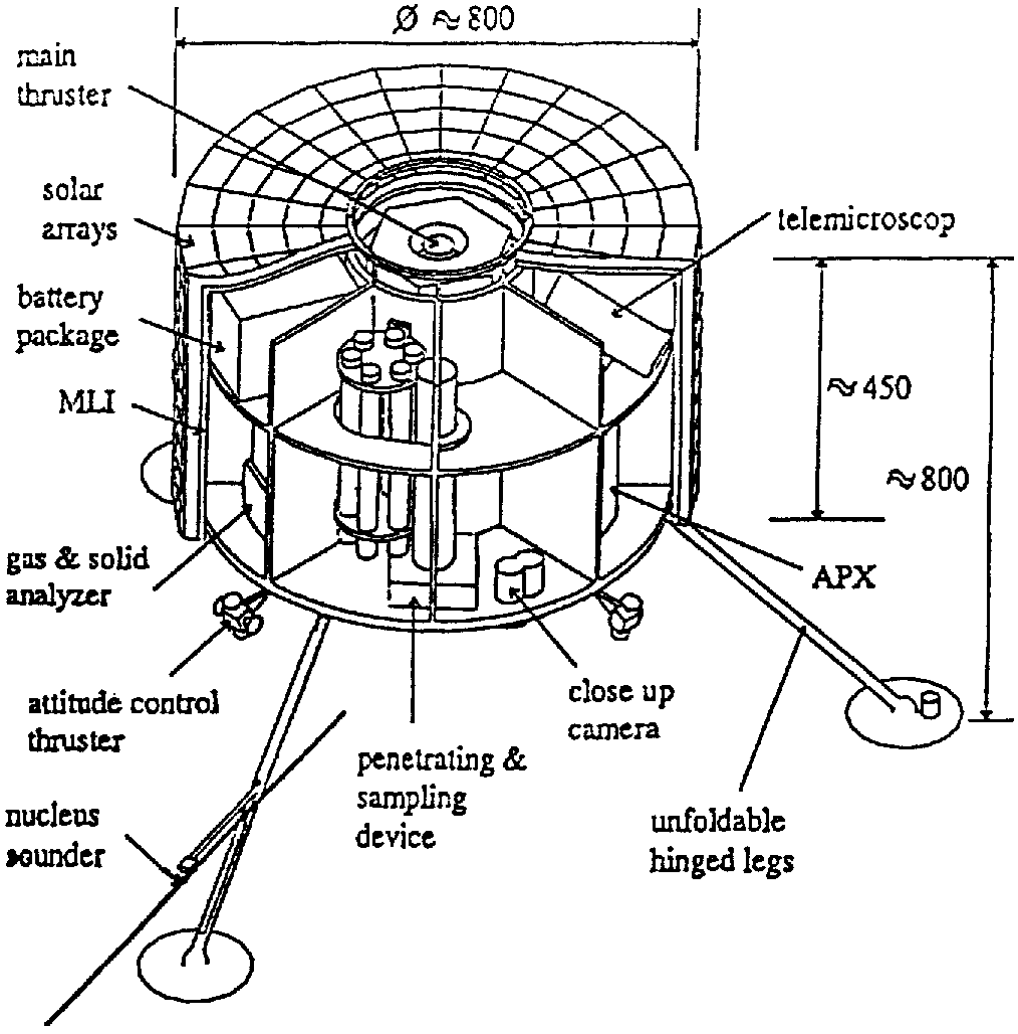

Figure 1.10. *RoLand* design presented in the preliminary proposal to ESA, 27 October 1994. The linear measurements are in mm.

On 1 March 1995 the two landers released Announcements of Opportunity for their science payloads, with proposals due by the end of June. A tentative selection was made in the autumn on the basis that there would then be a year-long definition phase before final confirmation. In November 1995 the two lander consortia presented their formal proposals to ESA based on these tentative payloads.

During summer 1996 ESA declared its preference for a single lander, then in September of that year NASA withdrew funding from the *Champollion* partnership. This left CNES to join the *RoLand* team to build a single, larger lander of 75 kg. This is called simply *Rosetta Lander*, though no doubt this will change to something more poetic before launch. JPL has, however, resurrected *Champollion* in the form of the lander stage of a comet nucleus sample-return mission for the New Millennium programme. An artist's impression of the JPL scheme, called *Deep Space 4* (*DS4*), is shown in Figure 1.11. In addition to the lander the Earth return stage is shown lifting off, as well as an orbiter in the background.

Figure 1.11. NASA JPL concept of the *Deep Space 4* / *Champollion* New Millennium mission, late 1996 (downloaded from the *DS4* web site at ds4.jpl.nasa.gov).

The scientific objectives of the *RoLand* lander (and hence the current *Rosetta Lander*), as given in the Proposal to ESA (1995) were as follows: –

- measurement of the composition of cometary material in terms of elemental and isotopic abundances, molecular and mineral constituents,
- observation of small scale structure and topography of the cometary surface,
- investigation of the internal structure of the cometary body, its stratigraphy and morphology,
- investigation of cometary properties and processes as a function of time and insolation, and
- ground truth measurements for Orbiter experiments.

These objectives are particularly appropriate for a lander for the *Rosetta* mission since they focus only on those questions (aside from ground truth) which cannot satisfactorily be answered by Orbiter investigations. There is ample scope for measurement of physical properties and their evolution with time, an aspect which perhaps reflects the strong KOSI heritage in Germany where the main Lander consortium institutes (DLR and MPG) are based.

In 1995 a demonstration model of the *RoLand* main structure was constructed, reflecting design changes such as a pentagonal rather than cylindrical body and the introduction of a ‘cold balcony’ on the baseplate. The model was constructed using representative lightweight carbon fibre materials (Figure 1.12).

A more up-to-date version of the larger *Rosetta Lander* design is shown in Figure 1.13. The main body of the Lander will be able to rotate with respect to the landing gear, allowing payload instruments to access different parts of the surface underneath and around the Lander. The three legs will be unfolded soon after ejection from the Orbiter. As soon as two of the feet sense touchdown on the surface an anchoring harpoon will be fired down into the surface from within the Lander to avoid rebound. The use of this harpoon for penetrometry is the subject of chapter 7.

Figure 1.12. *RoLand* Demonstration Model, 1995 (photo: DLR), showing the three-legged landing gear, baseplate (800 mm corner to corner diameter) and main body (height 640 mm) covered with solar cells.

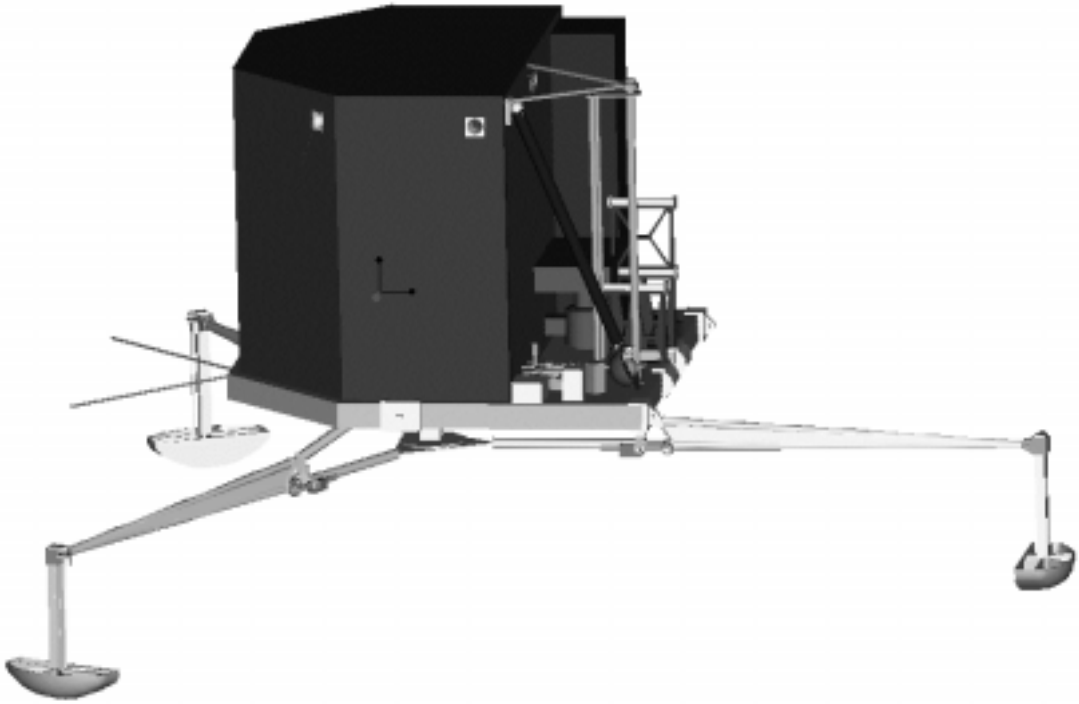

Figure 1.13. Computer-generated view of the *Rosetta Lander* published on the web site (roland.mpae.gwdg.de) in spring 1997. The Lander is shown after the landing gear has been deployed. The baseplate is a square 850 mm along each side, truncated at the two left-hand corners. The solar hood is 610 mm in height.

The confirmed payload of the *Rosetta Lander* is given in Table 1.2. A gamma ray spectrometer was to have been included but this was deleted due to lack of funding.

Table 1.2. Science payload of the *Rosetta Lander*.

Instrument Name	Brief Description		Principal Investigator	Mass Allocated (kg)
APXS	Alpha-Proton-X-ray Spectrometer (elemental composition)		R. Rieder, MPI für Chemie, Mainz, Germany	1.0
COSAC	Cometary Sampling and Composition Experiment (evolved gas analyser for elemental, isotopic, chemical and mineralogical composition)		H. Rosenbauer, MPI für Aeronomie, Lindau, Germany	4.5
MODULUS	Method of Determining and Understanding Light Elements from Unequivocal Stable Isotope Compositions (evolved gas analyser for elemental, isotopic, chemical and mineralogical composition)		C. Pillinger, Open University, UK	2.7
ÇIVA	Comet nucleus Infrared and Visible Analyser (camera system)		J.-P. Bibring, IAS, Orsay, France	3.0
MUPUS	Multi-Purpose Sensors for Surface and Sub-Surface Science (sensors for thermal and mechanical properties; surface density)		T. Spohn, IfP, Münster, Germany	1.5
SESAME	Surface Electrical, Seismic and Acoustic Monitoring Experiments			1.5
	CASSE	Comet Acoustic and Seismic Sounding Experiment	D. Möhlmann, DLR Cologne, Germany	
	PP	Permittivity Probe	H. Laakso, FMI, Helsinki, Finland	
	DIM	Dust Impact Monitor (detection of back-falling dust particles)	I. Apathy, KFKI, Budapest, Hungary	
ROMAP	*Rosetta Lander* Magnetic Field Investigation and Plasma Monitor (magnetometer and plasma package)		H. U. Auster, TU Braunschweig, Germany	0.6
CONSERT	Comet Nucleus Sounding Experiment by Radiowave Transmission		W. Kofmann, CNRS, St. Martin d'Hères, France	1.5

1.4 History of MUPUS

The *MUPUS* (Multi-Purpose Sensors for Surface and Sub-Surface Science) team was formed between late 1994 and the completion of the proposal to the *RoLand* lander in June 1995. Those institutes with major involvement in hardware development and construction are listed in Table 1.3. CIT joined the team in early 1997 after the deletion of the *Champollion* lander. Their experiment (*CPPP*) on *Champollion* payload was similar in many ways to *MUPUS* (thermal and mechanical properties and density measurements).

The author helped research and edit the *MUPUS* proposal (June 1995) which incorporated input from all the institutes listed in Table 1.3 (except CIT). Although *MUPUS* succeeded in the preliminary payload selection for *RoLand*, the lander's payload science committee did not choose all the experiment's subsystems. Those rejected are identified by crosses in Table 1.4.

Table 1.3. Institutes with major involvement in the *MUPUS* experiment.

Institute	**Country**	**Acronym**
Institut für Planetologie, Westfälische Wilhelms-Universität, Münster	Germany	IfP
Space Research Centre, Polish Academy of Sciences, Warsaw	Poland	SRC
Institut für Weltraumforschung, Österreichische Akademie der Wissenschaften, Graz	Austria	IWF
DLR Institut für Planetenerkundung, Berlin	Germany	DLR
Unit for Space Sciences and Astrophysics, University of Kent, Canterbury	United Kingdom	UKC
Mullard Space Science Laboratory, University College London, Holmbury St. Mary, Dorking	United Kingdom	MSSL
Department of Geology and Planetary Sciences, California Institute of Technology, Pasadena	USA	CIT (CalTech)

In parallel with *MUPUS* the same team proposed a slightly descoped suite of instruments for the *Champollion* lander. This proposal (1995), named *SuSI* (Suite of Spike Instruments) was narrowly rejected by the *Champollion* selection committee in favour of the *CPPP* proposal by Ahren's CIT-based team.

Table 1.4. Constituent experimental subsystems of *MUPUS* as originally proposed in June 1995.

Experimental Subsystem	Acronym	Proposed Measurements	Selected
Temperature Probe	PEN-TP	Sub-surface temperature profile	✓
Thermal Conductivity Probe	PEN-THC	Thermal conductivity	✓
Penetrometer	PEN-M	Mechanical and structural properties of surface layers	✓
Accelerometer	ACC	Analysis of landing dynamics and any subsequent motion	×
Compton Backscatter Densitometer	CBD	Bulk density of surface layers	✓
Pressure Sensor	PS	Gas pressure and flow rate	×
Microbalance Deposition Sensor	MDS	Mass and composition of deposited / condensed material	×
Optical Scattering Deposition Sensor	ODS	Optical properties of deposited / condensed material	×
Thermal Mapper	TM	Surface temperature (infrared sensors)	✓
Anchor Penetrometer	ANC-M	Mechanical and structural properties of surface layers	✓
Anchor Temperature Sensor	ANC-T	Sub-surface temperature	✓

Following further definition of *MUPUS* during 1996 and its firm acceptance on the payload of the *Rosetta Lander* in early 1997, the constituent measurement subsystems were as shown in Table 1.5. With the exception of the anchor accelerometer and temperature sensor and the body-mounted infrared temperature sensor, all the subsystems are incorporated into a thin probe deployed from the Lander and gradually hammered into the surface. Figure 1.14 shows the location of the *MUPUS* experimental subsystems on the Lander.

Table 1.5. Post-selection *MUPUS* measurement subsystems. †Subsystems that measure the evolution of these parameters with time (diurnal and orbital variations).

Experimental Subsystem	Measurements
Temperature Probe†	Sub-surface temperature profile
Thermal Conductivity Probe†	Thermal conductivity (line heat source technique)
Penetrometer	Mechanical and structural properties of surface layers
Densitometer†	Bulk density of surface layers (gamma ray attenuation technique during and after probe insertion)
Thermal Mapper†	Surface temp. (infrared sensors at 12-17 μm & 17-23 μm)
Anchor Penetrometer	Mechanical and structural properties of surface layers
Anchor Temperature Sensor†	Sub-surface temperature

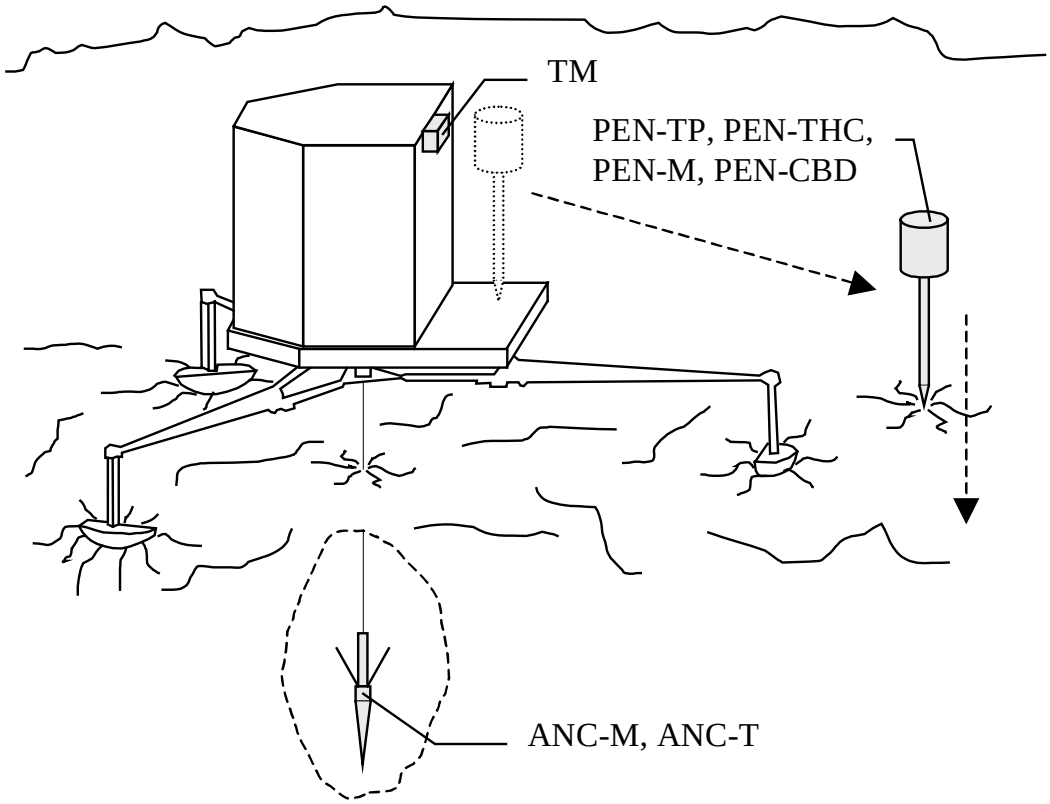

Figure 1.14. Schematic diagram of the *MUPUS* experimental subsystems (shaded) on the *Rosetta Lander* (see Table 1.5 for description).

The scientific objectives of *MUPUS* are as follows (adapted from the *MUPUS* Proposal, 1995): –

- To understand the properties and layering of the near-surface matter as these evolve with time as the comet rotates and approaches the Sun.
- To understand the energy balance at the surface and its variation with time and depth.
- To understand the mass balance at the surface and its evolution with time.
- To provide ground truth for thermal mapping from the Orbiter, and to support other instruments proposed for the *Rosetta Lander* (e.g. SESAME-CASSE).

The *MUPUS* concept as a whole– a synthesis of thermal, mechanical and density instruments in the same package– is relatively new in the history of planetary exploration. While all the separate techniques planned for *MUPUS* have been used in the past, this will be the first time they have been combined in such an integrated instrument. Penetrometers, densitometers, temperature sensors and thermal conductivity probes have all been used (or will be used) on the surfaces of the Moon, Mars, Venus or Titan. There are of course numerous terrestrial versions of the same techniques, most often found in the fields of geophysics and non-destructive testing.

Perhaps the only space instrument resembling the *MUPUS* probe is a device built for the Long-term Automated Landers (*LALs*) of the Soviet *Phobos* spacecraft (*Phobos 1* and *2*) launched in 1988. Since both spacecraft were lost before the landers could be deployed to the surface of Phobos there is very little information available in the scientific literature. However, the author recently obtained a diagram from an IKI document showing the *LAL* and its payload (Figure 1.15). The *RAZREZ* instrument is described as a "Penetrometer with temperature sensors and accelerometer". One presumes that it can be seen in the diagram as the central penetrating probe, apparently also performing the function of anchoring the lander to the surface. However Surkov (1997) states that the *LAL* was anchored using a tethered harpoon. It is also not certain whether the *RAZREZ* instrument was actually launched as part of the payload– it may have been dropped due to insufficient resources. A photo of a *LAL* on display at an exhibition is shown in Figure 1.16.

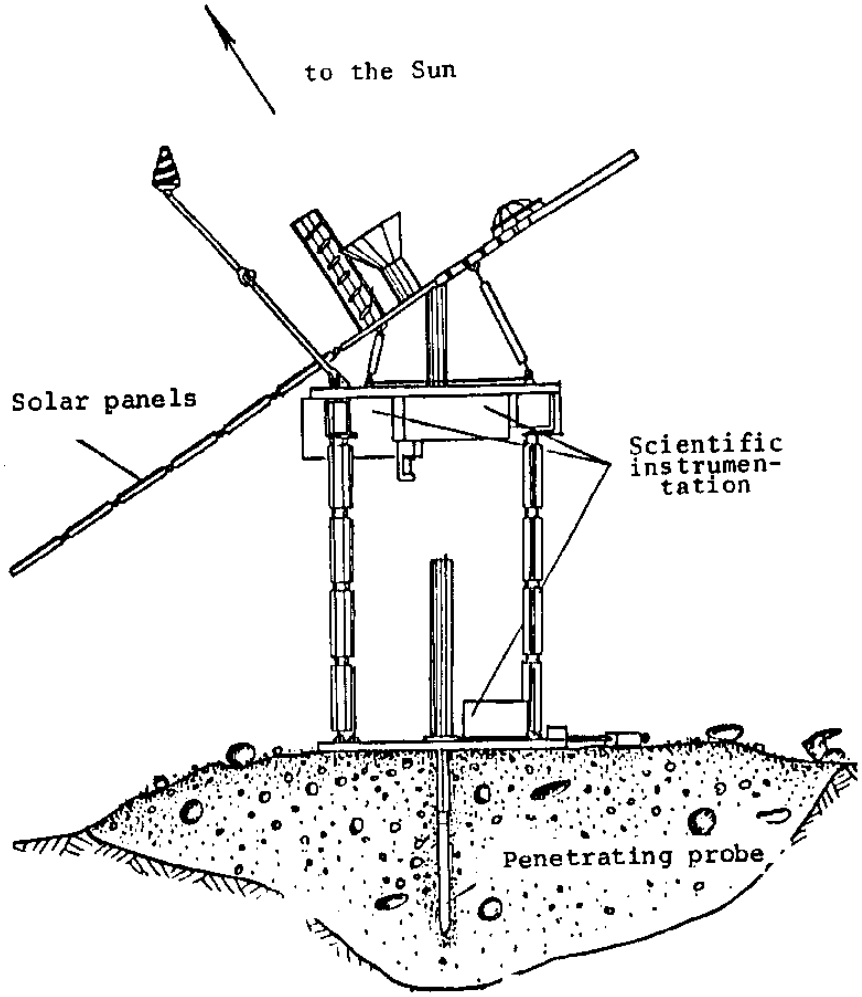

Figure 1.15. Diagram of the Long-term Automated Lander (*LAL*) carried on the *Phobos 1* and *Phobos 2* spacecraft (from an IKI document). Only *Phobos 2* reached Mars, however the mission failed before the *LAL* could be deployed to the surface of Phobos.

In the summer of 1996 NASA withdrew funding for its part of *Champollion*, leaving the CNES-led French participants to join with *RoLand* to develop a single, larger lander (‘*Rosetta Lander*’) of 75 kg mass. Since then, however, JPL has ‘recycled’ the *Champollion* lander design as part of a comet nucleus sample return mission for the New Millennium programme. *Deep Space 4*, as it has become known, will have an orbiter and a lander like *Rosetta*. The lander would incorporate an Earth return stage, mounted on a surface package derived from *Champollion*. It is hoped that the *MUPUS* team will have a chance to participate in *DS4* science activities when the opportunity arises.

Further opportunities to exploit heritage from *MUPUS* include possible ESA missions to Mars (*Mars Express*)– or even the Moon– early in the 21st Century. Other targets for investigations of the thermal and mechanical properties of regolith or porous ice include asteroids and the icy satellites of the outer planets.

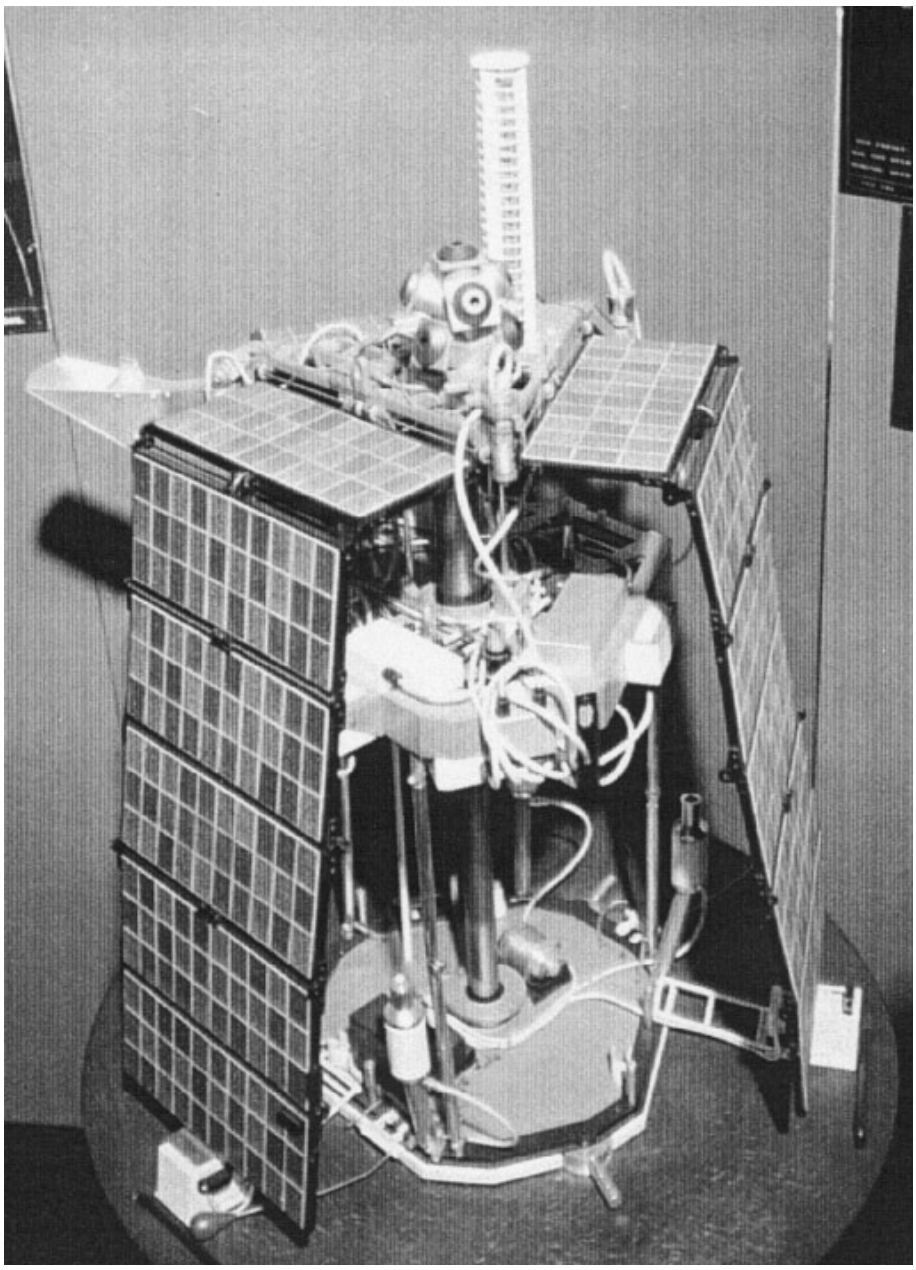

Figure 1.16. The Phobos *LAL* on display at Jodrell Bank (Cheshire, UK), part of an IKI exhibition (photo: Andy Salmon). Note the central penetrating probe.

1.5 Overview of this Thesis in the Context of Cometary Science

How does this thesis relate to cometary science, the *Rosetta* mission, the Lander and the *MUPUS* experiment package? Figure 1.17 is an attempt to show the inter-relation between topics in the form of a 'road map'. Grey boxes indicate areas of original work covered in this thesis. The white boxes indicate necessary input information, previous work and the eventual data produced. The start and end point is 'cometary knowledge'. This leads to the scientific objectives of the *Rosetta* mission, the Lander and the *MUPUS*

experiment. The resulting requirements for the *MUPUS* experiment form the basis for the work carried out for this thesis.

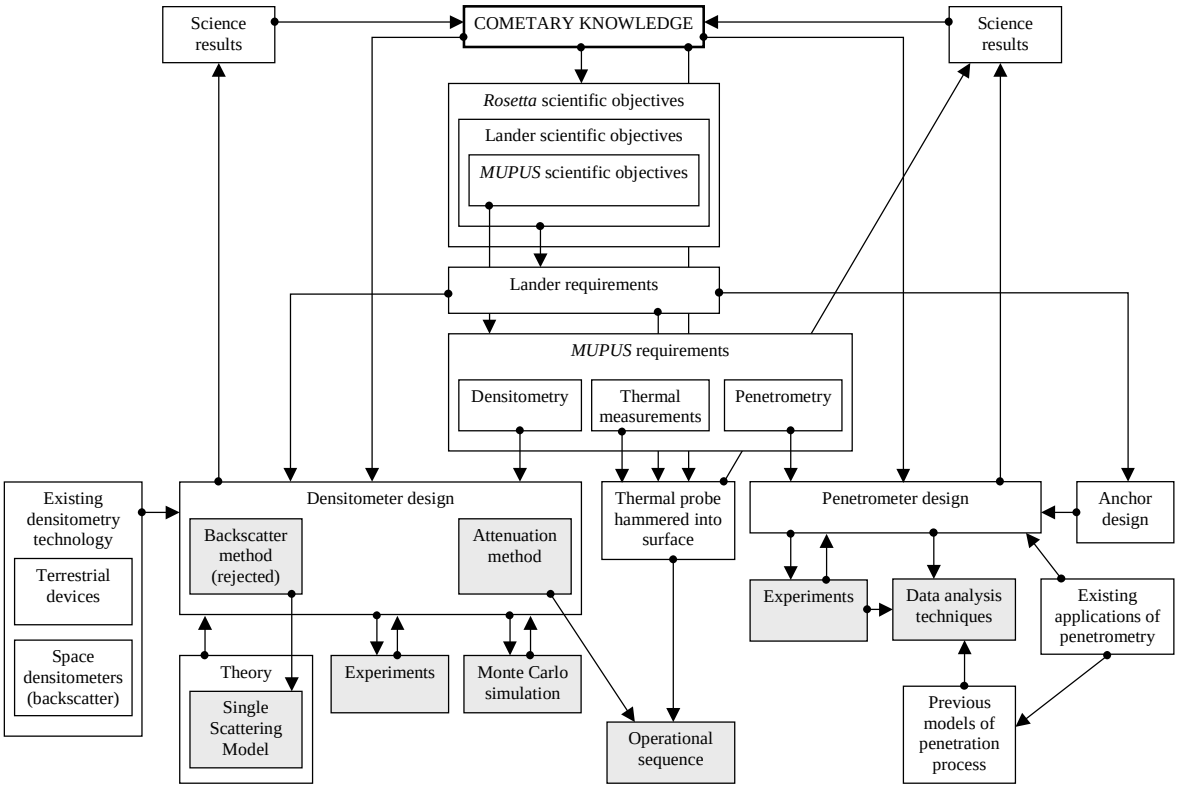

Figure 1.17. Road map for this thesis, showing how the topics inter-relate. Grey boxes indicate areas of original work (including collaboration).

Chapter 2 presents an overview of the relevant scientific and technological background. This includes discussion of the physical properties of cometary nuclei and the relation of density to other key physical parameters. The main questions to be answered by an *in situ* investigation such as *MUPUS* are identified. The technological background of density measurement is reviewed, including terrestrial examples as well as instruments previously flown to the Moon, Mars and Venus. Chapter 3 introduces the rationale and design concept of the *MUPUS* densitometer, taking into account the objectives and constraints for such an instrument. The current attenuation design is discussed, as is the previously considered backscatter design and the reasons for its eventual rejection. A scheme for combining density measurement with gradual insertion of the probe is suggested. Chapter 4 presents the results of a 'spin-off' investigation prompted by study of the backscatter densitometry technique. Consideration of the measurement volume of these devices and their susceptibility to density inhomogeneity led to an extension of the single scattering model approximation of their response. Chapter 5 discusses the application of Monte Carlo simulation to the attenuation design and its utility as a tool for evaluating

candidate configurations. Chapter 6 reports on collaborative experimental work carried out to evaluate the response of a cadmium telluride detector to radiation from a ^{137}Cs source attenuated by varying depths of water. Moving away from density measurement, chapter 7 results from collaborative experimental work on the *MUPUS* anchor penetrometer and techniques for analysing the data obtained. After a quantitative analysis of the rationale for lander anchoring the results of harpoon test shots are presented. The data is compared with results obtained using a recently published penetration model and discussed with respect to penetrometry of cometary surface material. The overall conclusions of the thesis are given in chapter 8.

2 Background

Section 2.1 outlines our current state of knowledge of cometary material with particular reference to its physical properties. The rationale for density measurement is then explained, citing particular areas where knowledge of density is an important constraint for models of the surface material (section 2.1.2). Previous work on the global bulk density of comet nuclei is then reviewed (section 2.1.3) with the aim of defining rough limits for the value to be encountered at the surface. Section 2.1.4 identifies key questions to be answered by a surface density investigation.

Section 2.2 then focuses on the technological background of density measurement using the Compton backscatter of gamma rays, citing examples used on Earth for applications such as borehole geophysics and soil science, as well as backscatter densitometers previously flown to the surfaces of the Moon, Mars and Venus.

2.1 Scientific Background

The physical properties of a comet nucleus are of interest since they constrain models of its formation, evolutionary history, current state and dynamic processes. It is thought that cometary nuclei may still contain pristine material from the formation of the Solar System. The reasons to expect this are the cold formation of cometary nuclei in the solar nebula, the absence of significant endogenic processing due to their small size, and their cold storage for most of their history in the outer Solar System or Oort cloud (*MUPUS* Proposal, 1995).

There are many processes that may have modified the cometary material present in a currently active comet, as shown in Table 2.1. It is important to understand the importance of these modification processes, both in their own right and from the point of view of gauging the degree of sample pristinity. For instance the balance between crust formation and surface erosion is a central issue for the study of nucleus activity, while the pristinity of a sample obtained from 1 m depth is of great concern to those investigators studying the chemical, mineralogical and isotopic composition of material obtained from beneath the surface by a sampling drill.

Table 2.1. Some physical processes capable of modifying cometary material.

Agent	Resultant processes
Solar radiation (heat flux)	sublimation of volatile components ejection of grains from surface by gas drag recondensation sintering of ices phase changes of volatile components thermally-induced chemical changes mechanical change due to thermal cycling
Radioactive decay (e.g. of ^{26}Al)	change in isotopic composition phase changes triggered by internal heating chemical change triggered by ionising radiation
Solar wind & UV	formation of organic material near surface
Cosmic rays	chemical modification (formation of tholins near surface– see McDonald *et al.* (1996))
Dust impacts	surface erosion accumulation of impactor residues chemical and physical changes at impact sites
Gravity	tidal disruption on close encounter with a planet self-gravitation if nucleus becomes large enough

When analysing cometary nucleus material, what physical parameters are (in principle) available for measurement? Key physical properties can be seen in Table 2.2, categorised into several broad areas. In addition to these there are of course the fundamental global parameters of the whole nucleus, including size, shape and rotation state. While measurements of many of these properties may in themselves only weakly constrain models of the nucleus, the combination of a sufficient number of synergistic properties is much more powerful.

Table 2.2. Key physical properties of cometary nucleus material.

Category	Property
Thermal	conductivity diffusivity specific heat capacity
Mechanical	strength (compressive, tensile, shear) Young's modulus, Poisson ratio density
Electromagnetic	dielectric constant (complex permittivity) magnetic field
Optical	spectral variation of absorption and scattering (e.g. albedo)
Structural	layering porosity grain size
Energy Balance	solar flux (reflection, absorption) thermal radiation phase changes (latent heat of sublimation, etc.) vapour transport
Evolution with Time	diurnal orbital activity-triggered events (e.g. erosion, seismic activity)

2.1.1 The physical nature of cometary material

The physical nature of cometary material is much more comprehensively reviewed elsewhere. Useful general starting points include the books *Comets in the Post-Halley Era* (eds. Newburn *et al.*, 1991); *Physics and Chemistry of Comets* (Huebner, 1990) and *Comet Halley: Investigations, Results, Interpretations* (ed. Mason, 1990). The proceedings of a workshop on the physics and mechanics of cometary materials have been published by ESA (ESA SP-302, 1989). Even more directly relevant to *Rosetta* are the Nucleus Reference Model (Möhlmann, 1st ed., 1996) and a paper by Klinger *et al.* (1996). Key physical parameters from the Reference Model are shown in Table 2.3. There are many

papers focussing on particular aspects, including a large number on the global characteristics of cometary nuclei and their structure (e.g. Hughes, 1996) as well as models of the thermal behaviour of porous ice / dust mixtures and their implications for the whole nucleus (Benkhoff and Huebner, 1995; Prialnik and Bar-Nun, 1990; Steiner and Kömle, 1991; Fanale and Salvail, 1990). Some papers discuss models applied directly to the *Rosetta* target comet (Benkhoff and Boice, 1996; Podolak and Prialnik, 1996). Of particular interest to *in situ* investigations from a lander are papers concerning the surface crust or regolith (Kührt and Keller, 1994; Möhlmann, 1994; Rickman *et al.*, 1990). For a discussion of the strength of cometary material see section 7.3, page 125.

In summary, cometary nuclei are now established to be solid bodies comprising a mixture of ices (dominated by H_2O and CO), minerals (e.g. silicates of Fe, Mg, Ca and Al) and hydrocarbon compounds (containing C, H, O, N). In addition to the general sources mentioned above, the *Rosetta* Mission and System Definition Document (ESA SP-1125) contains a review of cometary material composition.

Comet nuclei are thought to have formed in the solar nebula by some sort of collisional process (the details being dependent on such local conditions in the nebula as temperature and relative velocity– see Bridges *et al.* (1996)). Individual grains are thought to have accumulated into aggregates, which in turn collided to form macroscopic bodies (Donn and Meakin, 1989; Donn, 1990). Cometary nuclei may possibly be pseudo-fractal in nature, showing self-similar structure on a wide range of scales. This would reflect the collisional accumulation of fragments from the smallest grains to the largest building blocks.

Dynamic evolution of those comet nuclei not eventually swept up into planetary bodies can lead to their entry into the inner Solar System and resultant activity, or indeed their complete ejection from the Solar System. Close encounters with the Sun or planets can lead to tidal disruption, as was seen in the case of comet Shoemaker-Levy 9. There is some debate as to the end state of nuclei no longer able to sustain activity– will a nucleus completely disperse or might a non-volatile ‘dead’ nucleus remain? In the case of the latter, are the remnants distinguishable from asteroids?

As mentioned above, a significant fraction of the effort expended in the study of cometary nuclei is in the field of thermal evolution and the processes involved. Thermal inputs (beyond the background) come from the absorption of solar radiation, decay of radionuclides, chemical processes and phase changes. Conduction, radiation and gas flow are competing transport processes within the porous material, while mass and energy

balance provide boundary conditions at the surface. At the surface itself the physics of the thermal processes within the nucleus must interface with the physics of the inner coma.

Table 2.3. Summary of physical parameters from the first edition of the *Rosetta* Nucleus Reference Model (Möhlmann, 1996).

Property		Value		
		Min	**Nom**	**Max**
Nucleus size				
Spherical nucleus	Radius (m)	600	700	800
	Volume (m^3)	9.05×10^8	1.44×10^9	2.14×10^9
	Surface area (m^2)	4.52×10^6	6.16×10^6	8.04×10^6
2:1 prolate sphere	Large radius (m)	952	1111	1270
	Small radii (m)	476	556	635
	Surface area (m^2)	4.3×10^6	5.8×10^6	7.6×10^6
1:2 oblate sphere	Large radii (m)	756	882	1008
	Small radius (m)	378	441	504
	Surface area (m^2)	5.5×10^6	7.5×10^6	9.7×10^6
Mass-related properties				
Bulk density (kgm^{-3})		200	400	600
Porosity (material dominated by organics and silicates of density 3000 kgm^{-3})		0.80	0.87	0.90
Porosity (material dominated by ice of density 1000 kgm^{-3})		0.40	0.60	0.80
Mass (kg)		1.8×10^{11}	5.75×10^{11}	1.3×10^{12}
Escape velocity (ms^{-1})		0.17	0.331	0.54
Surface gravity (ms^{-2})		1.89×10^{-5}	7.83×10^{-5}	2.38×10^{-4}
Mechanical properties				
Tensile stress sufficient to disrupt nucleus (Pa)		50	500	950
Compressive strength (Pa)		10^3	10^4	10^5
Young's modulus (low-density dry snow approximation) (Pa)		3×10^6	3×10^7	3×10^8
Poisson ratio		0.1?	0.3	0.4?

Thermal properties			
Specific heat capacity ($Jkg^{-1}K^{-1}$) (Giauque and Stout, 1936)	$7.49 \times T[K] + 90$		
Thermal conductivity ($Wm^{-1}K^{-1}$) (porous dust & crystalline ice)	0.05	0.4?	1.0
Thermal conductivity ($Wm^{-1}K^{-1}$) (solid ice)	$567 / T[K]$		
Thermal conductivity ($Wm^{-1}K^{-1}$) (amorphous ice)		7.1×10^{-7}	
Coefficient of thermal expansion (K^{-1})		5×10^{-5}	
Latent heat of sublimation (Jkg^{-1})	$2.888 \times 10^{6} - 1.116 \times 10^{3} \times T[K]$		
Surface temperature (K) (active area)	130	170	215
Surface temperature (K) (inactive area)	130	260	380

Electromagnetic properties			
Static dielectric constant ε_0	4		15
High frequency dielectric constant ε_∞	1.3		2.3
Albedo	0.03	0.04	0.05
Emissivity	0.9		1.0

2.1.2 Rationale for density measurement

While a value for the bulk density of the entire nucleus can be obtained by the *Rosetta* Orbiter, we may expect there to be significant variations in density on a range of linear scales, as would be the case if the nucleus were a pseudo-fractal body (Hughes, 1996). We may also expect the density at the surface to have changed relative to the undisturbed material. The sublimation and loss of volatile components is the principal modifying process, with recondensation, crust formation (Kührt and Keller, 1994) and surface impacts (Matese and Whitman, 1994) as possible secondary processes. The model of Benkhoff and Huebner (1995) showed that density can not only decrease due to the loss of volatiles but also increase just below the 'sublimation fronts' of volatile components, due to the inward transport and condensation of volatiles.

The surface density at the landing site may tentatively be applied to other parts of the nucleus surface only if data from the Orbiter can demonstrate the landing site to be sufficiently representative of those areas. This is an issue that arises frequently in planetary

surface missions– great care must be taken in applying more widely the single-point measurements made at the landing site. A value of material density on its own is of course rather less important than the conclusions that may be drawn after combination with other measurements at the same location. In this way the physical state and physical processes may be better constrained and understood.

It is useful here to classify the characteristics and phenomena of cometary nuclei into those which can be considered to affect the density ('input parameters') and those which can be considered to be affected *by* the density ('output parameters'). This framework is then useful in the subsequent analysis of density data. The two groups are shown in Table 2.4 and Table 2.5.

Table 2.4. Features affecting the density of cometary nucleus material.

Environment and collision dynamics of the grains and fluffy aggregates which form planetesimals in the solar nebula (Donn, 1991). Impacts may either compress or 'porosify' the material.
Composition (sum over mineralogical components; determines density of grains); post-formation chemical evolution
Porosity (ϕ, defined as the fractional volume of voids)
Collision history (post-formation impacts of cosmic dust)
Thermal evolution (e.g. sublimation & recondensation)
Self-gravity of comet (compression if stress is large enough)

From the point of view of *MUPUS* the combination of density profile with thermal and mechanical measurements is of most interest. The temperature profile along the length of the probe will be monitored with resistance temperature detectors. The finite thermal conductivity along the length of the probe will tend to smooth out the temperature profile. For this reason the data will have to be inverted numerically to obtain the profile that would have existed had the probe not been there (Hagermann and Spohn, 1998).

Table 2.5. Features affected by or correlated with the density of cometary nucleus material.

Thermal properties (conductivity, diffusivity, temperature profile, specific heat capacity) (Seiferlin *et al.*, 1996).
Mechanical strength (compressive, tensile, shear)
Mineralogical profiles
Seismic velocity (depends on both density itself and the density dependence of the elastic constants)
Dielectric constant (complex permittivity)
Electrical resistivity
Balance between mantle formation and erosion (Kührt and Keller, 1994).
Attenuation coefficients for absorption and scattering of radiation
Gravitational field of comet

The *MUPUS* Thermal Mapper (TM) sensor (Knollenberg *et al.*, 1998) will provide the surface temperature boundary condition as well as a measure of the thermal inertia P (resistance of a material to temperature change), obtained using observations over day / night cycles:

$$P = \sqrt{\kappa_{\mathrm{p}} \rho_{\mathrm{b}} c} \quad , \tag{2.1}$$

where κ_{p} is the thermal conductivity of the porous material, ρ_{b} its bulk density and c the specific heat capacity.

The periodic solar heat flux due to the rotation of the nucleus (with period T_{rot}) will generate an evanescent heat wave propagating into the surface. Monitoring the evolution of the near-surface temperature profile may enable determination of the thermal skin depth, which will most easily be measurable if it is similar in scale to the probe. The skin depth d_{skin} is related to bulk density as follows:

$$d_{\mathrm{skin}} = \sqrt{\frac{\kappa_{\mathrm{p}} T_{\mathrm{rot}}}{\pi \rho_{\mathrm{b}} c}} \quad . \tag{2.2}$$

The line heat source technique will allow the thermal conductivity to be measured, as described by Seiferlin *et al.* (1996) and Banaszkiewicz *et al.* (1997). The heat transport

equation for porous, multi-component material with vapour flow is given in several publications including Benkhoff (1992) and Benkhoff and Huebner (1995):

Heat gained by material
= Heat acquired by conduction
- Heat lost by vapour transport
- Heat lost by sublimation of ice

$$\therefore \quad \left[(1-\phi)\rho_s c_s + \phi\rho_g c_g\right]\frac{\partial T}{\partial t} = \underline{\nabla}\cdot\left(\kappa_p \underline{\nabla} T\right) - \phi\rho_g c_g \underline{v}\cdot\underline{\nabla} T - \sum_{i=1}^{n}\Delta H_i q_i \quad , \tag{2.3}$$

where ϕ is the porosity, $\rho_{s,g}$ the densities of solid and gas, $c_{s,g}$ their specific heat capacities, $\partial T/\partial t$ the rate of change of temperature with time and $\underline{v}$ the vapour flow velocity. q_i and ΔH_i are the sublimation rate per unit volume and enthalpy of sublimation, respectively, of the i'th of n volatile components. The surface temperature is constrained by the balance between net solar flux, thermal reradiation, surface sublimation and heat transport across the surface.

The bulk density ρ_b is given by

$$\rho_b = (1 - \phi)\rho_s + \phi\rho_g \, , \tag{2.4}$$

though for the regime of cometary material $\rho_g << \rho_s$ so we can assume

$$\rho_b \approx (1 - \phi)\rho_s \, . \tag{2.5}$$

Knowledge of the chemical and mineralogical composition from other instruments on the Lander will provide a good estimate for ρ_s, enabling the porosity to be derived.

Density is also a key parameter in dynamic penetrometry since one of the decelerating forces is analogous to hydrodynamic drag and thus proportional to the density and the square of the velocity. Kömle *et al.* (1997) examine the use of the Lander's anchor for penetrometry.

The electrical properties of the nucleus material are also dependent on density, as outlined in the Reference Model (Möhlmann, 1996). On the *Rosetta Lander* one of the instruments of the SESAME experiment will measure electrical permittivity. One of the electrodes for this purpose will in fact be housed in the *MUPUS* thermal probe. The main aim of the permittivity experiment is to monitor changes in the abundance of H_2O (a polar molecule) in the surface layers.

The frequency dependence of relative permittivity (or relative dielectric constant) can be expressed in terms of a complex relative permittivity ε:

$$\begin{aligned} \varepsilon &= \varepsilon' - i\varepsilon'' \\ &= \varepsilon_\infty + \frac{(\varepsilon_0 - \varepsilon_\infty)}{(1 + i\omega\tau)} \quad . \end{aligned} \tag{2.6}$$

Hence, by equating real and imaginary parts,

$$\begin{aligned} \varepsilon'(\omega) &= \varepsilon_\infty + \frac{(\varepsilon_0 - \varepsilon_\infty)}{(1 + \omega^2\tau^2)} \\ \text{and} \quad \varepsilon''(\omega) &= \omega\tau \frac{(\varepsilon_0 - \varepsilon_\infty)}{(1 + \omega^2\tau^2)} \quad , \end{aligned} \tag{2.7}$$

where ε' and ε" are the real and imaginary parts of ε, and ε_∞ and ε_0 are the limits at infinite and zero frequency. ω is the angular frequency and τ is the dipole relaxation time.

Möhlmann (1996) presents the following information from Bader and Kuroiwa (1962) for the values of ε_∞ and ε_0: –

- For low temperatures, $\varepsilon_\infty = 3.2$ and $\varepsilon_0 = 95$ are reported to be standard values for pure compact ice.
- ε_0 increases if the ice is contaminated but decreases if it is cracked. ε_∞ remains unchanged in these cases.
- For dry snow of density 260 kgm^{-3} the values $\varepsilon_\infty = 1.5$ and $\varepsilon_0 = 6.5$ were reported for low temperatures.
- A few degrees below 0°C the values $\varepsilon_\infty = 2.5$ and $13 < \varepsilon_0 < 6.5$ were reported for compact, granular snow. ε_0 approaches 80 for water.
- Both ε_∞ and ε_0 show a more or less linear dependence with density, with $\varepsilon_\infty = 2$ and $\varepsilon_0 = 15$ for 600 kgm^{-3}, and $\varepsilon_\infty = 1.3$ and $\varepsilon_0 = 4$ at 200 kgm^{-3}.

The ranges of values in the Reference Model (Table 2.3) do not take into account mixing of the ice with refractories of unknown electromagnetic properties.

An empirical relation between the real part ε' and the bulk density ρ_b of rocks has been proposed by Ulaby *et al.* (1990). For a range of silicates, carbonates and other materials they obtained

$$\varepsilon' = (1.96 \pm 0.14)^{\rho_b} \tag{2.8}$$

(with ρ_b in gcm^{-3}), though the significant variation in mineralogical composition of the samples chosen resulted in a linear correlation coefficient of R = 0.72– only 50 % of the variance in the data was due to density.

The effective dielectric coefficient of a multi-phase or porous material is in general impossible to solve analytically. For a material whose spatial variations are small in comparison with the scale of the measurement, however, it is possible to determine lower and upper limits for the effective ε, according to the theory of Wiener (1912), which states that

$$\left(\sum_{k=1}^{N}\frac{\phi_k}{\varepsilon_k}\right)^{-1} \le \varepsilon_{\text{eff}} \le \sum_{k=1}^{N}\phi_k\varepsilon_k \quad , \tag{2.9}$$

where ϕ_k and ε_k are the volume fraction and dielectric constants of the k'th of N components. A porous material would thus have an effective dielectric constant ε_{eff} between the following limits:

$$\frac{\varepsilon_s}{1+\phi(\varepsilon_s-1)} \le \varepsilon_{\text{eff}} \le \varepsilon_s - \phi(\varepsilon_s - 1) \quad , \tag{2.10}$$

where ε_s is the dielectric constant of the material at zero porosity.

Scaife (1989) discusses the problem of heterogeneous dielectrics. One approximation attributed to Landau and Lifshitz (1984) applies to heterogeneous materials whose dielectric constant varies from the mean ε by only a small amount $\delta\varepsilon$. The expression is

$$\varepsilon_{\text{eff}}^{1/3} \approx \left\langle \varepsilon^{1/3} \right\rangle_v = \left\langle \left[\langle \varepsilon \rangle_v + \delta\varepsilon \right]^{1/3} \right\rangle_v \quad , \tag{2.11}$$

where $\langle \ldots \rangle_v$ denotes an average over the volume concerned.

Seismic properties are also related to density. The velocities V_P and V_S for P and S waves are given by equations 2.12 and 2.13. Although at first it would seem that V_P and V_S should decrease with density, in fact the elastic constants usually rise rapidly so the reverse is true.

$$V_P = \sqrt{\frac{E(1-\nu)}{(1+\nu)(1-2\nu)\rho_b}} \quad ; \quad V_S = \sqrt{\frac{E}{2(1+\nu)\rho_b}} \quad , \tag{2.12}$$

where E is Young's modulus and ν is Poisson's ratio. Alternatively

$$V_P = \sqrt{\frac{j}{\rho_b}} \quad ; \quad V_S = \sqrt{\frac{\mu}{\rho_b}} \quad , \tag{2.13}$$

where j is the elongational elasticity and μ the shear modulus. The quantity j can also be expressed in terms of the bulk modulus K and μ:

$$j = K + 4\mu/3 \, . \tag{2.14}$$

Nucleus density is a key parameter of relevance to possible future planetary defence systems. A number of methods of defence may require detailed physical knowledge of the nucleus material, including its density, strength and mechanism of activity. Applying a sufficient impulse to the nucleus to divert its orbit requires the nucleus mass to be known. Destroying the nucleus requires knowledge of its strength, while creating an artificial jet of activity on the nucleus requires knowledge of how activity may be initiated and sustained.

2.1.3 Cometary nucleus density measurement

Determination of the bulk density of minor bodies is particularly difficult. Unless an asteroid can be imaged and has a satellite of its own (e.g. Ida and its satellite Dactyl), a simple application of the laws of orbital motion (as can be achieved for all the planets except Mercury and Venus) is not possible. The mass of Ida was constrained by Galileo observations of Dactyl's orbit to $4.2 \pm 0.6 \times 10^{16}$ kg (Belton *et al.*, 1996), and the volume to 16100 ± 1900 km^3 (Thomas *et al.*, 1996). This gave a density of 2600 ± 500 kgm^{-3} (Belton *et al.*, 1995). The masses of several asteroids have been determined by measuring perturbations of the orbits of smaller asteroids or Mars. Only for Ceres, Pallas and Vesta, however, have corresponding volume estimates resulted in densities accurate to 35 % or better (Lewis, 1995). Densities have been obtained for Phobos (1900 ± 100 kgm^{-3}; Avanesov *et al.*, 1991) and Deimos (1340 ± 828 kgm^{-3}; Smith *et al.*, 1995) by means of spacecraft perturbation and imaging. The flyby of the asteroid Mathilde by the NEAR spacecraft produced a value for the mass of $1.033 \pm 0.044 \times 10^{17}$ kg from the radio science experiment (Yeomans *et al.*, 1997). Combined with a volume of 78000^{+12000}_{-11000} km^3 derived from the images this gives a density of 1300 ± 200 kgm^{-3} (Veverka *et al.*, 1997). Mass determination by spacecraft flyby becomes more difficult as the mass of the body decreases or the speed or distance of closest approach increase. This may be the reason why no estimate of the mass of Gaspra appears to have been obtained from the Galileo flyby.

The density of cometary nuclei has been a matter of much discussion (see Klinger *et al.*, 1996, for a review), but it is widely thought that reasonable densities must lie within the range $200 \rightarrow 1500$ kgm^{-3}. This was taken as the range over which a nucleus surface densitometer must operate. The measurement of both mass and volume is problematic.

Unless the nucleus can be imaged, as was the case for Halley (Keller, 1990), the volume of the nucleus can only be derived less directly. This often requires an assumed albedo or activity model. Even for Halley, the mass had to be derived using observations of the non-gravitational perturbations, assuming a model for the activity of the nucleus (Sagdeev *et al.*, 1988; Peale, 1989; Rickman, 1990). Sagdeev *et al.* produced a value of 600^{+900}_{-400} kgm^{-3}. Rickman *et al.* (1987) examined 29 short-period comets and from statistical arguments came to the conclusion that they were most likely to have typical densities below 500 kgm^{-3}.

The tidal break-up of comet Shoemaker-Levy 9 during its close encounter with Jupiter in July 1992 allowed estimates of the density of the parent body to be made, based on models of the disruption and subsequent evolution of the fragments. Boss (1994) calculated for a particular model lower and upper bounds of 702 ± 80 kgm^{-3} and 1500 ± 170 kgm^{-3} respectively, where the uncertainties result from an assumed uncertainty in the perijove radius of the close encounter. The type of model used is actually the dominant source of uncertainty, however. Asphaug and Benz (1994) determined that only a bulk density in the range of $300 \rightarrow 700$ kgm^{-3} would produce the observed chain of clumped fragments.

Rosetta will measure the bulk density of the entire nucleus using camera measurements of the nucleus size and spacecraft tracking measurements of the gravitational influence on the Orbiter. At present it is not clear how accurately the mass will be determined, given the potential problems caused by the non-gravitational forces gas and dust drag will introduce (Oria and Bowling, 1995).

To put the density of comets in context, a summary of the densities of bodies in the Solar System is shown in Figure 2.1. Since differentiation of a body tends to increase its density relative to the original material (due to the action of heat and gravity), we can say that the densities of terrestrial planets and differentiated asteroids and satellites are higher than those of the primordial bodies that formed them. The bodies most comparable in density to comets are thus likely to be the small icy satellites of Saturn (Nicholson *et al.*, 1992) and the most primitive asteroids. The extent to which the densities of captured interplanetary dust particles (Love *et al.*, 1994) reflect the densities of their parent bodies is perhaps rather limited– the grains are depleted of volatiles and their original ejection from a cometary surface would have removed porosity on scales larger than themselves.

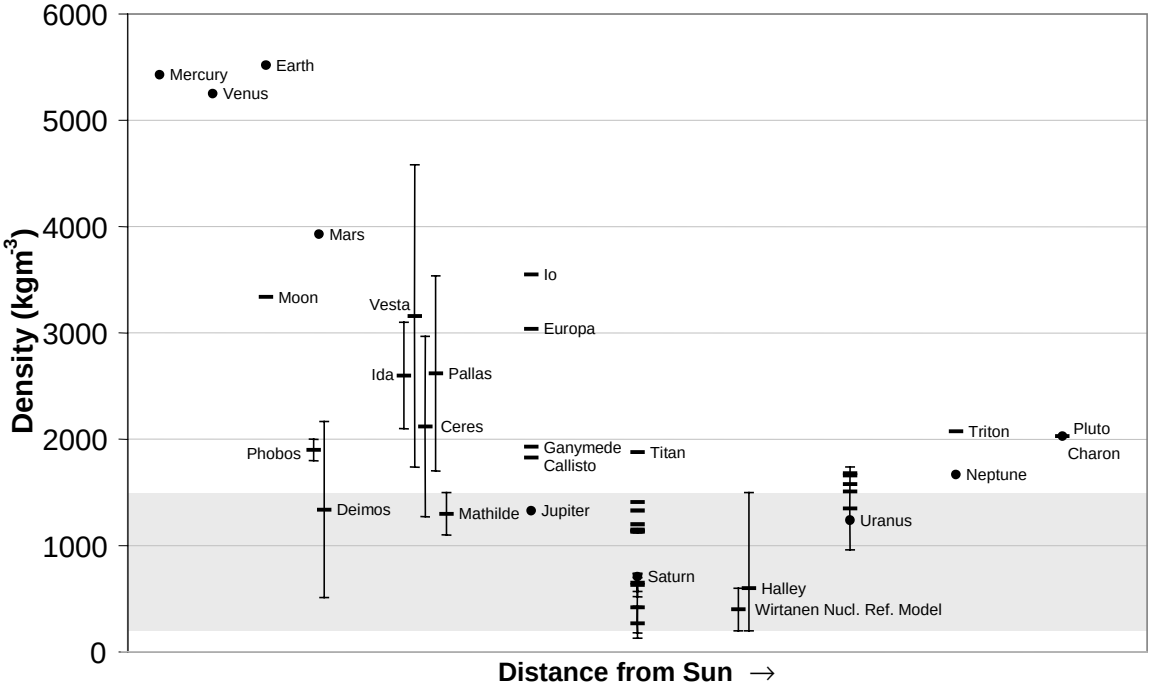

Figure 2.1. Densities of Solar System bodies, where known. Data sources not already cited above are Beatty and Chaikin, 1990, Lang and Whitney, 1991 and Surkov, 1997. The grey band indicates the range of possible densities over which the *MUPUS* densitometer should be able to operate.

2.1.4 Questions to be answered

Based on our current understanding of cometary material one can formulate key questions to be answered by surface densitometry and penetrometry investigations (often in conjunction with results from other instruments): –

- What is cometary nucleus material like? Current models provide only weak constraints on its density (both bulk and surface) and strength. Measurements of both would constrain characteristics such as the material's thermal properties and mechanical behaviour.
- The nature of the surface interface is key to understanding the relation between material in the interior and material emitted from the surface. To what extent is the material at the surface representative of that in the interior?
- What sort of layering does the surface material show, if any? Layering clearly indicates modification– fully pristine material cannot be found above the deepest detectable boundary.

- How does cometary activity affect the surface layers? What proportion of the material is lost from the surface itself, rather than sub-surface layers?

2.2 Technological Background of Backscatter Density Measurement

The low (and uncertain) surface gravity of minor bodies makes it very difficult to 'weigh' a sample of known volume reliably to obtain the local density of surface material. The likely porous, brittle nature of comet nucleus material makes sampling a known volume of material particularly difficult. Two basic methods of radiation densitometry are available– attenuation and backscatter. Neither makes assumptions regarding the local gravity or the material's mechanical properties. The attenuation method is simply the measurement of the change in detected count rate from a source when a material (of known thickness and absorption coefficient) is introduced in between.

The backscatter technique relies on the detection and analysis of Compton scattered photons at the surface of a bulk material that is being irradiated by a source placed some distance away. In comparison with attenuation densitometers the backscatter technique is useful for semi-infinite bulk materials (such as soil or concrete surfaces) or boreholes where the linear geometry of source, sample and detector is not achievable. The technique is also useful for slabs or the walls of long tubes where only one side of the material is accessible. The backscatter method is also attractive in that it requires no moving parts other than deployment to the surface of the material. The basic geometry is shown in Figure 2.2.

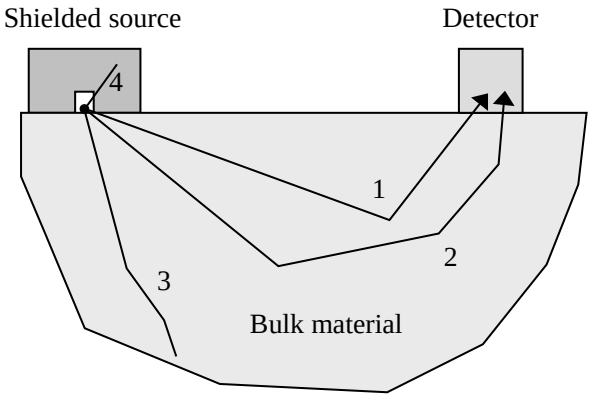

Figure 2.2. Diagram showing the basic geometry of gamma backscatter density gauges. Emitted photons are either 1) detected having scattered once in the material, 2) detected after multiple scattering, 3) lost by scattering and / or absorption in the material, or 4) stopped by the source shielding.

Gamma photons emitted from the source are either 1) detected having scattered once in the material, 2) detected after multiple scattering, 3) lost by scattering and absorption in the material, or 4) stopped by the source shielding. In many practical designs the source and detector are collimated. Table 2.6 lists the factors affecting the detected count rate.

Table 2.6. Parameters affecting detected count rate for a backscatter densitometer.

1	The characteristics of the source: energy, activity and emission direction (collimation).
2	The characteristics of the detector, such as aperture size, field of view, efficiency, energy window and susceptibility to background radiation.
3	The source-detector separation (sonde length).
4	The scattering and absorption characteristics of the bulk material underneath the instrument.

For the range of energies used in backscatter densitometry the dominant interaction is the Compton scattering process, though photoelectric absorption, coherent scattering and electron / positron pair production also occur (pair production can only occur for photon energies above twice the electron rest mass energy, 1.02 MeV). The probability that a photon will undergo Compton scattering is proportional to the number density of electrons in the material. This in turn, to a good approximation, is proportional to the mass density since A/Z is constant (approximately 2) for the commonest isotopes of most elements (as shown in Figure 2.3). Hence the mass attenuation coefficient is almost constant with composition. Hydrogen is the most significant exception, though its mass fraction in most materials is low enough for its effect to be small. Basic knowledge of the material's elemental composition enables the effect to be eliminated altogether. The mass absorption coefficient for pair production is proportional to atomic number, and so it is not a useful process for measurement of composition-independent density. The photoelectric effect becomes more significant with decreasing energy and increasing atomic number, again introducing composition dependence.

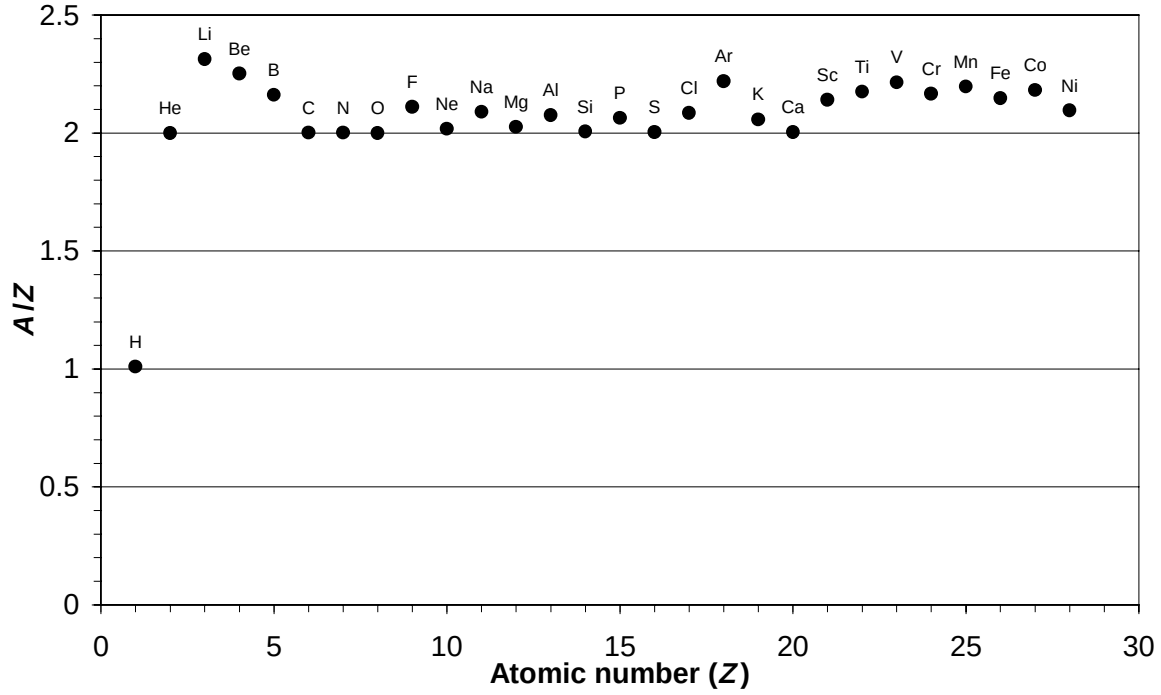

Figure 2.3. Ratio of atomic mass (*A*) to atomic number (*Z*) for elements 1 → 28. All except hydrogen have a ratio close to 2.0.

Most practical densitometers use ^{137}Cs which emits at 662 keV, within the energy range where the Compton process dominates. ^{60}Co (1.17 and 1.33 MeV) can also be used. Backscatter densitometry is feasible outside this range if the elemental composition is known (e.g. using the 59.5 keV emission of ^{241}Am– see Divós *et al.*, 1996). It is desirable to use radioisotopes that emit mostly at a single energy, otherwise source photons would encounter differing interaction cross-sections. The detector cannot distinguish between photons which, when originally emitted, had different energies. Thus an ambiguity arises and the variation of count rate with energy and density becomes much more complex.

The half-life of the radioisotope used is also a constraint– it must be long enough for the device to remain useful for an adequate length of time. ^{137}Cs, ^{241}Am and ^{60}Co have half-lives of 30.2, 433 and 5.27 years, respectively.

For an instrument with a particular sonde length, parameters 1, 2 and 3 in Table 2.6 are fixed and known. The count rate thus varies with density alone (assuming Compton dominance), reaching a maximum at some critical value. Above this density the count rate of scattered photons is reduced by a lack of photons– fewer penetrate far enough into the material to scatter into the detector. Below the critical density the count rate is reduced by a lack of electrons– lower density, therefore fewer scattering centres. Hence in general a particular count rate can correspond to two alternative densities, according to whether

scattering or attenuation dominates. This can cause confusion if both densities are within the range expected for the material in question. Figure 4.1 (page 68) shows an example calibration curve for a backscatter densitometer. Decreasing the sonde length increases the count rate and shifts the peak to higher densities.

Section 2.2.1 reviews the physics of absorption and scattering cross-sections, while sections 2.2.2 → 2.2.8 review selected densitometers already built for use on the Earth and terrestrial planets.

2.2.1 Interaction cross-sections

Figure 2.4 shows the mass attenuation coefficients (which have units of m^2kg^{-1}) for the three significant interaction processes (and their sum) for photons in bulk material, over the energy range 1 keV → 1 MeV. The data (from Storm and Israel, 1970) is shown for selected elements based on their likely abundance in cometary material. Compton scattering dominates the other processes from about 150 keV to beyond the threshold for e^-/e^+ pair production at 1.02 MeV. The Compton (and thus total) cross-sections converge in this region, for all elements except hydrogen since its A/Z ratio is around half that of the other elements. Photoelectric absorption increases rapidly for lower energies. For higher Z the photoelectric cross-section increases and the K edge moves to higher energies. Coherent scattering never dominates the other two processes.

Photon radiation from a ^{137}Cs source occurs almost entirely at 662 keV, with a few less intense emissions at 32 → 38 keV. 662 keV is well within the Compton dominant region, while ^{241}Am emission at 59.5 keV is in the photoelectric domain. Despite this, a small proportion of the photons do undergo Compton scattering– this can be used in cases where the elemental composition of the material is known, or at least constant.

For ideal mixtures of elements (i.e. compounds present in a single solid phase) the combined mass attenuation coefficient is simply the linear combination (by mass) of the constituent elements' coefficients. This also applies to materials where different phases are mixed finely. For coarser mixtures the situation is more complex, as shown in the paper by Umiastowski *et al.* (1977).

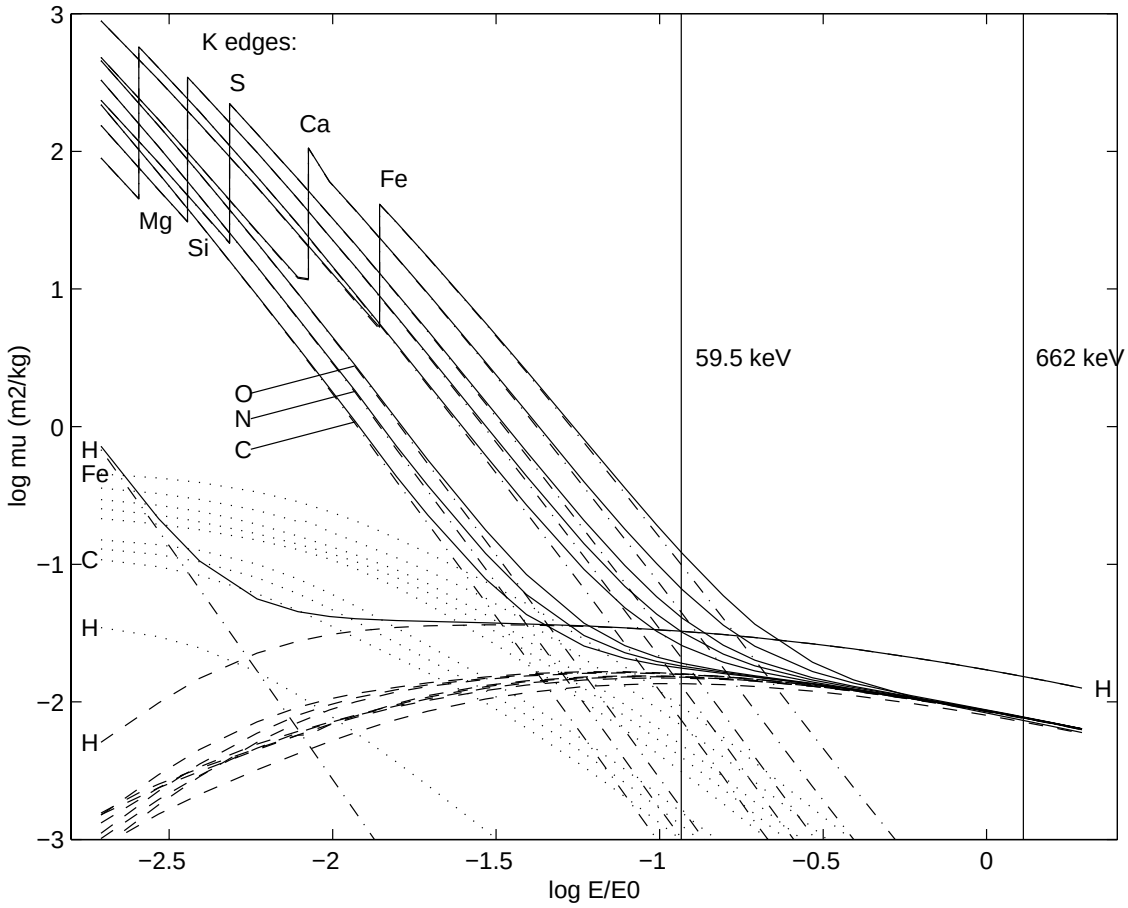

Figure 2.4. Log_{10} of the mass attenuation coefficients for photoelectric absorption (dots & dashes), coherent scattering (dotted line), incoherent (Compton) scattering (dashed line), and the total (solid line). The data is plotted vs. the log_{10} of the reduced energy[1]. The ^{241}Am and ^{137}Cs emission energies at 59.5 keV and 662 keV respectively are shown.

2.2.2 Borehole density logging tools

The most common terrestrial application of backscatter densitometers is in the field of borehole geophysics. The oil industry uses such devices on newly bored wells, hence the term ‘well logging’. The logging tool is slowly pulled up through the borehole, measuring density vs. depth using a backscattering device pressed against the rock. Densitometry is just one of a suite of tools for borehole analysis– a review of well logging in general was published by Snyder and Fleming (1985), and several books on the subject are available (Tittman, 1986; Ellis, 1987; Gorbachev, 1995). Density logging has been in use by geophysicists since the early 1950s (Pickell and Heacock, 1960; Tittman and Wahl, 1965),

[1] The reduced energy is the photon energy divided by the rest mass energy $m_e c^2$ of an electron, which equals 511 keV.

and analogous devices have been incorporated into cone penetrometers for use in soils (Lunne *et al.*, 1997). Figure 2.5 shows the basic arrangement of a gamma ray logging tool used for both density and lithology measurements (Czubek, 1983; Ellis, 1988). Two detectors are used in order to compensate for unevenness in the wall of the borehole and the presence of mudcake remaining from the drilling process. Lithology– related to the mean atomic number (Z) of the material– is determined by examining the lower energies of the detected spectrum (Bertozzi *et al.*, 1981). High Z rock formations give a lower count rate in the low energy window than do low Z formations. This is due to the Z-dependence of photoelectric absorption. The photoelectric parameter P_e is defined by

$$P_e = \left(\frac{Z}{10} \right)^{3.6} \quad , \tag{2.15}$$

and is proportional to the photoelectric cross-section per electron.

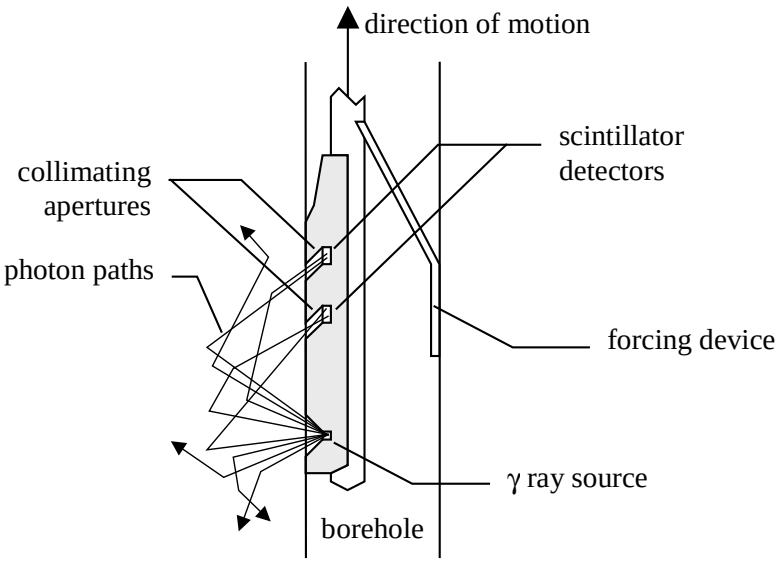

Figure 2.5. Schematic diagram of a borehole litho-density logging tool.

Clearly the borehole density log could form the basis of a device for examining planetary surface material. The detectors and electronics in the logging tool are already quite rugged in order to survive the high temperatures and pressures found in deep boreholes as well as the mechanical shocks as it is deployed and hauled along. The use of a second detector to compensate for irregularities in the rock surface and mudcake between the tool and the rock is also a useful feature.

On the negative side, the density logging tool only generates a point measurement, relying on its motion along the borehole to obtain spatial coverage. It also relies on gravity to reach the lower end of the borehole before logging can start. The instrument is inherently massive due to the shielding required between source and detectors.

2.2.3 Surface density gauges

The backscatter technique has also been applied to surface density gauges used in civil engineering and manufacturing. The density of tarmac, concrete or soil can be measured non-destructively *in situ*. A continuously produced material can be monitored using backscatter– for instance the wall thickness of tubes can be measured (see Putman *et al.*, 1954 for an early example) to provide control feedback to the manufacturing process. A prototype soil density gauge described by Devlin *et al.* (1969) improved the accuracy of the measurement by adjusting the position of the source to provide the optimum sonde length for the density under investigation. From simple scaling arguments one can deduce that smaller sonde lengths are better for higher densities. An associated general theory of backscatter response based on the principle of similitude (Christensen, 1971) was developed by Henderson and McGhee (1986).

2.2.4 Low energy backscatter densitometers

In cases where the elemental composition of the material is known, source energies below the 'Compton window' can be used despite the dominance of photoelectric absorption over Compton scattering. Divós *et al.* (1996) present results obtained by a device using an ^{241}Am source (59.5 keV) and an NaI scintillator detector. The purpose of the device is to examine wooden beams inside buildings for decay and defects. The elemental composition of wood is reasonably well constrained and does not vary significantly within a single piece. Thus changes in density are easily detected– Divós *et al.* (1996) were able to detect a knot in the sample of wood investigated.

Low energy backscatter densitometry can also be used for non-contacting measurement of the concentration of aqueous solutions (e.g. Gayer *et al.*, 1982) such as seawater. This relies on the increase in Z of the liquid rather than the change in density. Such a Z-sensitive measurement can equally be made using the lower end of the backscatter spectrum from a high-energy densitometer, in the same way as the lithology measurement made by borehole logging tools.

2.2.5 Single-sided Compton tomography

Single-sided Compton tomography using X-rays is a more advanced technique than simple backscatter densitometry, requiring relative motion of the sample and source / detector arrangement. It is usually applied to manufactured materials such as aerospace components whose composition is known, though this constraint is removed for systems using the higher energy gamma rays available from ^{137}Cs. Such devices can detect

corrosion or structural defects since they are capable of building up a three-dimensional map of density within the material. *NDT Using Compton Scattering* (1995) is a collected list of abstracts in the field and serves as a useful starting point. Working systems have been reported by authors including Thoe (1993a,b; 1994) and Harding and Kosanetzky (1989). This technique is not to be confused with Single Photon Emission Computed Tomography (SPECT), a medical physics technique where the source radioisotope is distributed through the material under examination.

A more appropriate method for investigation of the near-surface structure of planetary surface materials is ground-penetrating radar, however. The technique is well-developed in terrestrial geophysics and requires less massive equipment, though of course the connection between the radar response and material bulk density is much more complex.

2.2.6 The *Luna 13* densitometer

In December 1966 a backscatter densitometer was used on the surface of another planet for the first time. The Soviet lander *Luna 13* carried out an analysis of the physical properties of the Lunar regolith (Cherkasov *et al.*, 1968a,b). The densitometer ('*Plotnomer*') was deployed from the landing capsule on the end of an unfolding arm, as shown in Figure 2.6.

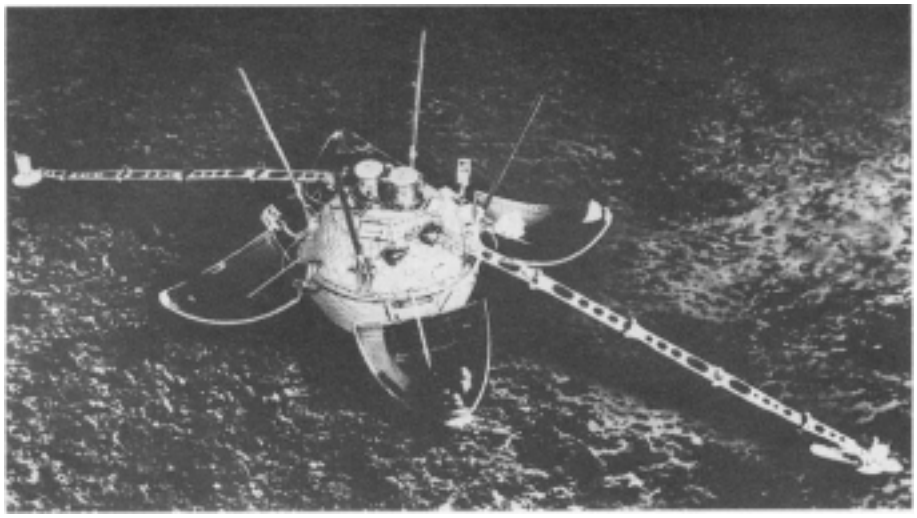

Figure 2.6. Artist's impression of *Luna 13* on the Lunar surface (from Wilson, 1987). The densitometer can be seen at the end of the deployed arm to the right of the picture; the other arm carries a penetrometer.

Although the instrument operated successfully, its reading was ambiguous since only one count rate was measured. The measured value corresponded to either 800 kgm^{-3} or

2100 kgm^{-3}. At first it was concluded that the lower density was more likely, though subsequent analysis of Lunar regolith showed that the upper value cannot be ruled out. A ^{137}Cs source was used together with three groups of gamma counters, whose count rates were presumably added before relay to Earth (hence the ambiguous calibration). The sensor head (shown in Figure 2.7) was 25.8 cm long and 4.8 cm wide.

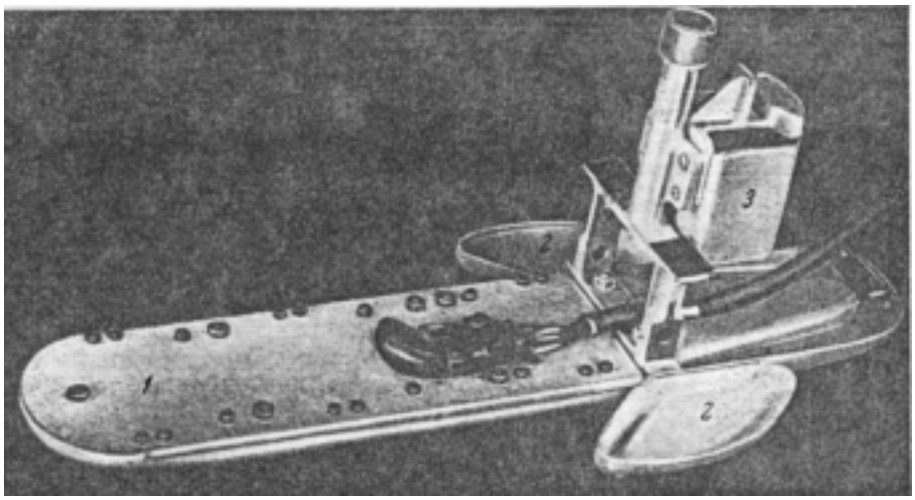

Figure 2.7. Photograph of the *Luna 13* densitometer, known as the 'plotnomer' (from Cherkasov *et al.*, 1968a): 1) detector body, 2) lateral segments, 3) superstructure. The source is mounted at the far right-hand end beyond the shielding block. The total length of the plotnomer was 25.8 cm.

2.2.7 The *Mars 2, 3, 6* & *7* densitometers

The landers of the Soviet *Mars 2* and *Mars 3* missions launched in May 1971 both carried small rovers. These were to have made measurements of density and mechanical strength across the surface. Each rover carried a penetrometer and a gamma backscatter densitometer. Figure 2.8 shows an artist's impression of the *Mars 3* lander– the rover can be seen on its unfolding deployment arm on top of the lander.

Unfortunately the *Mars 2* lander failed during descent through the atmosphere and the *Mars 3* lander failed only a few seconds after landing. *Mars 6* and *7* were launched in 1973, both carrying landers similar to those of *Mars 2* and *3*. The *Mars 7* lander missed the planet altogether, having separated from the orbiter prematurely. The *Mars 6* lander did transmit for 150 s after entry but the data was unreadable due to a problem with the computer chips. Harvey (1996) gives a fuller account.

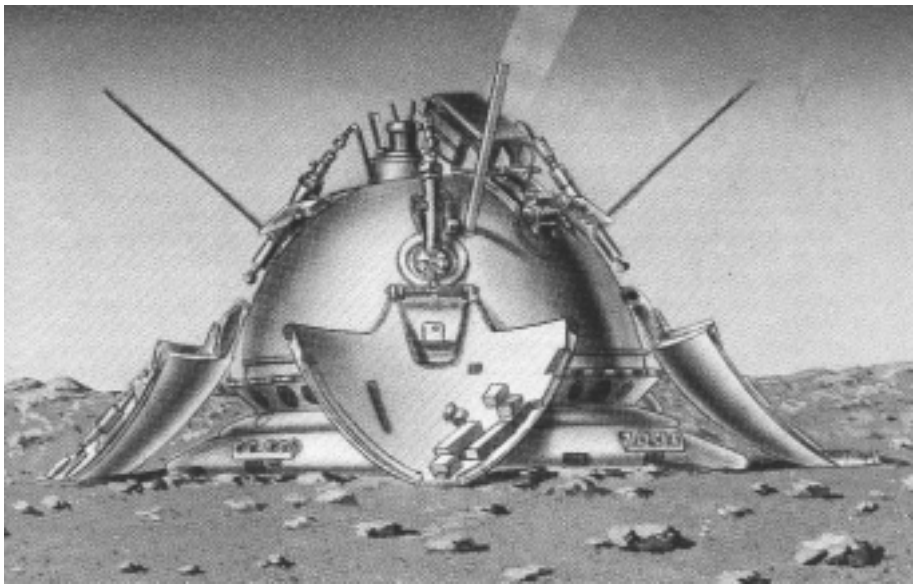

Figure 2.8. Artist's impression of the *Mars 3* lander on the surface of Mars, from the book *Course to Mars* (Markov, 1989). The rover is mounted on top of the lander on an unfolding deployment arm.

Kemurdzhian (1990) describes the rover used for *Mars 2* and *3* (Figure 2.9); other information is available in the proceedings of an international symposium on 'Missions, Technologies and Design of Planetary Mobile Vehicles' (Kemurdzhian *et al.*, 1993; Kovtunenko *et al.*, 1993).

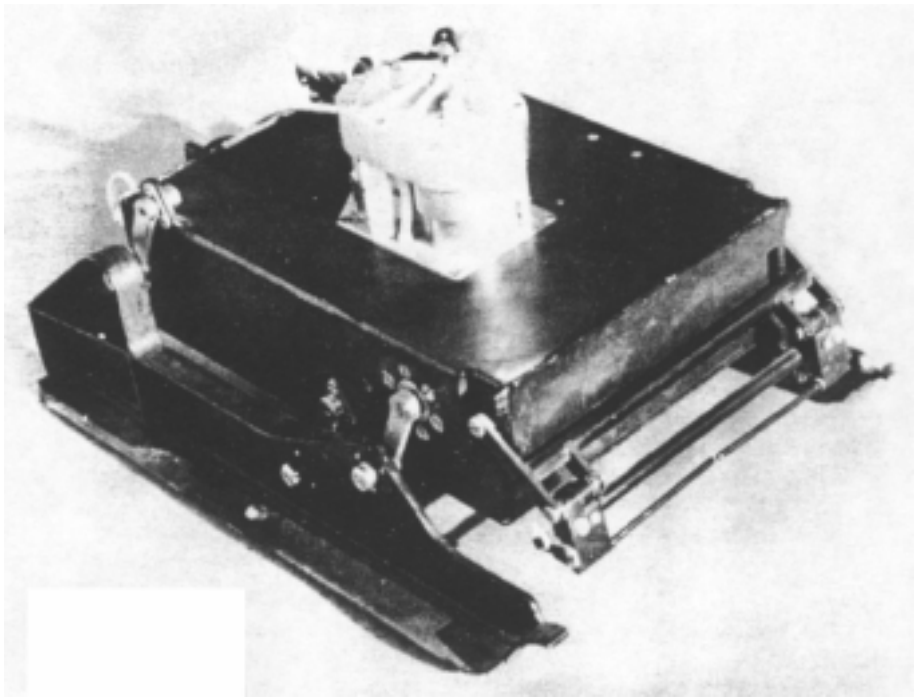

Figure 2.9. The small tethered rover (*PROP-M*) carried on the landers of *Mars 2,3,6 & 7* (from Kemurdzhian, 1990). Each rover carried a penetrometer and a gamma backscatter densitometer.

2.2.8 The *Venera* densitometers

Gamma ray densitometers were carried on the Soviet Venus probes *Venera 9* and *10* (Surkov, 1977 and 1997; Surkov *et al.*, 1976 and 1977a,b). Each lander carried a densitometer sonde at the end of a deployable arm. The cylindrical sensor head incorporated source, shielding and three Geiger counters, as shown in Figure 2.10.

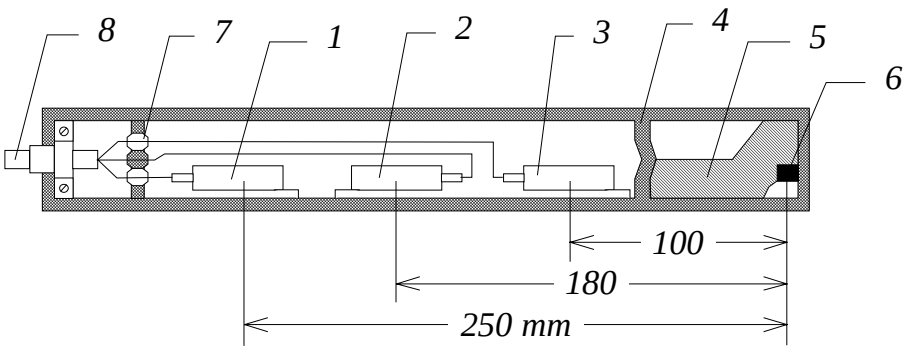

Figure 2.10. Schematic diagram of the *Venera* densitometer sonde (from Surkov *et al.*, 1976). Key: 1,2,3) Geiger counters; 4) titanium housing; 5) tungsten screen; 6) ^{137}Cs source; 7) sealed wire; 8) cable to electronics unit inside the main body of the lander.

This design was an improvement on the *Luna 13* version, particularly since the calibration of the three-detector arrangement had allowed for non-ideal deployment of the sensor head. If the head was deployed at an angle to the ground, making contact only at one end, the effect could be compensated for by comparison of the three count rates. This technique is analogous to that used by borehole logging tools to compensate for mudcake and unevenness in the rock surface.

The method of measurement used by the *Venera* instrument involved taking the ratio of count rates between the first and third detectors. This ratio was found to be reasonably linear with density across the required range and thus a convenient way to extract a density measurement.

Despite the improvements the *Venera 9* densitometer failed to return any useful data, although the panoramic images show that it was successfully deployed (Surkov *et al.*, 1977b). However *Venera 10* succeeded in measuring a surface rock density, producing a value of 2800 ± 100 kgm^{-3}.

3 Design Concept of the Densitometer

This chapter presents the design concept for the *MUPUS* density instrument, based on the requirements and constraints for such a device. The device will use attenuation of 662 keV gamma radiation emitted by a ^{137}Cs source mounted at the tip of the thermal probe, which will be inserted into the surface of the nucleus by a hammering mechanism. Cadmium telluride (CdTe) or cadmium zinc telluride (CZT) semiconductor detectors at the top of the probe will measure the attenuated count rate at intervals during the penetration process to obtain density vs. depth, to a maximum penetration of about 350 mm (the maximum probe length that can be accommodated on the Lander). Due to the density and depth dependence of the required integration time, an algorithm for budgeting the available operation time during the penetration process is proposed.

3.1 Introduction

Density is a fundamental parameter for investigation and was measured at the landing sites of *Luna 13* (Cherkasov *et al.*, 1968a,b) on the Moon[2] and *Venera 10* (Surkov *et al.*, 1977a) on Venus. Density measurements were also intended for the *Mars 2, 3, 6 and 7* rovers. Section 2.1.2 examined the rationale for density measurement of the cometary surface material found at the landing site. It is clear that a measurement of density profile vs. depth is much more valuable than a single value of bulk density at the surface. Near-surface density profile measurements are particularly appropriate for cometary nuclei due to the importance of the surface material's thermal behaviour and the possibility of activity-related layering.

The *MUPUS* densitometry investigation will be performed at the same location as thermal and mechanical measurements by means of a single inserted probe. This co-location aspect will be crucial for combined analysis of the data. Table 3.1 lists the measurement subsystems of *MUPUS*, most of which are incorporated into the probe shown in Figure 3.1. This ensemble of instruments could be applied to other surface missions and would be particularly useful for the regolith of minor bodies and other surface materials likely to be porous or layered. *MUPUS* is of course intended for a cometary surface where the flow of volatiles adds much complexity to the transport of heat.

---

[2] Unfortunately the measurement was ambiguous since the same data could imply two different densities, as discussed in section 2.2.6.

Table 3.1. Post-selection *MUPUS* measurement subsystems. †Subsystems that measure the evolution of these parameters with time (diurnal and orbital variations).

Location	Experimental Subsystem	Measurements
Rosetta Lander Anchor (ANC; primary and backup anchors stowed inside Lander body)	Anchor Penetrometer (ANC-M)	Mechanical and structural properties of surface layers derived from accelerometry
	Anchor Temperature Sensor (ANC-T)†	Sub-surface temperature at final position of anchor
Top of *Rosetta Lander* body above the cold balcony	Thermal Mapper (TM)†	Surface temperature (infrared sensors at 7, 10, 13 & 18-24 μm)
MUPUS Penetrator (PEN; deployed from the Lander's cold balcony)	Temperature Sensors (PEN-TP)†	Sub-surface temperature profile
	Thermal Conductivity Probe (PEN-THC)†	Thermal conductivity using the line heat source technique
	Penetrometer (PEN-M)	Mechanical and structural properties of surface layers (distance penetrated per hammer blow)
	Densitometer (PEN-CBD)†	Bulk density of surface layers by attenuation of γ rays

The backscatter method described in section 2.2 was initially (until about a year after the original proposal) adopted as baseline for the *MUPUS* densitometer (Ball *et al.*, 1996). This decision was based on the space-proven heritage of the technique and its apparent simplicity to implement. The instrument was proposed to be mounted in one of the Lander's feet, offering guaranteed good contact with the ground on landing without any additional deployment mechanisms.

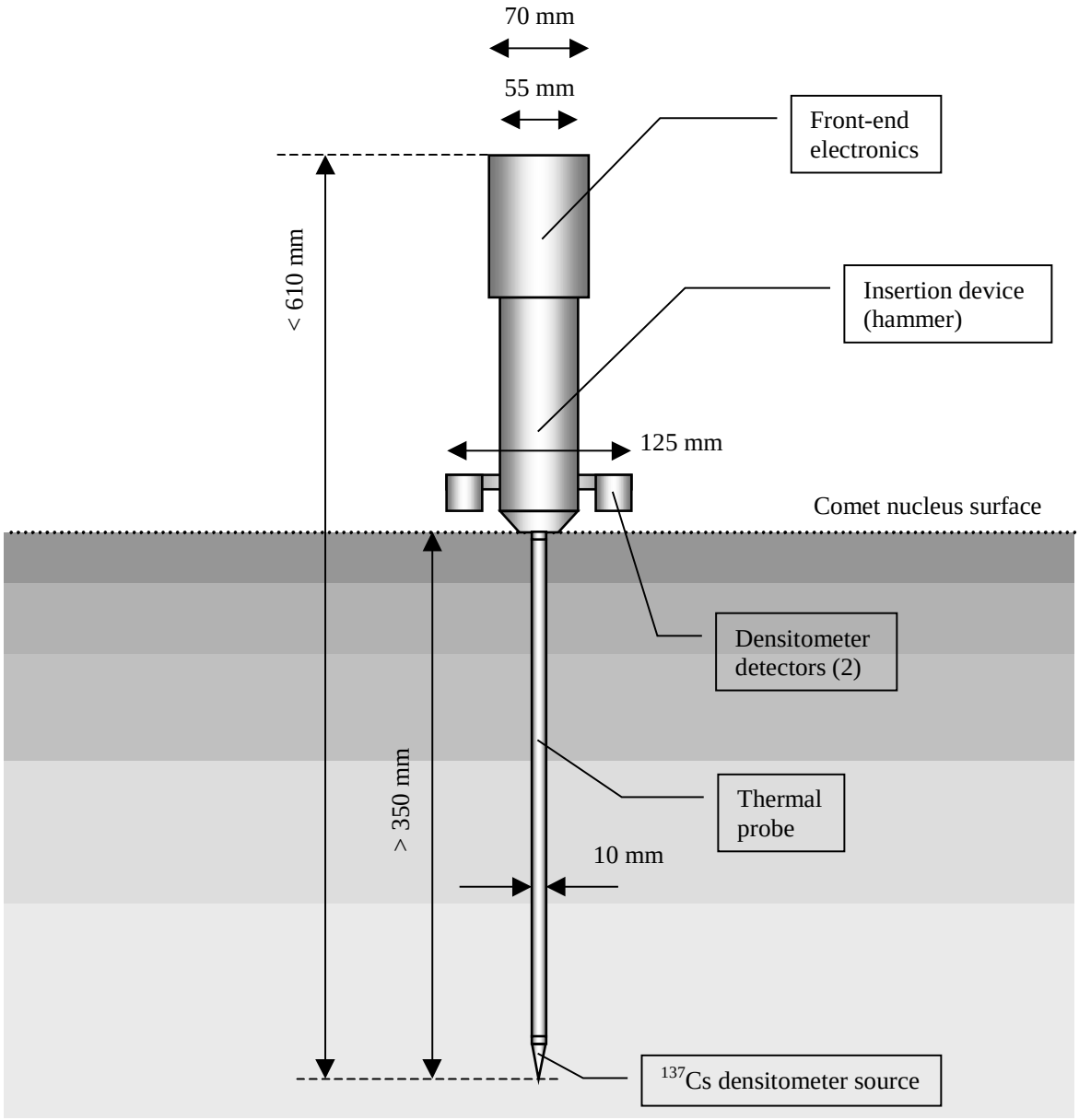

Figure 3.1. Diagram of the *MUPUS* probe after penetration of the nucleus surface, showing the sensors for measurement of density, thermal and mechanical properties.

A ^{137}Cs-based device such as the borehole logging or *Venera* designs would have placed an unreasonable demand on the mass budget, however, due to the shielding required between source and detectors. Initially it was thought that relatively large and delicate scintillator / photomultiplier detectors or Geiger tubes would be required for detection of the ^{137}Cs γ rays. Hence it was thought that an ^{241}Am device could be used, allowing the use of smaller semiconductor detectors such as cadmium telluride (CdTe) or cadmium zinc telluride (CZT). Elemental composition would be required from other instruments on the Lander for density to be determined, however. The ^{241}Am backscatter densitometer would have had three to five detectors at different distances from the source. The uncertainty in elemental composition (and thus photoelectric cross-section), combined with the wide

range of possible densities ($200 \rightarrow 1500\ \mathrm{kgm^{-3}}$) resulted in a larger uncertainty in the optimum sonde length than for a ^{137}Cs device. Multiple detectors would thus have covered this range. Under unfavourable circumstances a single detector may have had a calibration curve which was too flat at the density encountered for the measurement to have been acceptably accurate. A possible further advantage of multiple detectors may have been the crude depth resolution obtainable– measurements with larger sonde lengths penetrate more deeply into the material. Section 4.3 (page 74) explains this idea more fully using the Single Scattering Model.

Although at first sight mounting the densitometer on one of the Lander's feet is an appealing idea, two overriding problems arose. Firstly the presence of a payload instrument on the landing gear (a critical Lander subsystem) would have caused conflicts of requirements. The foot would have had to ensure a successful landing as well as accommodate the instrument safely and provide good contact with the ground. During deployment of the landing gear the more massive foot carrying the densitometer would have caused the Lander's centre of mass to move, complicating the Lander's attitude control system. Secondly it was never confirmed that modelling could have compensated for the likely compression of the soil under the foot. Certainly landing deceleration data would have been required, together with a measurement of the depth to which the foot had sunk into the surface.

3.2 The MUPUS Densitometer Concept

Having finally rejected the foot-mounted ^{241}Am densitometer design it was decided that a better solution was to incorporate a densitometer into the *MUPUS* probe. Since the length of the probe is many times the attenuation length of ^{241}Am photons a ^{137}Cs source would have to be used. By this stage, however, it had been found that CdTe or CZT semiconductor detectors did in fact provide a viable alternative to the scintillator or Geiger tube devices. Since no mass was available for source / detector shielding the attenuation method was adopted in preference to the backscatter method.

On balance this solution improves on the previous design for reasons of simplicity, improved interface requirements and the co-location of the density measurement with the other *MUPUS* probe measurements. One potential problem, however, was increased disturbance of the thermal measurements due to heat dissipation in the detectors and / or increased shadowing of the surface by the protruding detectors.

The new design involves mounting a ^{137}Cs source at the tip of the probe, the 662 keV radiation from which is viewed by detectors at the surface. Thus the radiation is attenuated by any intervening cometary material. As mentioned already the mass attenuation coefficient at 662 keV is almost independent of composition. The degree of attenuation is intended to be measured by monitoring the count rate of unscattered photons reaching the detectors through the material. The column density thus obtained would, together with knowledge of the depth below the surface to which the source had penetrated, allow bulk density to be determined. In practice the presence of lower-energy scattered photons and imperfect resolution of the 662 keV peak, as well as detector noise, complicate the detection of primary photons. This means that the count rate needs to be measured over some finite energy window, and that some degree of 'contamination' by non-662 keV counts is to be expected. Chapter 6 discusses the results of initial experiments to view ^{137}Cs through attenuating material using a CdTe detector.

3.2.1 Constraints on the detection system

This section presents a brief overview of detection system design issues, investigated in collaboration with Mr. Matt Whyndham of University College London's Mullard Space Science Laboratory. A much more detailed analysis can be found in the internal *MUPUS* documents *Requirements of the MUPUS Densitometer* (Trow *et al.*, 1997a) and *Densitometer Instrument of MUPUS– Design Thoughts* (Trow *et al.*, 1997b).

As discussed in section 3.1, cadmium telluride (CdTe) or cadmium zinc telluride (CZT) semiconductor detectors were identified as the baseline technology for the densitometer, operating in photon counting (rather than spectroscopic) mode. At the time of writing, however, many questions regarding the detection system remain open due to lack of resources for further development. These issues include: –

- The exact specification of the detectors (e.g. dimensions) and their housing
- The analogue stage and digital electronics associated with pulse processing and counting
- Interfaces (especially electrical) with the rest of the *MUPUS* experiment
- The power supply required (and the level of the detector bias voltage)
- The details of any on-board software required to control the measurement (see section 3.3.4 for a possible scheme to be implemented as on-board software)

A significant constraint is the time available to make the measurement– perhaps 12 hours for the initial phase including the hammering process. This has a bearing on the source activity and the required size and efficiency of the detectors. The density of CdTe is 6200 kgm^{-3}, so using the mass attenuation coefficient at 662 keV (8.3×10^{-3} m^2kg^{-1}) one can calculate, for instance, that to interact with 10 % of the incoming photons a detector 2.05 mm thick would be required. A 5 mm thickness would raise this efficiency to 22.7 %.

The system may have to compensate for drifts in gain, which could arise due to temperature variations (for example). It would also be desirable to examine different regions of the detected spectrum– this capability may allow some degree of compensation for noise, scattered photons or primary photons scattering out of the detector.

3.3 Application of Attenuation Method to an Inserted Thermal Probe

The gradual insertion of the *MUPUS* probe by the hammering mechanism allows column density to be measured over a range of depths during the insertion process. Thus the profile of bulk density vs. depth may be obtained. After full insertion any long-term changes in the density or erosion of the surface layer may be monitored. This section examines some of the issues arising from the combination of penetration and density measurement.

3.3.1 Direction of photon path

Since the source is mounted at the tip of a rod the detectors have to be mounted off-axis; otherwise the direct photon path would pass only through the probe instead of the cometary material. It is, however, desirable to have the photon path as parallel to the insertion direction as possible. Increasing the angle between these two directions increases the possible confusion between vertical density variation (layers) and horizontal variations such as lumps or voids inside the material or unevenness of the surface. These opposing effects are illustrated in Figure 3.2. A compromise has to be reached such that deep measurement is sacrificed to keep the photon path as parallel as possible to the insertion direction. Two detectors are used for redundancy and to provide two different paths through the cometary material. Density variations seen along both paths can more confidently be ascribed to layering. This aspect gives rise to the requirement that the count rate in each detector be measurable independently (simultaneously if this is feasible).

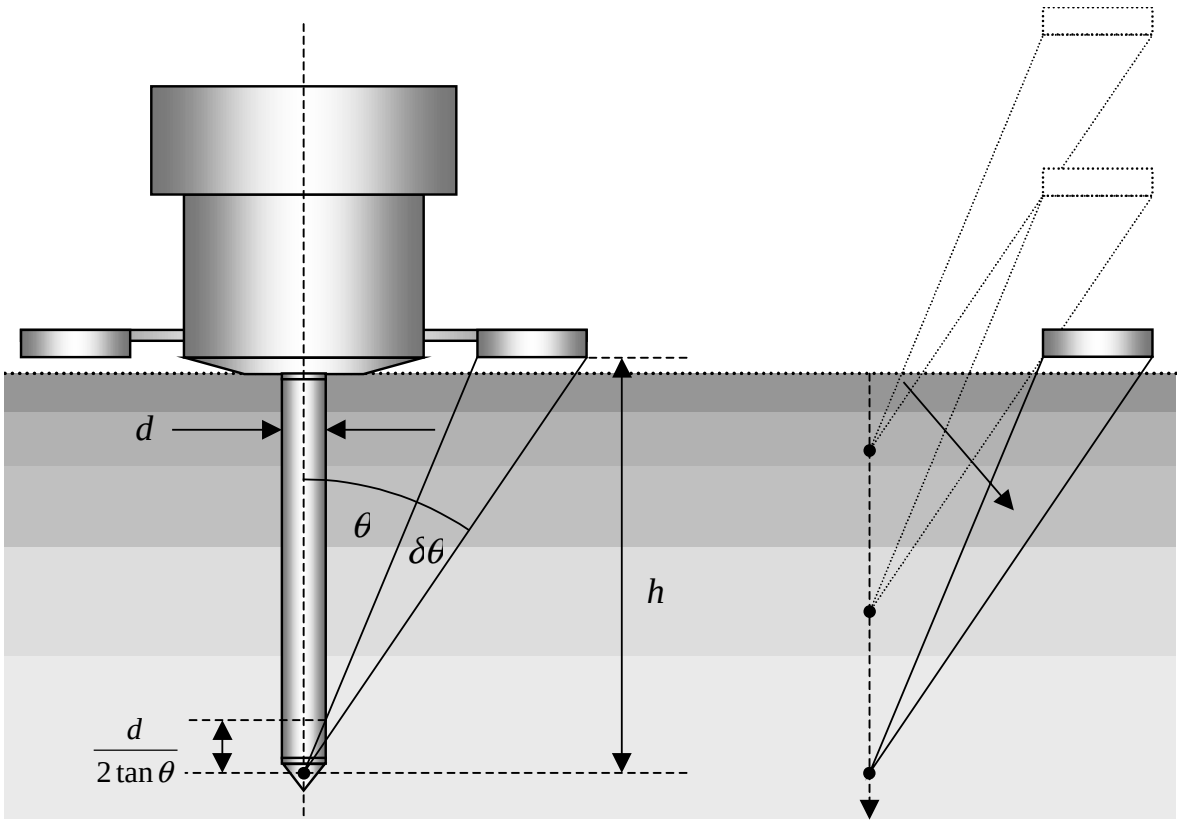

Figure 3.2. Source / detector geometry. The horizontal scale is exaggerated to show the angles more clearly. A vertical height of $d/(2\tan\theta)$ is lost due to the passage of the transmitted beam through the material of the probe, where d = 10 mm. As the probe is inserted the finite angle between the transmitted beam and the insertion direction can cause ambiguity between vertical density variations (i.e. layering) and horizontal variations such as lumps, voids or surface unevenness.

In practice the detectors are of finite extent so there is no sharp cut-off– the maximum outer diameter of the protruding detectors is 125 mm, so for h = 0.35 m and d = 10 mm we have $\theta+\delta\theta = 10.1°$ and a height of 28 mm lost in the probe. Assuming the detectors are 20 mm in size, photon paths from the source to their inner edge would have $\theta = 6.9°$ and lose 41 mm in the probe. Thus there is little value in pausing the hammering process to measure the count rate before the probe is more than 41 mm into the surface.

3.3.2 Required integration time

How long would it take to make a density measurement? An estimate can be made based on a simple calculation. For this we shall assume the following configuration: –

- Activity S of ^{137}Cs source = 7.4 MBq (≡ 0.2 mCi), with yield α of 662 keV photons = 0.85.

- Source-detector distance d = 0.35 m.
- Mass attenuation coefficient $\mu = 8.31 \times 10^{-3}$ m^{2}kg^{-1} (for water ice, based on data from Storm and Israel, 1970).
- Detector area $A_d = 4 \times 10^{-4}$ m^2, efficiency $\eta_d = 0.1$.
- Range of density $\rho = 200 \rightarrow 1500$ kgm^{-3}.
- Required accuracy of measurement $\Delta\rho = 10$ kgm^{-3}.

Attenuation through 0.35 m of material would thus be by a factor of between 1.79 and 78.5 depending on the density (18.3 for 1000 kgm^{-3}). In free space the source would produce a flux of 4.09×10^6 photons m^{-2}s^{-1} at a distance of 0.35 m. This would then fall to between 2.28×10^6 and 5.21×10^4 photons m^{-2}s^{-1} (2.23×10^5 for 1000 kgm^{-3}) once the probe had been fully inserted. For the 4 cm^2 detector (with 10 % efficiency) the count rate would then have fallen from 163 s^{-1} to between 2.08 and 91.4 s^{-1} (8.92 s^{-1} for 1000 kgm^{-3}).

To measure the density to an accuracy $\Delta\rho$, the count rate needs to be measured to within a factor of $\mu \cdot d \cdot \Delta\rho$. This is because for an exponentially decaying function of density (such as count rate) $f(\rho) = e^{-\mu\rho d}$, we can differentiate with respect to density to give $df/d\rho = -\mu \cdot d \cdot f$, which then gives $df/f = -\mu \cdot d \cdot d\rho$. Hence the fractional error in count rate for a density error $\Delta\rho$ is $\mu \cdot d \cdot \Delta\rho$. This gives 2.91 % for $\Delta\rho = 10$ kgm^{-3} (or 5.82 % for $\Delta\rho = 20$ kgm^{-3}). Counting statistics thus means at least $0.0291^{-2} = 1183$ counts (or 296 counts for $\Delta\rho = 20$ kgm^{-3}) must be registered. It would thus take between 12.9 and 568 seconds (or 133 s for 1000 kgm^{-3}) to accumulate 1183 counts, or between 3.24 and 142 s (or 33.2 s for 1000 kgm^{-3}) for $\Delta\rho = 20$ kgm^{-3}.

Summarising the above calculation algebraically we obtain an expression for the integration time $\tau_{int}(d)$ required at full penetration depth d:

$$\tau_{\text{int}}(d) = (\mu d \Delta\rho)^{-2} \cdot \left(\frac{S\alpha}{4\pi d^2} \cdot e^{-\mu\rho d} \right)^{-1} \cdot (A_d \eta_d)^{-1} \quad ,$$

$$\therefore \quad \tau_{\text{int}}(d) = \frac{4\pi e^{\mu\rho d}}{\mu^2 \Delta\rho^2 S\alpha A_d \eta_d} \quad . \tag{3.1}$$

This expression can be simplified using the count rate $C(0)$ at zero penetration:

$$C(0) = \frac{S\alpha A_d \eta_d}{4\pi d^2} \quad , \tag{3.2}$$

$$\therefore \quad \tau_{\text{int}}(d) = \frac{e^{\mu\rho d}}{C(0)(\mu\Delta\rho d)^2} \quad . \tag{3.3}$$

Thus we can see that ρ and d are the dominant factors due to their presence in the exponential factor.

3.3.3 Variation of integration time with depth

During penetration the required integration time varies with depth z. Extending the above expression to obtain the function $\tau_{\text{int}}(z)$ gives

$$\tau_{\text{int}}(z) = \frac{e^{\mu\rho z}}{C(0)(\mu\Delta\rho z)^2} \quad . \tag{3.4}$$

Thus the ratio of $\tau_{\text{int}}(z)$ to $\tau_{\text{int}}(d)$ is

$$\frac{\tau_{\text{int}}(z)}{\tau_{\text{int}}(d)} = \frac{d^2}{z^2 e^{\mu\rho(d-z)}} \quad . \tag{3.5}$$

This function shows a minimum at $z = 2/(\mu\rho)$. At low z the low attenuation factor means a large integration time is needed to detect the small fractional change in count rate. At high z a large integration time is required due to the low count rate. Figure 3.3 shows the required integration time vs. depth for a range of densities, for an accuracy $\Delta\rho$ of 10 kgm^{-3}.

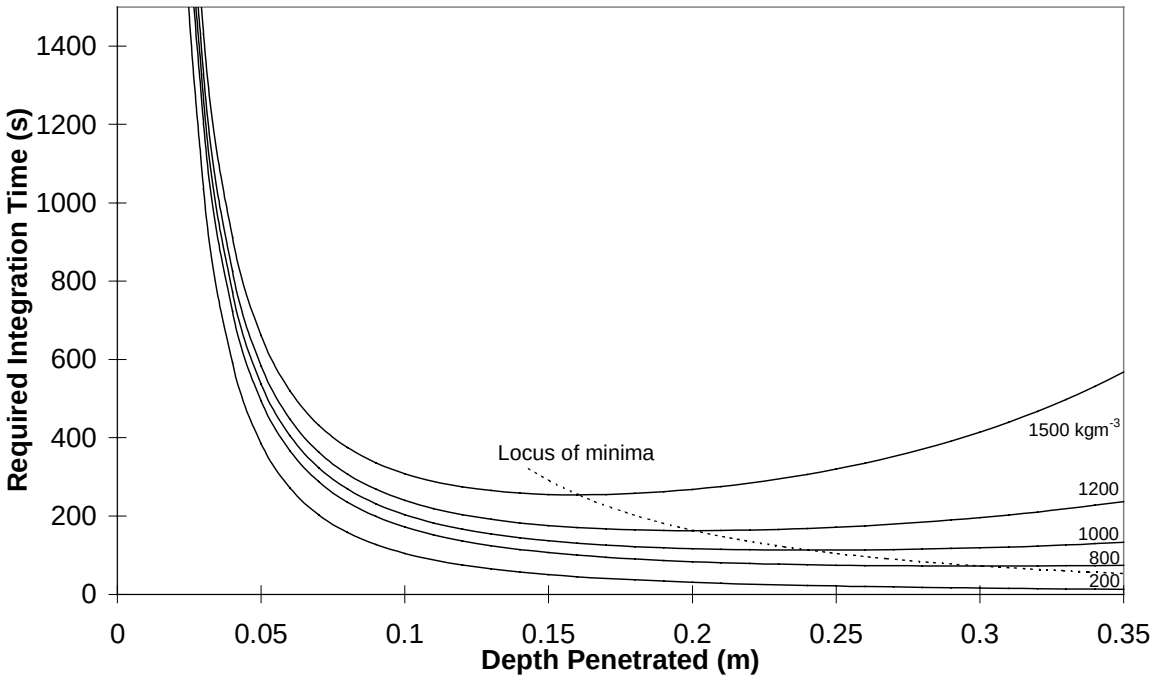

Figure 3.3. Required integration times vs. depth for a range of material densities. This assumes $\mu = 8.31 \times 10^{-3}$ kgm^{-3}, $\Delta\rho = 10$ kgm^{-3} and $C(0) = 163$ s^{-1}.

3.3.4 Active control system

The variation in required integration time with depth and density presents a problem. The measurement must be made to the required accuracy and within a fixed length of time– a constraint imposed by the Lander's operational sequence. Having penetrated to a particular depth it will not be possible to go back to a previous location to perform further integration. The uncertainty in the strength of the surface material means that the number of hammer blows required to reach a certain depth cannot be predicted accurately.

As a result of these uncertainties and constraints there is thus a danger that any plan for spending a predetermined amount of time at each of several depths will not meet the measurement accuracy requirements– in the case of a high density material the count rate may be too low to accumulate enough counts. For low density this would not be a problem– each data point would have an improved accuracy. The 'spare' time may have been better spent on improving the depth resolution, however.

An alternative way to perform the integration would be to wait at each integration point for a predetermined number of counts to be detected. Again this is not ideal– for high density there may be insufficient time remaining for the deepest points, or for low density the measurement may proceed so quickly that time that could have been used to improve the measurements is wasted.

The author has thus devised an active control system to modify the number of measurement depths chosen and the time spent counting at each depth, with the aim of performing the measurement in exactly the time allocated and obtaining the optimum combination of accuracy and depth resolution. The algorithm for achieving this is outlined in Figure 3.4. This would be encoded as on-board software to govern the process autonomously since the signal delay would make interactive control of each measurement step from Earth impractical. Before the start of hammering the instrument would integrate for a fixed length of time to determine the count rate without the presence of any attenuating material. Hammering would then start to take the probe down to some initial depth. This would have to be greater than the path length lost in the probe (see section 3.3.1) and sufficiently deep to ensure a significant attenuation factor (i.e. a measurable change in count rate). 60 mm would perhaps be a suitable value for the current configuration. Integration would then take place at this depth for long enough to obtain a good measurement of density whatever its value (within the range $200 \rightarrow 1500$ kgm^{-3}).

The most critical point in this algorithm is the need to derive a value of density from the count rate immediately on board the Lander. Extensive laboratory experiments beyond

those in chapter 6 would be required to establish that this could be done reliably. The response of real detectors makes it difficult to determine the actual count rate of unscattered photons.

The value of density thus obtained would enable a first guess to be made regarding the density to be encountered in the deeper layers. A projected time budget can then be made, using a curve similar to those shown in Figure 3.3. Given the time required at each depth and the time available, the instrument can then determine the optimum combination of accuracy and depth resolution, based on pre-set targets for accuracy ($\Delta\rho$) and the finest depth resolution (Δz_{min}). Time is first spent on improving the depth resolution; if the limit Δz_{min} is reached any remaining time is spent on improving the accuracy. Under the least favourable conditions the instrument would proceed directly to full penetration and integrate there for the remaining time. Under the most favourable conditions high accuracy measurements would be made approximately every Δz_{min} from the initial point. This algorithm produces target values for the next depth to be reached and the time that should be spent there. Once the probe has reached this depth and the integration has been completed a new value of density is obtained.

The new value of density is then fed back into the re-budgeting algorithm to determine where the next sampling point should be and the integration time that will be required. The process continues round the loop until the final depth is reached. In this way the instrument responds to density variations, though it does assume that the next density encountered will not be too dissimilar to the current one. The method will also cope with small overshoots by the hammering mechanism. No attempt is made to reach exactly the depths required since each hammer blow will cause the probe to advance by an amount rather smaller than the finest depth resolution required.

The method clearly does require a reliable way to measure the depth penetrated at any time between hammer blows. At the time of writing this issue is not settled but some sort of optical encoder is the solution most likely to be implemented. Such a device should be able to determine the penetrated depth to an accuracy better than about half the finest depth resolution of the density measurement.

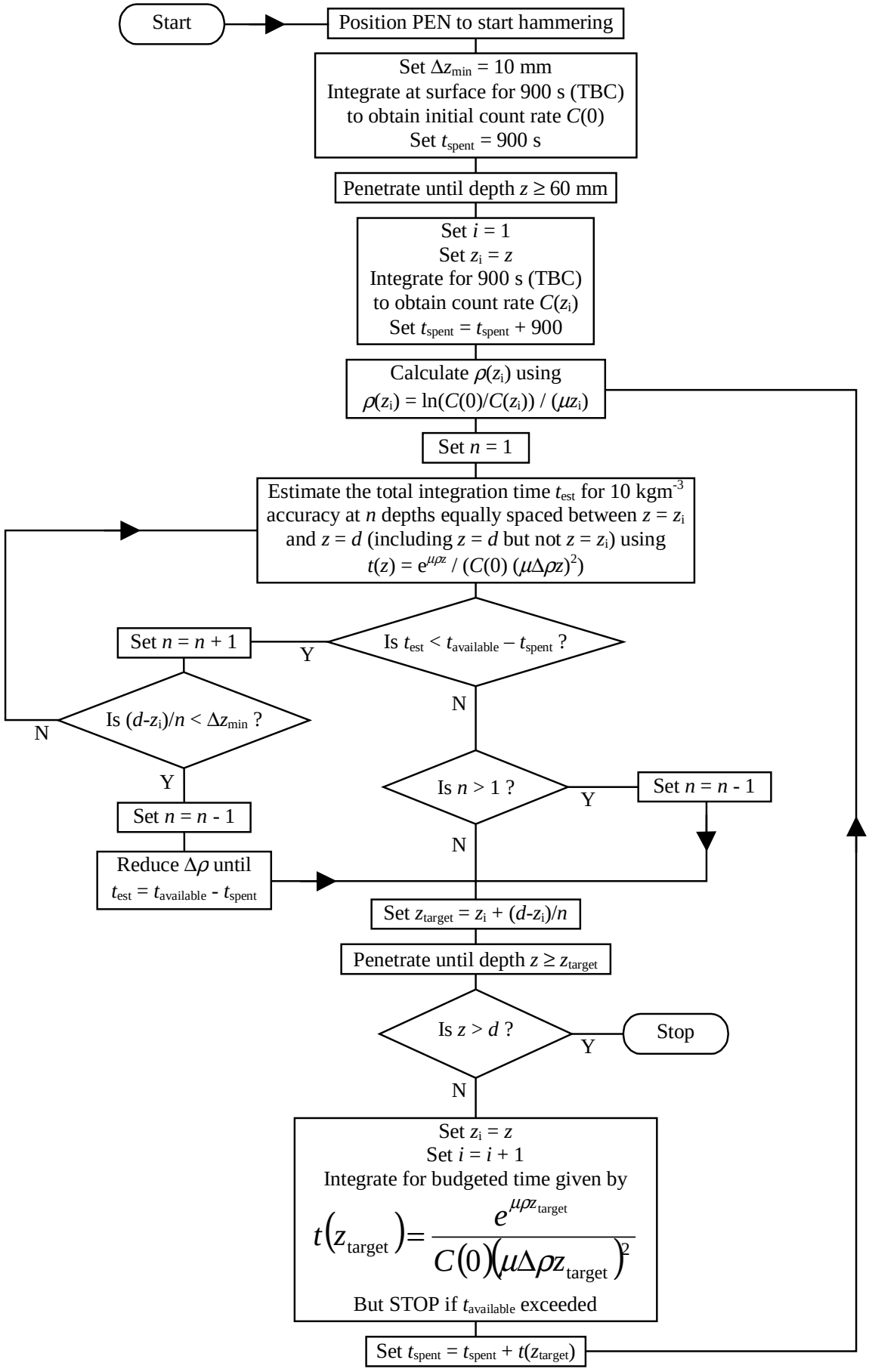

Figure 3.4. Flowchart for the penetration algorithm.

It would be interesting to test the proposed algorithm for robustness. The following factors should be introduced into such a computer model: –

- reasonable variations of density with depth,
- finite accuracy of the density determination at each point (from photon counting statistics),
- overshoot by the hammering process, and
- finite accuracy of the depth measurement.

The algorithm would be tested for a range of 'real' density profiles and realistic values for the non-attenuated count rate and total time available. The output of each simulation would be a plot of density vs. depth with error bars in both dimensions for each data point. Density vs. depth would of course be derived by differentiating the integrated density (i.e. column density) produced by the attenuation measurement.

3.3.5 Data rate

To estimate the data rate produced by the densitometer we can build on the calculation in sections 3.3.2 and 3.3.3. Suppose each pulse in a single desired counting window is added to a counter that is read and reset once every 10 s. For the count rates discussed in section 3.3.2 a 12-bit number would be sufficient. For gain control a 4-bit number would be needed at a similar rate, assuming the range over which it could vary is divided into 16 channels (this is less than would be required for spectroscopic measurements, rather than coarse counting in a window). An 8-bit temperature measurement could be made slightly less frequently, say every 60 s. All these rates would be double for two detectors operating simultaneously. In addition one could assume a small number (~4) housekeeping parameters to be measured at a similar rate to the temperatures. This gives a total of 240 bits every 60 s or an average of 4 bits s^{-1} during the measurement. If measurements were made for a total of 12 h the total data volume would then be 172.8 kbits.

Some of the housekeeping data may not need to go further than the Lander (gain control perhaps), while the number of counts could be totalled and transmitted rather less frequently than once every 10 s. An increase in data rate would be required if counts were accumulated in more than one energy window simultaneously, a feature which could conceivably be useful, as stated in section 3.2.1. In any case the total data volume for the

density profile measurement appears rather less than that required by imaging instruments or measurements which require high frequency sampling or spectral resolution.

3.3.6 Safety considerations

It is of course worth stating the safety constraints for handling a radioisotope source of the type considered here for the densitometer. The main emission emanating from the encapsulated ^{137}Cs source capsule is in the form of 662 keV photons (^{137}Cs beta emission is stopped by the encapsulation). The dose D is given by

$$D = \frac{ME}{6r^2} \quad , \tag{3.6}$$

in microSieverts / hour (μSv h^{-1}), where M is the activity in MBq, E is in MeV and r in m. So for M = 7.4 MBq, E = 0.662 MeV, r = 0.5 m, D = 3.27 μSv h^{-1} the annual dose limit (for a postgraduate research student at least) is 15 mSv[3], so in one year one can stand 0.5 m from the source capsule for a maximum of 4593 h, equivalent to 12.6 h per day every day. One ought to aim for at least one order of magnitude below that limit, however. One way in which the dose to workers might be minimised is if the tip of the probe housing the source is made in such a way that it can be attached to the probe at a relatively late stage in the assembly sequence. For shielding such a ^{137}Cs source it is worth remembering that the exponential attenuation length of 662 keV photons in lead is 11 mm (for 1/e attenuation).

[3] From schedule 1 of the Ionising Radiations Regulations 1985, Statutory Instrument 1985 No.1333.

4 The Response of Gamma Backscatter Density Gauges to Spatial Inhomogeneity– an extension of the single scattering model

The single scattering model for gamma backscatter density gauges has been extended to describe how the total detected count rate changes in response to localised density variations within the material. This extended model suggests there is a spatial region where density perturbations have a contradictory effect on the measured density value, an effect that has already been shown experimentally by previous workers. Here we compare their results with those predicted by application of the extended single scattering model. Since a complete description of their experimental apparatus was not available, only a crude fit could be achieved. However, all the basic features of the data could be reproduced.

This chapter is almost identical to a paper submitted to the journal *Nuclear Instruments and Methods, Section B (Beam Interactions with Materials and Atoms)* in August 1997 (Ball *et al.*, 1998). Co-authors were Dr. C. J. Solomon and Dr. J. C. Zarnecki (Ph.D. supervisor). Both co-authors contributed by means of discussion and constructive advice rather than generation of the material itself.

4.1 Introduction

Gamma backscatter density gauges use the Compton scattering of γ ray photons in bulk material to measure density. Such devices are widely used in well logging, soil science and the manufacturing and construction industries (see section 2.2). Unlike transmission densitometers, where the linear geometry of source, sample and detector can be a limitation, backscatter density gauges can be applied to semi-infinite bulk materials (such as rock or soil), boreholes or structures where the other side is inaccessible (the walls of long tubes, for example).

A beam of photons from a collimated radioisotope source (usually ^{137}Cs) is injected into the material under study. One or more detectors are placed along the surface to count the backscattered photons. Since the cross-section for Compton scattering is proportional to the number density of electrons, and the ratio of atomic mass to atomic number is 2.0, or nearly so, for all elements (except hydrogen), the backscattered count rate is a function of the bulk density. An approximate functional form for this calibration curve has been suggested (Hearst and Carlson, 1969):

$$I(\rho) = K_1 \rho e^{-C_1 \rho} + K_2 \rho^2 e^{-C_2 \rho} \quad , \tag{4.1}$$

where I is the total count rate detected, ρ is the material's density and $K_{1,2}$ and $C_{1,2}$ are constants. This function is plotted in Figure 4.1. The count rate reaches a maximum at some critical density, dependent on the sonde length (source-detector separation) and the source energy. Below this density the count rate falls due to the reduced concentration of electrons to scatter photons into the detector, while above this density the count rate falls due to the increased attenuation of the source beam.

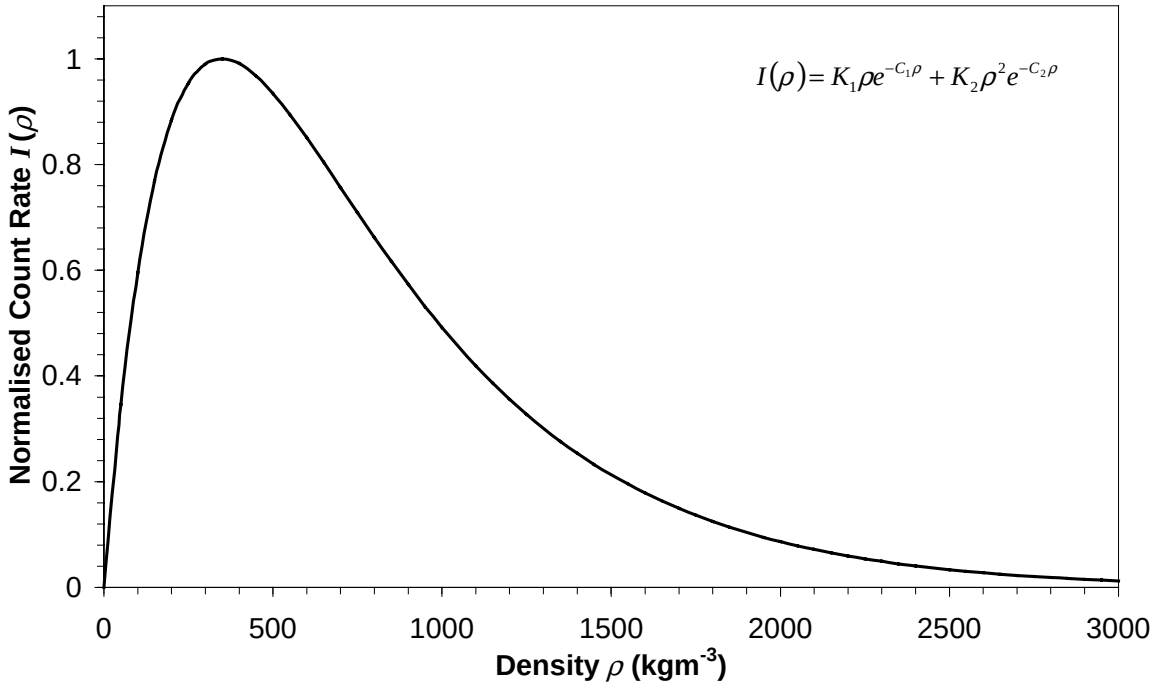

Figure 4.1. Example calibration curve for a gamma backscatter densitometer, showing detected count rate vs. density, normalised to the maximum. The parameters are from Hearst and Carlson (1969): C_1 = 3.45 m^{3}kg^{-1}, C_2 = 2.6 m^{3}kg^{-1}, K_1 = 0.4754 s^{-1}kg^{-1}m^3, K_2 = 1.8735 × 10^{-4} s^{-1}kg^{-2}m^6. Backscatter densitometers usually operate on materials with a density above the critical value, i.e. where an increase in count rate implies a decrease in density.

At the ^{137}Cs source energy (662 keV), Compton scattering is the dominant interaction. At energies below about 150 keV the photoelectric effect is significant, while e^-/e^+ pair production occurs only at energies above twice the electron rest mass energy (1.02 MeV). Both these processes have mass attenuation coefficients that are heavily

dependent on elemental composition, which is why only those source energies within the "Compton window" are useful for densitometry[4].

Equation 4.1 assumes that the value of density ρ is either constant throughout the material or varies only on scales much smaller than the instrument's size. Many real materials such as soil show porosity or other density variations on macroscopic scales, however. It is thus important to understand the behaviour of backscatter density gauges in terms of their spatial response and response to density inhomogeneity. Reducing this question to the single linear dimension of depth below the surface, Czubek (1983) notes that the range of investigation of such devices can be defined in a number of different ways. Several studies have been performed to answer the question, employing the single scattering model (SSM) (Devlin and Taylor, 1970), Monte Carlo methods (Watson, 1983; Petler, 1990; Picton *et al.*, 1992; James, 1993) and experiment (Devlin and Taylor, 1970; IAEA, 1971; Sherman and Locke, 1975).

Picton *et al.* (1992) discuss a number of alternative measures of 'depth of investigation'. The function $S_1(h)$ was defined by them as the fraction of the detected count rate which remains after the material beyond a depth h has been removed. However $S_1(h)$ was found to suggest that the instrument measures density to a greater depth than is actually the case, since photons with maximum penetration depths beyond h have nevertheless 'sampled' shallower layers along the way. Although Picton *et al.* (1992) and Gulin (1975) define the region beyond h to be a vacuum (more easily achieved in a Monte Carlo simulation than in the laboratory), several sources report experiments where another material is used (IAEA, 1971; Sherman and Locke, 1975). The IAEA experiments reported the fractional change in count rate as an increasing thickness of glass is placed between a surface density gauge and a concrete block. Sherman and Locke investigated borehole density gauges using nested cylindrical annuli of dry sand. The annuli were sequentially saturated with water, starting with the inner one. They then expressed the variation of response with depth as the ratio of the change in measured density (for saturation to a depth h) to the change measured once all the annuli had been saturated. Based on these approaches we can thus define an alternative response function $S_{1a}(h)$ as the ratio of the change in count rate (when the material from the surface to a depth h is changed) to the total change as $h \to \infty$. The functions $S_{1a}(h)$ (sometimes called "J-factor") and $S_1(h)$ give

[4] Lower source energies such as 59.5 keV from ^{241}Am are sometimes used in cases where the elemental composition is known (e.g. Ball *et al.*, 1996; Divós *et al.*, 1996).

rise to the commonly used 50 % and 90 % response depths h_{50} and h_{90}. Taking the limit of an infinitesimal density change, Picton *et al.* (1992) go further to define an improved function $S_2(h)$ as follows:

$$S_2(h) = \lim_{\Delta\rho \to 0} \left[\frac{\rho_a(\Delta\rho, h) - \rho_b}{\Delta\rho} \right] \quad , \tag{4.2}$$

where the density of the material from the surface to a depth h has been increased with respect to that beyond from ρ_b to $\rho_b + \Delta\rho$, leading to an apparent density ρ_a, as measured by the instrument. Since the calibration curve can be considered linear over a sufficiently small density range, density can be replaced by count rate in the expression above. The function $S_2(h)$ is of course only one-dimensional so it does not carry any information regarding the variation of response in the two perpendicular directions.

Two types of importance function (which can potentially be evaluated in three dimensions) are also discussed by Picton *et al.* (1992) as tools for measuring depth of investigation. One type is the flux of eventually detected photons, while the other is the spatial density of scattering events, ignoring photons which pass through unscattered. The latter can be approximated by the SSM (Devlin and Taylor, 1970) or determined accurately by Monte Carlo simulation (Watson, 1983). A variation on this was used by Ao and Gardner (1995), who chose to base the importance of a volume element on the proportion of photons emitted isotropically from that element which are eventually detected. It is not clear in their paper how the assumption of isotropic emission might affect the subsequent Monte Carlo analysis– neither the flux of incoming photons nor the differential scattering cross-section is actually isotropic. James (1993) computed the 'weights' of volume elements in material under a real device, using a correlated Monte Carlo perturbation technique. This work showed (positive) peaks in 'weight' under both source and detector, decaying with both depth and lateral distance from the baseline.

While the function $S_2(h)$ represents the best measure so far proposed for depth of investigation, a three-dimensional equivalent would be useful. This would examine the effect on the measured density of increasing the density of a small volume element and would also be useful for studying the effect of inhomogeneities. While this can be achieved for specific cases by Monte Carlo simulation, the author proposes here an extension to the SSM to handle such a situation. The experimental results of Devlin and Taylor (1970) reproduced in Figure 4.2 show that a localised density perturbation can either increase or decrease the count rate depending on where in the material it is placed. This interesting effect seems not to be highlighted by any of the previous investigations discussed above.

The physical reason for the effect is clear– the density reduction increases the count rate where the attenuating role of the material it replaces is dominant, while it reduces the count rate where scattering into the detector is the important effect. This is evident in Figure 4.2, where the count rate is increased in a region near the source but decreased in a region near the detector. The peaks (at about 40 and 100 mm respectively) show where each of these effects is most important. Thus the apparent density measured by the instrument gives a false indication when the perturbation lies beyond about 74 mm from the source, assuming the instrument was operating in the regime where a decrease in bulk density should give an increase in count rate.

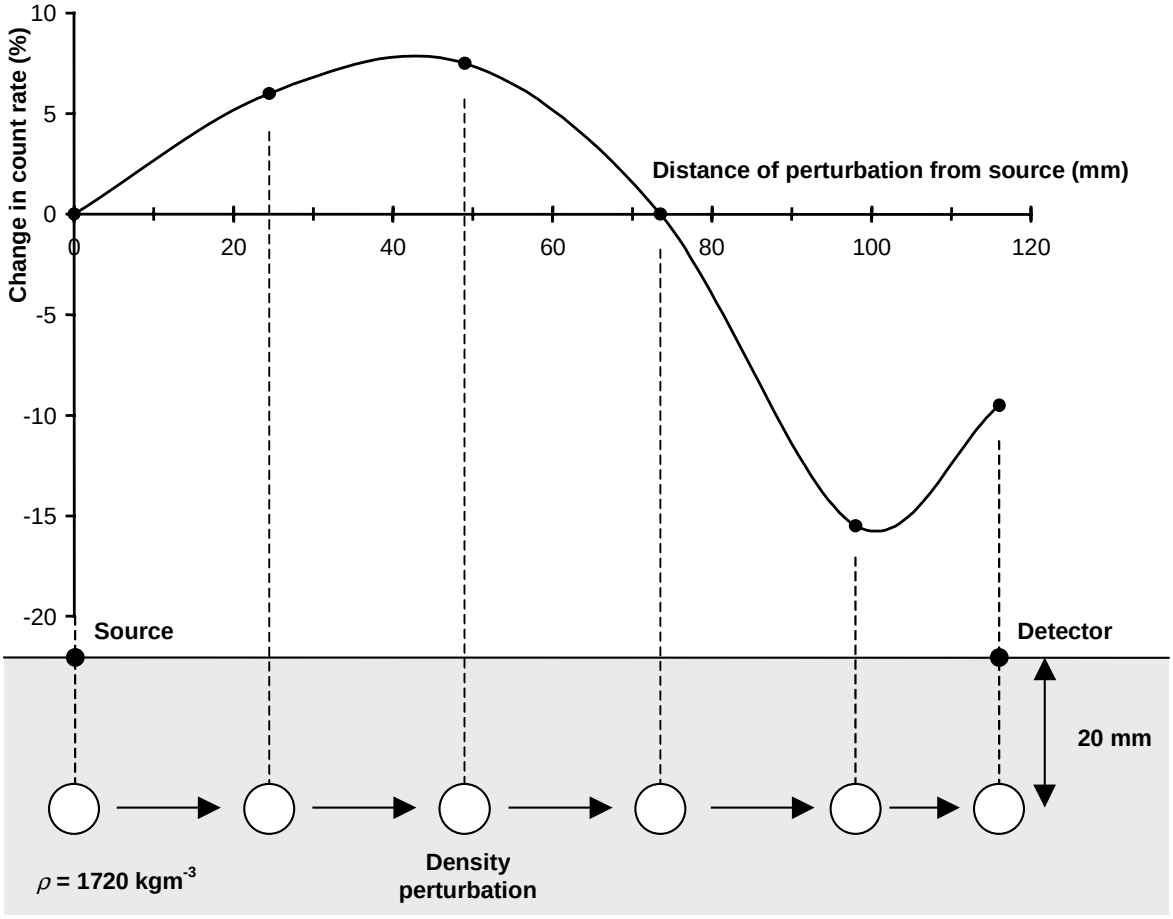

Figure 4.2. Experimental results from Devlin and Taylor (1970), showing that a localised decrease in density can either increase or decrease the detected count rate, depending where the perturbation is placed in the material.

Devlin and Taylor used the SSM to generate maps of the density of scattering events in a hemispherical volume under the instrument– a quantity that is of course positive everywhere. This chapter will show that it is possible to extend the model to show the two regions implied by the results in Figure 4.2.

In section 4.2 the single scattering model, as introduced by Uemura (1965) and Taylor and Kansara (1967), was defined. Section 4.3 revisits the spatial distribution of scattering events as outlined by Devlin and Taylor (1970), including the evaluation of scatter density vs. depth. This is then extended in section 4.4 to examine the effect on the total count rate (and hence measured density) of a small localised density change. Section 4.5 compares results from the extended SSM with the experimental results published by Devlin and Taylor.

4.2 Basic Definition of the Single Scattering Model (SSM)

The SSM has been used for many years (Uemura, 1965; Taylor and Kansara, 1967; Devlin and Taylor, 1970) to explain the basic behaviour of backscatter densitometers. Monte Carlo methods are preferred for modelling real devices (Petler, 1990; James, 1993; Picton *et al.*, 1995) but the SSM can nevertheless be of use to examine basic features of the measurement technique.

The SSM assumes that photons reaching the detector have been scattered only once in the material. This assumption is not valid for real instruments which have large source-detector separations or operate on particularly high densities (the upper limit scale length for single scattering being the attenuation length of source photons in the material). Despite this, however, the competition between scattering and absorption must still exist outside the domain of the SSM. Hence one may expect the SSM to retain some qualitative importance even in the multiple scattering regime. The basic geometry for a surface density gauge is shown in Figure 4.3, though the model can easily be adapted for the cylindrical geometry of borehole devices. Photons of energy E emitted from a source at S propagate into the semi-infinite material underneath the device. A detector of sensitive area A is placed on the surface at a distance d (the sonde length) from the source. Both the source and detector are considered to be point-like in order to simplify the geometry and subsequent analysis.

A general path for singly scattered photons is shown in Figure 4.3, the emission direction being at an angle α to the baseline SD. Compton scattering is assumed to occur at a point P in the material, though some proportion of the photons may not reach P, having undergone absorption or scattering somewhere along the path SP of length r_1. Those photons scattered at P towards the detector make an angle β with the baseline, and may of course be lost along the path PD (of length r_2). The plane of the photon path SPD may be at some angle θ ($-\pi/2 < \theta < +\pi/2$) to the downward vertical. The point P may be defined

either in Cartesian co-ordinates (x,y,z) or by the angular co-ordinates (α,β,θ) together with the sonde length d.

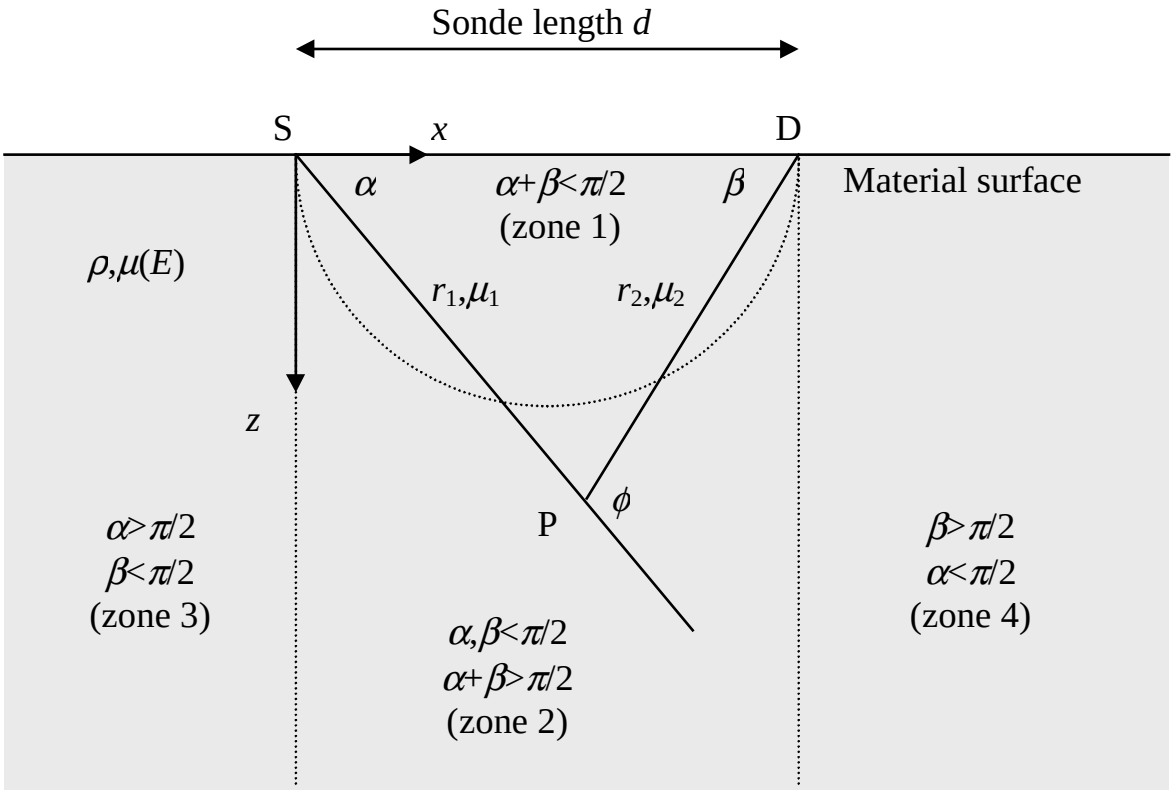

Figure 4.3. Basic geometry of the single scattering model, showing the photon path SPD through the material from the source S to the detector D.

The material under investigation is assumed to be of uniform density ρ. The mass attenuation coefficient μ for photons is a function of their energy. Since one assumes a mono-energetic source (such as the most commonly used radioisotope ^{137}Cs, which emits at 662 keV), the attenuation coefficient μ_1 for primary photons is fixed (at about 7.7×10^{-3} m^2kg^{-1}). However, the mass attenuation coefficient for scattered photons (μ_2) varies with the scattering angle (ϕ), since the scattered photon energy E' is related to ϕ by the Compton formula (4.3). Note that E and E' are dimensionless since they are the ratio of photon energy over the electron mass-energy $m_e c^2$ (= 511 keV).

$$E' = \frac{E}{1 + E(1 - \cos\phi)} \quad . \tag{4.3}$$

For computing μ_2 an energy dependence approximated by a cubic function fitted to tabulated Compton cross-section data (from Storm and Israel, 1970) was used for the appropriate composition (SiO_2 was used for all the examples in this paper since quartz sand

is a common test material). The fit was done in log-log space so the function $\mu(E)$ was of the following form:

$$\log_{10}\mu(E) = a_1 + a_2\log_{10}E + a_3(\log_{10}E)^2 + a_4(\log_{10}E)^3 \quad , \tag{4.4}$$

where $a_{1,2,3,4}$ are fitted coefficients (a_1 = -2.0715, a_2 = -0.38455, a_3 = -0.020659, a_4 = 0.089562).

Using simple trigonometry one can obtain the basic relations (4.5-4.8) between the angular and linear parameters in the diagram. These are useful when transforming between angular and Cartesian co-ordinate systems and when writing computer codes for the SSM.

$$r_1^2 = x^2 + y^2 + z^2 \quad ; \quad r_2^2 = (x-d)^2 + y^2 + z^2 \tag{4.5}$$

$$r_1 = \frac{d\sin\beta}{\sin\phi} \quad ; \quad r_2 = \frac{d\sin\alpha}{\sin\phi} \tag{4.6}$$

$$\phi = \alpha + \beta \tag{4.7}$$

$$\alpha = \tan^{-1}\frac{\sqrt{y^2+z^2}}{x} \quad ; \quad \beta = \tan^{-1}\frac{\sqrt{y^2+z^2}}{d-x} \tag{4.8}$$

In Figure 4.3 the dotted lines define four zones according to whether the angles α or β are greater than or less than $\pi/2$. We shall see that, as one would expect, most of the scattering leading to detection occurs in zone 1. This is also significant in that scattering angles there are less than $\pi/2$, which (due to (4.3)) limits the energy loss of ^{137}Cs photons to avoid lower energies where the interaction cross-section (and thus the density measurement) becomes much more composition dependent.

4.3 Distribution of Scattering Events for Detected Photons

To examine the count rate detected using the SSM one first needs to consider a small volume element *dV* at P, scattering photons towards the detector. The geometry of the volume element *dV* in angular co-ordinates is shown in Figure 4.4.

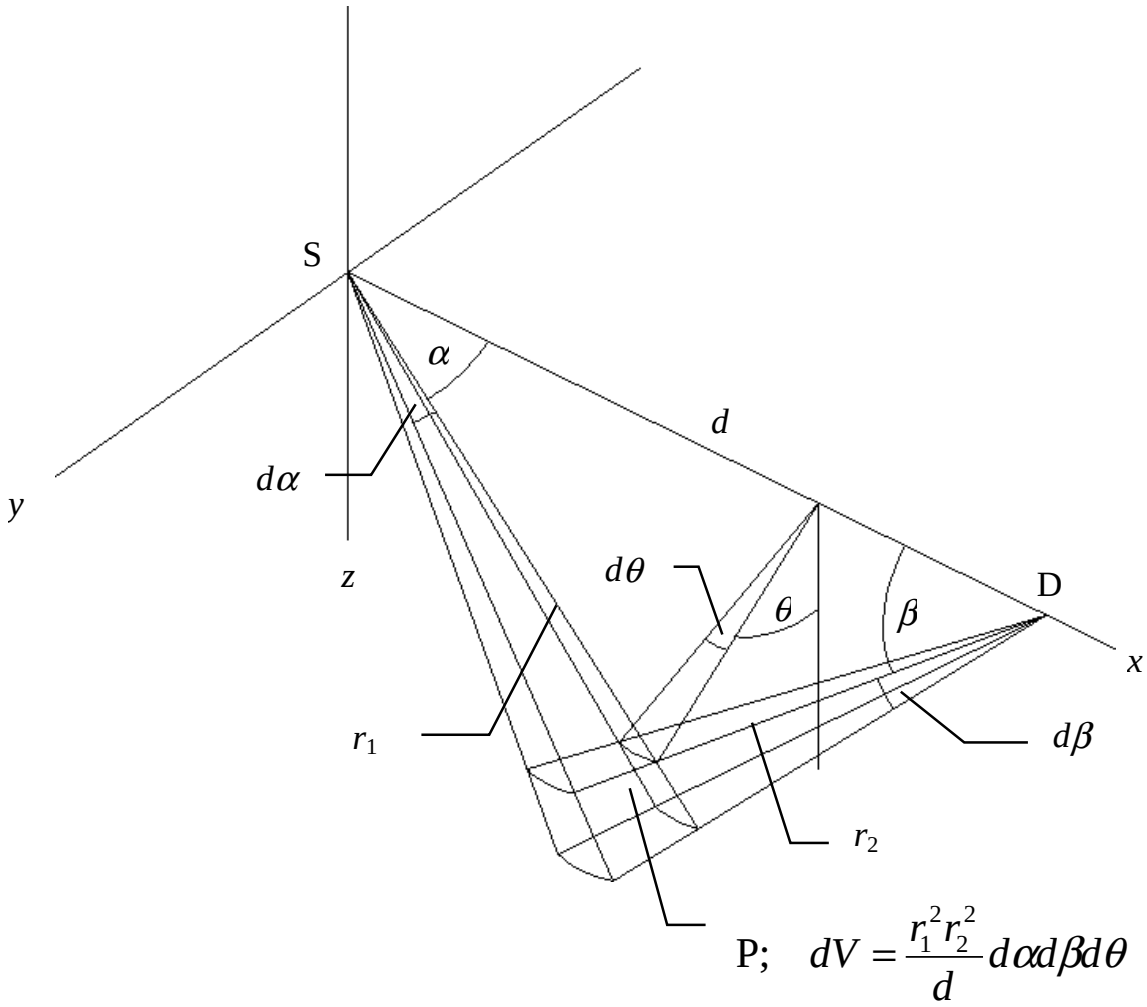

Figure 4.4. Three-dimensional geometry of the volume element *dV* at the scattering point P defined by (α,β,θ) and *d*.

Consider a count rate *dI* resulting from scattering in the volume element *dV*. The primary photon flux emitted from the source is subject to both the inverse square law and exponential attenuation by the material. The differential scattering cross-section is given by the Klein-Nishina formula (Klein and Nishina, 1929). The scattered flux is also subject to the inverse square law and exponential attenuation, though the mass attenuation coefficient is different for scattered photons, which are of lower energy than the primary photons. The detection of scattered photons depends on the area of the detector as well as the geometric factor resulting from the smaller projected area seen by photons incident at oblique angles. Hence that part *dI* of the detected count rate resulting from scattering at P is given initially by the following 'word equation': –

dI = flux from source (photons m^{-2} s^{-1})

$\times$ exponential attenuation factors along primary and scattered photon paths

$\times$ number of electrons in volume element

$\times$ differential cross-section (m^2)

$\times$ solid angle subtended by the detector at the volume element.

$$\therefore \quad dI = \frac{S}{4\pi r_1^2} e^{-\rho(\mu_1 r_1 + \mu_2 r_2)} n dV \frac{d\sigma}{d\Omega} \frac{A \sin\beta \cos\theta}{r_2^2} \quad , \tag{4.9}$$

where S is the source activity (photons s^{-1}) and n is the number density of electrons in the material.

The differential cross-section $d\sigma/d\Omega$ for Compton scattering of a photon of initial energy E is given by the Klein-Nishina formula (4.10).

$$\frac{d\sigma}{d\Omega} = \frac{r_0^2}{2}\left[1 + E(1-\cos\phi)\right]^{-2}\left[1 + \cos^2\phi + \frac{E^2(1-\cos\phi)^2}{1 + E(1-\cos\phi)}\right] \quad , \tag{4.10}$$

where r_0 is the classical electron radius. Using (4.3) to generate the substitution

$$P(E,\phi) = \left[1 + E(1-\cos\phi)\right]^{-1} \tag{4.11}$$

simplifies (4.10) to

$$\frac{d\sigma}{d\Omega} = \frac{r_0^2}{2}\left(P - P^2 \sin^2\phi + P^3\right) \quad . \tag{4.12}$$

The electron number density n can be expressed in terms of mass density ρ, Avogadro's constant (N_A), the mean atomic number (Z) and the mean atomic mass (M) using the relation

$$n = \frac{N_A Z \rho}{M} \quad . \tag{4.13}$$

Using (4.12) to substitute for $d\sigma/d\Omega$ in (4.9) and (4.13) to substitute for n gives us an expression (4.14) for dI including the functional dependence of the Klein-Nishina cross-section.

$$dI = C\rho\left(P - P^2 \sin^2\phi + P^3\right)\frac{e^{-\rho(\mu_1 r_1 + \mu_2 r_2)}}{r_1^2 r_2^2} \sin\beta \cos\theta dV \quad , \tag{4.14}$$

where

$$C = \frac{SN_A ZAr_0^2}{8\pi M} \quad . \tag{4.15}$$

Equation 4.14 can be used to show graphically the density of scattering events (of detected photons) inside the material. Assuming a slice down through the material in the (x,z) plane (i.e. $\theta = 0$), the plot in Figure 4.5 is obtained. The vertical axis is calibrated such that it shows the ratio of the detected scatter density to that which would be obtained if the detected scattering events were distributed uniformly through the hemispherical volume zone 1 (= $\pi d^3/12$). The scatter density at non-zero values of θ is simply less by a factor of $\cos\theta$. Two peaks in response are clearly visible, one under the detector and a smaller one under the source. The results obtained from this calculation are consistent with those shown by Devlin and Taylor (1970), though they limited the calculation to zone 1. It should be noted that this distribution is for an uncollimated device– collimation can be included by setting limits for θ, α (for source collimation) and β (for detector collimation). A contour plot of the data in Figure 4.5 is shown in Figure 4.6.

In Cartesian co-ordinates, however, it is difficult to see both the peaks and the low-level detail elsewhere. As an aid to visualisation it is useful to view the function on the (α,β) plane. As shown in Figure 4.4, the volume element dV is given by

$$dV = \frac{r_1^2 r_2^2}{d} d\alpha d\beta d\theta \quad . \tag{4.16}$$

Substituting (4.16) into (4.14) and expressing r_1 and r_2 in terms of α, β and d, one obtains an expression (4.17) for dI in the angular co-ordinate system (α,β,θ).

$$dI = \frac{C\rho}{d} F_1(\alpha,\beta)\cos\theta d\alpha d\beta d\theta \quad , \tag{4.17}$$

where

$$F_1(\alpha,\beta) = \left(P - P^2\sin^2\phi + P^3\right)\exp\left[-\frac{\rho d\left(\mu_1\sin\beta + \mu_2\sin\alpha\right)}{\sin\phi}\right]\sin\beta \quad . \tag{4.18}$$

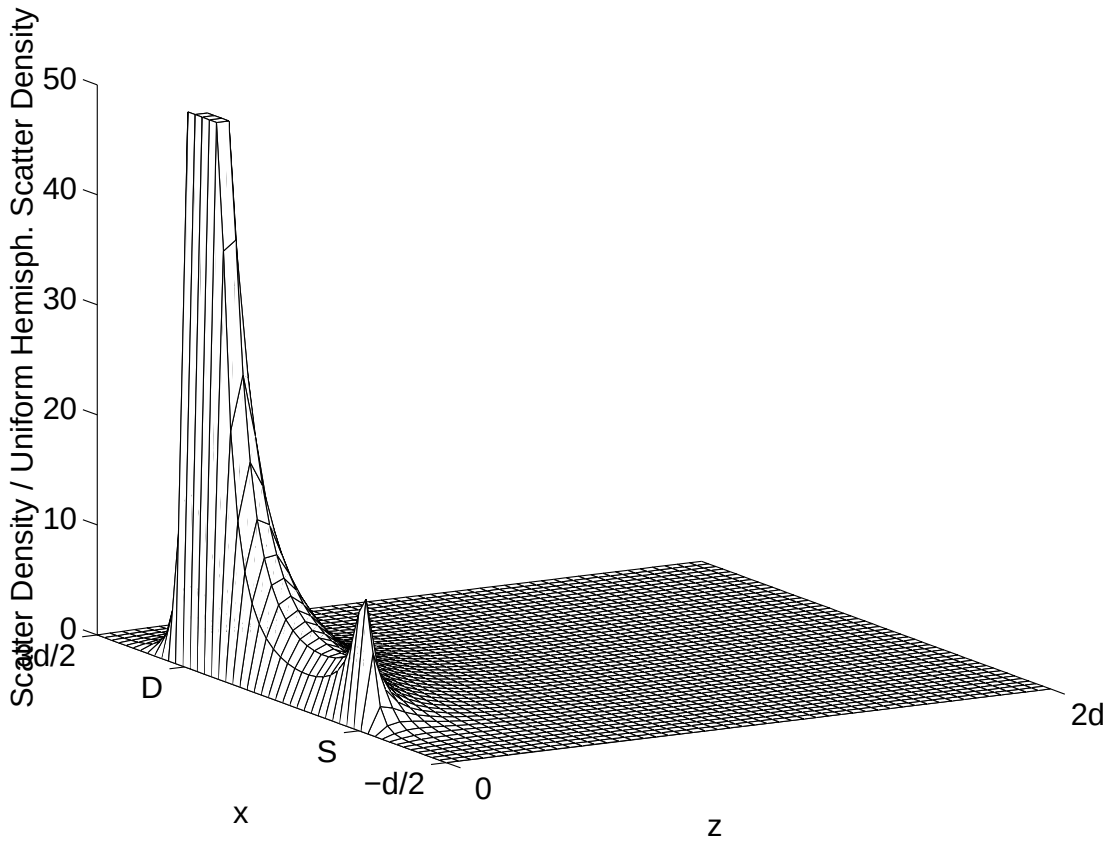

Figure 4.5. Density of scattering events of detected photons, showing a slice down through the material in the (*x*,*z*) plane, for -*d*/2 < *x* < 3*d*/2 and 0 < *z* < 2*d*. The quantity is normalised to the scatter density one obtains by assuming the scattering events to be distributed uniformly through the hemispherical volume zone 1. A large peak is visible below the detector D (truncated for clarity), while a smaller peak exists below the source S. Neither is actually a singularity due to the geometric factor sinβ for the detector in (4.14). Input parameters for this plot are as follows: *E* = 662 keV, *d* = 100 mm and ρ = 1000 kgm^{-3}.

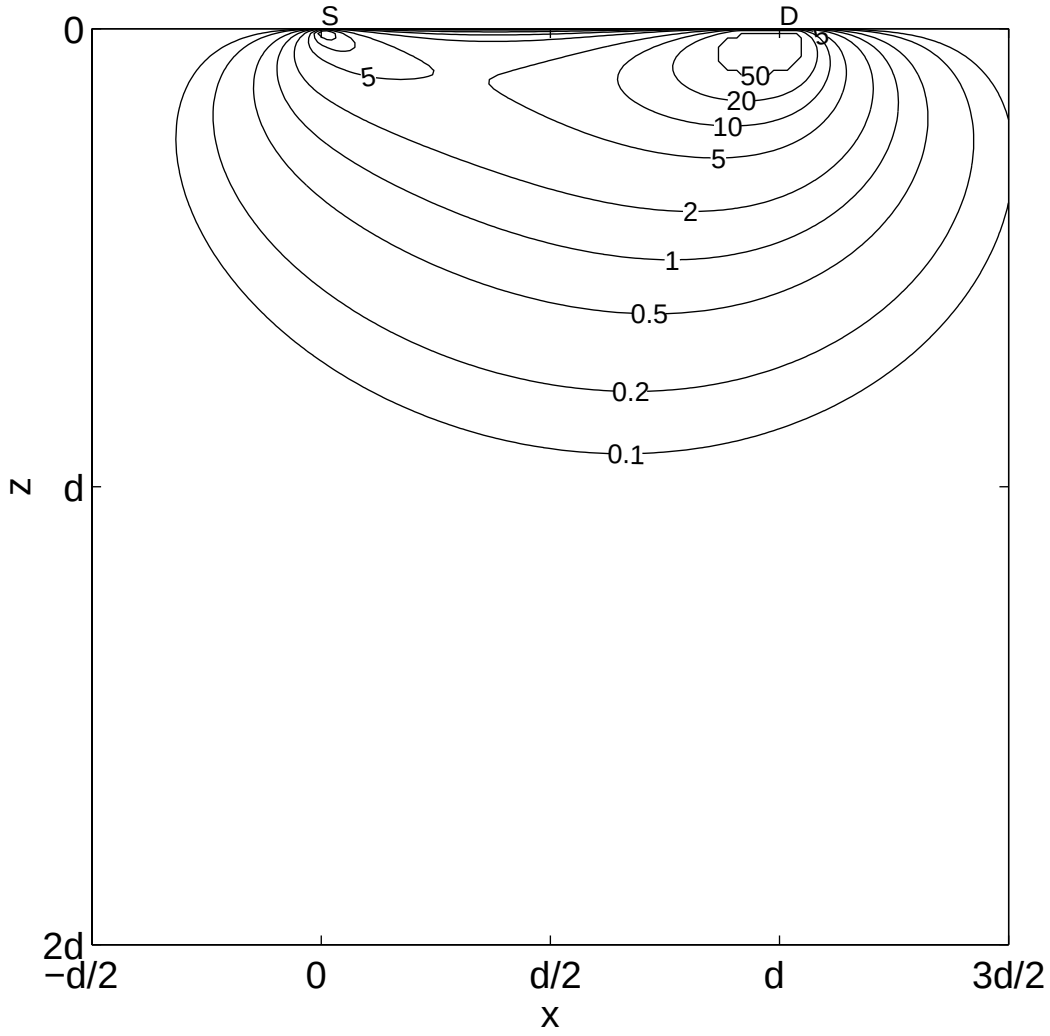

Figure 4.6. Density of scattering events of detected photons, showing the same slice down through the material as in Figure 4.5 and the same input parameters, but as a contour plot. Again the large peak below the detector is truncated for clarity.

The dimensionless function $F_1(\alpha,\beta)$ is shown in Figure 4.7. This representation shows the angular dependence of the scattering and absorption more clearly by using a co-ordinate system more suited to the problem. Figure 4.8 shows how the Cartesian co-ordinates x and z map onto the (α,β) plane. Contours of constant depth z are of the form

$$\alpha = \cot^{-1}\left(\frac{d}{\sqrt{y^2 + z^2}} - \cot\beta \right) \quad , \tag{4.19}$$

while those of constant x are of the form

$$\alpha = \tan^{-1}\left(\left(\frac{d}{x} - 1 \right) \tan\beta \right) \quad . \tag{4.20}$$

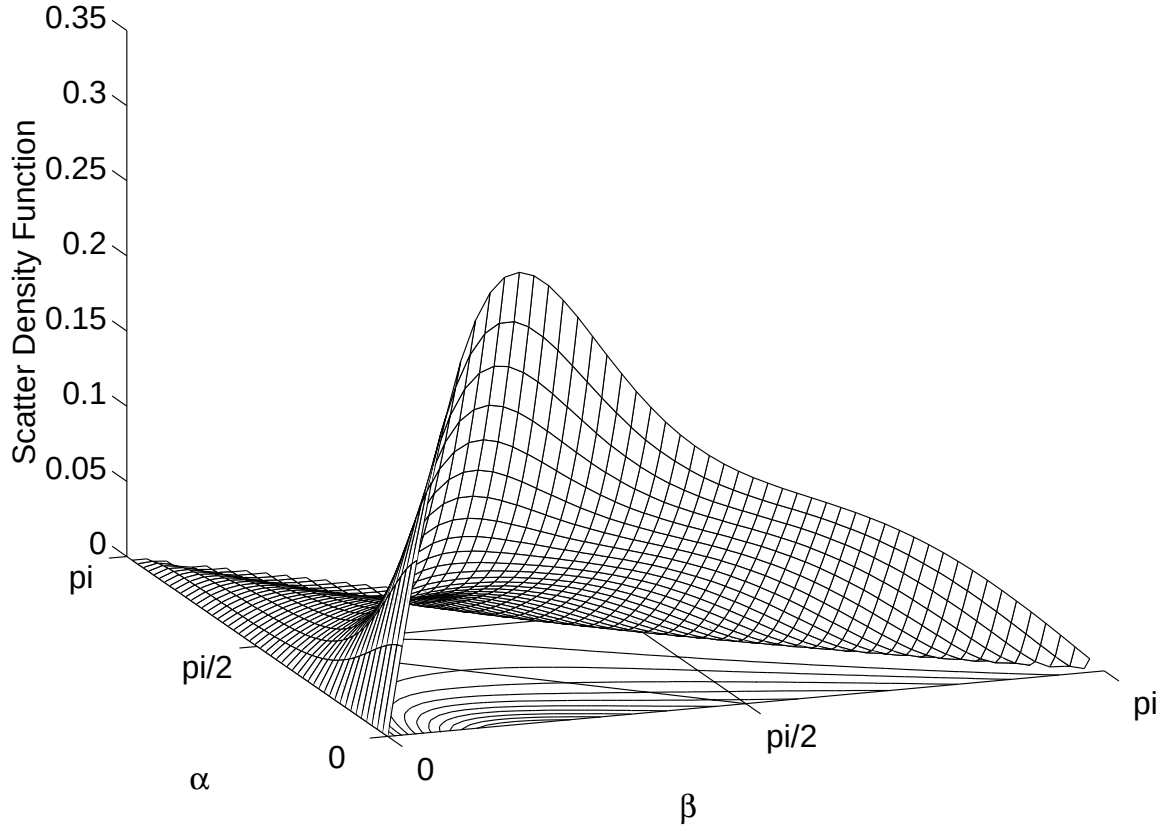

Figure 4.7. Dimensionless scatter density function $F_1(\alpha,\beta)$. $F_1(\alpha,0) = 0$ and $F_1(\alpha,\pi-\alpha) = 0$. The fact that only a single peak is seen here compared with the Cartesian version in Figure 4.5 is a result of the mapping to the (α,β) plane.

Integrating $F_1(\alpha,\beta)$ under contours of constant depth can be used to show how the density of scattering events varies with depth. The numerical integration (4.21) is easier to perform on the more well-behaved function $F_1(\alpha,\beta)$ than the Cartesian form.

$$\int_{z'=0}^{z} dI = \frac{C\rho}{d} \int_{\theta=-\frac{\pi}{2}}^{+\frac{\pi}{2}} \int_{\beta=0}^{\pi} \int_{\alpha=0}^{\cot^{-1}\left(\frac{d\cos\theta}{z'}-\cot\beta\right)} F_1(\alpha,\beta)\cos\theta\, d\alpha\, d\beta\, d\theta \quad . \tag{4.21}$$

The result of this integration (shown differentially and normalised to the integral for $z = \infty$) is shown in Figure 4.9, for a density of 1000 kgm^{-3}. A FORTRAN code was used, including NAG numerical library routines D01AHF and D01DAF. As expected the density of scattering events leading to detection falls off almost exponentially with depth. The decay with normalised depth is steeper for greater sonde lengths since the unchanged attenuation length becomes ever smaller in comparison. The mean depth data can be

plotted as absolute depth vs. sonde length, as shown in Figure 4.10. A power law fit shows that doubling the sonde length increases the mean depth by a factor of about 1.51. The author leaves it as an open question whether a similar figure can be determined for real devices.

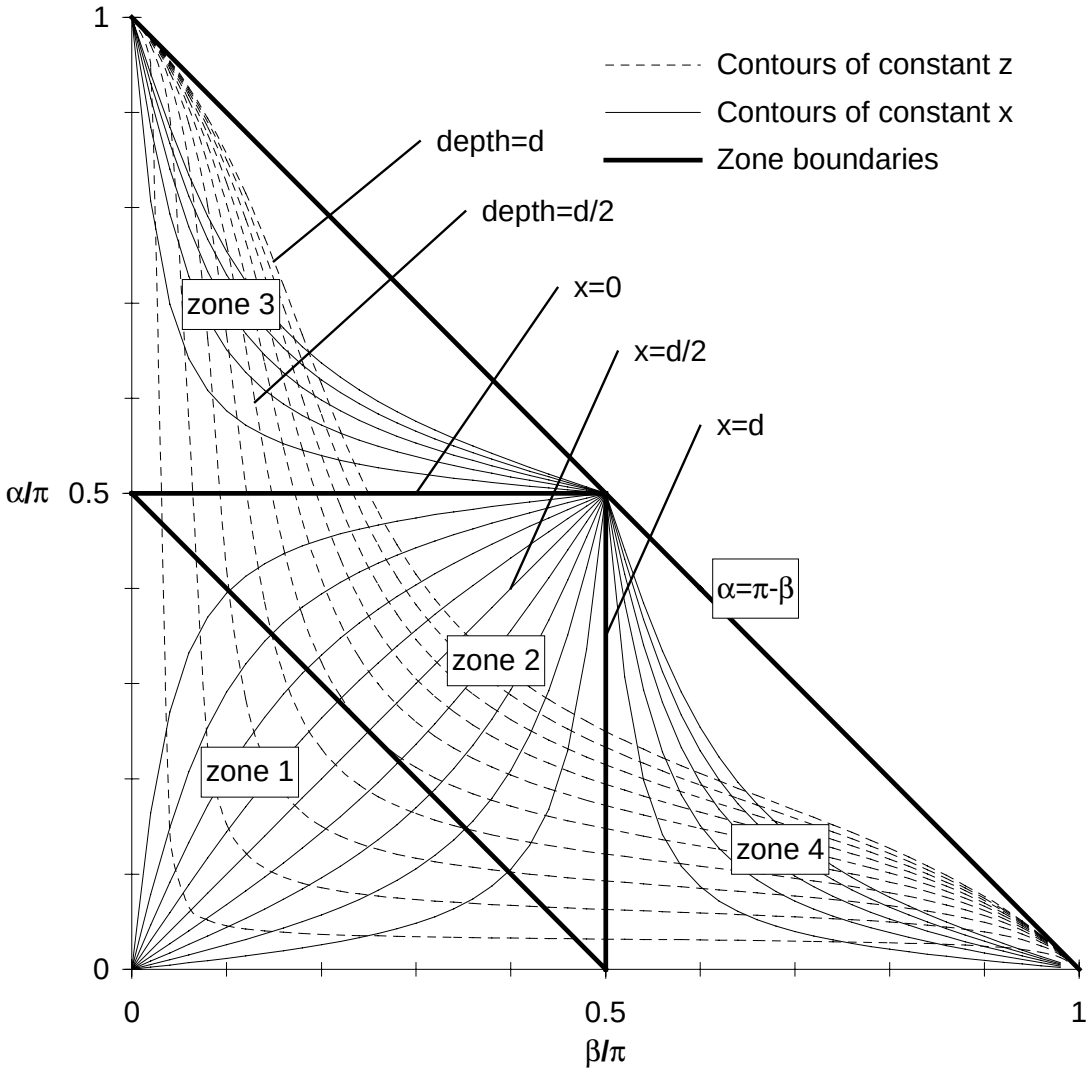

Figure 4.8. Contours of constant *z* (depth) and *x* in (α,β) space (θ = 0). The four triangular zones correspond to those shown in Figure 4.3. Values of *z* are from *d*/10 to *d* in steps of *d*/10. Values of *x* are from -*d*/2 to +3*d*/2 in steps of *d*/10.

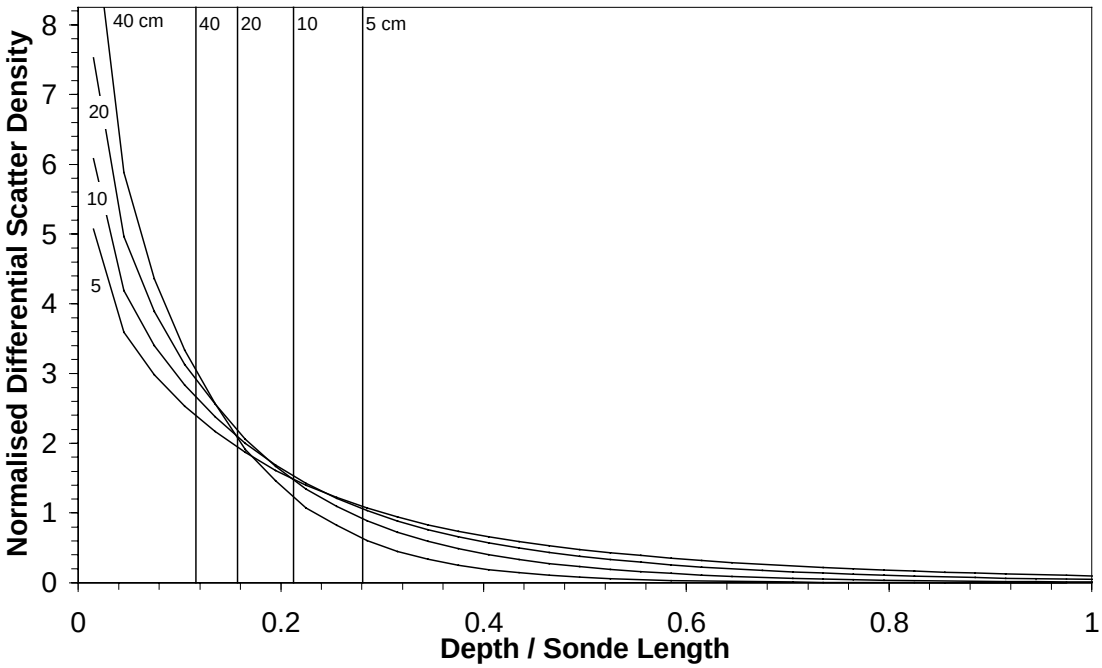

Figure 4.9. Spatial density of scattering events leading to detection plotted vs. depth into the material. The density of scattering events is normalised to the total (i.e. the area under each curve is unity). The depth is expressed as a fraction of the sonde length. The curves represent sonde lengths of 5, 10, 20 and 40 cm; in each case the mean depth is indicated. The results are for a material density of 1000 kgm^{-3}.

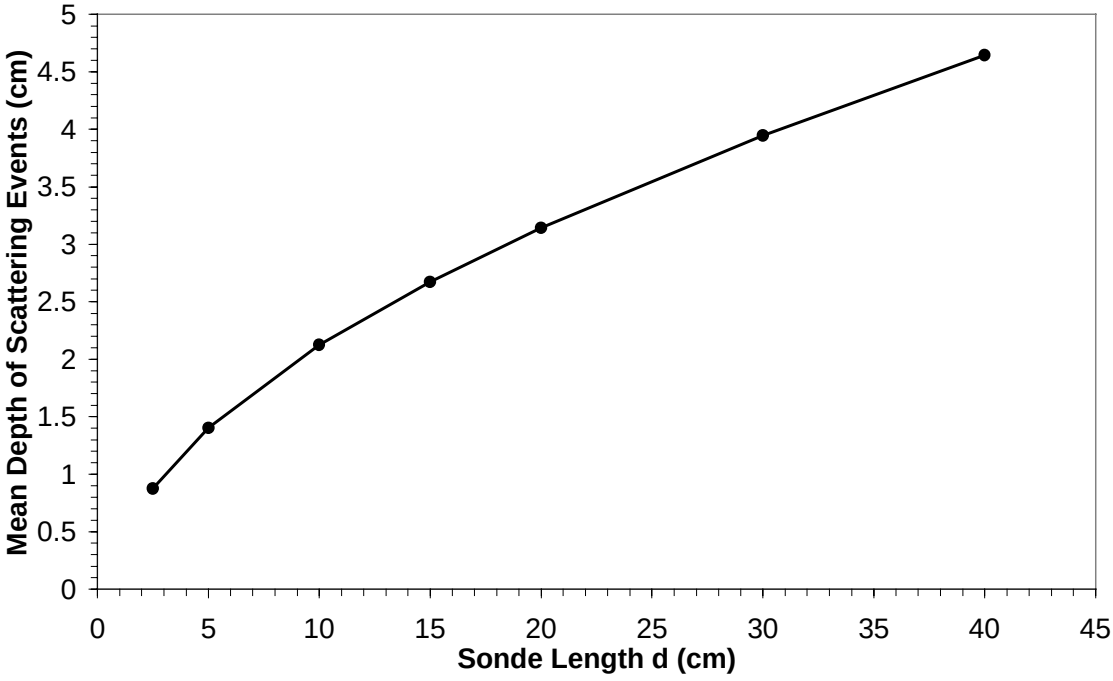

Figure 4.10. Mean depth of scattering events leading to detection plotted vs. sonde length, as determined using the single scattering model. A power law fit gives an exponent of 0.5965 and a regression coefficient of 0.99925.

4.4 Extension of the Single Scattering Model

The SSM will now be extended to examine the effect on the detected count rate (and hence measured density) of a small localised density change. Consider a small volume element *dV* at a general point P in the material, with enhanced density $\rho + \delta\rho_P$. The effect of this will be threefold, as illustrated in Figure 4.11: –

- The increased number of electrons will increase the scattering at P.
- The increased density will cause increased attenuation of primary photons.
- The increased density will cause increased attenuation of scattered photons.

Equation 4.17 can be adapted to account for these three effects, producing an expression for the resultant change in count rate $\delta(dI)$ due to the density change in *dV*. Expressing $\delta(dI)$ as the sum of $\delta_1(dI)$, $\delta_2(dI)$ and $\delta_3(dI)$ for each of the three effects respectively, one obtains equations 4.22, 4.24 and 4.25.

$$\delta_1(dI) = \frac{C}{d} F_2(\alpha,\beta)\sin\beta\cos\theta\, d\alpha\, d\beta\, d\theta\, \delta\rho_P \quad , \tag{4.22}$$

where

$$F_2(\alpha,\beta) = \left(P - P^2\sin^2\phi + P^3\right)\exp\left[-\frac{\rho d\left(\mu_1\sin\beta + \mu_2\sin\alpha\right)}{\sin\phi}\right] \quad . \tag{4.23}$$

Equation 4.22 is equivalent to $dI \times \delta\rho_P/\rho$.

$$\begin{aligned}\delta_2(dI) &= -\frac{C\rho}{d}\left(\int_{\beta'=\beta}^{\pi-\alpha} F_2(\alpha,\beta')\sin\beta' d\beta'\right)\cos\theta\, d\alpha\, d\theta\left(1 - e^{-\delta\rho_P\mu_1 r_2 d\beta}\right) \\ &\approx -\frac{C\rho}{\sin\phi}\mu_1\sin\alpha\left(\int_{\beta'=\beta}^{\pi-\alpha} F_2(\alpha,\beta')\sin\beta' d\beta'\right)\cos\theta\, d\alpha\, d\beta\, d\theta\, \delta\rho_P \quad .\end{aligned} \tag{4.24}$$

$$\begin{aligned}\delta_3(dI) &= -\frac{C\rho}{d}\left(\int_{\alpha'=\alpha}^{\pi-\beta} F_2(\alpha',\beta) d\alpha'\right)\sin\beta\cos\theta\, d\beta\, d\theta\left(1 - e^{-\delta\rho_P\mu_2 r_1 d\alpha}\right) \\ &\approx -\frac{C\rho}{\sin\phi}\mu_2\sin^2\beta\left(\int_{\alpha'=\alpha}^{\pi-\beta} F_2(\alpha',\beta) d\alpha'\right)\cos\theta\, d\alpha\, d\beta\, d\theta\, \delta\rho_P \quad .\end{aligned} \tag{4.25}$$

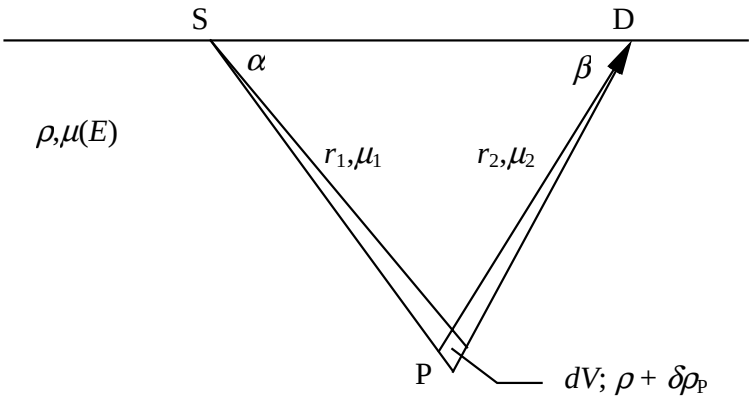

1) Increased number of scattering centres in volume element at P.

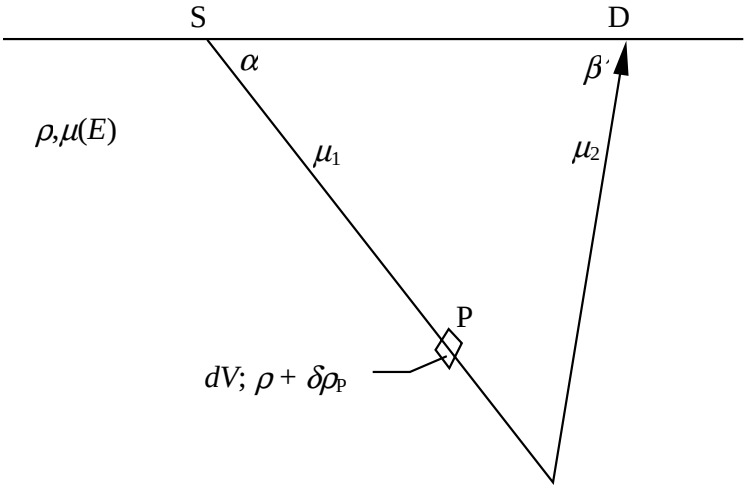

2) Increased absorption for primary photon paths passing through volume element at P.

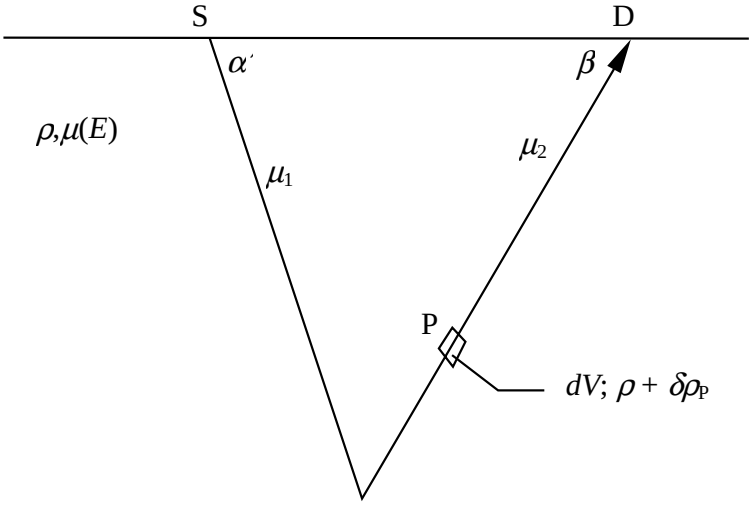

3) Increased absorption for scattered photon paths passing through volume element at P.

Figure 4.11. Enhanced density in volume element *dV* at P has three effects: 1) increased number of scattering centres, 2) increased attenuation of primary photons, and 3) increased attenuation of scattered photons.

Primary photon paths passing through the region of enhanced density always have angular co-ordinates β greater than that of point P, hence the integral expression for $\beta < \beta' \leq \pi\text{-}\alpha$ in (4.24). Similarly, for scattered photon paths passing through P there is an integral expression in (4.25) over the range $\alpha < \alpha' \leq \pi\text{-}\beta$. The primed co-ordinates are dummy variables. In (4.24) and (4.25) the approximation made assumes the additional attenuation factor through the perturbed volume element to be small, i.e. $\delta\rho_P \mu_1 r_2 d\beta \ll 1$ and $\delta\rho_P \mu_2 r_1 d\alpha \ll 1$ respectively. This is reasonable since $d\alpha$ and $d\beta$ are infinitesimal.

By summing the three terms one obtains

$$\delta(dI) = \frac{C}{d}\left[F_2(\alpha,\beta)\sin\beta - \frac{\rho d}{\sin\phi}\left(\mu_1 \sin\alpha \int_{\beta'=\beta}^{\pi-\alpha} F_2(\alpha,\beta')\sin\beta' d\beta' + \mu_2 \sin^2\beta \int_{\alpha'=\alpha}^{\pi-\beta} F_2(\alpha',\beta) d\alpha'\right)\right]\cos\theta d\alpha d\beta d\theta \delta\rho_P \,. \quad (4.26)$$

This expression for sensitivity of total count rate to a small change in local density is not simply a differentiation of (4.17) with respect to density, since one is now making a distinction between the local density ρ_P in the volume element dV and the bulk density ρ of the surrounding material.

Figure 4.12 shows the dimensionless quantity

$$\frac{\delta(dI)d}{C\cos\theta d\alpha d\beta d\theta \delta\rho_P} \quad , \quad (4.27)$$

i.e. the part which varies with α and β (again, the NAG library routine D01AHF was used). Clearly there are both positive and negative regions. This shows that a local increase in density can cause either an increase or decrease in count rate, depending on the location of the density enhancement. The location of the two regions can be seen plotted in Cartesian co-ordinates in Figure 4.13, the units of which are m^{-4}.

To examine the function in Cartesian co-ordinates one can write

$$\delta(dI) = C\left[F_2(\alpha,\beta)\sin\beta - \frac{\rho d}{\sin\phi}\left(\mu_1 \sin\alpha \int_{\beta'=\beta}^{\pi-\alpha} F_2(\alpha,\beta')\sin\beta' d\beta' + \mu_2 \sin^2\beta \int_{\alpha'=\alpha}^{\pi-\beta} F_2(\alpha',\beta) d\alpha'\right)\right]\frac{\cos\theta}{r_1^2 r_2^2} dV \delta\rho_P \,. \quad (4.28)$$

To show the functional part of this the quantity

$$\frac{\delta(dI)}{C\cos\theta dV \delta\rho_P} \quad , \quad (4.29)$$

(which has units of m^{-4}) was plotted in Figure 4.13.

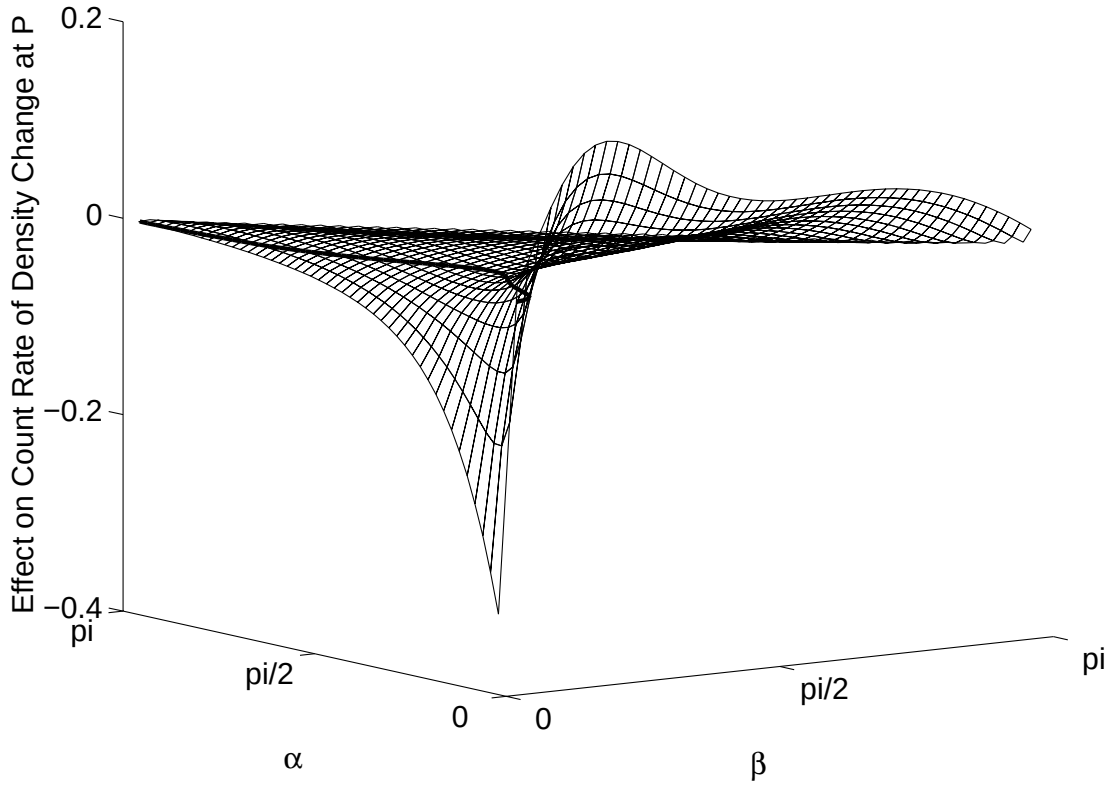

Figure 4.12. Plot of the dimensionless function (4.27), showing the effect on count rate of small local changes $\delta\rho_P$ in density, as a function of α and β. There are both positive and negative regions, showing that a local increase in density can either cause an increase or decrease in count rate, depending on the location of the density enhancement. The zero contour is shown to identify the boundary between positive and negative regions.

The existence of these two regions means that a localised change in density can actually cause the backscatter densitometer to give a false indication if the density variation is in the 'wrong' region. Whether this is the case or not depends not only on whether (4.26) is positive or negative, but also whether $dI/d\rho$ is positive or negative on the calibration curve. Since most backscatter devices operate in the region where $dI(\rho)/d\rho < 0$, it is the positive region in Figure 4.13 which will produce a contradictory response when a perturbation is introduced.

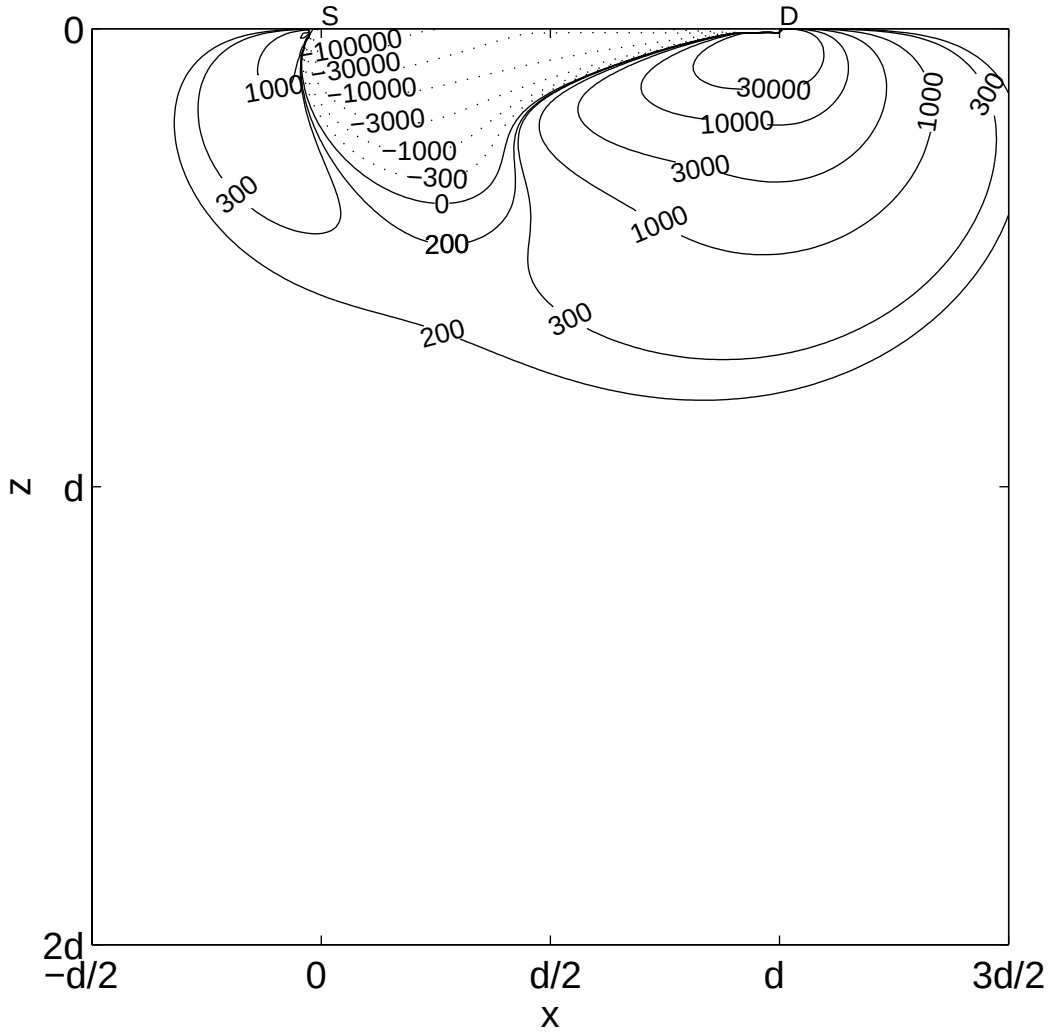

Figure 4.13. Contour plot in Cartesian co-ordinates of (4.29), illustrating the sensitivity of the detected count rate to a localised density perturbation $\delta\rho_P$. The contour values are in units of m^{-4}.

4.5 Comparison with Experimental Results

As a first test for the predictions of the extended SSM the author tried to reproduce the results of Devlin and Taylor (1970) shown in Figure 4.2. The key parameters of their experiment were included in their paper (d = 116 mm, ρ = 1720 kgm^{-3}, depth of perturbation = 20 mm), with the exception of the size and density of the perturbing volume element. However, their diagram indicates a sphere perhaps 10 mm in diameter which they state was made of expanded polystyrene. This was assumed to have had a density of around 100 kgm^{-3}, much lower than that of the surrounding material. For the bulk material the author assumed the mass attenuation coefficient of SiO_2 (as used in sections 4.3 and 4.4) to be an adequate approximation for their "standard soil".

To derive a quantity equivalent to the percentage change in count rate quoted by Devlin and Taylor the author evaluated (4.28) for the appropriate range of depths (centred on 20 mm) covered by the finite size of the perturbation, with $\theta = 0$. These were then combined, weighted according to the fractional volume of sphere present at each depth value. This quantity was then divided by the total count rate from (4.21) and multiplied by the value of $dV\delta\rho_P$ obtained using the radius of the sphere and the assumed density change (-1620 kgm^{-3}). In addition an offset was introduced to match the model to zero at the source, since the experimental data concerns the change relative to the count rate for the perturbation below the source rather than uniform material.

The model was run for several sets of parameters, reflecting their uncertainty in the original experiment. The results are shown in Figure 4.14 together with the experimental data. The model consistently shows the positive and negative peaks reported by Devlin and Taylor, however no single set of parameters produces a model that follows the data closely everywhere.

Assuming a radius of 5 mm, the model predicts a change in count rate far smaller than that reported. However, the degree of collimation of the source and detector may be responsible for reducing the total count rate and increasing the relative importance of the region where the perturbation is placed. Collimation to limit the range of θ would have such an effect, for instance. Line A shows the model data amplified by a factor of 112 to match the peak heights of the data. The main difference in shape is that the model shows the negative peak to be nearer the detector. This could be the effect of detector collimation to limit β, concentrating the instrument on the region between source and detector. A good fit is obtained without an 'artificial' amplification factor by increasing the radius of the perturbation to 19 mm (line B). Not only do both peaks match in height, the zero point between them also coincides with the data. The positive peak is now also displaced from the data, however.

The extended SSM clearly shows the two regions of opposite effect, though without better knowledge of the collimation and characteristics of the perturbing sphere in the original experiment it is difficult to match the model more closely. The location of the model's negative peak closer to the detector does suggest collimation in β, while the need for a large amplification factor to fit the model to the peak heights also suggests collimation in θ.

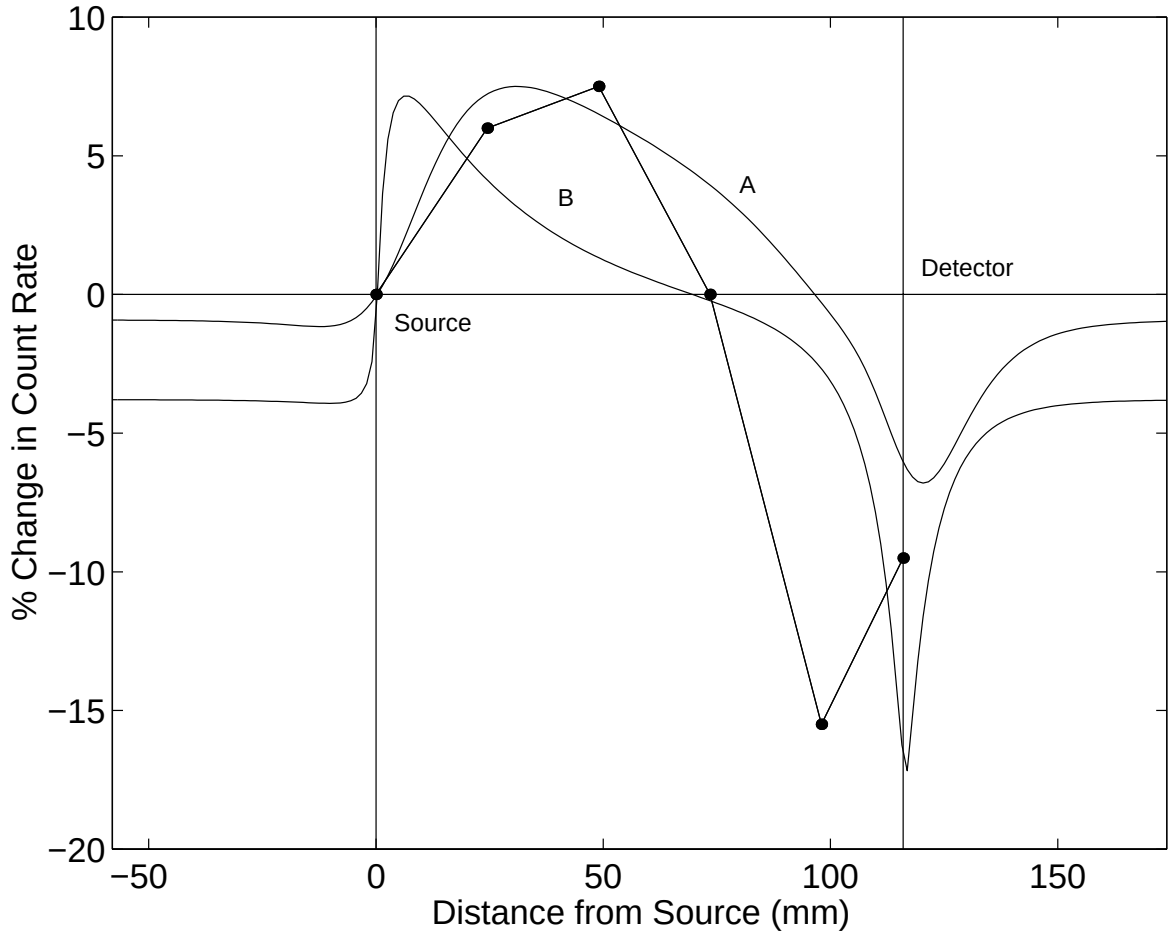

Figure 4.14. Comparison of experimental data (connected points) from Devlin and Taylor (1970) with results from the extended single scattering model (smooth lines).

4.6 Conclusions and Further Work

This paper explains how the effect shown by Devlin and Taylor (1970) can be examined by extending the single scattering model for gamma backscatter density gauges. Understanding how a backscatter density gauge responds to inhomogeneities in the target is clearly important since voids and density enhancements are common in natural materials.

Since the apparatus used by Devlin and Taylor is not fully described in their paper it is difficult to make a full comparison between the extended SSM and the data. However the basic features are reproduced by the model, namely a positive peak near the source and a negative peak near the detector. The positive peak is also seen to be broader than the negative one. Although the model cannot yet claim to reproduce quantitative results perfectly, it does provide a basic theoretical framework that could be extended further. Collimation and the energy dependence of the detector could certainly be incorporated, for

instance. A Monte Carlo method would have to be applied to incorporate multiple scattering effects.

Since most real gauges operate in the regime where $dI(\rho)/d\rho < 0$, the most important 'contradictory' region lies under the detector, where decreases in density *reduce* the count rate. This was shown in Figure 4.13 for the example set of model parameters. Further investigation is required to show how the sizes and shapes of the regions change for different cases.

It is interesting to consider the effect on the count rate of a single perturbation as the density gauge passes over the surface parallel to the baseline, as is the case for borehole density logging. The count rate would rise and fall– or fall and rise– before returning to the response from the uniform material. The asymmetry between the positive and negative peaks (as seen in Figure 4.14) could maybe be used to distinguish between positive and negative density perturbations. Simply applying the calibration curve to the count rate would incorrectly suggest adjacent regions of higher and lower density in the bulk material, rather than a single region of different density. Similar scenarios might be considered for stationary devices examining bubbles or solid lumps carried past the instrument in a liquid, or imperfections in a continuously produced material.

The author does not currently have access to facilities suitable for a comprehensive study of real backscatter density gauges, nor is an in-depth application of Monte Carlo codes anticipated. Rather, it is hoped that other workers more directly involved in soil science, borehole logging or non-destructive testing might carry this topic forward.

4.7 Summary of Key Mathematical Symbols

Symbol(s)	Description	Units
I	Total count rate detected at D	photons s^{-1}
dI	Number of photons per second from volume element dV scattered into the detector	photons s^{-1}
dV	Volume element at point P	m^3
S	Source activity	photons s^{-1}
n	Number density of electrons	m^{-3}
A	Area of detector (in (x,y) plane)	m^2
$\frac{d\sigma}{d\Omega}$	Differential cross-section for Compton scattering	$m^2 str^{-1}$
μ_1,μ_2	Mass attenuation coefficient of photon in the material before and after scattering	$m^2 kg^{-1}$
ρ	Bulk density of material	kgm^{-3}
ρ_P	Material density in volume element at P	kgm^{-3}
$\delta\rho_P$	Small change in ρ_P	kgm^{-3}
α,β	Angles of primary and scattered photon paths to the surface	radians
ϕ	The angle of scattering, equal to $\alpha + \beta$	radians
θ	Angle made by photon path to the downward vertical	radians
r_1,r_2	Length of primary and scattered photon paths	m
d	Source-detector separation (sonde length)	m
r_0	Classical electron radius ($= e^2/(4\pi\varepsilon_0 m_e c^2) = 2.818 \times 10^{-15}$ m)	m
E	Ratio of source photon energy relative to the electron mass-energy $m_e c^2$ (= 511 keV)	

5 Monte Carlo Simulations

To model the densitometer design presented in chapter 3, Monte Carlo simulation can be employed. The author developed a FORTRAN Monte Carlo code to examine the absorption and scattering of photons in bulk material. Photons are emitted from a point source and tracked as they are scattered or absorbed. The code does not model the detector response but can provide the basic properties (position, direction and energy) of photons passing through one or more 'virtual detectors' at or above the material's surface. For a source placed beneath the surface on the *z*-axis of the instrument the code can take advantage of axial symmetry to improve the counting statistics. The detector positions are thus defined by their inner and outer radii from the *z*-axis. The code then integrates all detected counts in an annulus around the axis to determine the number of counts per unit area. This is then multiplied by the desired effective detector area to obtain the number of counts detected. The code enables effects due to scattering and absorption alone to be investigated in isolation. In this way the source / detector configuration can be optimised independently from the detector response.

5.1 FORTRAN Code

The code was first used to study the backscatter of ^{241}Am photons for the previous MUPUS densitometer design concept (Ball *et al.*, 1996). This confirmed that for selected mineral components (that are thought to be present in cometary material) the density does have a measurable effect on the detectable backscatter. Since then the code has been extended and used to simulate the attenuation concept. The key new features of the current version are as follows: –

- For computing the mass attenuation coefficients of coherent, incoherent (Compton) and photoelectric interactions the energy dependence is now approximated by a cubic function fitted to tabulated Compton cross-section data (from Storm and Israel, 1970). The fit was done in log-log space so the function $\mu(E)$ is of the following form:

$$\log_{10}\mu(E) = a_1 + a_2\log_{10}E + a_3(\log_{10}E)^2 + a_4(\log_{10}E)^3 \quad , \tag{5.1}$$

where $\mu(E)$ is the appropriate mass attenuation coefficient (in m^2kg^{-1}), E is the reduced energy[5] and $a_{1,2,3,4}$ are fitted coefficients. The fit was done for each element (for $Z = 1 \rightarrow 28$) independently, between 1 keV and 1 MeV. Where an element's K edge lies within this range, two separate fitted curves are used. The position of the K edge is also found using a fitted cubic function– this gives the K edge energy as a function of Z. The fitting was done using the general linear least squares method found in *Numerical Recipes* (Press *et al.*, 1992).

- The elemental abundances are set as input parameters. These are then used to generate the combined mass attenuation coefficients for the material. The speed of calculation is improved for the coherent and Compton coefficients since the combined function over all elements can also be expressed as a single cubic polynomial. The presence of K edges prevents the use of this for the photoelectric cross-section, however.
- A loop has been added to simulate several material densities in a single run of the code; generally these are $200 \rightarrow 2000$ kgm^{-3} in steps of 200 kgm^{-3}.
- Several 'virtual detectors' can be positioned where required. Where axial symmetry can be used (as is the case for the current *MUPUS* densitometer design) the counting statistics are improved. This is done by integrating around the axis to obtain count rate per unit area vs. radius from the axis. The number of counts reaching each detector is then determined by multiplying the number of counts per unit area (within the appropriate radius limits) by the effective area of the detector.

The input parameters for the Monte Carlo code are summarised in Figure 5.1. The source can be positioned anywhere on or below the surface and collimated if necessary– otherwise the half-cone angle of the beam is set to 180°, producing an isotropic source.

[5] The reduced energy is the photon energy divided by the rest mass energy $m_e c^2$ of an electron, which equals 511 keV.

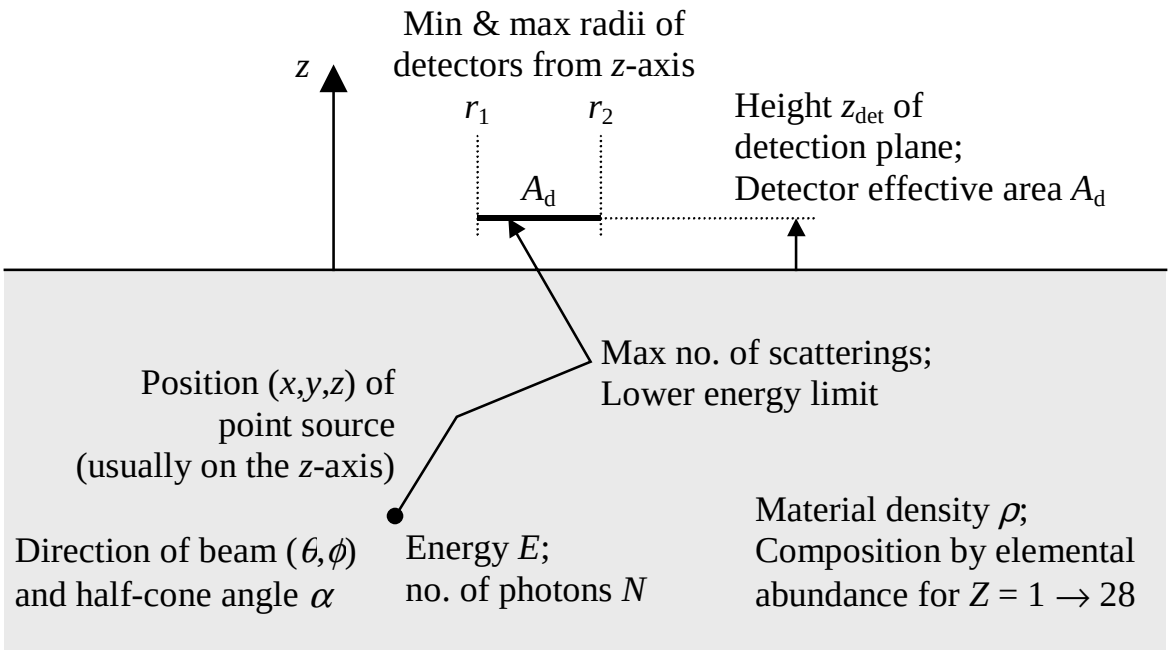

Figure 5.1. Schematic diagram showing the input parameters of the Monte Carlo simulation code.

5.2 Monte Carlo Algorithm

The photon source is assumed to be point-like and located at or below the surface of a semi-infinite bulk material of uniform density. Monte Carlo simulation is used to follow a large number of photon histories in order to determine the spatial, directional and spectral distribution of the backscattered radiation. A pseudo-random number generator (NAG numerical library routine G05CAF) is used to obtain a uniform distribution of random numbers ν in the range $0 \le \nu < 1$. Simulation of a single photon history requires the following steps: –

1. Sampling for emission direction (polar and azimuthal angles θ and ϕ, respectively). Random sampling is required unless the beam is perfectly collimated. For a beam of half-cone angle $\Delta\theta$ centred on the direction (θ_0,ϕ_0), sampling is done first for the polar and azimuthal angles θ_L and ϕ_L relative to this axis. The resultant direction is then transformed back to the laboratory frame. For two random numbers ν_θ and ν_ϕ the angles θ_L and ϕ_L are given by

$$\theta_L = \cos^{-1}\left(1-\nu_\theta\left(1-\cos\Delta\theta\right)\right) \tag{5.2}$$

$$\text{and} \quad \phi_L = 2\pi\nu_\phi \quad . \tag{5.3}$$

The transformation back to the co-ordinates θ_1 and ϕ_1 in the laboratory frame is done using spherical trigonometry, as shown in Figure 5.2.

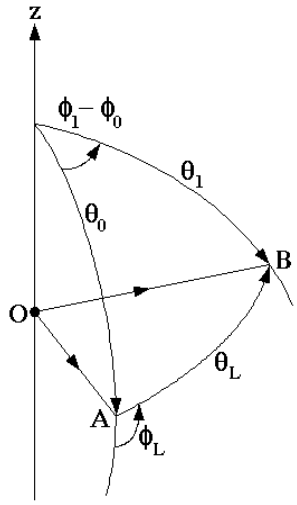

Figure 5.2. Spherical triangle for transformation between spherical co-ordinate systems. Given (θ_0,ϕ_0) and (θ_L,ϕ_L), (θ_1,ϕ_1) can be calculated. This is used for both the initial source beam and for calculating the new direction after scattering. Original direction is OA, new direction is OB.

First, θ_1 is found via $\cos(\theta_1)$ using spherical trigonometry (5.4, 5.5).

$$\cos\theta_1 = \cos\theta_0 \cos\theta_L - \sin\theta_0 \sin\theta_L \cos\phi_L \tag{5.4}$$

$$\therefore \quad \sin\theta_1 = \sqrt{1-\cos^2\theta_1} \tag{5.5}$$

Spherical trigonometry is then used to obtain $\sin(\phi_1-\phi_0)$ and $\cos(\phi_1-\phi_0)$ (5.6, 5.7).

$$\frac{\sin(\phi_1-\phi_0)}{\sin\theta_L} = \frac{\sin\phi_L}{\sin\theta_1}, \quad \therefore \quad \sin(\phi_1-\phi_0) = \frac{\sin\theta_L \sin\phi_L}{\sin\theta_1} \tag{5.6}$$

$$\cos\theta_L = \cos\theta_0 \cos\theta_1 + \sin\theta_0 \sin\theta_1 \cos(\phi_1-\phi_0)$$

$$\therefore \quad \cos(\phi_1-\phi_0) = \frac{\cos\theta_L - \cos\theta_0 \cos\theta_1}{\sin\theta_0 \sin\theta_1} \tag{5.7}$$

The trigonometric relations for the sine and cosine of two angles are then used to evaluate ϕ_1. Both $\sin(\phi_1)$ and $\cos(\phi_1)$ are required to determine ϕ_1 uniquely in the range $-\pi \le \phi_1 \le +\pi$.

$$\sin\phi_1 = \sin(\phi_1-\phi_0)\cos\phi_0 + \cos(\phi_1-\phi_0)\sin\phi_0 \tag{5.8}$$

$$\cos\phi_1 = \cos(\phi_1-\phi_0)\cos\phi_0 - \sin(\phi_1-\phi_0)\sin\phi_0 \tag{5.9}$$

2. Sampling for source energy. This would only be used for non-monochromatic sources, e.g. ^{60}Co which has two emission peaks.
3. Determination of the attenuation length l_0 of the photon in the material, using $l_0 = \mu(E)^{-1}$, where $\mu(E)$ is the mass attenuation coefficient multiplied by the density and E is the photon energy. For speed of calculation the mass attenuation data is best expressed as a fitted function such as parabolae in log-log space.
4. Sampling for the actual path length l of the photon in the material, using (5.10).

$$l = -l_0 \ln(1-\nu), \quad \text{where} \quad l_0 = \mu(E)^{-1} \quad . \tag{5.10}$$

5. Calculation of the position of the interaction using direction and path length.
6. Sampling for interaction process. This requires fitted functions (of the form of equation 5.1) for the probabilities of possible processes. In the case of photoelectric absorption or pair production, the photon is discarded. Scattered photons proceed to the next step.
7. Sampling for the new photon energy after Compton scattering. This is done by random sampling of the Klein-Nishina distribution. The most appropriate sampling method for this application is the Kahn method, which is not an approximation (being derived directly from the Klein-Nishina cross-section) and works for any incident photon energy (Blomquist and Gelbard, 1983; Raeside, 1976; Wood, 1982). The method works by non-uniform rejection sampling and requires the generation and analysis of at least one set of three random numbers (ν_1, ν_2, ν_3) in the range $0 \le \nu_i < 1$. The procedure for a single Compton event is shown in Figure 5.3.
8. Calculation of the polar angle of scattering using the Compton formula (5.11) (old and new energies E and E' are known, m_0c^2 = electron rest mass energy).

$$\cos\theta = 1 - \left(\frac{1}{E'} - \frac{1}{E}\right) m_0 c^2 \tag{5.11}$$

9. Sampling for the azimuthal angle of scattering ϕ (uniform distribution from 0 to 2π, so $\phi = 2\pi\nu$).
10. Calculation of the new photon direction in the laboratory frame, using the same transformation as for the initial direction in step 1.
11. Loop back to step 3.

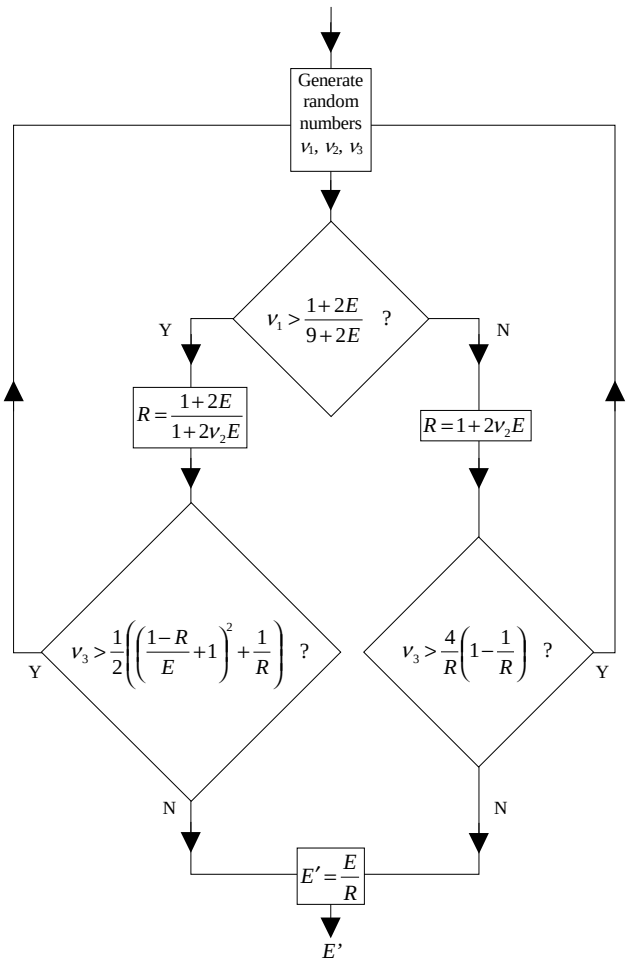

Figure 5.3. Method for random sampling of the Klein-Nishina distribution by the Kahn method. ν_i are random numbers uniformly distributed in the range $0 \leq \nu_i < 1$, E and E' are the initial and final photon energies (in units of the electron rest mass energy), and R is the ratio E/E'.

Photons are discarded if a) they exceed some limiting radial distance from the source, or b) if they fall below some limiting energy. If the photon escapes up through the surface, its position, direction and energy are recorded. After a large number of photon histories have been tracked, this data can be analysed.

5.3 Simulation of Inserted Attenuation Densitometer

The code is equally suited to the previously considered backscatter technique and the current attenuation method. Several runs of the code were performed to model the latter, the results of which are presented here.

Figure 5.4 shows the results from one such simulation for 10^6 photons from a ^{137}Cs source 0.4 m below the surface of H_2O (of density 1000 kgm^{-3}). The spectrum is integrated over a circular area of 60 mm radius at the surface. Clearly visible is the peak of

unscattered photons at 662 keV– the attenuation factor of which was verified successfully against theory. At lower energies one can see the continuum of Compton scattered photons which peaks at about 50 keV. The noise in the spectrum is the result of counting statistics. Increasing the number of photons simulated improves the situation, though doubling the number makes only a $\sqrt{2}$ improvement in the noise. Re-binning the spectral data more coarsely reduces the noise on each data point at the expense of energy resolution.

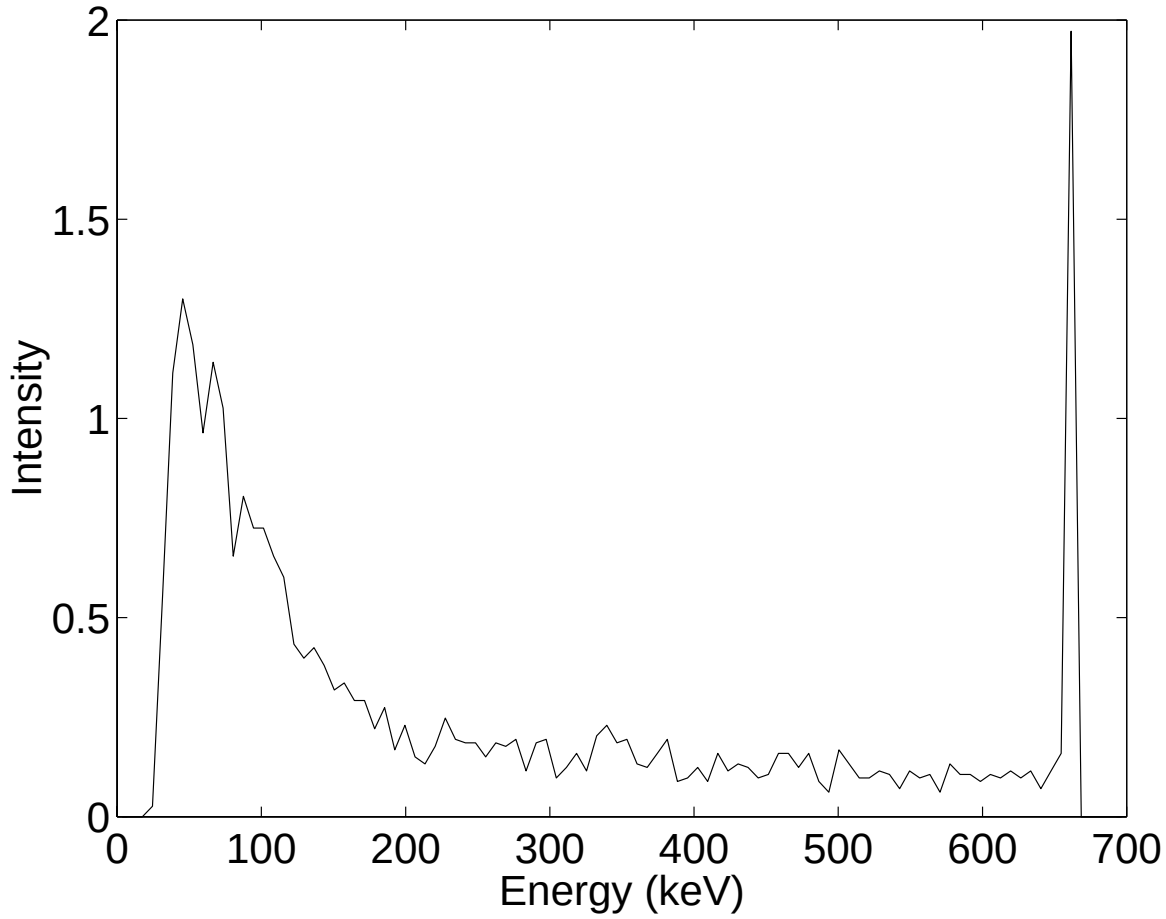

Figure 5.4. Example spectrum from a simulation of a *MUPUS* attenuation densitometer design, with a 662 keV source placed 0.4 m below the surface of a material of density 1000 kgm^{-3} (H_2O). 10^6 photons were used to obtain adequate counting statistics, taking ~10 hours to run on a Sun multiprocessor campus host. A detector was placed at the surface with an effective area of 1 cm^2 but spread over a 60 mm radius around the *z*-axis (again, to improve counting statistics). It was assumed that for a source at 0.4 m depth the radiation at the surface 60 mm from the axis was not significantly different from that on the axis.

To simulate the operation of an inserted attenuation densitometer the configuration shown in Figure 5.5 was used. A 0.4 m probe was used, the detection region placed slightly off-axis, level with the top of the probe. Five positions along the insertion path were

simulated, including the starting point and full penetration. Ten densities were used in each case, spread between 200 and 2000 kgm^{-3}. The results of this series of runs are shown in Figure 5.6, Figure 5.7, Figure 5.8, Figure 5.9 and Figure 5.10.

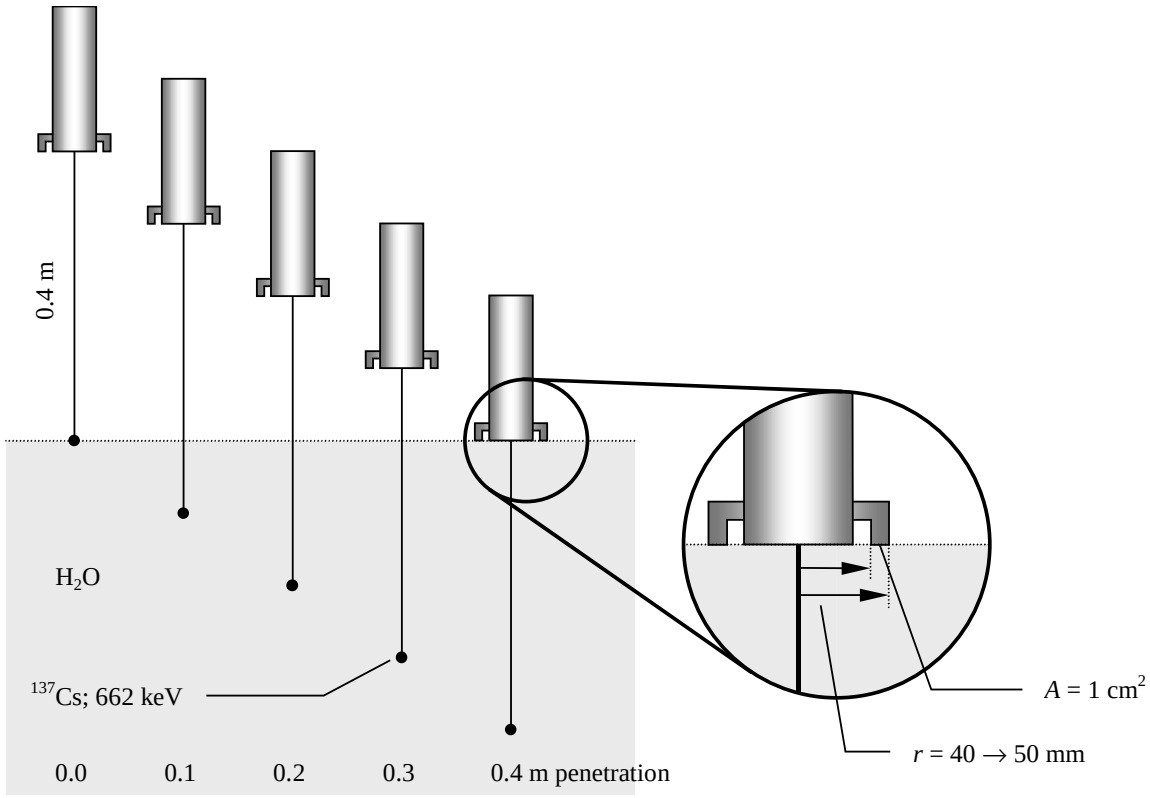

Figure 5.5. Diagram of simulated scenario. An isotropically emitting 662 keV source is pushed into the material (H_2O) on the end of a 0.4 m probe. A 1 cm^2 detector is placed at the top of the probe, positioned between 40 and 50 mm from the axis.

The results in Figure 5.6 show clearly the dominant peak of the 662 keV primary photons– as expected this is attenuated exponentially with depth, with an attenuation length which falls as density increases in the subsequent figures. At zero penetration there is a finite count to be seen at about 1/3 of the primary energy. Since there can be no attenuation taking place this must be due to backscatter (both single and multiple scatter). The minimum energy a primary photon can have after Compton scattering is 184 keV, corresponding to a 180° scattering angle. Thus any photons seen below this energy must be multiply scattered. The peak seen at zero penetration does not vary significantly with density, though the peak at 200 kgm^{-3} does appear a little smaller.

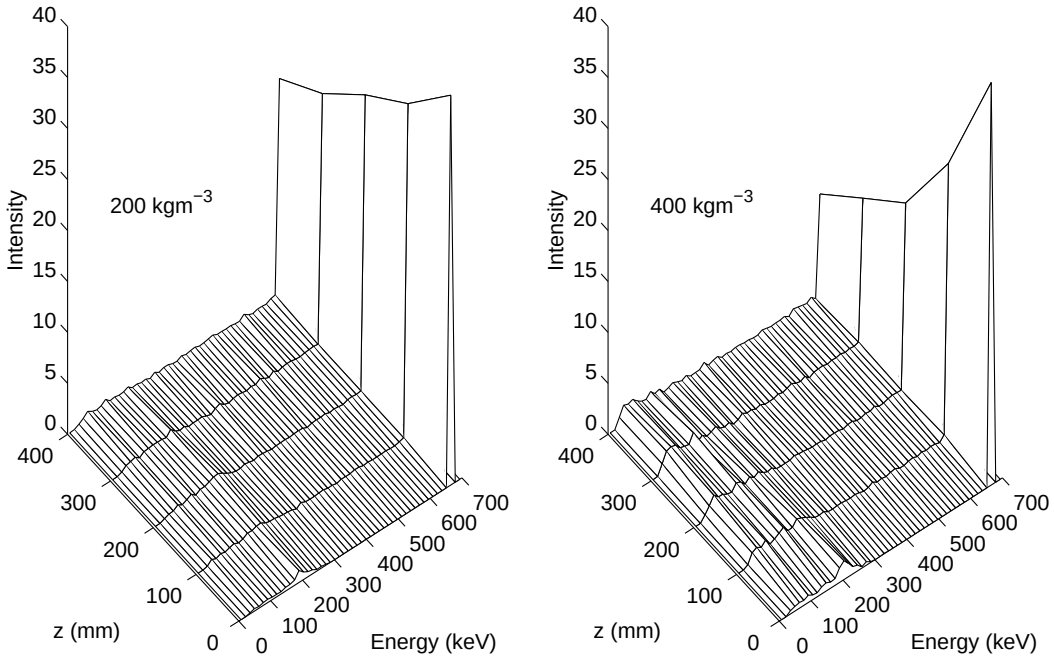

Figure 5.6. Intensity vs. energy and depth penetrated for densities of 200 and 400 kgm^{-3}.

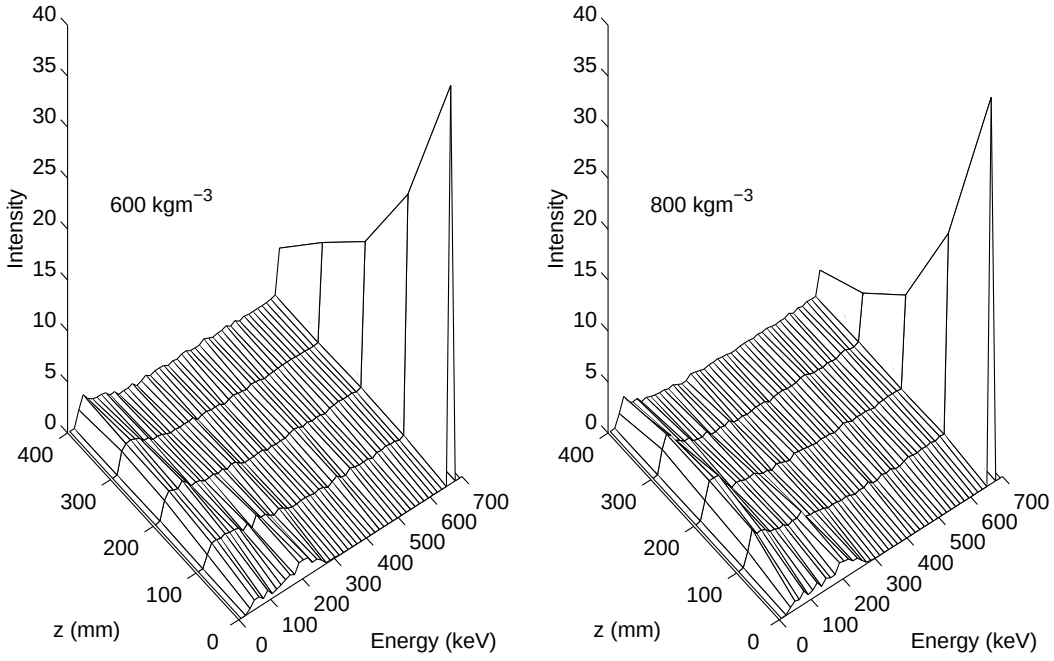

Figure 5.7. Intensity vs. energy and depth penetrated for densities of 600 and 800 kgm^{-3}.

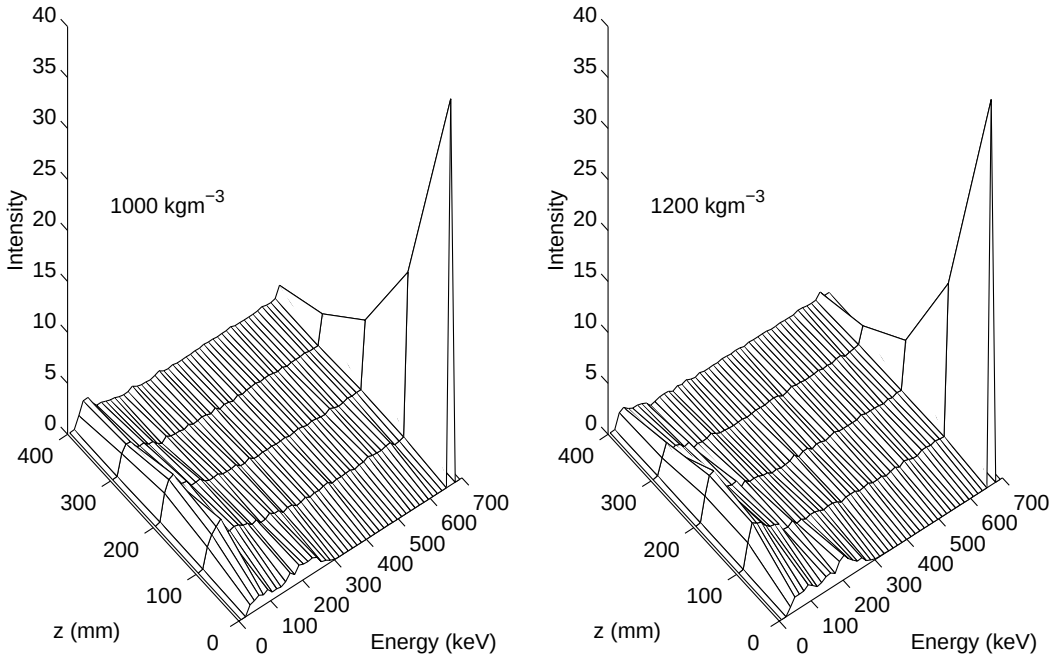

Figure 5.8. Intensity vs. energy and depth penetrated for densities of 1000 and 1200 kgm^{-3}.

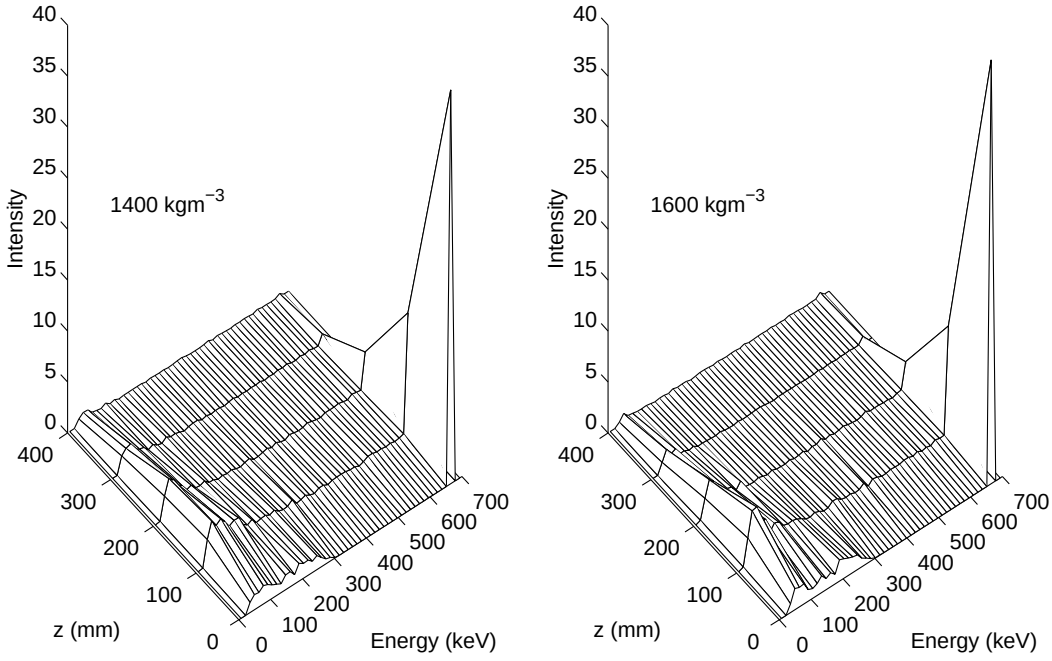

Figure 5.9. Intensity vs. energy and depth penetrated for densities of 1400 and 1600 kgm^{-3}.

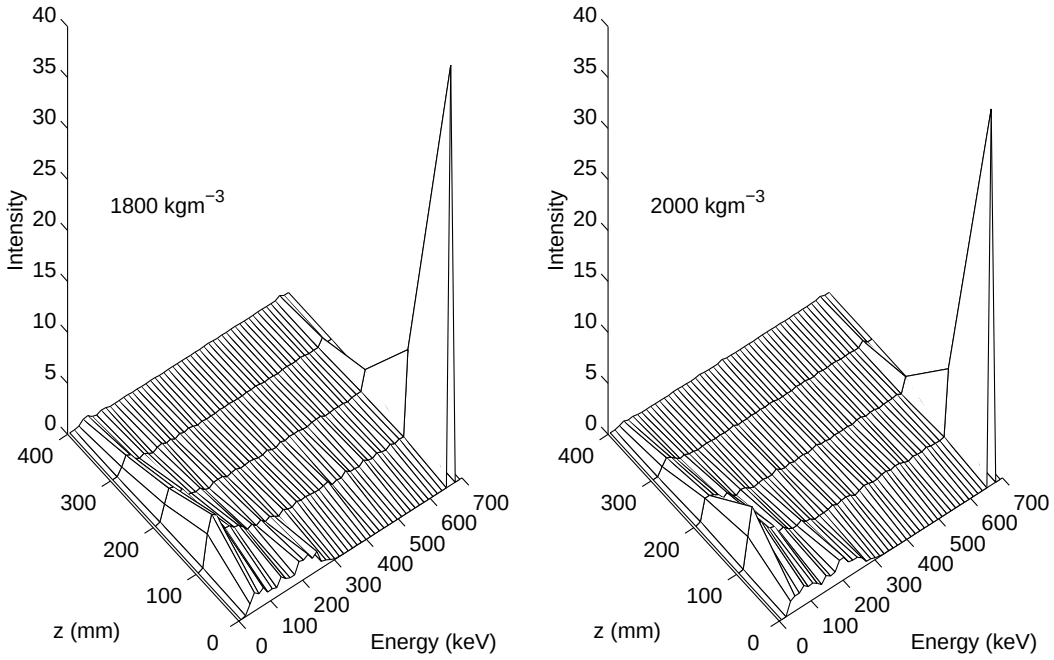

Figure 5.10. Intensity vs. energy and depth penetrated for densities of 1800 and 2000 kgm^{-3}.

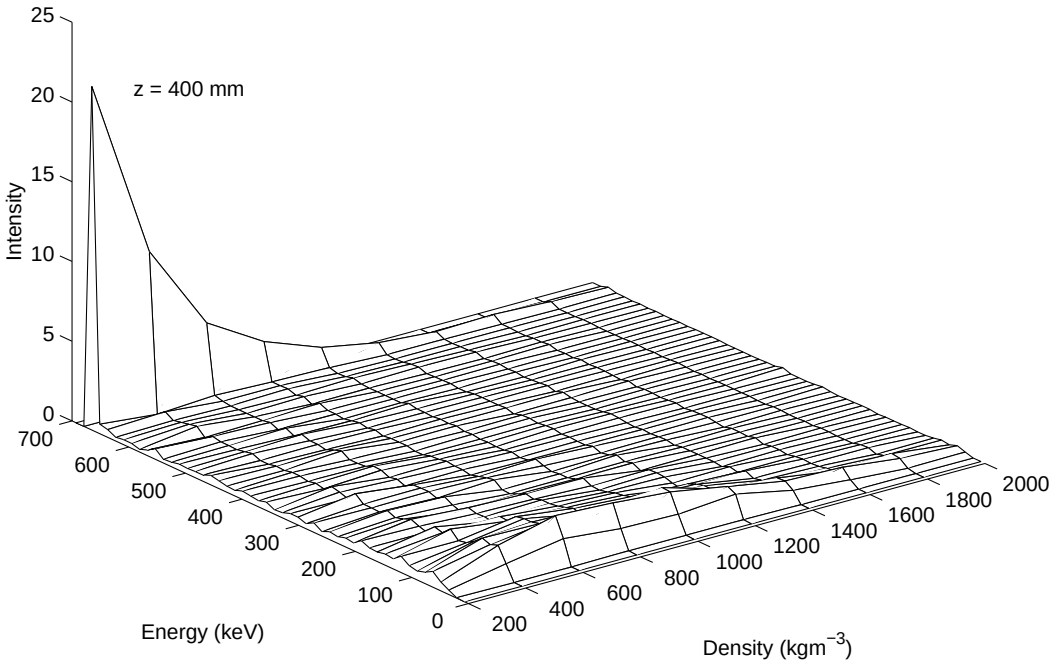

Figure 5.11. Results of a simulation where the density is varied from 200 to 2000 kgm^{-3} at the full penetration depth of the probe (400 mm).

Figure 5.11 shows a concentration of scattered photons below 100 keV, peaking at around 800 kgm^{-3}. This occurs for essentially the same reason as the peak in the backscatter densitometer calibration curve– scattering is dominant below the critical density while attenuation dominates above this density (see page 44). Figures 5.4 to 5.8 also show the radiation below 100 keV to peak at a particular depth below the surface– this depth becomes shallower for higher densities. A similar explanation can again be offered– an increase in the column density of intervening material increases the flux of scattered photons in this part of the spectrum until the shielding effect becomes dominant.

These simulations show that most of the scattered photons reaching the detector lie below about 300 keV. At zero penetration the radiation singly- or multiply-backscattered from the surface produces a peak around 200 keV that falls off as the probe is inserted. It does so more rapidly for higher densities (compare Figure 5.6 with Figure 5.10).

6 Experimental Work on Detection of Attenuated ^{137}Cs Radiation with Cadmium Telluride

This chapter describes the laboratory experiments carried out at University College London's Mullard Space Science Laboratory in collaboration with Mr. Matthew Whyndham (formerly Trow) with the support of Dr. Alan Smith. Data analysis and interpretation have also been conducted collaboratively, resulting in an interim publication on the attenuation experiments (Ball *et al.*, 1997).

6.1 Attenuation Densitometry Using a ^{137}Cs source and a Cadmium Telluride Detector

The aims of this initial series of experiments were: –

- to examine the spectrum obtained when a CdTe semiconductor detector is used to observe the radiation from a ^{137}Cs source,
- to evaluate the particular type of CdTe detector obtained on loan from the manufacturer, and
- to observe modification of the observed spectrum as the thickness of intervening material is increased to mimic insertion of the *MUPUS* densitometer probe.

An experimental apparatus was set up at MSSL using standard rack-mounted nuclear detection equipment. A surplus ^{137}Cs source was obtained at no cost from Bristol University. The source was encapsulated in a stainless steel bead approximately 3 mm in diameter and had a nominal activity of 1.04 MBq (0.028 mCi). A CdTe detector was obtained on loan from the company Eurorad. Figure 6.1 shows the arrangement of the source, detector and intervening sample. Tap water was chosen as the intervening material. In addition to being easy to handle, cheap and readily available, water has the advantage of a well-known density that is within the operation range desired for the *MUPUS* instrument. Water ice may of course be present in the surface layers of the nucleus (except for the case of a thick crust of outgassed material).

Figure 6.2 shows a block diagram of the detection and counting system. The data was logged by a PC equipped with a multi-channel analyser card, saved in binary format and transferred to a Unix machine running IDL. An IDL script was then developed to process and display the raw data. The raw data was re-binned more coarsely to improve the

counting statistics. An array of the processed data was written to a text file that could be transferred to other software packages.

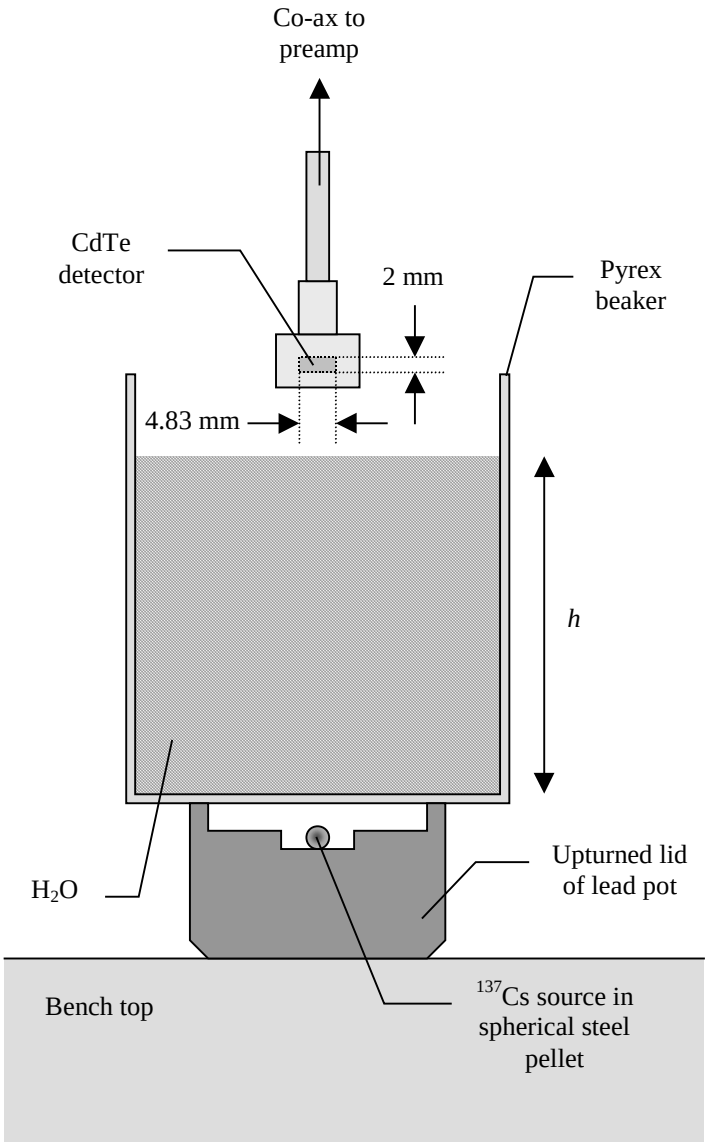

Figure 6.1. Diagram showing the arrangement of the source, detector (Eurorad CdTe S5.2A M30) and intervening material. The nominal activity of the ^{137}Cs source was 1.04 MBq (0.028 mCi). A wall of lead bricks (~40 mm thick) was placed to one side of the apparatus to act as shielding for safety reasons.

Having placed the source on the upturned lead lid of its container the detector was suspended by its co-axial cable, which in turn was attached to the pre-amplifier box held above the apparatus by a retort stand. The source-detector distance remained constant throughout the experiment. An ordinary Pyrex beaker was placed on the lead lid to hold the water. An initial spectrum was obtained at this point before any water was added. The presence of the glass beaker would obviously contribute to the attenuation and scattering of the radiation but it was necessary to include it for the 'dry' run so that all other parameters

were kept constant as the water was added. Further spectra were then obtained for four depths of water, to a limit of 87.9 mm set by the depth of the beaker.

Figure 6.3 shows the five spectra obtained, the count rate plotted logarithmically. The gain was normalised using test pulses placed beyond the upper limit of the region of interest. The number of counts in each channel was divided by the (dead-time corrected) integration time to obtain the count rate. The data shown in Figure 6.3 is binned eight times more coarsely than the raw data obtained by the multi-channel analyser. The magnitude of 1σ error bars on this data would be within the extremes of the visible statistical noise.

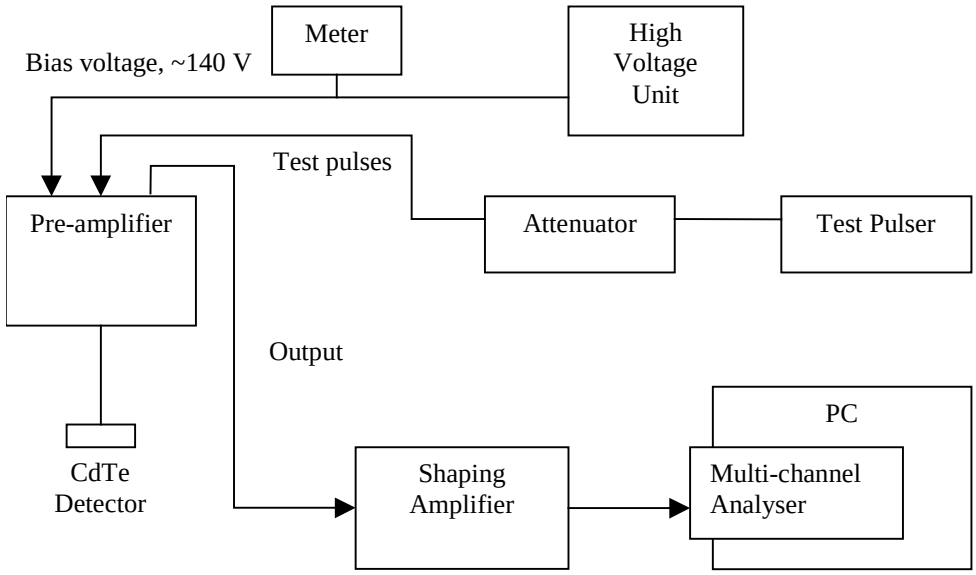

Figure 6.2. Block diagram of the detection and counting apparatus for the water attenuation experiment. The detector was a Eurorad CdTe S5.2A M30; the pre-amplifier a Canberra 2001A; the high voltage unit a J+P NM 231; the shaping amplifier an Ortec 572; and the multi-channel analyser an Ortec ACE 216A(2K) with Maestro II software.

Before discussing the effect of changing water depth one must first identify and explain the features seen in the basic spectrum. The main features are as follows: –

1. An overlying downward trend in counts with increasing channel number.
2. A peak at around channel 18.
3. A falling edge at around channel 118.
4. A peak at around channel 161.

The downward trend (1) can be attributed to the rapid decrease in detection efficiency with increasing energy, due to the fall in photon interaction cross-section. The upper peak (4) is the 662 keV photo-peak. The dominant Kα1 fluorescence energies are

23.173 keV (for Cd) and 27.472 keV (for Te) (Kaye and Laby, 1973). Thus the escape peaks associated with the 662 keV photo-peak would lie at 639 and 635 keV for Cd and Te, respectively. The energy resolution is too poor to resolve these escape peaks– at best one might see a very slight shoulder on the photo-peak. The falling edge (3) is the Compton edge associated with the 662 keV photons. This occurs because 662 keV photons scattering once in the detector before escaping must retain at least 184 keV, corresponding to a 180° scattering angle (according to the Compton formula, equation 4.3 on page 73). Thus a maximum of 662-184 = 478 keV is left in the detector. The continuum of counts at lower energies than the Compton edge is thus not only due to photons scattered before entering the detector but also photons escaping from the detector.

While the detector has a thickness (2 mm) sufficient to interact with almost 10 % of the primary photons, most of these interactions result in scattering out of the detector. A thicker detector would retain more of these as well as capture more of the primary radiation. Commercially produced CdTe crystals are available in standard sizes up to approximately 5 mm thickness.

The lower peak (2) can be attributed to K fluorescence from the lead shielding– using the upper photo-peak (4) to calibrate the spectrum the energy of the lower peak (around 74 keV) agrees well with the tabulated values of lead fluorescence (see Kaye and Laby, 1973). Measures to reduce the incidence of lead fluorescence on the detector could be taken, perhaps using some kind of detector collimation.

Looking now at the variation with water depth, one can see that the insensitivity of the lower peak to water depth confirms its origin as fluorescence of the shielding. Most of this radiation would not have passed through the beaker since the lead wall is positioned to one side of the source / beaker / detector arrangement. With the exception of this peak, an increase in water depth increases the count rate, up to a neutral point at around channel 46. Above this point the net effect of the water is to attenuate the spectrum. Looking closely at the 662 keV photo-peaks one can see that they do not all coincide exactly– in particular the 87.9 mm water peak is shifted to the right slightly. This calls into question the quality of the test pulses and the resultant gain correction factors. A shift of the photo-peak to the right suggests that the addition of extra water has actually *increased* the flux of primary photons in the right-hand edge of the peak. This seems less likely than a drift in the detection system not compensated for by the gain correction applied using the test pulse peak.

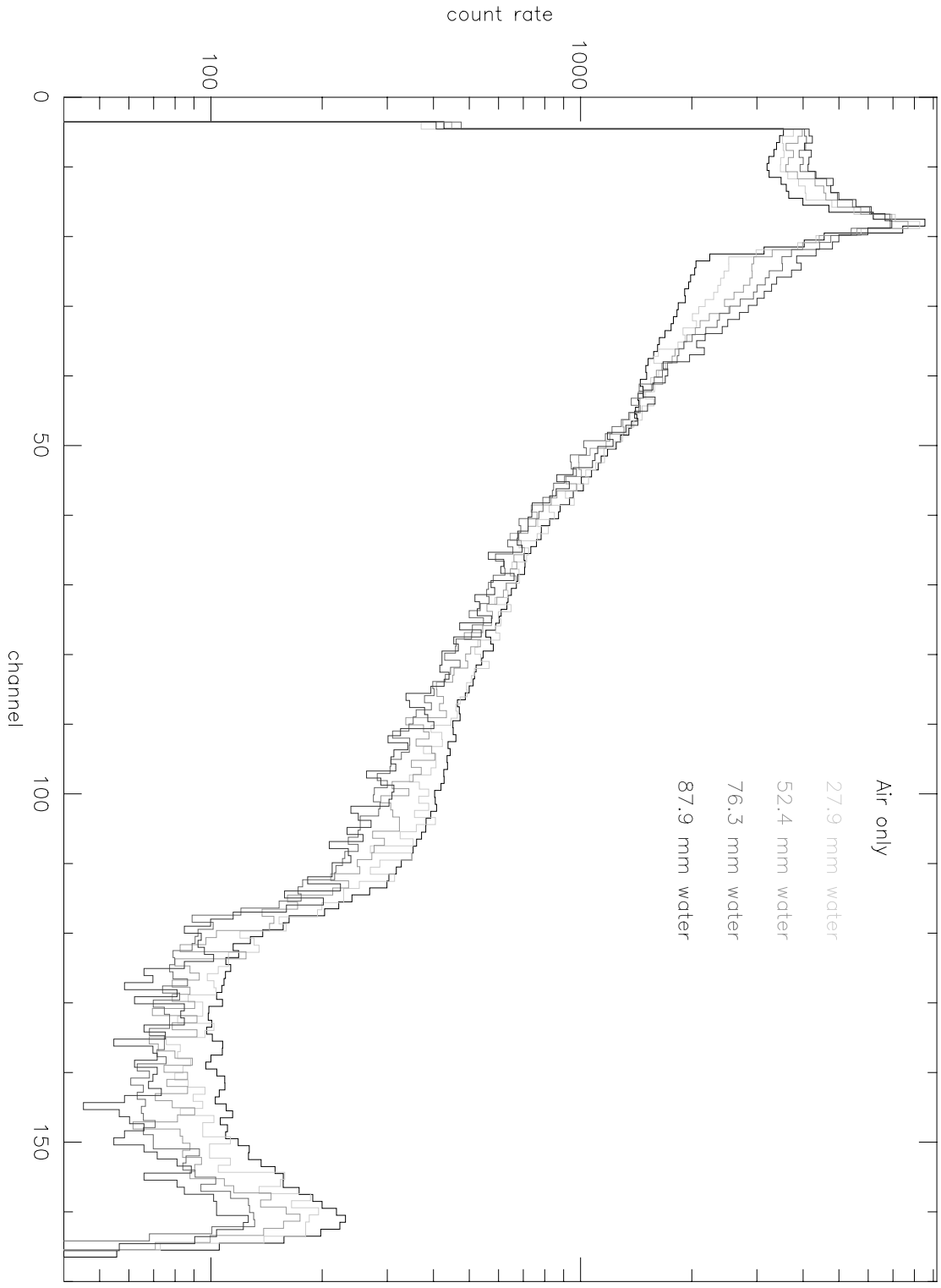

Figure 6.3. Experimental data from the water attenuation experiment. A preliminary analysis was published by Ball *et al.* (1997). Five spectra are shown, corresponding to increasing depths of water. The progressively attenuated 662 keV peak is visible at the right hand edge (at around channel 161)– the highest peak (at around channel 18) is in fact fluorescence from the experiment's lead shielding and is independent of water depth. Also visible in each spectrum is the Compton edge due to 662 keV photons scattering in the detector before escaping.

To examine the effect of the water in more detail one can process the data to obtain the fractional change in count rate vs. energy channel, relative to the 'air only' data. This is shown in Figure 6.4 for each of the four water depths. Also shown for comparison are the attenuation factors one would expect for 662 keV photons passing through these depths of water. The data has again been re-binned to a total of 50 windows but for clarity the same horizontal scale as before has been used.

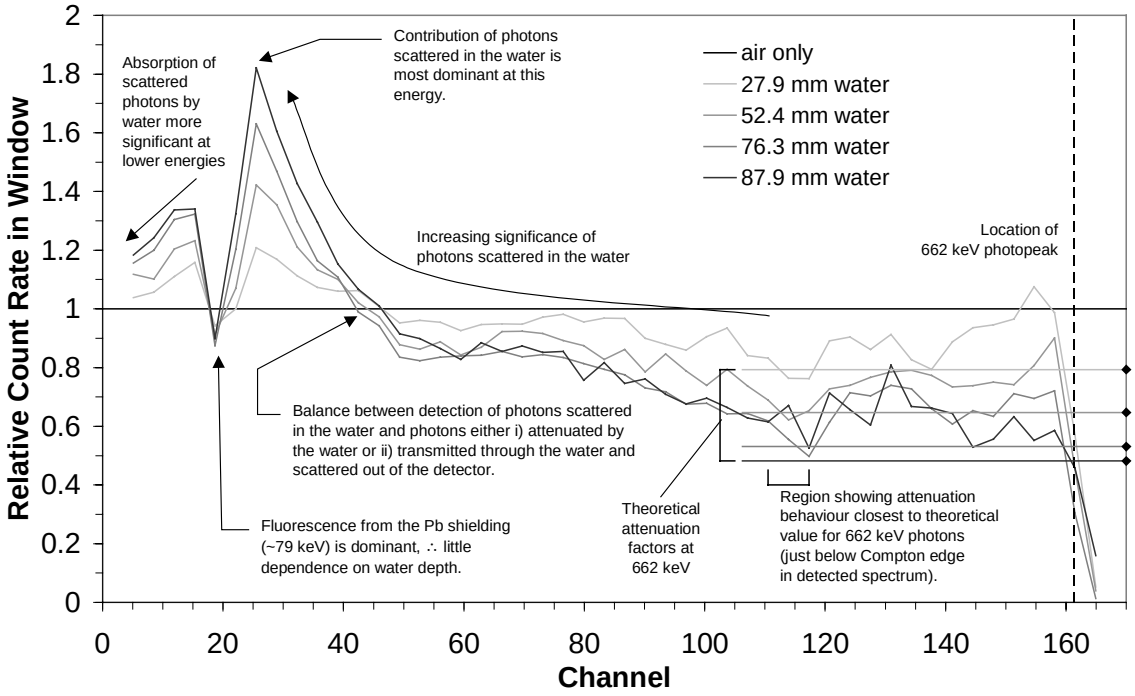

Figure 6.4. Fractional change in count rate vs. energy channel, relative to the profile for air only. As water is added attenuation is seen at the upper end of the spectrum but at lower energies the contributions of fluorescence from the shielding and photons scattered in the water become dominant.

The best agreement between the experimental data and the theoretical values is not actually achieved at the photo-peak but around channel 115 near the Compton edge. Improved resolution around the photo-peak may, however, reveal a narrow band of close agreement– the experimental plots do pass through the theoretical values close to the plotted position of the photo-peak. The close agreement near the Compton edge could be attributed to the contribution of 662 keV photons just below the Compton edge which backscatter out of the detector. These would show the correct attenuation behaviour for 662 keV but would not be present in the gap between the Compton edge and the photo-peak.

From channels $120 \rightarrow 160$ the attenuation is clearly less than that for 662 keV photons. The most likely explanation for this is the contribution of photons scattered in the water with small scattering angles. Such forward-scattered photons would retain most of their original energy (at least 480 keV for scattering angles less than 45°).

Below about channel 115 the contribution of photons scattered in the water becomes increasingly significant. At around channel 46 scattered photons become dominant, causing an increase in counts as water is added. At the very low energies beyond the lead fluorescence, however, absorption of the scattered photons by the water increases in significance, reducing the degree to which additional water adds to the count rate.

Figure 6.5 shows results from the three windows (centred on channel numbers 110.5, 113.9 and 117.3) just below the Compton edge which show the closest match to the theoretical attenuation coefficient of 662 keV photons (an attenuation length of 120 mm in water). The outlying points from the 87.9 mm data serve to reinforce the impression that this profile shows slightly higher gain than the others. The overlying trend for the count rate to fall with increasing channel number would cause a higher than expected count rate at any point for a profile shifted to the right.

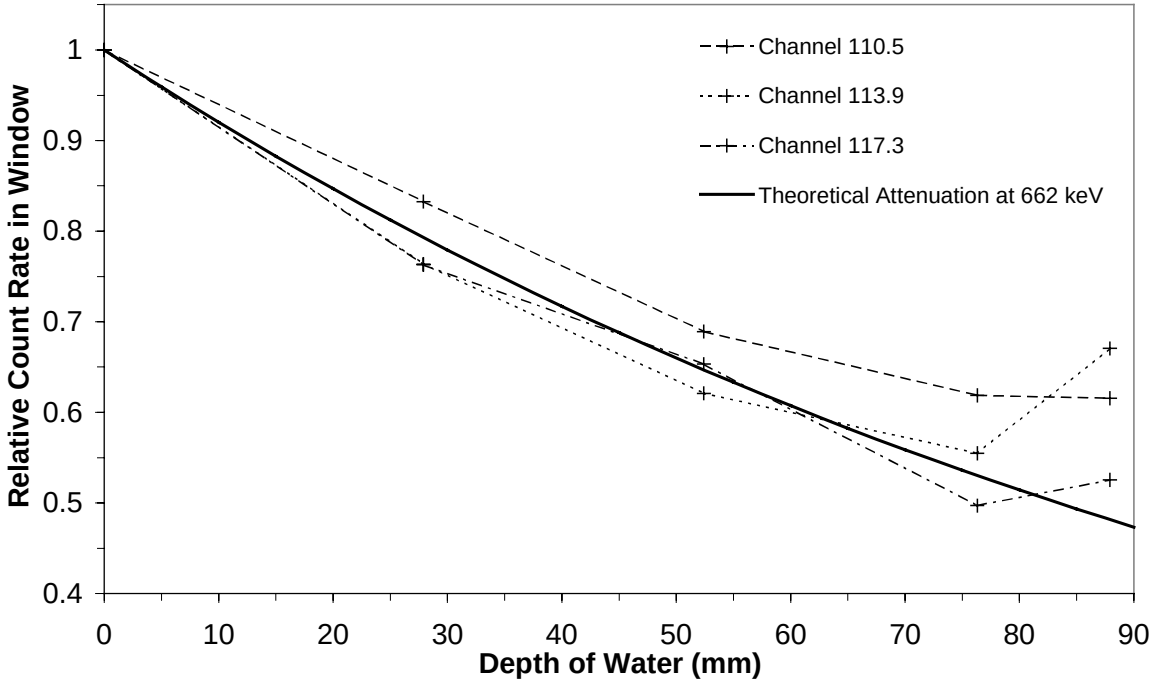

Figure 6.5. Comparison of attenuation seen in the three windows (centred on channel numbers 110.5, 113.9 and 117.3) just below the Compton edge (indicated in Figure 6.4) with the theoretical attenuation for 662 keV. The actual value for 662 keV should be 8.31×10^{-3} m^2kg^{-1}.

For comparison with experiment the Monte Carlo code discussed in chapter 5 was run for the first and last water depths (27.9 and 87.9 mm). Thus a 662 keV point source was placed at these distances below the surface of a semi-infinite volume of water, while the detection plane was placed such that the source-detector distance was 87.9 mm (i.e. first at 60 mm above the surface, then on the surface). The results are plotted in Figure 6.6.

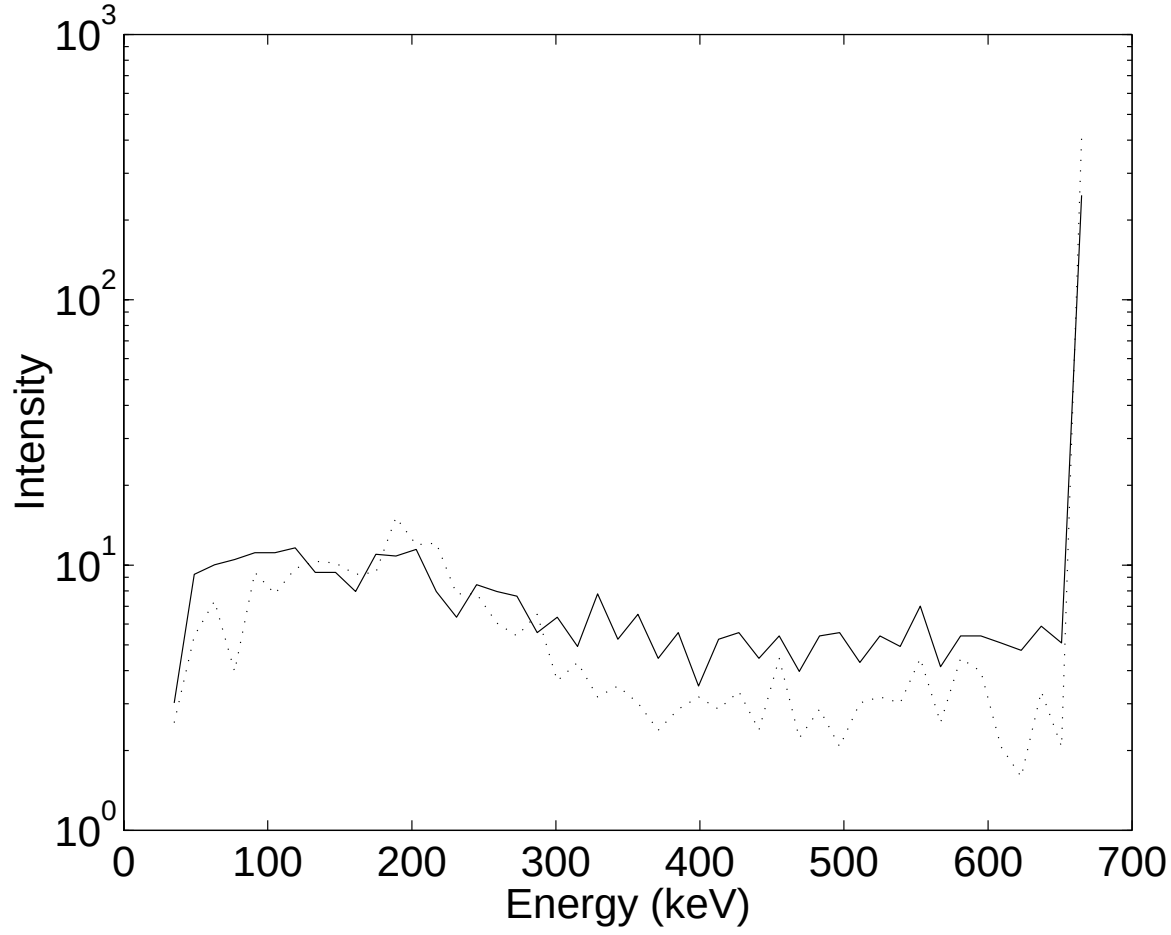

Figure 6.6. Results of a Monte Carlo simulation corresponding to two depths of water (solid line: 87.9 mm; dotted line: 27.9 mm). Increasing the water depth causes an increase in the flux of scattered photons as well as attenuation of the primary peak. In addition the peak of scattered photons moves to lower energies– the increased depth causes more photons to be multiply scattered to yet lower energies.

Clearly the Monte Carlo simulation is only a very crude approximation to the real apparatus– most importantly the detector response and fluorescence from the lead shielding are removed. Both spectra show an increase in scattered photons as energy decreases, though this peaks at a lower energy for the deeper water.

6.2 Backscatter Densitometry

To investigate the possibility of backscatter density measurement with a low energy source (^{241}Am at 59.5 keV), a test rig was designed by the author and M. Whyndham and built at UKC. The purpose of this is to hold an ^{241}Am source (encapsulated in a small stainless steel cylinder) and allow an adjustably collimated beam to be projected into the sample material.

Since the design of the *MUPUS* densitometer changed from the backscatter to the attenuation technique experiments with the collimation device were accorded a lower priority. Useful work could certainly be done with this system, however, and it remains available for future use. Attenuation experiments could be performed as well as the backscatter experiments for which it was originally designed. Figure 6.7 shows the apparatus in cross-section.

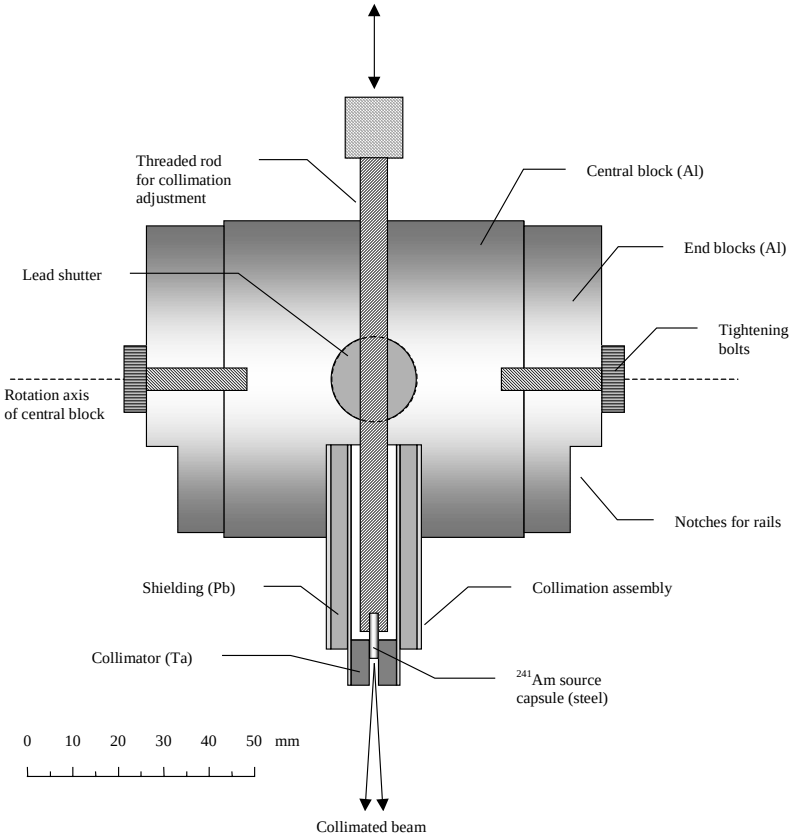

Figure 6.7. Diagram of the apparatus designed by the author and built to house the ^{241}Am source purchased. The device is designed to provide an adjustable collimated beam of 59.5 keV photons. Both backscatter and attenuation experiments could be carried out with this apparatus. For a space instrument with fixed collimation the housing would be much smaller– < 10 mm in diameter and perhaps 20 mm in length depending on the collimation required.

6.3 Conclusions

The initial series of attenuation experiments in section 6.1 verified that a CdTe detector could be used to detect 662 keV radiation from a ^{137}Cs source and observe its attenuation by an increasing thickness of intervening material. The attenuated spectra clearly show effects attributable to scattering outside the detector and detector response phenomena. These effects produce an apparent attenuation that is close to the theoretical value (for 662 keV photons) in two distinct windows. The first lies just below the Compton edge while the second lies close to the photo-peak. In this experiment the second region is rather less well identified than the first, which spans approximately three of the coarse channel bins.

Extensive further work is required to optimise the detection system, using a larger CdTe detector. The current detector is 2 mm thick and thus has an efficiency at 662 keV of just below 10 %. Off-the-shelf commercially produced detector crystals are available in different sizes up to about 5 mm thickness, though larger custom-made crystals can certainly be made up to about three times this value. The implementation of rise time compensation may be worth considering– this would improve the resolution of the photo-peak. So-called ‘co-planar grid’ detectors may also offer an improvement.

A range of different materials should be tried to determine the energy threshold below which elemental composition affects the measurement as well as density. This information would then be used to set the lower limit of the counting window in the real instrument. In view of the results presented here, calibration work would then be required to determine the real density dependence of the count rate.

CdTe and CZT detectors should be compared to enable an informed decision on their relative suitability. Both types of detector should also be characterised over the range of temperatures to be encountered on the comet surface– information on their performance below -40°C is sparse. The two competing effects are the decrease of leakage current (a source of noise) with decreasing temperature and the increase in the lifetime of charge traps in the detector material (resulting in a loss of gain and resolution).

7 Penetrometry Measurements using the *Rosetta Lander's* Anchoring Harpoon

Measurements of the deceleration or force encountered by a penetrating body may be used to derive information about the mechanical properties of the target material. Several parts of the *Rosetta Lander* are potentially available to perform penetrometry. These are listed in Table 7.1.

Table 7.1. Penetrometry measurements on the *Rosetta Lander*.

Opportunity for Penetrometry Measurements	Details
Landing gear (feet)	Information on the compressive strength of the surface material may be derived from the impact deceleration and the depth to which the feet sink into the surface on landing. Accelerometry measurements will be made by the Lander system itself rather than the payload.
Anchoring harpoon	The *MUPUS* accelerometer (ANC-M) in the anchoring harpoon will record its deceleration in the surface material. An identical backup harpoon will be available.
MUPUS thermal probe	Measurement of depth penetrated per hammer blow will provide information on the strength vs. depth of the surface material.
Sampling drill	Measurements of resistance to drilling vs. depth may provide information on the strength vs. depth of the surface material.

This chapter is concerned with the *MUPUS* ANC-M subsystem, an accelerometer mounted in the Lander's anchoring harpoon which will be fired into the surface immediately after touchdown of the Lander. While the prime purpose of the anchor is to secure the Lander on the surface to prevent rebound and allow mechanical operations, it also provides a convenient means to study the mechanical properties and possible layering of the near-surface material. Much of the chapter is derived from a collaborative publication (Kömle *et al.*, 1997). The author worked with Dr. Norbert Kömle at the Institut für Weltraumforschung in Graz for a total of nearly eight weeks during summer 1996 and spring 1997. The literature survey, experiments, data analysis, interpretation and

generation of the text and many of the diagrams were all carried out collaboratively with Dr. Kömle. The main series of experiments were carried out using an amplifier designed by H. S. Jolly and with the assistance and advice of M. Dziruni. G. Kargl provided input throughout the process, including help with the data analysis. J. Stöcker and M. Thiel provided input for the section concerned with the anchoring system itself, though this is not included in its entirety here.

The anchor will have a mass of about 0.1 kg, a diameter of 15 mm and a total length of about 154 mm. The tip will be a sharply pointed cone of length ~60 mm, protruding from which will be a number of barbs. Behind the cone a cylindrical section will hold the *MUPUS* accelerometer and temperature sensor, as well as hinged flukes to dig into the soil as the harpoon cable is rewound after firing. The anchor will be fired into the surface at $40 \rightarrow 60$ ms^{-1}. An identical backup anchor will be available immediately if the first fails to secure the Lander.

7.1 Introduction

The main task of the *Rosetta Lander* is a detailed investigation of the chemical, isotopic and mineralogical composition and physical state of the near-surface material of the target comet (46P/Wirtanen). A particular challenge of this project is the need to land on a body with almost zero gravity and to perform various operations over an extended period of time. The Long-term Automated Landers (*LALs*) of the *Phobos* missions launched in 1988 represent the only previous attempt to do this, though both *Phobos* craft were lost before the landers could be deployed (Surkov, 1997). In the case of the *Rosetta Lander* the mission is intended to last at least six months, following initial landing on the nucleus at about 3 AU heliocentric distance.

In this chapter the forces that may act on the spacecraft after it has come to rest on the surface are investigated (section 7.2) and the expected range of material properties of the surface matter (section 7.3) are reviewed. Based on this analysis, technical concepts are presented which should lead to a safe anchoring of the Lander on the cometary surface and thus allow for the planned surface operations (drilling and sample collection, deployment of instrument sensors, etc.; see the RoLand Proposal to ESA (1995) and the *Rosetta Lander* ESA Critical Design Review (1997) for more detailed descriptions). A secondary purpose of this anchoring device is its use as a scientific instrument that may yield valuable data concerning the physical properties of the cometary near-surface layers. It will be equipped with a shock accelerometer and a temperature sensor. These two sensors are part of the

MUPUS experiment, which has been selected as part of the Lander payload (*MUPUS* Proposal, 1995; Spohn *et al.*, 1996).

As described in more detail by Kömle *et al.* (1997), the anchor will be shot into the cometary soil with the aid of a cartridge-driven piston. The accelerometer is used to record the deceleration history, when the projectile (anchor) penetrates the surface. From the signal obtained during this process, conclusions concerning the strength and other properties of the penetrated material will be derived. In particular, it should be possible to detect discontinuous changes of the material's strength (at least on a qualitative level) by comparing the signal with results from laboratory experiments on analogue materials. Structural and mechanical properties measured by the accelerometer can be compared with depth profiles from the *MUPUS* thermal probe as it is hammered in, as well as other sub-surface devices such as the sampling drill. It may also be possible to correlate the penetrometry profiles with variations in thermal properties and density (Ball *et al.*, 1997) as measured by the *MUPUS* probe, and with chemical profiles obtained by the sampling drill.

The development of distinct boundaries, across which both the chemical composition and the physical / mechanical properties of the material change abruptly, is predicted by various theoretical models describing the thermal evolution of an originally homogeneous low density mixture of minerals with ices of different volatility (Espinasse *et al.*, 1991; Steiner and Kömle, 1993; Kossacki *et al.*, 1994; Seiferlin *et al.*, 1995). It has also been experimentally observed in comet simulation experiments (KOSI) performed at DLR Cologne (Grün *et al.*, 1991; Hsiung and Rössler, 1991) and related experiments at IWF Graz (Kömle *et al.*, 1996; Kossacki *et al.*, 1997).

7.1.1 Penetrometry of planetary surface materials– a brief review

Early work in the field of dynamic penetrometry (as opposed to the constant rate or static cone methods) with application to space missions was performed by NASA in the 1960s (McCarty and Carden, 1962). Penetrometry and other soil mechanics studies conducted by the *Surveyor* and *Apollo* missions produced values for cohesion, friction angle and shear strength (Scott and Robertson, 1969; Mitchell *et al.*, 1972, 1974). The Soviet Union used penetrometry to analyse the surface of the Moon in the *Luna 13* (Cherkasov *et al.*, 1968a) and *Lunokhod 1* and *2* (Leonovich *et al.*, 1974, 1975; Mitchell *et al.*, 1972) missions. A useful summary of Lunar surface penetrometry can be found in chapter 9 of the Lunar Sourcebook (Heiken *et al.*, 1991). Penetrometry was also used on

Venus by *Venera 13* and *Venera 14* (Kemurdzhian *et al.*, 1983; Surkov *et al.*, 1984). Penetrometers were carried on the *PROP-M* rovers of the *Mars 2, 3, 6* and *7* landers– they were all lost before the rovers could be operated, however (Kemurdzhian, 1990; Kemurdzhian *et al.*, 1993). Both the *PROP-F* hopper (Kemurdzhian *et al.*, 1989) and the Long-term Automated Landers (*LALs*) of the *Phobos* missions launched in 1988 carried penetrometers, though again the spacecraft were lost before the landers could operate. Soil mechanics investigations were carried out using the two *Viking* landers though no dedicated instrumentation was included in the payload (Moore *et al.*, 1977). More recently, an impact penetrometer (ACC-E) was developed for the Surface Science Package of the *Huygens* Titan probe (Lorenz *et al.*, 1994).

Two large Martian surface penetrators were carried by *Mars 96* (Surkov, 1997). The New Millennium mission *Deep Space 2* will send two small 'Microprobe' penetrators to the surface of Mars on board the *Mars Surveyor 1998* Lander spacecraft. The Japanese spacecraft *Lunar-A* will carry two penetrators to the Moon (Mizutani, 1995), though three were originally intended. In these cases, however, the primary goal is safe delivery of the payload into the surface, rather than penetrometry alone. NASA's ill-fated *CRAF* mission proposal also included a penetrator. Many missions in the future will no doubt employ a wide range of payload-delivery penetrators.

On Earth, penetrometry has been used for many years in soil science (Lunne *et al.*, 1997), civil engineering, military applications and for studies of snow and ice (Young and Keck, 1971; Swinzov, 1972; Cole and Stevens, 1987). Many models of the penetration process for a number of different regimes have been put forward, including those of Allen *et al.* (1957), Young (1969), Wang (1971), Forrestal and Luk (1992), Boguslavskii *et al.* (1996) and Anderson *et al.* (1996). In this chapter experimental accelerometry data is interpreted in terms of the strength of the penetrated material. In particular the model proposed by Anderson *et al.* (1996) is applied.

7.2 Force Balance on the Surface of a Comet Nucleus- the Rationale for Lander Anchoring

In order to demonstrate the need to anchor a comet lander one needs to consider the forces that may act on the lander after it has come to rest on the surface, as shown in Figure 7.1. Here the following have been considered:

1. F_{grav}, the gravitational attraction between nucleus and lander (i.e. weight of the lander),
2. F_{cent}, the repulsive centrifugal 'force',

3. F_{drag}, the drag force due to outflow of volatiles from active areas (the gas flow may also carry dust particles which give rise to an additional force F_{dust} due to impacts),
4. F_{rad}, the solar radiation pressure,
5. F_{seis}, due to seismic motion of the cometary surface (this may be induced thermally or by impact of dust particles on the nucleus),
6. F_{el}, electrostatic repulsion,
7. F_{reac}, the reaction from lander components accelerated during deployment or pushed into the surface during lander operations, and
8. F_{anc}, the tension achieved in the anchoring cable.

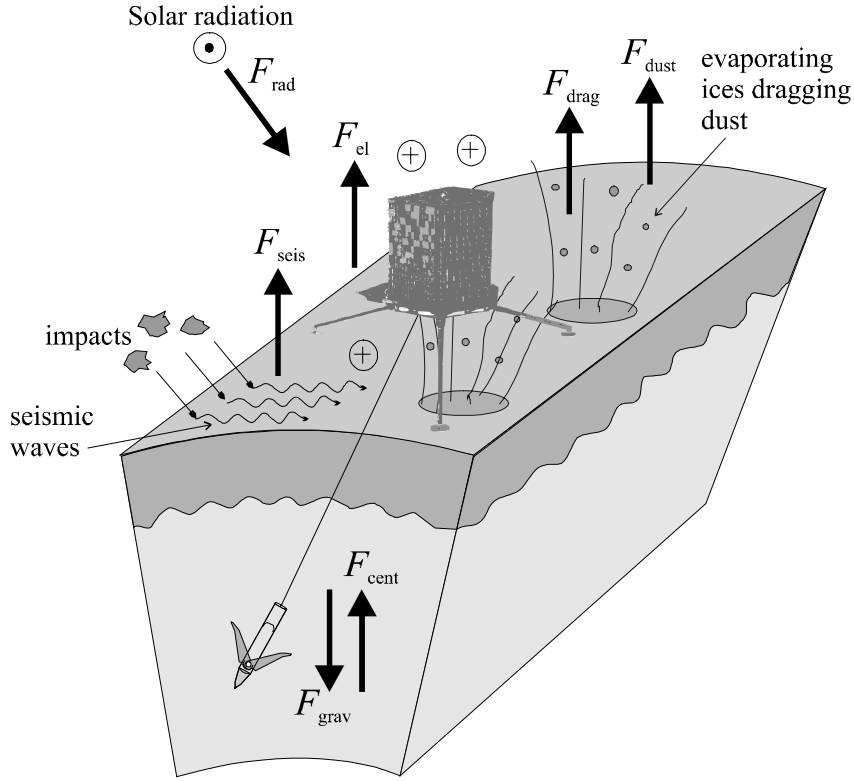

Figure 7.1. Schematic diagram of the *Rosetta Lander* on the surface of the comet nucleus, showing the main natural forces acting on the Lander (*RoLand* demonstration model photo: DLR).

A summary of these forces and their directions is given in Table 7.2. Considering the worst case (all repulsive forces acting in parallel), the Lander is only certain to remain at the surface without anchoring if

$$F_{grav} > F_{cent} + F_{drag} + F_{dust} + F_{rad} + F_{seis} + F_{el} + F_{reac} \, . \qquad (7.1)$$

Table 7.2. Forces acting on a cometary lander. See text for definition of symbols.

Force	Direction(s)	Magnitude
Weight of the lander (gravitational force)	Towards centre of mass of nucleus	$F_{\text{grav}} = M \cdot \frac{4}{3}\pi R_c \rho_c G$
Centrifugal force	Outwards from nucleus rotation axis	$F_{\text{cent}} = M \cdot \frac{4\pi^2 R_c \cos\delta}{P^2}$
Drag from evolved gas	Mostly radial away from nucleus, possibly some tangential component (wind)	$F_{\text{drag}} = 4R^2 C_D a e^{-\frac{b}{T}}$
Impact of dust particles	Complex (mostly radial) flux, partially coupled to gas flow	F_{dust} = momentum transferred per unit time; related to gas flow
Solar radiation	Anti-solar direction (day only)	$F_{\text{rad}} = \frac{\pi R^2}{c} \cdot \frac{1371[\text{Wm}^{-2}]}{(d\ [\text{AU}])^2}$
Passage of seismic waves	Many	$F_{seis} = \frac{4\pi^2 M z_0}{\tau^2}$
Electrostatic	Normal to nucleus surface (repulsive)	$F_{\text{el}} = \pi R^2 \cdot \frac{e n_e \Phi_s}{2}$
Reaction from moving parts (e.g. drill & deployable experiments)	Many (upwards for devices lowered to surface or drilling into it)	F_{reac} = mass of moving part × velocity / acceleration time
Anchor cable tension	Downwards	F_{anc}, determined by harpoon rewind motor

To consider the sizes of these forces one should take as input parameters the current dimensions of the *Rosetta Lander* design, which has a mass M of 75 kg and a radius R of 0.45 m. For the nucleus of 46P/Wirtanen the first edition of the nucleus reference model compiled by Möhlmann (1996) will be used. In particular the values given therein for nucleus radius R_c (700 ± 100 m), surface gravity g (1.89×10^{-5} (min), 7.83×10^{-5} (nom), 2.38×10^{-4} (max) ms^{-2}) and active region surface temperature T ($130 \rightarrow 215$ K) are employed. In addition rotation periods P of 5, 7 and 10 hours will be considered. The

results of the following estimates for the various forces are also displayed graphically in Figure 7.2.

The weight of the lander is given by

$$F_{\text{grav}} = Mg \ , \tag{7.2}$$

which produces values of 1.4×10^{-3} (min), 5.9×10^{-3} (nom) and 1.8×10^{-2} (max) N. The quantity g can of course be expressed in terms of the density of the comet ρ_c, the radius R_c and the gravitational constant G, to give

$$F_{\text{grav}} = M \cdot \tfrac{4}{3} \pi R_c \rho_c G \quad . \tag{7.3}$$

From rotational dynamics the expression for the centrifugal "force" is:

$$F_{\text{cent}} = M \cdot \frac{4\pi^2 R_c \cos\delta}{P^2} \quad , \tag{7.4}$$

where δ is the angular distance from the equator (i.e. latitude). Here δ is assumed to be 0 to obtain an upper limit. For periods of 5, 7, and 10 hours one obtains values for F_{cent} of 6.4×10^{-3}, 3.3×10^{-3} and 1.6×10^{-3} N respectively.

Following Grün and Jessberger (1990), the gas drag force can be expressed as

$$F_{\text{drag}} = \pi R^2 C_D \cdot \frac{\rho_g u_g^2}{2} \quad , \tag{7.5}$$

where ρ_g is the gas density and u_g is the average emission velocity of the sublimated molecules. The drag coefficient C_D is usually taken to be equal to 2 (Probstein, 1968), which corresponds to elastic collision of the molecules with a sphere and no collisions among the molecules on the size scale of the sphere (in this case the comet lander).

The drag force in an active area (e.g. free sublimation of H_2O ice) is actually controlled by the local ice temperature. Taking the outflow velocity as equal to the average thermal speed,

$$u_g = \sqrt{\frac{8kT}{\pi m}} \quad . \tag{7.6}$$

The sublimation rate (emitted molecules per unit area) is given by the Clausius-Clapeyron equation:

$$Z = \frac{a e^{-\frac{b}{T}}}{\sqrt{2\pi m k T}} \tag{7.7}$$

and the gas density according to the ideal gas law is

$$\rho_{\mathrm{g}} = \frac{ae^{-\frac{b}{T}}m}{kT} \quad , \tag{7.8}$$

where the pressure is assumed to be approximately equal to the saturation pressure $ae^{-b/T}$. The expression for the drag force may thus be re-written as

$$F_{\mathrm{drag}} = 4R^2 C_{\mathrm{D}} ae^{-\frac{b}{T}} \quad . \tag{7.9}$$

For water ice the vapour pressure constants are: $a = 3.56 \times 10^{12}$ Pa, $b = 6141.667$ K (Fanale and Salvail, 1984). The temperature range $130 \rightarrow 215$ K has been used for an active area, as given in the nucleus reference model. 170 K was chosen as an intermediate temperature. This produces 1.8×10^{-8}, 1.2×10^{-3} and 2.3 N with increasing temperature.

In addition to drag produced directly from the gas flow, dust particles accelerated by the gas will also produce a force F_{dust} on the lander, namely the rate of transfer of momentum from particle impacts. This will add to F_{drag} in some complex way, though one can probably say that it will be of the same order as the gas drag on the basis that dust to gas ratios are of order 1.

Radiation pressure, acting in the anti-solar direction, is given by

$$F_{\mathrm{rad}} = \frac{\pi R^2}{c} \cdot \frac{1371\left[\mathrm{Wm}^{-2}\right]}{\left(d\left[\mathrm{AU}\right]\right)^2} \quad , \tag{7.10}$$

with the assumption that the lander's surface, most of which is covered by solar cells, has zero reflectivity. From (7.10) one obtains for the solar radiation force on a sphere with 0.45 m radius a value of $F_{\mathrm{rad}} = 2.9 \times 10^{-6}$ N at 1 AU, 7.3×10^{-7} N at 2 AU and 3.2×10^{-7} N at 3 AU.

Both Earth-based radar and infrared observations (Campbell *et al.*, 1989; Campins *et al.*, 1990) and model calculations (Richter and Keller, 1995) give strong hints that comet nuclei are accompanied by a cloud of debris of decimetre- or even metre-sized particles. These particles may collide either with the lander itself or (hopefully the more probable case!) with the cometary surface. This may cause seismic oscillations at a range of frequencies and amplitudes depending on the specific conditions. To see how seismic forces might act on the lander due to such impacts, or indeed any internally induced oscillations due to thermal processes one can use the following very basic example. Consider the passage of a wave with maximum displacement z_0 (normal to the surface) and

period τ. The peak acceleration associated with such a wave is then $4\pi^2 z_0/\tau^2$. With z_0 = 1 nm and τ = 1 s (one may expect such a period for the lowest vibrational mode of the nucleus), one obtains an acceleration of 3.9×10^{-8} ms^{-2}, and thus a force of 3.0×10^{-6} N on a 75 kg lander. A displacement of 1 μm would produce a force of 3.0×10^{-3} N. Higher frequency modes would produce larger forces for the same displacement.

To quantify the electrostatic repulsive force between comet and lander, one can use the expression from Mendis *et al.* (1981):

$$F_{\mathrm{el}} = \pi R^2 \cdot \frac{e n_{\mathrm{e}} \Phi_{\mathrm{s}}}{2} \quad . \tag{7.11}$$

The electrostatic repulsion is determined by the magnitude of the electrical potential Φ_S on the comet surface and the local electron density n_e ($e = 1.602 \times 10^{-19}$ C, the elementary charge). According to Mendis *et al.* (1981) a positive potential of the order $5 \rightarrow 10$ V may exist near the sub-solar point of the nucleus surface, while near the terminator and on the night side much higher negative potentials (up to several thousand volts!) could be present. The reason for this expected charging of the nucleus is the interaction of solar wind particles with the solid nucleus surface on the one hand and the emission of photoelectrons due to the solar UV flux on the other. Thus it might only play a role as long as no substantial coma and magnetic cavity have formed at the comet.

With the assumption of 5 V near the sub-solar point and -2000 V on the dark hemisphere one certainly covers the range of possibilities. In order to calculate the electrostatic force on the lander at solar distance *d*, the electron number density given by Mendis *et al.* (1981),

$$n_{\mathrm{e}} = \frac{3.4 \times 10^7 \left[\mathrm{m}^{-3}\right]}{\left(d\left[\mathrm{AU}\right]\right)^2} \quad , \tag{7.12}$$

is used. Taking values for the magnitude of the electric potential as 5, 100 and 2000 V one obtains forces of 8.7×10^{-12}, 1.7×10^{-10} and 3.5×10^{-9} N respectively.

Reaction forces from lander parts accelerated during deployment or pushed into the surface during lander operations can only be estimated without detailed knowledge of the mechanisms concerned. As a numerical example, however, consider a 0.1 kg package accelerated to a velocity of 10^{-3} ms^{-1} within 1 s. This case might correspond to a sensor being lowered slowly to the nucleus surface from the lander body by an electrical motor. The corresponding force is 10^{-4} N. Velocities of 10^{-2} and 10^{-4} ms^{-1} are also used as alternative examples.

Summarising, one arrives at the following conclusions:

1. Electrostatic forces can be safely neglected. Even under the most extreme conditions (night side potentials) and a very low density comet they remain orders of magnitude below the gravitational force.
2. Solar radiation pressure can also be neglected, though by a smaller margin.
3. For a fast-rotating low density nucleus, centrifugal forces at the equator can exceed the gravitational force.
4. The strongest repulsive force is the gas drag in an active region. At 3 AU the drag force in a sublimating water ice region may well exceed the gravitational attraction considerably. As the comet approaches perihelion the drag force becomes two orders of magnitude larger than gravitational attraction, thus being the dominant force.
5. Reactive forces due to lander activities would become significant for accelerations only slightly higher than those considered here– the minimum F_{grav} is only 40 % higher than the maximum F_{reac}.
6. Seismic oscillations are worthy of further investigation. If the assumptions made here are realistic, seismic forces could be the third most significant natural force opposing weight on a comet nucleus.

Based on these conclusions one can now examine the balance between weight and gas drag as the main issue with regard to the lander remaining on the nucleus surface unaided by anchoring.

With the *Rosetta Lander's* polygonal shape the gas drag will be rather larger than for the assumed sphere of 0.45 m radius. Apart from securing the Lander as a whole, it must be kept in mind that sensors or experiment units deposited loosely on the surface (i.e. only connected to the main body by a cable) could be levitated by gas drag, if the size to weight ratio exceeds a critical value. From the equations for gravitational attraction (7.3) and gas drag (7.9) one obtains an expression for the critical radius R_{max} of a spherical body of mass M:

$$R_{\mathrm{max}} = \sqrt{\frac{\pi R_{\mathrm{c}} \rho_{\mathrm{c}} GM}{3C_{\mathrm{D}} a e^{-\frac{b}{T}}}} \quad . \tag{7.13}$$

Spherical particles with a radius greater than R_{max} for their particular mass are ejected from the surface by gas drag.

Figure 7.3 shows R_{max} versus mass for spheres ($C_D = 2$) above an active area, for three different temperatures of a freely sublimating H_2O surface. Minimum, nominal and maximum values of surface gravity were again taken from the nucleus reference model (Möhlmann, 1996). The radius and mass of the Lander are also shown, as well as contours bounding an estimated density range for surface experiments. The lower bound might correspond to an enclosed package such as the Lander's main body, while the upper bound might represent some kind of solid-state sensor or mechanism deposited on the surface.

The results obtained from the model calculations clearly indicate that some additional fixation of the spacecraft to the cometary surface is an absolute necessity for the success of the mission, in particular for a long term lander, which is intended to perform measurements from the time of landing until the comet approaches perihelion.

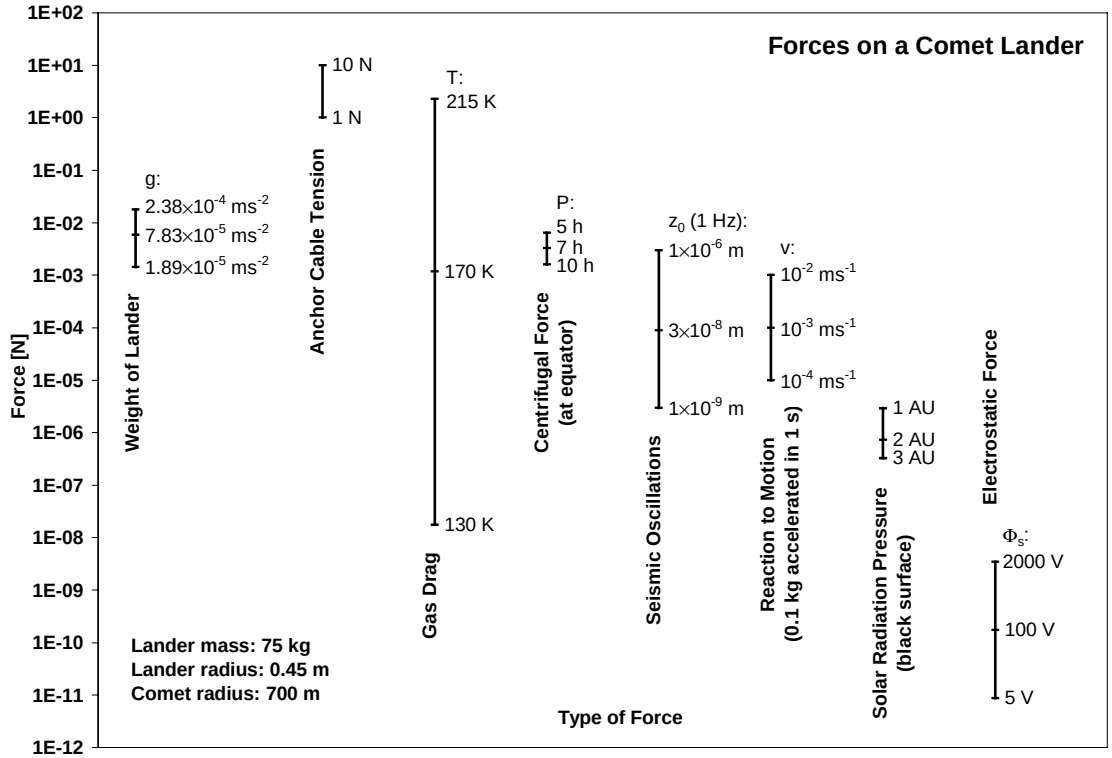

Figure 7.2. Comparison of the various forces acting on the Lander, based on the calculations in the text.

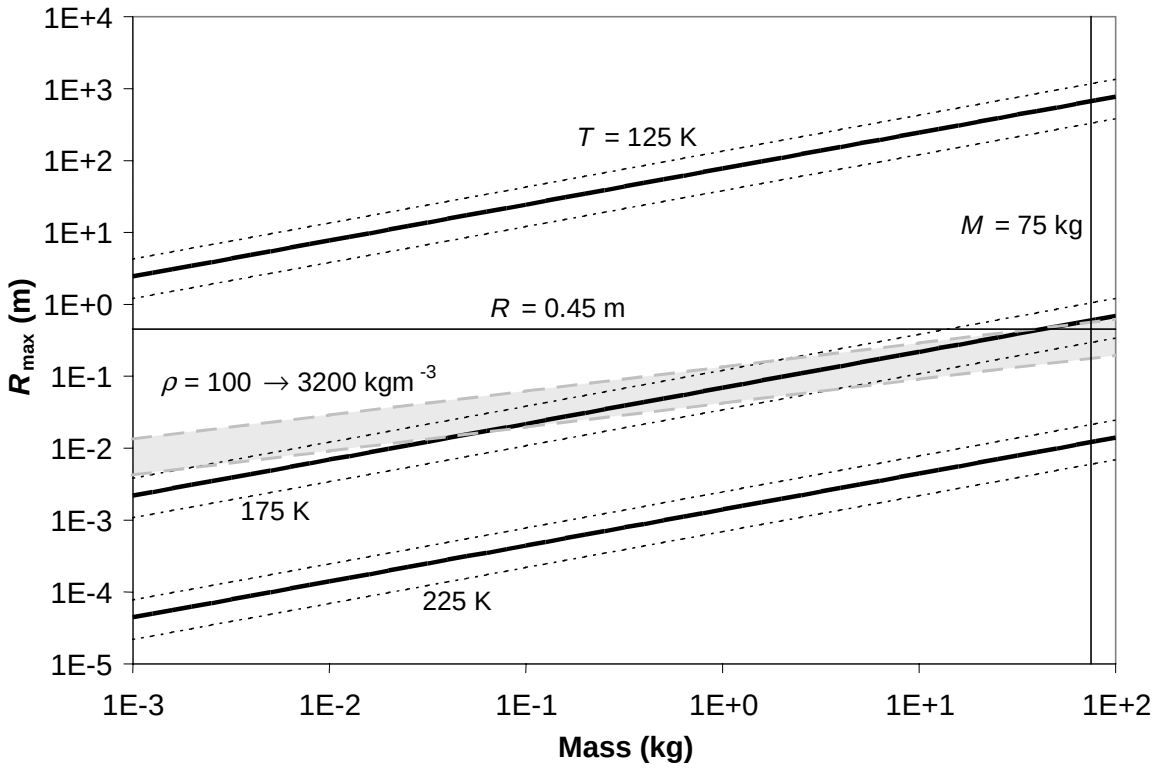

Figure 7.3. Critical radius for a sphere (i.e. the radius above which it would be ejected by gas drag) as a function of its mass, shown for three temperatures of exposed water ice surface. The continuous lines are for a nominal surface gravity of 7.83×10^{-5} ms^{-2}, with dotted lines above and below for maximum (2.38×10^{-4} ms^{-2}) and minimum (1.89×10^{-5} ms^{-2}) values. The radius and mass of the Lander are shown for comparison. Also shown in grey are contours of constant density for 100 kgm^{-3} (upper line) and 3200 kgm^{-3} (lower line), corresponding to an estimated density range for objects placed on the surface (e.g. main body of the Lander or a deployed sensor).

7.3 Probable Mechanical Properties of the Cometary Surface

One of the critical parameters determining both the penetration depth and the holding capacity of an anchor is the shear strength of the cometary surface material. The currently available information is derived from four sources and has recently been summarised by Kührt *et al.* (1997) and by Möhlmann (1995):

1. Observations of splitting cometary nuclei give a lower limit for the tensile strength in the range 10 → 100 Pa. Klinger *et al.* (1989) discuss constraints on the tensile strength of Sun-grazing comets.

2. Compact ices (with or without embedded minerals) give values of the order $10^6 \rightarrow 10^7$ Pa. This should be considered an absolute upper limit for compressive strength.
3. The (tentatively) most realistic values for the strength of the cometary surface come from laboratory simulations (KOSI experiments, DLR Cologne, 1987-1993). Mixtures of porous ice / mineral powders heated under vacuum conditions undergo a sintering process, which leads to the formation of cohesive, but still porous ice crusts with a resistance to penetration of $10^4 \rightarrow 5 \times 10^6$ Pa (Kochan *et al.*, 1989; Thomas, 1992). As an example, a measured strength profile of the experiment KOSI-3 is reproduced in Kömle *et al.* (1997). On comets, additional hardening of the near-surface material might occur due to the presence of organic substances (Kömle *et al.*, 1996) and the influence of ionising radiation (Strazzula and Johnson, 1991).
4. A value in the range from 10^5 up to several times 10^6 Pa appears also consistent with the estimated internal strength of cometary fireballs, as pointed out by Kührt *et al.* (1997).

The Wirtanen Nucleus Reference Model (Möhlmann, 1996) takes a value of 500 ± 450 Pa for the tensile stress required to disrupt the nucleus.

7.4 Penetration Model Including Friction and Dynamic Resistance

There are several models of penetration available in the published literature. Many derive from the same basic form (e.g., Allen *et al.*, 1957):

$$-\frac{du}{dt} = \alpha u^2 + \beta u + \gamma \quad , \tag{7.14}$$

where u is the velocity, t is time and α, β and γ are parameters which may be a function of distance s. An equivalent expression to the above can be obtained using $du/dt = u\, du/ds$:

$$-\frac{du}{ds} = \alpha(s)u + \beta(s) + \frac{\gamma(s)}{u} \quad . \tag{7.15}$$

The parameter γ is the static force resisting penetration, a combination of friction between the material and the penetrator and the strength of the material. β is associated with viscosity and wave propagation in the material and, according to Boguslavskii *et al.* (1996), is negligible for impact speeds below about 100 ms^{-1}. Other workers disagree on

this point– see the survey of penetration models by Wang (1971). αu^2 is the dynamic resistance, analogous to a hydrodynamic drag force.

Here we shall make use of the model by Anderson *et al.* (1996), which is one of the easiest to apply. Anderson *et al.* assume $\beta = 0$, giving a deceleration equation as follows:

$$-\frac{du}{dt} = \frac{1}{M}\iint_{S_w} (C_D P_d + \sigma_d)(\cos\theta' + \mu_f \sin\theta')dS \quad , \tag{7.16}$$

where M is the mass of the penetrator. P_d is the dynamic pressure on a surface inclined at an angle θ' to the direction of motion:

$$P_d = \frac{1}{2}\rho u^2 \cos^2\theta' \quad . \tag{7.17}$$

For a conical tip of half cone angle θ, $\theta' = \pi/2 - \theta$ (see Figure 7.4). ρ is the bulk density of the target material and C_D is analogous to a hydrodynamic drag coefficient. μ_f is the coefficient of friction and σ_d is the 'deviatoric stress' of the target material as it fails, and is thus a measure of its strength– presumably some complex combination of compressive and shear strength which may also depend on the strain rate.

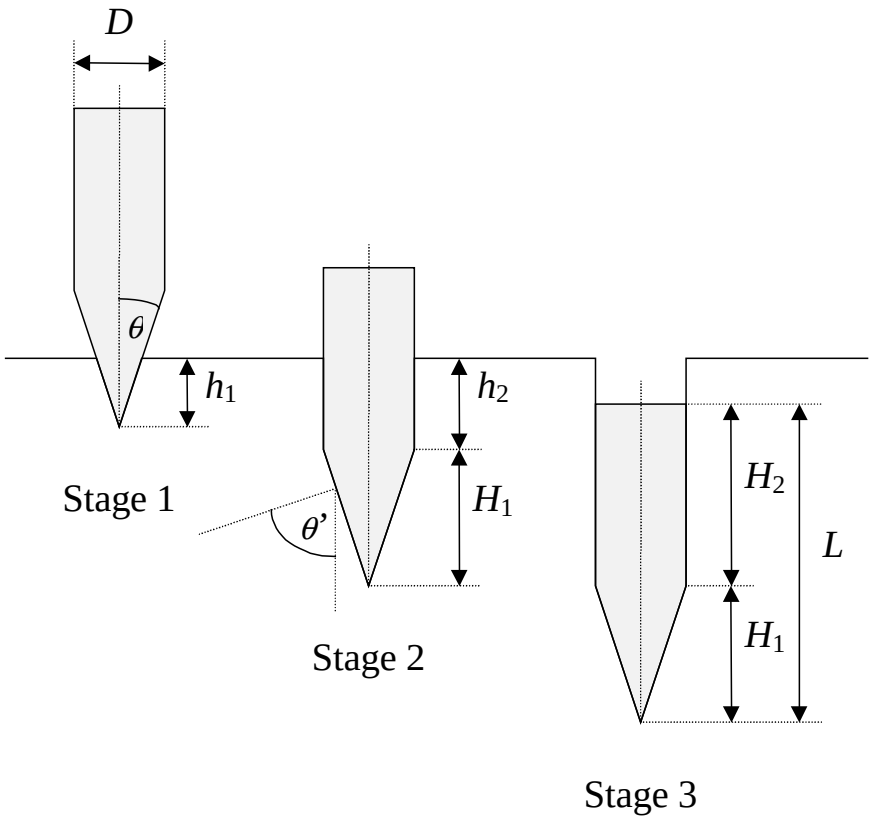

Figure 7.4. Schematic diagram showing the three stages of penetration and the associated variables for each case. Note that $\theta' = \pi/2 - \theta$.

The integral in equation 7.16 is made over the 'wetted' surface of the penetrator in contact with the target material. It can be evaluated numerically at a particular time *t*; one can then apply a finite difference scheme to find the evolution of the velocity *u* and path *s* of the penetrator tip. During the penetration of the anchor into the soil three stages have to be considered, as illustrated in Figure 7.4. Evaluation of the surface integral in terms of spatial co-ordinate *h* along the anchor symmetry axis ($h = 0$ corresponds to the anchor tip) gives for: –

stage 1 (anchor tip not yet fully penetrated):

$$-\frac{du}{dt} = \frac{2\pi}{M}\int_0^{h_1}\left(C_D\,\frac{1}{2}\rho\sin^2\theta\,u^2 + \sigma_d\right)\left(\sin\theta + \mu_f\cos\theta\right)\frac{\sin\theta}{\cos^2\theta}\;h\,dh \quad , \tag{7.18}$$

stage 2 (anchor tip fully penetrated, but after-body not):

$$-\frac{du}{dt} = \frac{2\pi}{M}\left[\int_0^{H_1}\left(C_D\,\frac{1}{2}\rho\sin^2\theta u^2 + \sigma_d\right)\left(\sin\theta + \mu_f\cos\theta\right)\frac{\sin\theta}{\cos^2\theta}\,h\,dh + \int_{H_1}^{H_1+h_2}\sigma_d\mu_f\,\frac{D}{2}\,dh\right] \tag{7.19}$$

and stage 3 (anchor tip and after-body fully penetrated):

$$-\frac{du}{dt} = \frac{2\pi}{M}\left[\int_0^{H_1}\left(C_D\,\frac{1}{2}\rho\sin^2\theta\,u^2 + \sigma_d\right)\left(\sin\theta + \mu_f\cos\theta\right)\frac{\sin\theta}{\cos^2\theta}\,h\,dh + \int_{H_1}^{L}\sigma_d\mu_f\,\frac{D}{2}\,dh\right] \quad . \tag{7.20}$$

For a stratified sample, these integrals must be computed numerically prior to each timestep. However, for a homogeneous target, they can be evaluated analytically for each penetration depth *s*, because in this case μ_f and σ_d are independent of the current penetrator depth. One obtains then a simplified form of Allen *et al.*'s penetration equation with $\beta = 0$ and α, γ depending on the current depth *s*.

With the initial conditions $s = 0$ and $u = u_0$ at $t = 0$ the following finite difference scheme is applied:

$$s_{i+1} = s_i + u_i\delta t \quad . \tag{7.21}$$

In order to calculate u_{i+1}, the parameters α_{i+1} and γ_{i+1} are required. These are evaluated for the current stage as follows: –

For stage 1 ($s_{i+1} < H_1$):

$$\alpha_{i+1} = c_1\,\frac{s_{i+1}^2}{2} \tag{7.22}$$

$$\gamma_{i+1} = c_2 \frac{s_{i+1}^2}{2} \tag{7.23}$$

For stage 2 ($H_1 < s_{i+1} < L$):

$$\alpha_{i+1} = c_1 \frac{H_1^2}{2} \tag{7.24}$$

$$\gamma_{i+1} = c_2 \frac{H_1^2}{2} + c_3 (s_{i+1} - H_1) \tag{7.25}$$

For stage 3 ($s_{i+1} > L$):

$$\alpha_{i+1} = c_1 \frac{H_1^2}{2} \tag{7.26}$$

$$\gamma_{i+1} = c_2 \frac{H_1^2}{2} + c_3 (L - H_1) \tag{7.27}$$

Now the new velocity u_{i+1} can be evaluated:

$$u_{i+1} = u_i - (u_i^2 \alpha_{i+1} + \gamma_{i+1}) \delta t \quad . \tag{7.28}$$

The calculation is terminated when the condition $u_{i+1} = 0$ is approached, i.e. when the anchor tip comes to rest at a depth s_{max}. The constants c_1, c_2 and c_3 are

$$c_1 = \frac{2\pi}{M} C_D \frac{1}{2} \rho \sin^2\theta \, (\sin\theta + \mu_f \cos\theta) \frac{\sin\theta}{\cos^2\theta} \quad , \tag{7.29}$$

$$c_2 = \frac{2\pi}{M} \sigma_d \, (\sin\theta + \mu_f \cos\theta) \frac{\sin\theta}{\cos^2\theta} \quad , \tag{7.30}$$

$$c_3 = \frac{2\pi}{M} \sigma_d \mu_f \frac{D}{2} \quad . \tag{7.31}$$

Allen *et al.* also give a general analytical solution for a differential equation of the form (7.14), which can be used when α, β, γ are constants. This condition applies to that part of the penetration process into a homogeneous target, where the 'wetted surface' does not change any more with increasing depth, i.e. for stage 3 (and for stage 2 if friction is neglected). Adapting it to the case $\beta = 0$ and applying as initial conditions the impact velocity $u = u_0$ at the target surface $s = 0$, one arrives at the following expressions for the velocity $u(t)$, path $s(t)$, and deceleration $a(t)$:

$$u(t) = \sqrt{\frac{\gamma}{\alpha}} \tan\left[\tan^{-1}\left(u_0 \sqrt{\frac{\alpha}{\gamma}} \right) + \frac{1}{u_0} \sqrt{\frac{\gamma}{\alpha}} - t\sqrt{\gamma\alpha} \right] \quad , \tag{7.32}$$

$$s(t) = \frac{1}{2\alpha}\left[\ln\left(\alpha u_0^2 + \gamma\right) - \ln\left(\alpha u^2 + \gamma\right)\right] \quad , \tag{7.33}$$

$$a(t) = \alpha u^2 + \gamma \quad . \tag{7.34}$$

These analytical solutions could be used to check the accuracy of the numerical code.

In addition to models based on the acceleration equation (7.14), the model of Forrestal and Luk (1992) is worthy of investigation in the context of *MUPUS* anchor penetrometry. It considers axi-symmetric elastic deformation, Mohr-Coulomb failure and plastic deformation of independent discs of target material as the penetrator moves through them, opening a circular void in the material. Since the model is already based on stacked layers it could be applied rather naturally to layered targets.

7.5 Harpoon Test Shots

This section describes the harpoon apparatus set up at IWF Graz and the results of penetration tests using various targets. The results for sand, sharp gravel and a coarse, low-density granular material are compared with model calculations based on equations 7.21 $\rightarrow$ 7.28.

7.5.1 Experimental set-up

As a first step towards the realisation of the anchoring harpoon device a test rig was installed at IWF Graz (Figure 7.5). It consists of a commercial pneumatic harpoon, which allows the acceleration of an approximately 0.7 m long metal arrow to an initial speed of about 21 ms^{-1}. Instead of the original arrow tip a model anchor containing the accelerometer sensor was attached at the front end. The half cone angle of the model anchor was 15°, its diameter 20 mm and its length 110 mm. The accelerometer cable is stored to an appropriate length (to allow for the motion of the arrow in response to the shot) in loose coils close to the harpoon and finally connected to the data acquisition system. Shots were performed vertically downwards into a sample container of about 1 m depth.

Two different types of shock accelerometers were tested. Initially a piezoelectric sensor with high impedance output was used. This sensor needs a charge amplifier in order to obtain a detectable signal (for a more detailed description, see the report by Dziruni and Kömle, 1995). Spurious signal components caused by the fast motion of the coaxial cable (in particular unpredictable zero shifts of the voltage output) make the quantitative

interpretation of these accelerometer signals quite difficult. In order to overcome these difficulties, subsequently a sensor with a built-in electrometer amplifier was used, which gives a low impedance signal already at the sensor output side, with no need for further amplification. Conditioning of the accelerometer signal was performed by an electronic circuit built at UKC. This unit represents also the first breadboard model for a part of the *MUPUS* experiment. As the results presented in the following subsection show, use of a sensor with internal amplification circumvents most of the problems encountered in connection with the fast moving cable.

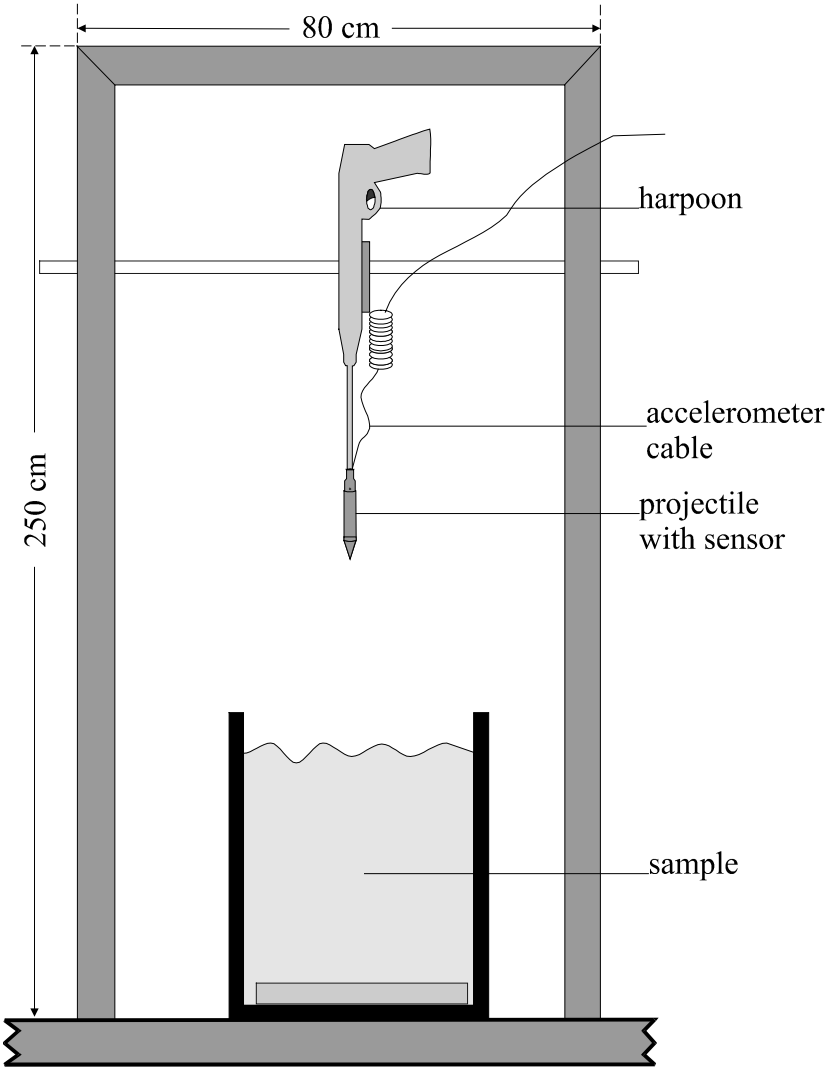

Figure 7.5. Experimental apparatus for test shots. A model anchor containing the accelerometer sensor was mounted in the tip of a (commercial) pneumatic harpoon and shot into various samples. A reasonable length of cable was coiled close to the harpoon nozzle, in order to avoid cable damage during the shot. The arrow achieved a velocity of about 21 ms^{-1}.

7.5.2 Results

During the first test campaign using the shock accelerometer with internal amplification (June-July 1996), 28 harpoon shots into various samples were performed. From this data set six shots were selected for closer analysis and interpretation, based on their differing target characteristics and the typicality of the signals obtained. Table 7.3 summarises the composition and structure of these six samples and lists the penetration depth of the arrow after the shot. The acceleration time histories are shown in the upper panels of Figures 7.5, 7.6, 7.7, 7.8, 7.9 and 7.10. The lower panels show the result of successive integration to obtain velocity and distance vs. time.

Table 7.3. Samples used for harpoon shots and final penetration depths of the arrow tip.

Sample	Sample composition and structure (top to bottom)	Penetration depth [m]	Remarks
# 1 (Figs. 7.5 & 7.11)	0.78 m water 30 mm hard wood 10 mm soft wood fibre board	0.82	wooden plate split due to shot
# 2 (Figs. 7.6 & 7.12)	0.9 m quartz sand: grain size 0.7 $\rightarrow$ 1.2 mm average density: 1330 kgm^{-3}	0.67	
# 3 (Figs. 7.7 & 7.13)	0.26 m quartz sand 10 mm soft wood fibre board 0.26 m quartz sand 10 mm soft wood fibre board 0.48 m quartz sand	0.54	Arrow stopped by second wood fibre board
# 4 (Figs. 7.8 & 7.14)	0.5 m sintered water ice, rather inhomogeneous (hard ice chunks of several cm size mixed with small ice grains) average density: 570 kgm^{-3}	0.25	Sample prepared by KOSI method at liquid nitrogen temperature; warmed up and re-cooled several times in order to allow for sintering processes to take place.
# 5 (Figs. 7.9 & 7.15)	Homogeneous sample of sharp gravel; average diameter: 5 mm, average density: 1390 kgm^{-3}	0.44	
# 6 (Figs 7.10 & 7.16)	Homogeneous sample of *Leca*-porous baked clay grains of roughly spherical shape; often used as mulch in large plant containers. diameter 10 $\rightarrow$ 20 mm. average density: 260 kgm^{-3}.	0.535	

There are a few features common to all shots that should be discussed first. Upon release of the shot, the harpoon undergoes a constant acceleration of approximately 50 g for about 40 ms (the start of the acceleration period is denoted by A in Figure 7.6). As the rear end of the arrow leaves the harpoon nozzle (and simultaneously the piston accelerating the arrow is stopped inside the harpoon), it experiences a sharp deceleration pulse (indicated by B in Figure 7.6), which excites eigen vibrations of the arrow. These oscillations occur in all records and have nothing to do with the nature of the penetrated material. Filtering or smoothing can be applied if the mean level of the acceleration signal needs to be studied, but for the purposes of integration (to obtain velocity and distance) the oscillations cancel out over short timescales and become insignificant, as shown in the centre and lower panels of the figures. For all shots the surface of the target material is indicated (denoted by C).

7.5.3 Preliminary analysis

On integrating the raw data, one found that a small mean offset in the acceleration (which was probably caused by the amplifier) had to be subtracted. This constrained the data in such a way that the total velocity change from start to stop was zero. Having done this the data was integrated to produce a profile of velocity vs. time as shown in the centre panels. The slight deceleration visible in each case during the free flight phase is possibly due to the drag caused by acceleration of the cable. The velocity data was then integrated once more to produce profiles of distance vs. time.

Having obtained both acceleration vs. time and distance vs. time, these data sets were combined to produce acceleration vs. distance, which enables easier interpretation of the signal in terms of variation of properties with target depth. These profiles are shown in the upper panels of Figures 7.11, 7.12, 7.13, 7.14, 7.15 and 7.16, where the sign convention is now such that distance travelled increasing from zero at the firing position. On comparing the total distance travelled obtained in this way with that actually measured after each shot, it can be seen that the signal-derived value is slightly less than the real value in each case. This could be explained by the decrease in sensitivity of the sensor at lower frequencies, which would result in an underestimate of the true accelerations and decelerations.

Figure 7.6 shows the motion of the arrow through a 0.78 m deep water layer. The time when the arrow tip enters the water is almost invisible on the plot (point C). On arrival at the bottom, the arrow tip hits a 30 mm thick wooden plate, splits the plate, and penetrates slightly the underlying soft sheet. Both events (D and E) are clearly resolved on

the record. The deceleration within the water is very low, as can be seen from the almost symmetric shape of the oscillation envelope. The eigen frequency mode of the arrow at about 2.5 kHz is seen as a distinct feature when the signal is Fourier transformed.

In Figure 7.7 a shot into a sample of quartz sand is shown. At point C the arrow tip hits the surface, and in a depth of 0.67 m it comes to rest, without having reached the sample bottom. The average level of deceleration in the sand is about 30 g in the lower part and 50 g in the upper part. Figure 7.8 shows again a shot into a quartz sand sample, which is, however, interrupted by two soft wood fibre boards of 10 mm thickness. After having hit the sand surface (point C) the arrow moves through the upper sand layer (0.25 m), penetrates the first board (point D), and finally comes to rest when it hits the second board in a depth of 0.54 m (point E).

Figure 7.9 shows a shot into sintered water ice. The sample was prepared by applying the method known from KOSI experiments (spraying of water droplets into a Dewar filled with liquid nitrogen). The resulting sample was a mixture of large ice chunks (several centimetres size) with fine grains. The average density of the sample was 570 kgm^{-3}, corresponding to a porosity of about 30 %. The arrow penetrated the hard surface, moved through a softer layer of finer material, and finally got stuck at a depth of approximately 0.25 m by hitting an ice chunk (this was verified after removal of the arrow).

Figure 7.10 shows a shot into sharp gravel, average grain size ~5 mm, average density 1390 kgm^{-3}. The penetration depth was 0.44 m, rather shallower than the sand of similar density (#2). This could be due to the sharpness of the grains which results in a more rigid, interlocked packing structure than the sand. As with shot #2 the largest deceleration peak is seen just below the surface. The velocity profile shows the boundaries between the three penetration stages particularly clearly.

Figure 7.11 was obtained using *Leca*, a mulching material consisting of roughly spherical, porous baked clay grains. The average density obtained with this material was 260 kgm^{-3}, the lowest target density used so far in this shot programme. A penetration depth of 0.535 m was achieved. Again the greatest deceleration is seen just below the surface. The stage boundaries are seen less clearly in the velocity profile, which is more curved than shot #5. Small bumps can be seen in the profile, most noticeably in the 80 $\rightarrow$ 100 ms region.

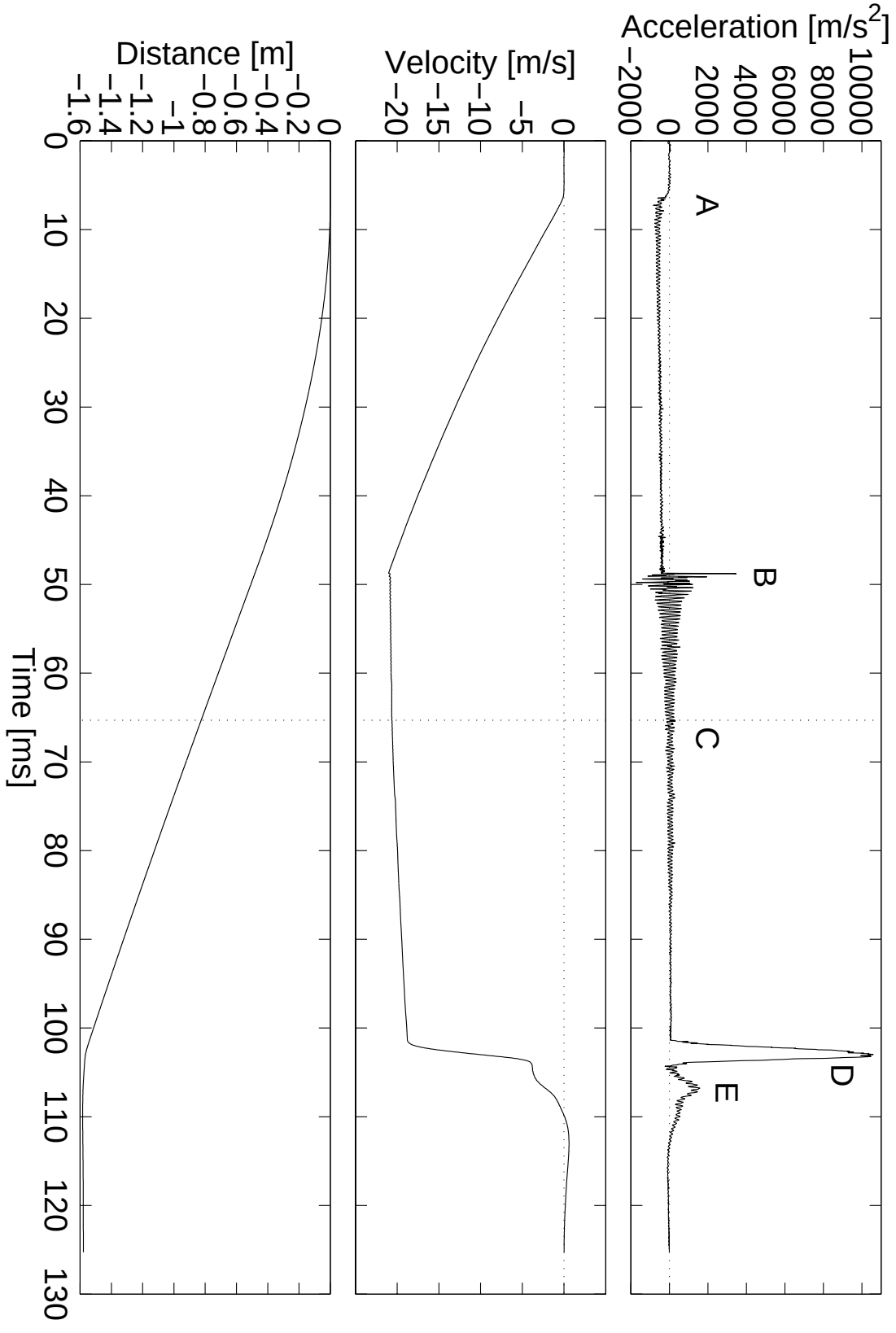

Figure 7.6. Harpoon shot (#1) into water + wooden plate. The upper panel shows the accelerometer signal for the duration of the shot, with a small offset correction to ensure that the total velocity change from start to finish is zero. The centre panel shows the velocity as obtained by integrating the accelerometer signal. The lower panel shows the distance travelled as obtained by integrating the velocity.

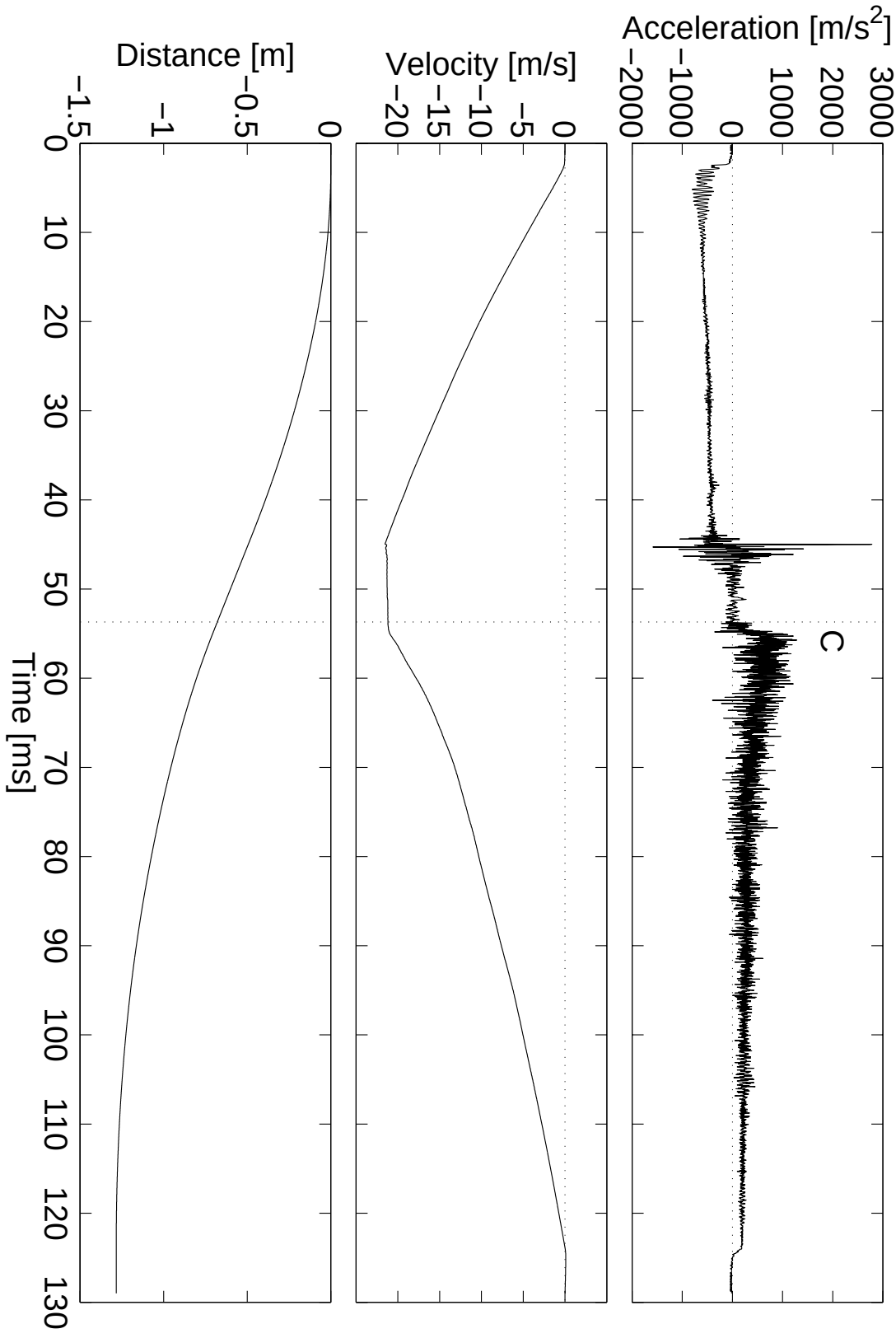

Figure 7.7. Harpoon shot (#2) into quartz sand. The format of the plots is analogous to Figure 7.6.

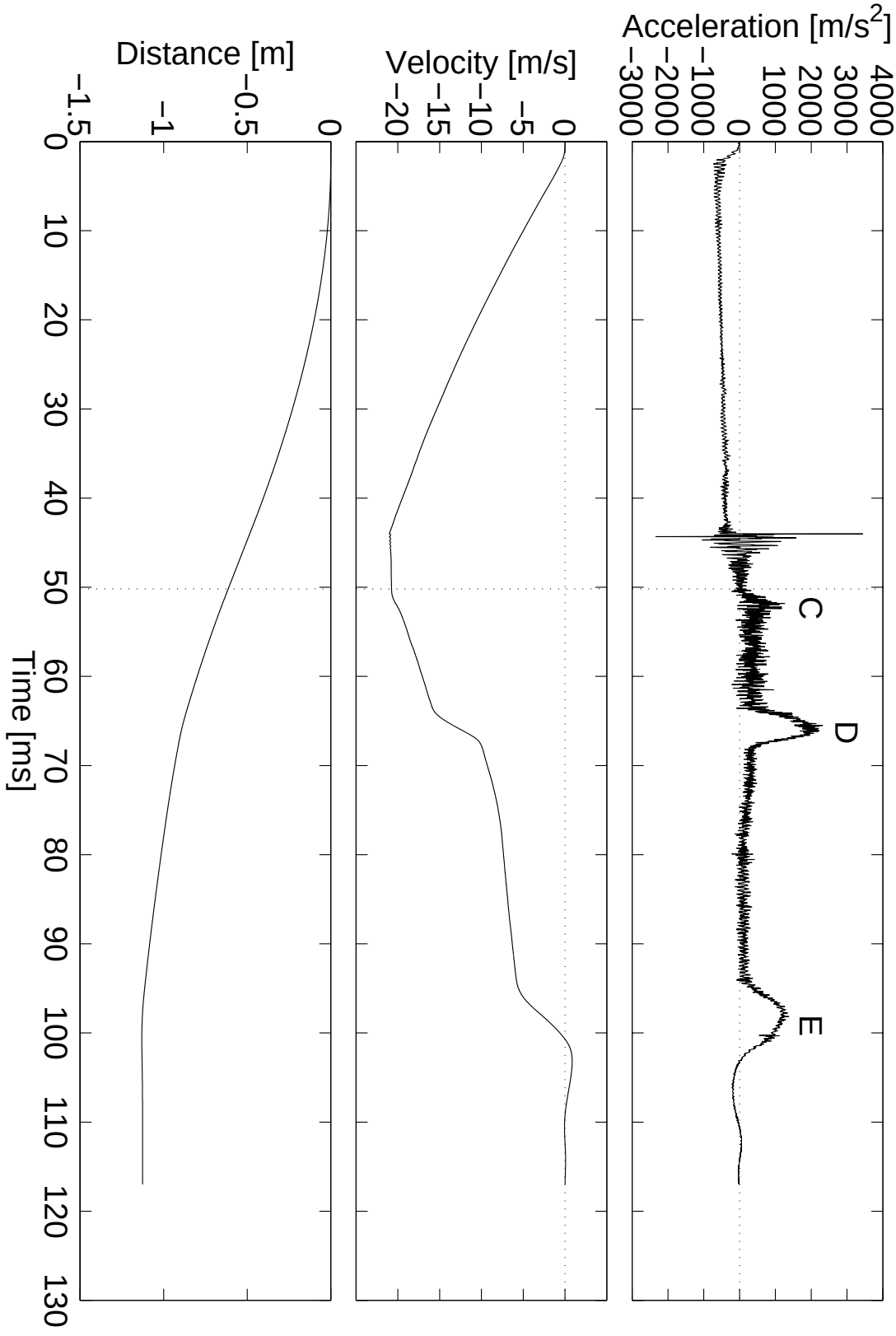

Figure 7.8. Harpoon shot (#3) into sand + 2 soft plywood plates. The format of the plots is analogous to Figure 7.6. D and E denote the positions of the harder layers.

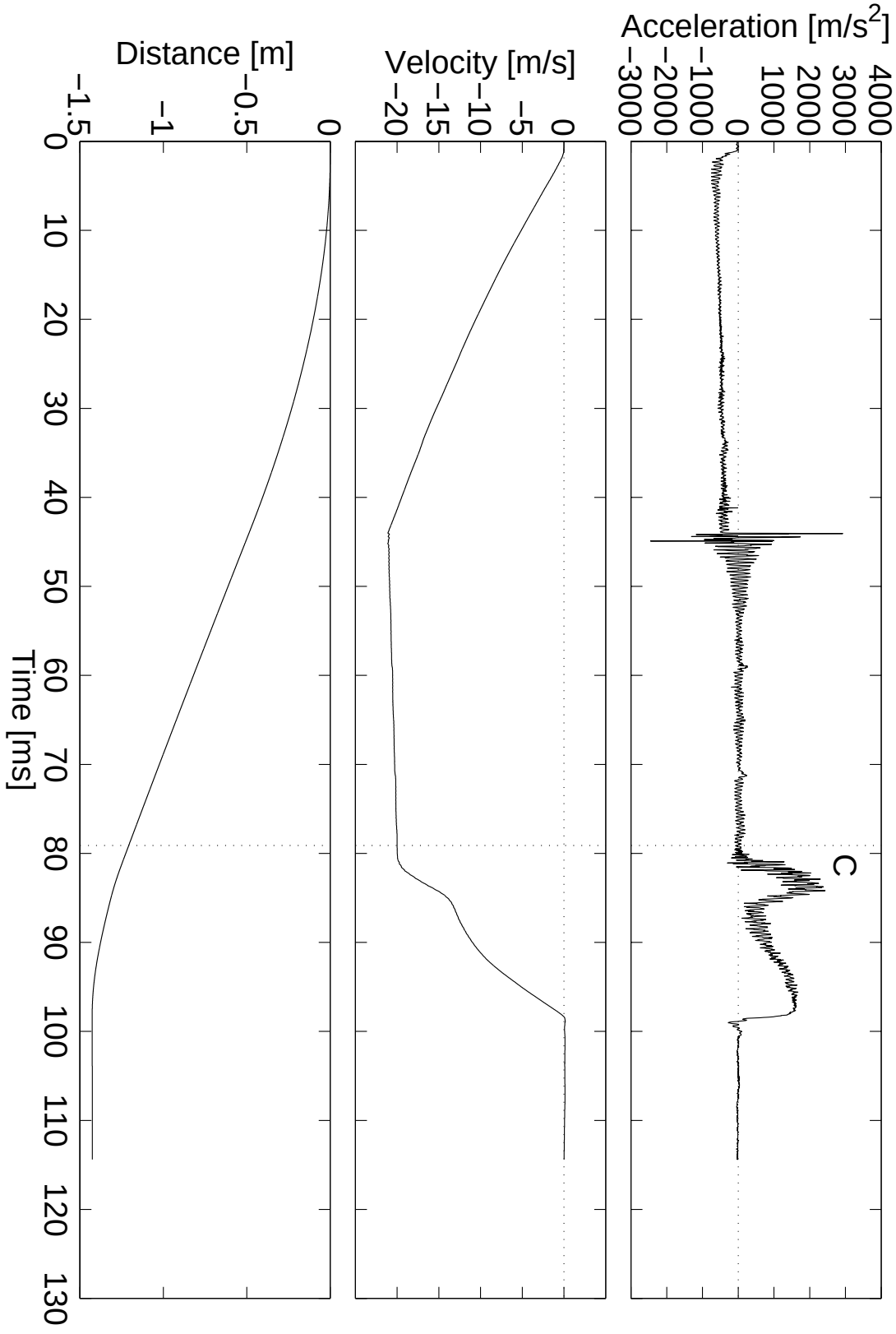

Figure 7.9. Harpoon shot (#4) into porous ice. The format of the plots is analogous to Figure 7.6.

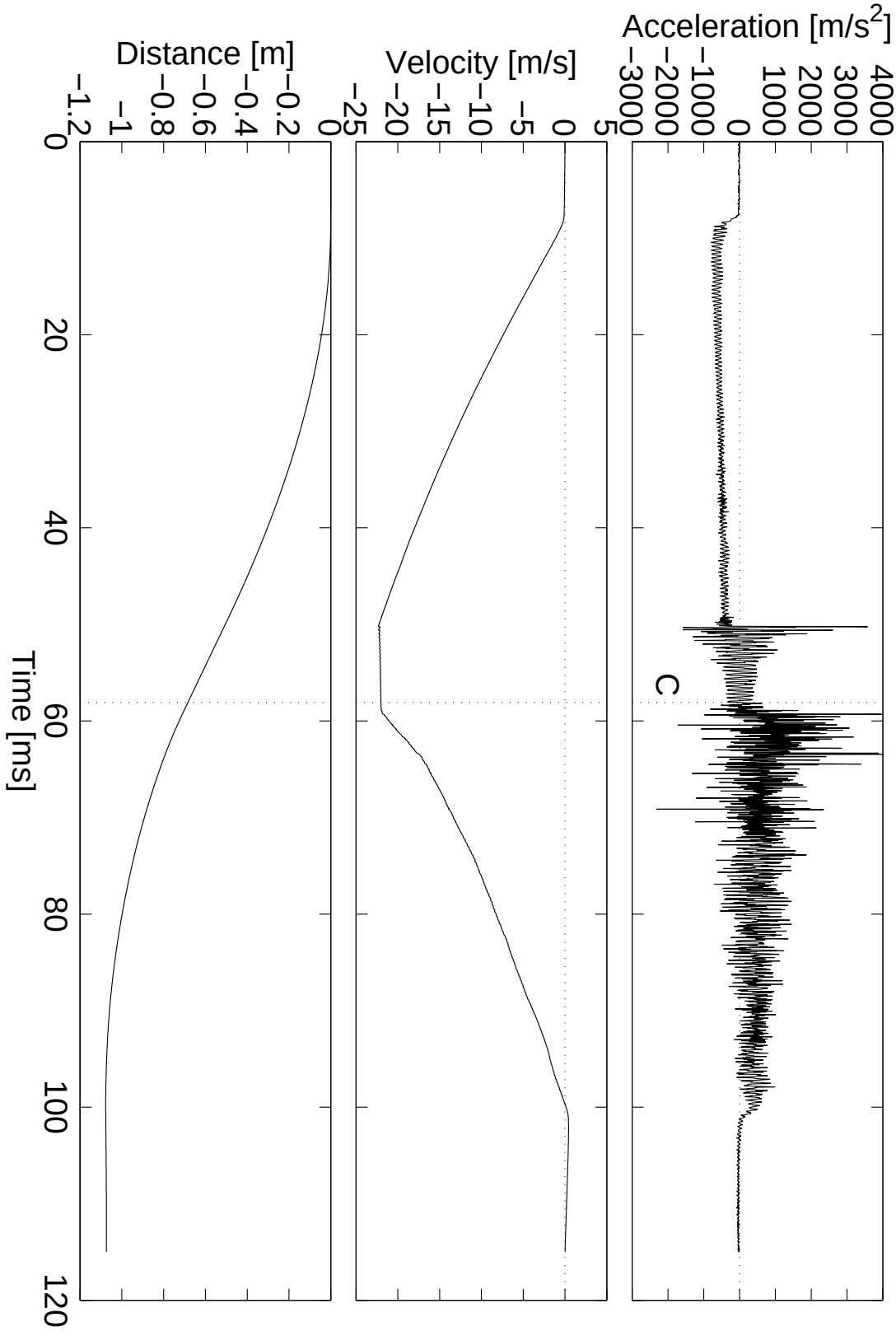

Figure 7.10. Harpoon shot (#5) into sharp gravel. The format of the plots is analogous to Figure 7.6.

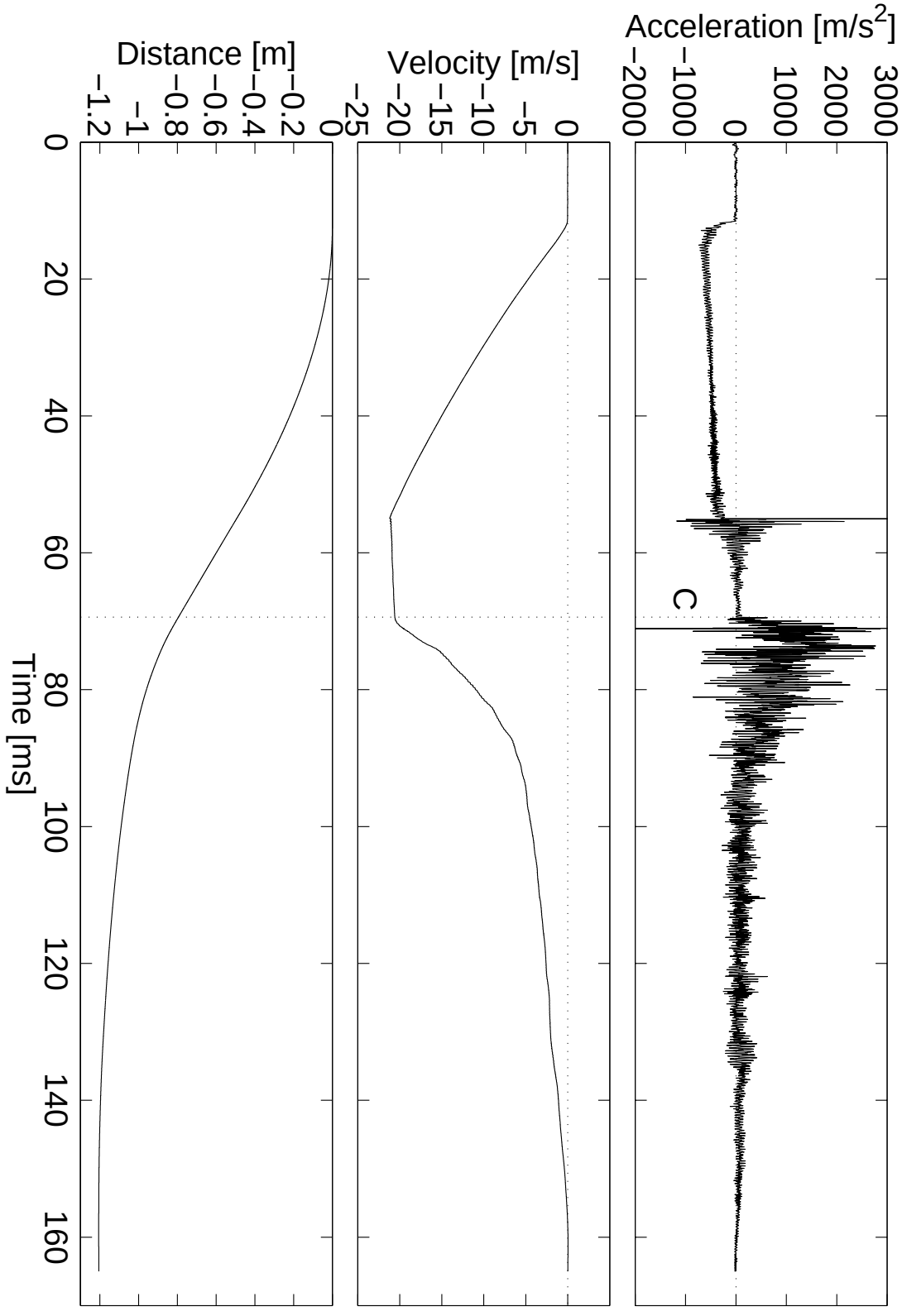

Figure 7.11. Harpoon shot (#6) into *Leca* (porous baked clay grains, roughly spherical in shape with diameters in the range 10 → 20 mm). The format of the plots is analogous to Figure 7.6.

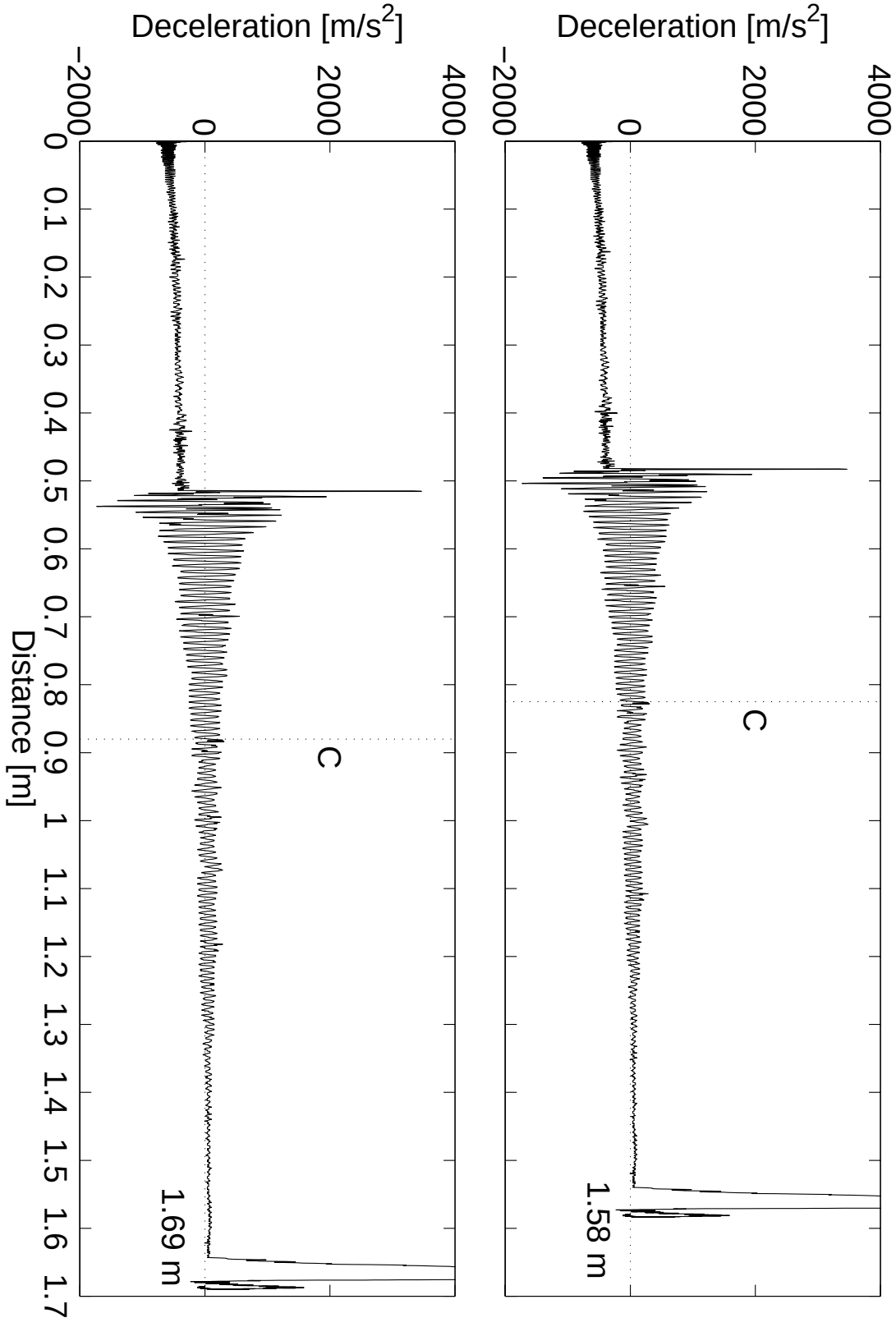

Figure 7.12. Harpoon shot (#1) into water + wooden plate. The acceleration signal is plotted vs. distance travelled from the firing position. The upper panel uses the distance obtained by double integration, while the lower panel shows the profile stretched to fit the measured distance.

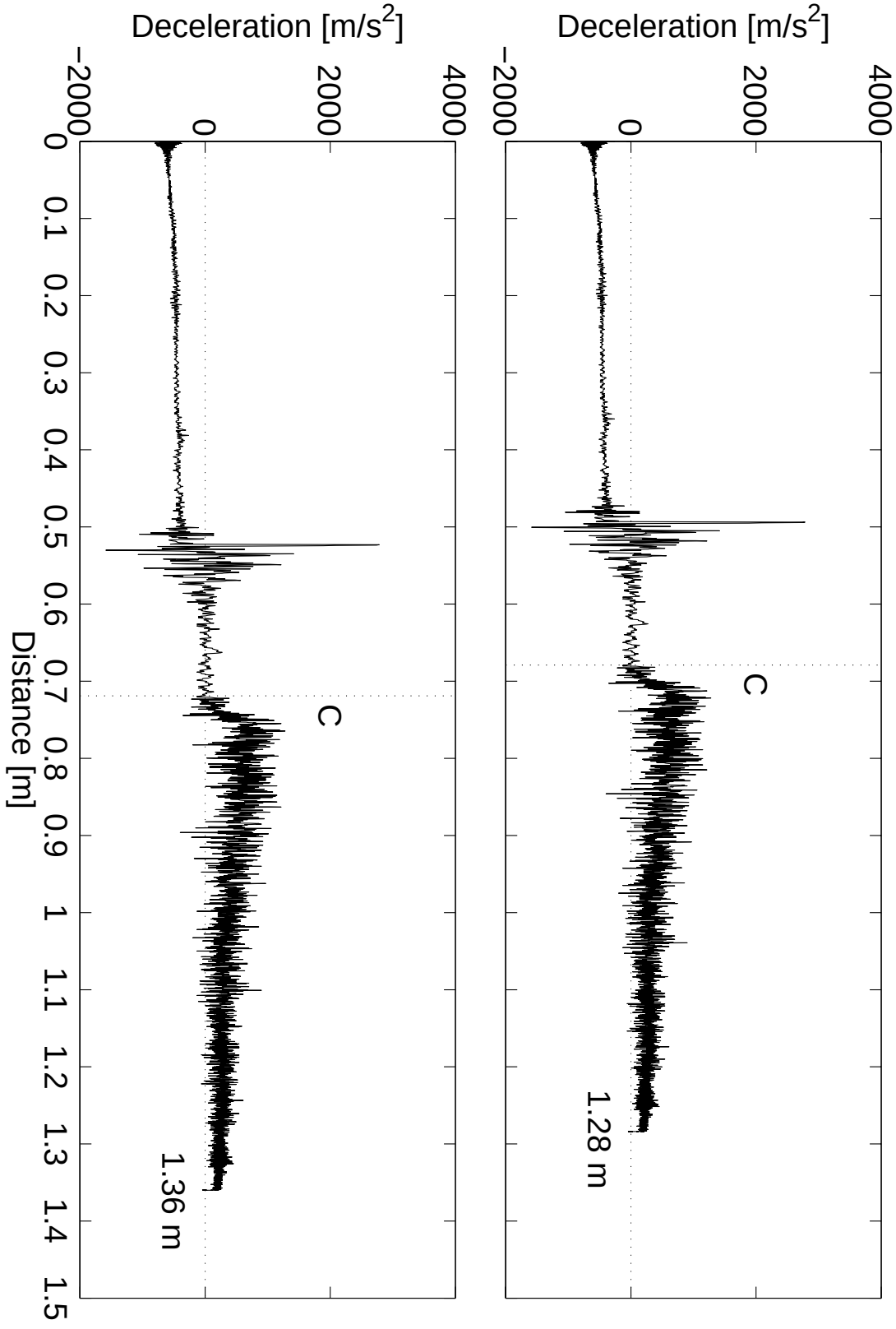

Figure 7.13. Harpoon shot (#2) into quartz sand. The format of the plots is analogous to Figure 7.12.

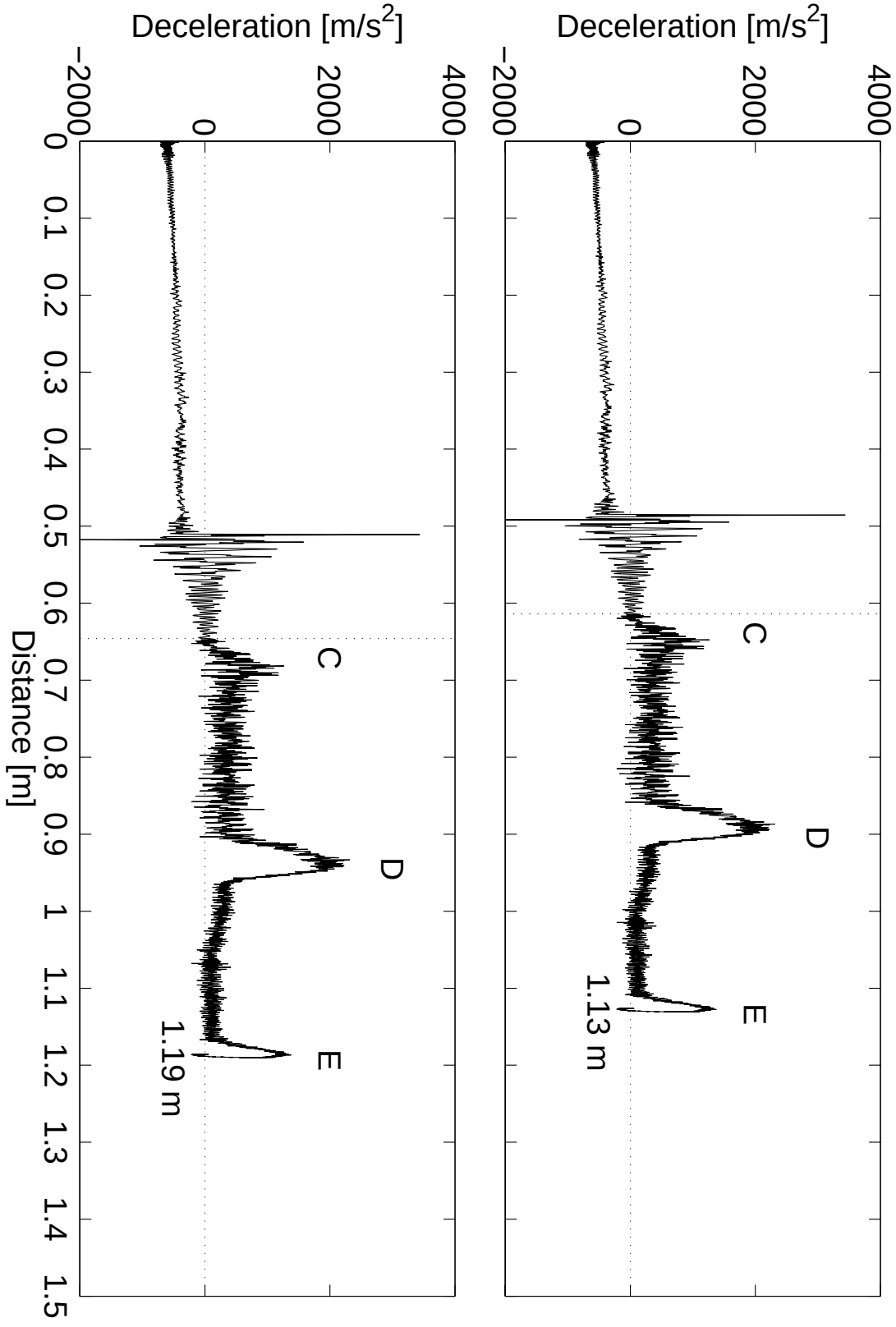

Figure 7.14. Harpoon shot (#3) into sand + 2 soft plywood plates. The format of the plots is analogous to Figure 7.12. D and E denote the positions of the harder layers.

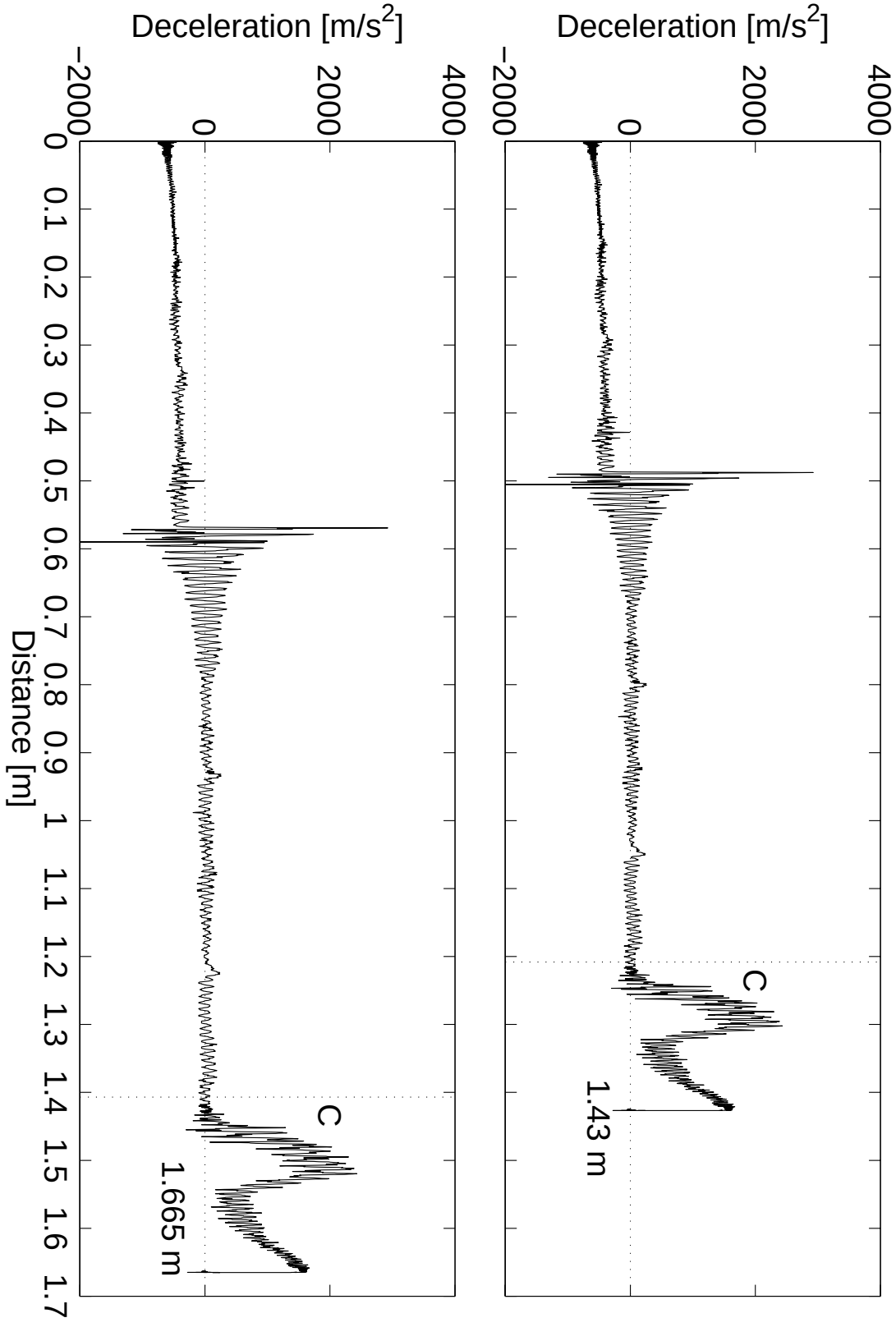

Figure 7.15. Harpoon shot (#4) into porous ice. The format of the plots is analogous to Figure 7.12.

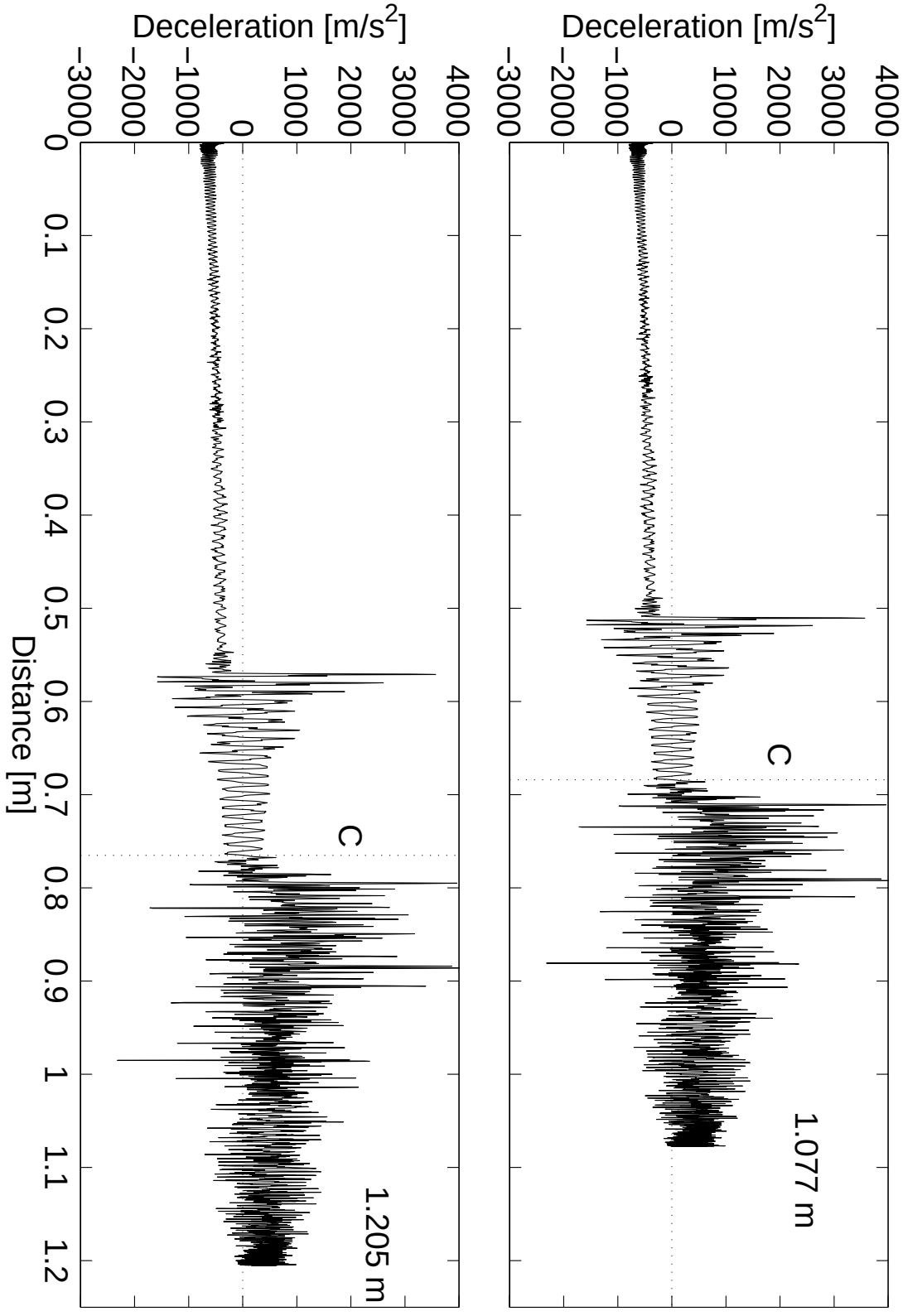

Figure 7.16. Harpoon shot (#5) into sharp gravel. The format of the plots is analogous to Figure 7.12.

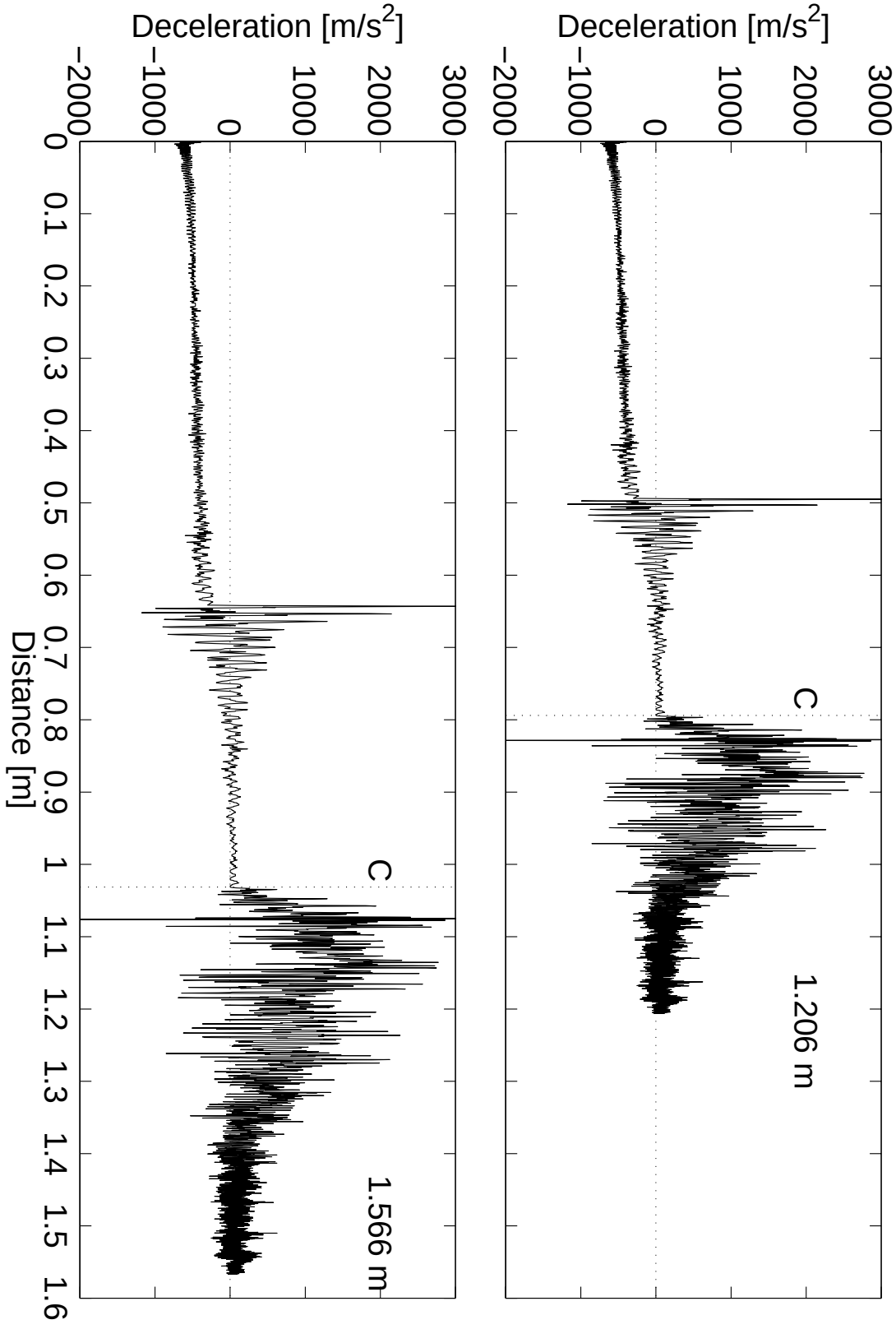

Figure 7.17. Harpoon shot (#6) into *Leca*. The format of the plots is analogous to Figure 7.12.

7.5.4 Comparison with modelling results

In the following analysis the penetration model of Anderson *et al.* (1996) is applied first to the harpoon shot #2, namely the penetration of the arrow into a quartz sand sample. As this sample had a more or less homogeneous structure, the semi-analytic version worked out in section 7.4 can be used. Table 7.4 lists the constrained and fitted parameters. The mass M of the arrow, its main dimensions and shape (diameter D, length L, half cone angle θ), and the impact velocity u_0 are rather well constrained. Furthermore, the bulk density of the sand ρ and the final penetration depth s_{max} of the arrow tip, have been independently determined. As fit parameters there remain σ_d, μ_f, and the drag coefficient C_D. Figure 7.18, Figure 7.19 and Figure 7.20 summarise the results of the parameter study, while the values of the fitted parameters are shown in Table 7.5. In all three figures the measured deceleration signal (from the point of impact to the final penetration depth) is plotted vs. depth penetrated in the background, together with a version filtered digitally to remove frequencies above 2 kHz. This was done using a FORTRAN code written by Dr. Neil McBride of UKC using an FFT-based method from *Numerical Recipes* (Press *et al.*, 1992). The filtering removes the arrow oscillations and shows more clearly the underlying acceleration to be compared with the model results.

The friction parameter μ_f is varied from zero (Figure 7.18) via 0.01 (Figure 7.19) to 0.1 (Figure 7.20). This covers approximately the range of values found by Anderson *et al.* for their shots into cohesive samples. In each figure the calculated deceleration profiles for various values of C_D are plotted. For each curve the strength parameter σ_d is adapted in such a way that the measured total penetration depth is matched. In each figure the 'best fit' plot is highlighted by a thicker line. The three different penetration stages of the projectile can be clearly discerned on the figures, in particular on Figure 7.20, where the friction has the strongest effect.

A numerical model-fitting code has not yet been developed, so all the 'fits' here were obtained manually by repeatedly running the model and varying the parameters. The model results and data were compared visually. Clearly a numerical routine to carry out this task would greatly improve the quality and speed of the data analysis. Such an iterated manual fitting exercise as used here is nevertheless instructive– the user acquires a feel for how each parameter affects the model.

A numerical routine to fit the model to an acceleration vs. distance dataset would not be a trivial exercise. The first major difficulty is that the model produces an acceleration vs. distance profile which is not an analytic function. To evaluate the acceleration at any

desired point the model must be run from the start of penetration. Secondly, the model must match not only the magnitude of the acceleration but also the final penetration depth.

Table 7.4. Model parameters and boundary conditions used for the application of the model by Anderson *et al.* (1996) to shot #2.

Parameter	Value
M, the mass of the arrow	0.34 kg
D, the diameter of the penetrator tip	20 mm
L, the length of the penetrator including the conical tip	110 mm
θ, the half cone angle of the penetrator tip	15°
ρ, the bulk density of the target material (sand)	1330 kgm^{-3}
s_{max}, the final depth of penetration	0.67 m
σ_d, the material strength	fitted
μ_f, the coefficient of friction between the penetrator surface and target material	fitted
C_D, a parameter analogous to the hydrodynamic drag coefficient	fitted

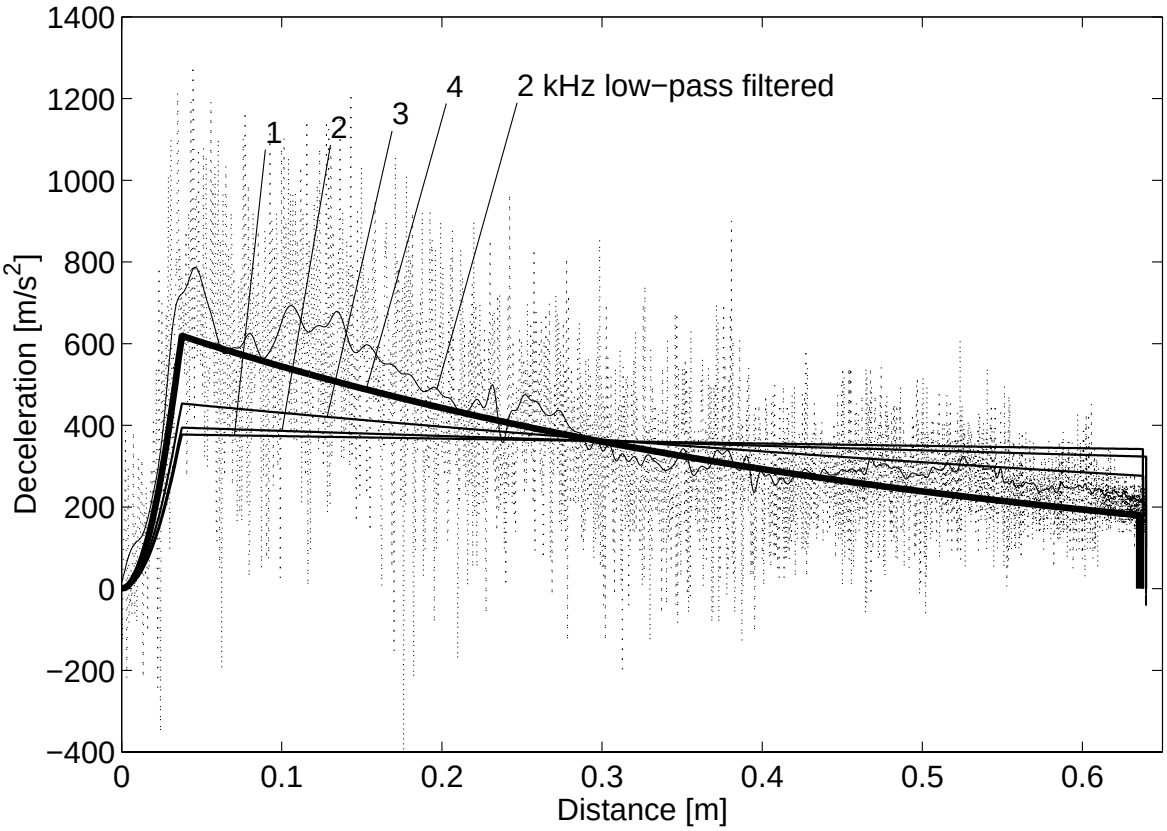

Figure 7.18. Comparison of acceleration data for quartz sand (shot #2) with modelling results for $\mu_f = 0$. Curves 1, 2, 3 and 4 show the modelling results for $C_D = 2$, 4, 10 and 25 respectively. Values of σ_d were adjusted in each case to meet the condition that the total penetration depth should agree with the data. This resulted in the values listed in Table 7.5. Curve 4 is the best fit.

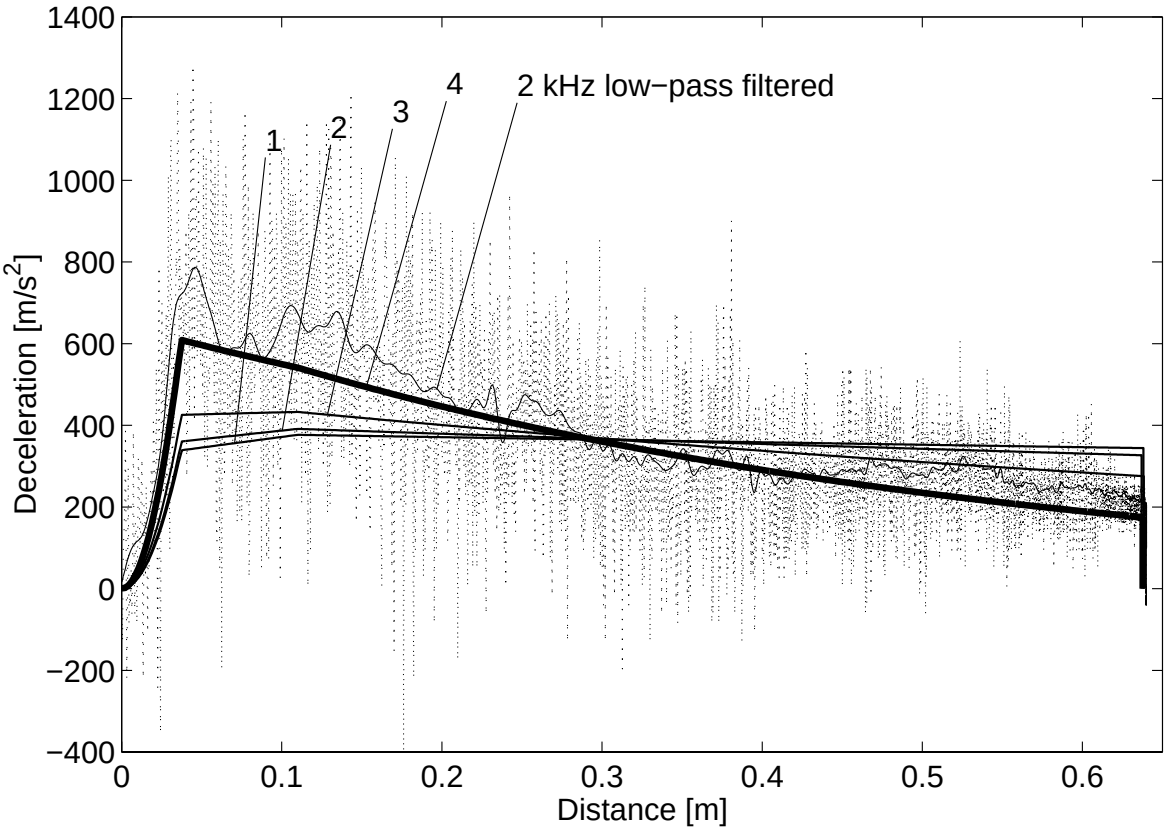

Figure 7.19. Comparison of acceleration data for quartz sand (shot #2) with modelling results for μ_f = 0.01. Curves 1, 2, 3 and 4 show the modelling results for C_D = 2, 4, 10 and 25 respectively. Values of σ_d were adjusted in each case to meet the condition that the total penetration depth should agree with the data. This resulted in the values listed in Table 7.5. Curve 4 is the best fit.

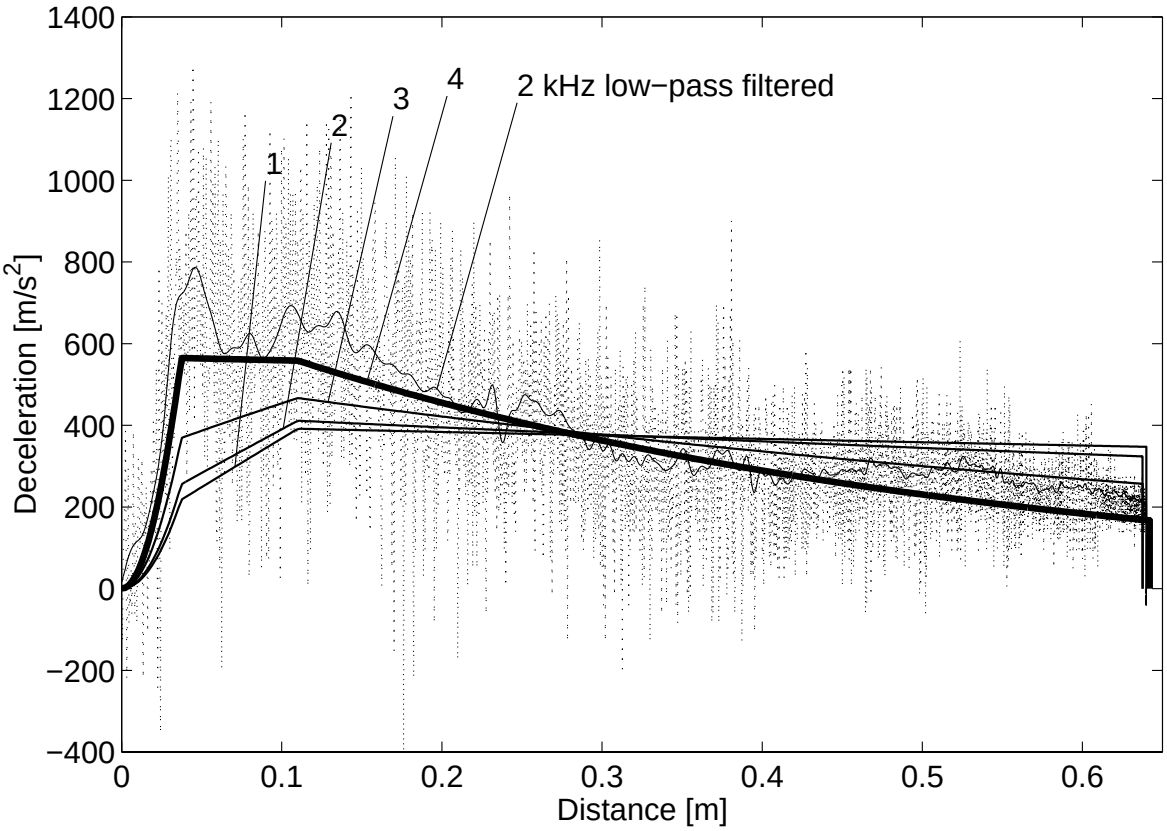

Figure 7.20. Comparison of acceleration data for quartz sand (shot #2) with modelling results for μ_f = 0.1. Curves 1, 2, 3 and 4 show the modelling results for C_D = 2, 4, 10 and 20 respectively. Values of σ_d were adjusted in each case to meet the condition that the total penetration depth should agree with the data. This resulted in the values listed in Table 7.5. Curve 4 is the best fit.

Table 7.5. Values for the fitted parameters μ_f, C_D and σ_d as used in Figures 22, 23 and 24.

μ_f	C_D	σ_d [Pa]
0.0	2	3.70×10^5
	4	3.50×10^5
	10	2.99×10^5
	25	1.95×10^5
0.01	2	3.15×10^5
	4	2.99×10^5
	10	2.52×10^5
	25	1.60×10^5
0.1	2	1.33×10^5
	4	1.24×10^5
	10	9.83×10^4
	20	6.40×10^4

Two main conclusions can be drawn from the fits to the data:

1. The model allows one to find a reasonable fit to the data by changing the parameters C_D, μ_f and σ_d.
2. In order to reproduce the measured decrease of the deceleration during penetration, a considerably higher C_D value than usually assumed in hydrodynamic theory of fluids is necessary. With values in the range 2 to 4 no close fit to the data can be obtained, as one gets in this case a flatter profile than observed, and there is no way to obtain a more inclined profile by varying the parameters μ_f and σ_d.

One can imagine several reasons for this somewhat surprising result. First, it seems to indicate that the analogy of the dynamic resistance force with a hydrodynamic drag force should be considered with care. While Anderson *et al.* propose a value of 2 for C_D, they have not confirmed this by corresponding experiments, since their experimental

results refer to much harder and more cohesive materials than sand. In the paper of Allen *et al.* (1957) it is reported that their results for projectile penetration into sand imply a strong increase of C_D with decreasing velocity in the range $u < 50$ ms^{-1}. While several authors confirm that the functional form $\alpha u^2 + \gamma$ for the resistance force to penetration provided the most satisfactory representation of their data, most of them consider the constant related to the dynamical drag coefficient simply as an additional fit parameter, which does not necessarily have a value close to 2 as in classical fluid dynamics (e.g. Kohno *et al.*, 1990; Boguslavskii *et al.*, 1996). If one does interpret C_D in the fluid dynamic sense it is necessary to assume that additional forces act on the penetrating projectile which are proportional to u^n, where $n < 2$ (this would produce the apparent increase of C_D with decreasing velocity). Using the more general equation (7.14 on page 126) with $\beta \neq 0$ would undoubtedly result in a smaller C_D value while still giving a reasonable fit to the data.

On the other hand, looking at the values obtained for σ_d when varying C_D while keeping the penetration depth constant, one recognises that the strength parameter σ_d varies only by a factor 1.5 over the whole μ_f range shown. The absolute value obtained also appears reasonable.

7.5.5 Model fitting to additional shots

This section presents fits to shots #5 and #6, neither of which appeared in the publication by Kömle *et al.* (1997). These additional fits were made manually by the author using essentially the same Matlab code as before. Figure 7.21 shows the fits for shot #5 into gravel. The values $\mu_f = 0.2$ and $C_D = 27$ were found to offer a reasonable fit– matching the height and width of the initial broad peak, though falling away slightly towards the final depth. The value of σ_d was adjusted to match the final penetration depth. This initial fit is shown as the thickest line (5) in the figure. To see how sensitive the value of σ_d was to changes in μ_f and C_D, eight more fits were made, varying μ_f and C_D both up and down while still maintaining a reasonable fit. The results of this exercise are shown in Table 7.6. All the values for σ_d are within a factor of 2.2. The results seem to confirm the need for a large value of C_D suggested by shot #2 in the previous section. It is also worth remarking that all the curves seem to coincide at a particular depth, around 0.17 m.

Table 7.6. Model parameters for the curves in Figure 7.21.

Curve number	μ_f	C_D	σ_d [Pa]
1	0.25	29	3.30×10^4
2	0.25	27	3.63×10^4
3	0.20	29	4.48×10^4
4	0.25	25	3.97×10^4
5	0.20	27	4.88×10^4
6	0.15	29	6.33×10^4
7	0.20	25	5.29×10^4
8	0.15	27	6.81×10^4
9	0.15	25	7.30×10^4

Figure 7.22 shows the results of fitting the model to shot #6. The low bulk density of the target material meant that a particularly high value for C_D had to be used to fit the initial peak. A high value of μ_f also appeared to improve the fit by reducing the rate at which the deceleration falls off after the initial peak. Curve 1 is the best fit achieved, with $C_D = 120$, $\mu_f = 0.7$ and $\sigma_d = 0.353 \times 10^4$ Pa. To test whether such high values of C_D and μ_f were necessary for a good fit, four more model curves were produced using lower values of either C_D and μ_f. In each case the value of σ_d was again adjusted to match the final penetration depth. The parameters used for the five curves are summarised in Table 7.7. Curves 2-5 show that decreasing either C_D or μ_f reduces the quality of the fit, both by reducing the height of the initial peak and increasing the level of deceleration just before the penetrator comes to a halt. The latter is a result of having to increase σ_d to reduce the final penetration depth– reducing either C_D or μ_f increases the final depth. Again the five curves meet at almost the same point, around $0.16 \rightarrow 0.17$ m.

Table 7.7. Model parameters for the curves in Figure 7.22.

Curve number	μ_f	C_D	σ_d [Pa]
1	0.7	120	0.353×10^4
2	0.5	120	0.828×10^4
3	0.7	80	0.839×10^4
4	0.7	60	1.256×10^4
5	0.2	120	3.850×10^4

The value of σ_d obtained for curve 1 is consistent with the observation that the porous *Leca* grains have rather less strength under compression than the gravel particles, which gave a higher value for σ_d. The value of σ_d obtained for the best fit to the shot #2 data ($\mu_f = 0.1$, $C_D = 20$) into sand was 6.4×10^4 Pa, within the range of values for shot #5 into gravel. Meaningful quantitative comparison of the fitted strength parameter will have to wait until reliable numerical model-fitting software is available, however.

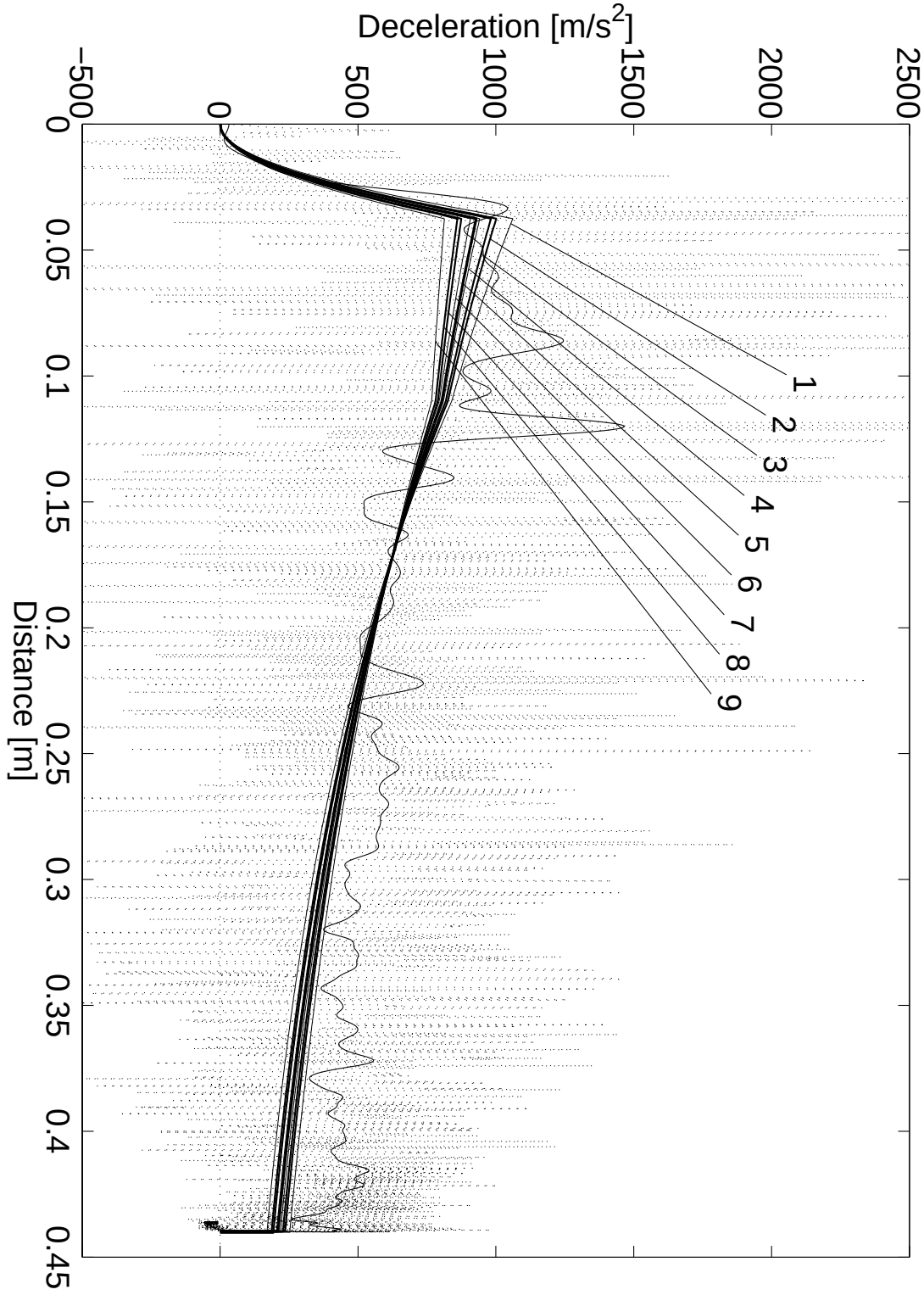

Figure 7.21. Comparison of model results with acceleration vs. time data for shot #5 into sharp gravel. The initially selected fit was curve 5. Values of μ_f and C_D were then varied in either direction, producing the other curves. Values of σ_d were constrained to within a factor of 2.2. As for the fits to shot #2 the 2 kHz low-pass filtered data is also shown.

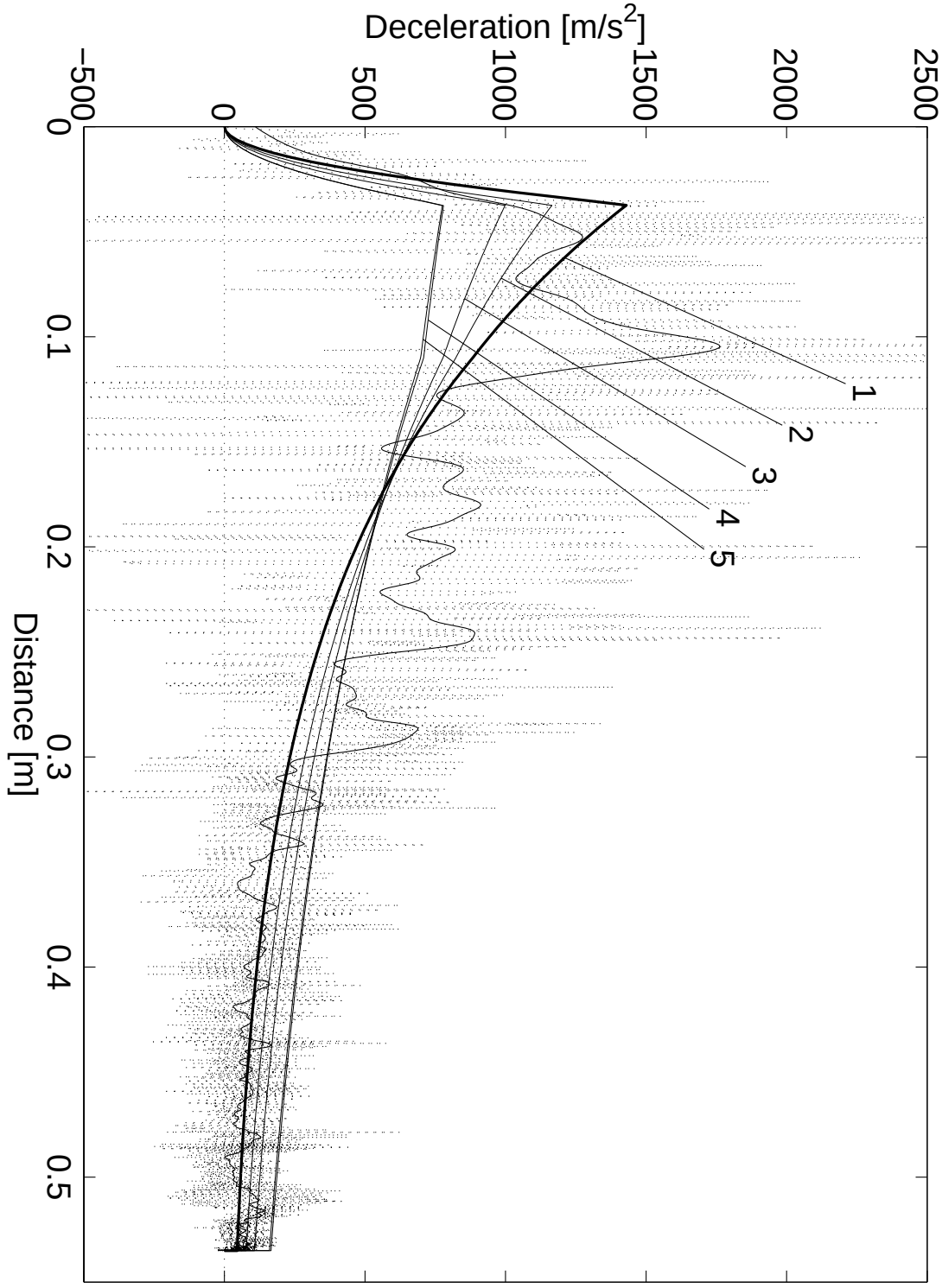

Figure 7.22. Comparison of model results with acceleration vs. time data for shot #6 into *Leca*. The best fit is curve 1, the other curves being the result of reducing either μ_f or C_D and adjusting σ_d to match the final penetration depth. Again the low-pass filtered data is also shown.

7.6 Conclusions

This chapter has shown that the *Rosetta Lander* needs to be anchored to the cometary surface. Even without activities such as drilling or hammering of the *MUPUS* probe the gas drag from sublimating H_2O may eject the lander if the landing site is in an active area and the temperature exceeds the threshold value.

While clearly the primary purpose of the anchor is to fix the Lander to the surface, the design adopted is able to usefully accommodate a shock accelerometer to perform penetrometry measurements of the cometary surface. The experiments described in this chapter verify that such a device is capable (at least qualitatively) of detecting layers in the target material and (by the double integration method) measuring their depth.

In order to interpret the signals obtained from the accelerometer it is necessary to obtain independent measurements of the material's density (e.g. using the *MUPUS* densitometer) and the final penetration depth of the anchor. The latter will be obtained by counting the turns of the harpoon cable rewind motor.

The experimental results and model calculations presented here show that the strength parameter σ_d can be constrained to with a factor of 2.2 (for the gravel) and 1.5 (for the sand). Further investigation of the meaning of C_D is clearly required given the high values obtained here, an effect which may be an artefact of neglecting other velocity-dependent terms in the deceleration equation. Other penetration models should certainly be applied to this experimental data, though it would first be useful to develop numerical fitting software for the current model.

Further test shots have more recently been performed at MPI für Extraterrestrische Physik, Garching using a more representative anchoring harpoon. These experiments and the subsequent analysis will be reported in a future publication. Such experiments will continue to expand the dataset available for comparison with models. It is clearly important that future experiments include the use of well-characterised cometary analogue target materials.

In summary the *MUPUS* anchor penetrometry experiment on the *Rosetta Lander* will, together with other investigations of the surface material, serve to constrain the relevant physical properties of the material found at the landing site. In particular, the penetrometry results will prove or disprove the existence of layers (above the final penetration depth of the anchor) with distinctly differing strengths. Such layers may be expected from theoretical models of cometary activity.

8 Conclusion

First it is worthwhile bringing together the main conclusions arising from each of the previous chapters.

- In the introduction we see that there are a number of reasons why cometary nucleus material is worthy of *in situ* investigation by an integrated experiment package such as *MUPUS*. Key to its success is the co-location of the thermal, mechanical and density measurements (performed by the *MUPUS* probe) and nearby measurements such as those from the *MUPUS* thermal infrared sensor (TM), the anchor penetrometer (ANC-M) and anchor temperature sensor (ANC-T). Results from *MUPUS* will also be useful in combination with those from other investigations of the near-surface material. In particular one can cite those instruments able to obtain a depth profile– these include the two evolved gas analysers (COSAC and MODULUS) which will analyse material sampled from different depths by the drill, and the acoustic and seismic sounding experiment (SESAME-CASSE) which may be able to corroborate evidence for layering found by mechanical, thermal, compositional or density measurements.

- The *Rosetta Lander* offers a better chance to perform the *MUPUS* investigations than did the surface stage of the previous *Rosetta* Comet Nucleus Sample Return (CNSR) concept, which would not have been able to examine 'living' cometary material *in situ* for more than a few days.

- Although the bulk density of the entire nucleus will be determined using the volume and mass obtained from Orbiter camera images and spacecraft tracking data, the local surface density at the landing site may be different and is worthy of measurement. While both terrestrial and space-borne densitometers suggest techniques for density measurement on *Rosetta*, the current ^{137}Cs attenuation concept provides the best solution in terms of mass, payload accommodation and its capability for depth profile measurements.

- The algorithm for controlling combined density measurement and hammered penetration presented in section 3.3.4 (page 62) represents a novel approach to the uncertainties and constraints associated with the operation of this instrument. The algorithm does, however, require an on-board ability to use output from the detectors to determine density for feedback into the control system. It would of course be necessary to test the algorithm for robustness, as outlined in the text.

- Much work remains to be done on the densitometer's detection and counting system, in particular to characterise further the response of candidate CdTe (and CZT) detectors, and do so for the range of operating temperatures expected. The detectors would need to be thicker than the 2 mm CdTe detector used in the experiment discussed in chapter 6. A range of test materials of different elemental composition and density should be used to verify the composition-independence of Compton-dominant part of the detected spectrum, above about 150 keV.

- Comparing the Monte Carlo results (chapter 5) with the experimental results suggests that the detector response is a more important constraint on the performance of the instrument (i.e. efficient counting of the 662 keV photons) than contamination by photons scattered in the material.

- The Single Scattering Model work (chapter 4) is rather less specific to the *in situ* analysis of planetary surfaces than the rest of this thesis. It shows how the spatial region of contradictory response for gamma backscatter density gauges can be explained using the SSM approximation. This advances our theoretical understanding of the technique (whatever the context of the investigated material) and should be of use in terrestrial geophysics, soil science and non-destructive testing. Perhaps at some point in the future the backscatter technique will be used again on another planet– maybe borehole density logging will one day be used on the Moon or Mars.

- The preliminary calculations in section 7.2 (page 117) show the need for anchoring of the *Rosetta Lander*. There is scope for refinement of these calculations, which could easily be adapted for other target comets. A similar exercise for other minor bodies or small satellites might be interesting, though clearly the influence of cometary activity would be removed.

- The penetrometry work in section 7.5 shows that, at least on a quantitative level, near-surface layers can be detected by an accelerometer in the Lander's anchoring harpoon. Double integration can be applied to measure the depth of any features, given an independent measurement of the final depth of penetration of the anchor. Application of the penetration model used here suggests that the deviatoric stress (a strength parameter) can be constrained to within a factor of about 2.2 for the shots carried out.

- Further work is required to develop a model-fitting code for the penetrometry shots. The current manual method is clearly not satisfactory since it is slow and produces no quantitative information on the quality of the fit. The modelling work in general should

be developed and applied to experiments already under way with a more representative harpoon system.

Taking a step back from the individual topics in this thesis to look at the *in situ* physical measurements as a whole, one can identify a trend towards increased integration of basic sensors into larger ensembles. Comparing the *MUPUS* (**Multi-Purpose** Sensors for Surface and Sub-Surface Science) experiment with previous investigations of density, mechanical and thermal properties (on the Moon, Mars and Venus) it becomes apparent how much more integrated today's approaches are. While adding complexity (interfaces, testing, management, etc.) it does save duplication of resources, since each sensor need not have its own separate electronics box for signal conditioning, power supply and data processing. In the case of *MUPUS* one has a combination of thermal profile, thermal conductivity, mechanical strength and density measurements. An additional non-*MUPUS* sensor will be an electrode of the SESAME-PP (Permittivity Probe) experiment, built into the shaft of the probe. If funding had been available there may also have been a silicon micro-seismometer mounted on top of the probe to obtain better coupling to the ground and isolation from vibrations caused by the Lander.

Taking the theme of integration a step further, one could imagine several such devices as separate 'Autonomous *MUPUS*' penetrators that could be deployed from a single spacecraft to different sites on the planetary body (planet, satellite, asteroid, comet, etc.). Missions with some similarity to this technique are now starting to be realised: namely *Mars 96*, *Lunar-A* and *Deep Space 2* (Mars Microprobe). One has to consider, of course, whether resources are best spent on achieving broader coverage or better measurements at a single site. Seismometers, for instance, are co-operative in nature, in that to locate a seismic event at least three separate stations are required. The density, thermal and mechanical properties measurements made by *MUPUS*, however, are non-co-operative. Using multiple probes would improve coverage of different sites on the body but would not add an extra dimension to the measurement.

Another advantage of such integration is the so-called synergistic effect. While each individual measurement on its own is of little use, the collection of basic parameters together serves to constrain models of the material much more strongly. This is why co-location of the measurements is so important.

Another development of the *MUPUS*-style instrument suite would be to incorporate thermal, mechanical, electrical, seismic, compositional or even imaging sensors into a sub-surface 'mole' penetrator. Gromov *et al.* (1997) have recently demonstrated such a device,

which could perform a sub-surface ‘mission’ to examine material otherwise inaccessible. This could form the basis of a worthy experiment proposal for a future comet nucleus or other minor body or planetary surface mission.

Successful penetrometry, densitometry and thermal measurements by *MUPUS* should, in 2012, lead us to a greater understanding of the nature of comet nuclei, the processes involved in their activity and their evolution with time. It will provide data against which models of the nucleus can be tested, and enable us to gauge the degree to which the material found has been modified since its formation. By then, of course, *in situ* measurement techniques on Earth will have improved still further, enhancing our toolbox for the exploration of the Solar System.

References

Allen, W. A., Mayfield, E. B. and Morrison, H. L., Dynamics of a Projectile Penetrating Sand. *J. Appl. Phys.* **28**(3), 370-376, 1957.

Anderson, W. W., Ahrens, T. J., Gibson, A., Scott, R. and Suzuki, K., Emplacement of Penetrators into Planetary Surfaces. *J. Geophys. Res.* **101**(E9), 21137-21149, 1996.

Announcement of Opportunity for Champollion Surface Science Instruments. AO No. 95-OSS-01, March 1995.

Announcement of Opportunity for RoLand Surface Science Instruments. RoLand consortium, March 1995.

Ao, Q. and Gardner, R. P., The McLDL Code with Subspace Weight Window-biasing Combined with the Monte Carlo Multiply Scattered Components Approach for Simulation of Gamma-Gamma Litho-density Logging Tools. *Nucl. Geophys.* **9**(6), 497-515, 1995.

Asphaug, E. and Benz, W., Density of Comet Shoemaker-Levy 9 Deduced by Modelling Breakup of the Parent 'Rubble Pile'. *Nature* **370,** 120-124, 1994.

Atzei, A., Schwehm, G., Coradini, M., Hechler, M., De Lafontaine, J. and Eiden, M., Rosetta/CNSR– ESA's Planetary Cornerstone Mission. *ESA Bulletin* **59,** 18-29, 1989.

Avanesov, G., Zhukov, B., Ziman, Ya., Kostenko, V., Kuzmin, A., Murav'ev, V., Fedotov, V., Bonev, B., Mishev, D., Petkov, D., Krumov, A., Simeonov, S., Boycheva, V., Uzunov, Yu., Weide, G.-G., Halmann, D., Pössel, W., Head, J., Murchie, S., Schkuratov, Yu. G., Berghänel, R., Danz, M., Mangoldt, T., Pihan, U., Weidlich, U., Lumme, K., Muinonen, K., Peltoniemi, J., Duxbury, T., Murray, B., Herkenhoff, K., Fanale, F., Irvine, W. and Smith, B., Results of TV Imaging of Phobos (Experiment VSK-FREGAT). *Planet. Space Sci.* **39**(1/2), 281-295, 1991.

Bader, H. and Kuroiwa, D., *The Physics and Mechanics of Snow as a Material.* Publ. of U.S. Army Cold Regions Research and Engineering Laboratory, Hanover, New Hampshire, 1962.

Ball, A. J., Solomon, C. J. and Zarnecki, J. C., A Compton Backscatter Densitometer for the RoLand Comet Lander- design concept and Monte Carlo simulations. *Planet. Space Sci.* **44**(3), 283-293, 1996.

Ball, A. J., Solomon, C. J. and Zarnecki, J. C., The Response of Gamma Backscatter Density Gauges to Spatial Inhomogeneity– an Extension of the Single Scattering Model. *Nucl. Instrum. and Meth. in Phys. Res. B* **140**(3/4), 449-462, 1998.

Ball, A. J., Trow, M. W., Smith, A. and Zarnecki, J. C., Laboratory Development of the MUPUS Densitometer for the Rosetta Comet Lander. Poster PS076 at the European Geophysical Society, Vienna, 21-25 April 1997. Abstract in *Ann. Geophysicae* **15**(suppl. III), C810, 1997.

Banaszkiewicz, M., Seiferlin, K., Spohn, T., Kargl, G. and Kömle, N., A New Method for the Determination of Thermal Conductivity and Thermal Diffusivity from Linear Heat Source Measurements. *Rev. Sci. Instrum.* **68**(11), 4184-4190, 1997.

Beatty, J. K. and Chaikin, A. (editors), *The New Solar System.* 3rd. ed., Cambridge University Press, 1990.

Belton, M. J. S., Chapman, C. R., Thomas, P. C., Davies, M. E., Greenberg, R., Klaasen, K., Byrnes, D., D'Amario, L., Synnott, S., Johnson, T. V., McEwen, A., Merline, W. J., Davis, D. R., Petit, J.-M., Storrs, A., Veverka, J. and Zellner, B., Bulk Density of Asteroid 243 Ida from the Orbit of its Satellite Dactyl. *Nature* **374,** 785-788, 1995.

Belton, M. J. S., Mueller, B. E. A., D'Amario, L. A., Byrnes, D. V., Klaasen, K. P., Synnott, S., Breneman, H., Johnson, T. V., Thomas, P. C., Veverka, J., Harch, A. P., Davies, M. E., Merline, W. J., Chapman, C. R., Davis, D., Denk, T., Neukum, G., Petit, J.-M., Greenberg, R., Storrs, A. and Zellner, B., The Discovery and Orbit of 1993 (243)1 Dactyl. *Icarus* **120**(1), 185-199, 1996.

Benkhoff, J., *Laborexperimente und Modellrechnungen zur Untersuchung der thermischen Evolution poröser Eis-Staub-Proben unter Weltraumbedingungen: Konsequenzen für Kometen und andere planetare Eiskörper.* Ph.D. thesis, Institut für Planetologie, Westfälische Wilhelms-Universität, Münster, Germany. Reihe Geowissenschaften, Shaker Verlag, Aachen, 1992.

Benkhoff, J. and Boice, D. C., Modeling the Thermal Properties and the Gas Flux from a Porous, Ice-Dust Body in the Orbit of P/Wirtanen. *Planet. Space Sci.* **44**(7), 665-673, 1996.

Benkhoff, J. and Huebner, W. F., Influence of the Vapor Flux on Temperature, Density, and Abundance Distributions in a Multicomponent, Porous, Icy Body. *Icarus* **114**(2), 348-354, 1995.

Bertozzi, W., Ellis, D. V. and Wahl, J. S., The Physical Foundation of Formation Lithology Logging with Gamma Rays. *Geophysics* **46**(10), 1439-1455, 1981.

Blomquist, R. N. and Gelbard, E. M., An Assessment of Existing Klein-Nishina Monte Carlo Sampling Methods. *Nucl. Sci. Engng* **83**(3), 380-384, 1983.

Boguslavskii, Yu., Drabkin, S. and Salman, A., Analysis of Vertical Projectile Penetration in Granular Soils. *J. Phys. D: Appl. Phys.* **29**(3), 905-916, 1996.

Boss, A. P., Tidal Disruption of Periodic Comet Shoemaker-Levy 9 and a Constraint on its Mean Density. *Icarus* **107**(2), 422-426, 1994.

Bridges, F. G., Supulver, K. D., Lin, D. N. C., Knight, R. and Zafra, M., Energy Loss and Sticking Mechanisms in Particle Aggregation in Planetesimal Formation. *Icarus* **123**(2), 422-435, 1996.

Campbell, D. B., Harmon, J. K., and Shapiro, I. I., Radar Observations of Comet Halley. *Astrophys. J.* **338**(2), 1094- 1105, 1989.

Campins, H., Walker, R. G., and Lien, D. J., IRAS Images of Comet Tempel-2. *Icarus* **86**(1), 228-235, 1990.

Cherkasov, I. I., Kemurdzhian, A. L., Mikhailov, L. N., Mikheev, V. V., Morozov, A. A., Musatov, A. A., Savenko, I. A., Smorodinov, M. I. and Shvarev, V. V., Determination of the Density and Mechanical Strength of the Surface Layer of Lunar Soil at the Landing Site of the Luna 13 Probe. *Kosmich. Issled.* **5**(5), 746-757, 1967 (in Russian). Translation in *Cosmic Res.* **4,** 636-645, 1968a.

Cherkasov, I. I., Vakhnin, V. M., Kemurjian, A. L., Mikhailov, L. N., Mikheyev, V. V., Musatov, A. A., Smorodinov, M. I. and Shvarev, V. V., Determination of the Physical and Mechanical Properties of the Lunar Surface Layer by Means of Luna 13 Automatic Station. *Moon and Planets* **2** (ed. A. Dollfus), North-Holland 70-76, 1968b.

Christensen, E. R., Comments on the Moving-Source Soil Density Gauge. *Nucl. Instrum. Meth.* **96**, 483-484, 1971.

Cole, D. M. and Stevens, H. K., Saline Ice Penetration. Cold Regions Research and Engineering Laboratory (Hanover, New Hampshire), Special Report 87/14**,** 1-34, 1987.

Czubek, J. A., Advances in Gamma-Gamma Logging. *Int. J. Appl. Radiat. Isot.* **34**(1), 153-172, 1983.

Devlin, G. and Taylor, D., The Spatial Response Pattern of Gamma Backscatter Density Gauges. *J. Soil Sci.* **21**(2), 297-303, 1970.

Devlin, G., Henderson, I. A. and Taylor, D., Design and Performance of a Moving Gamma-Source Soil Density Gauge. *Nucl. Instrum. Meth.* **76,** 150-156, 1969.

Divós, F., Szegedi, S. and Raics, P., Local Densitometry of Wood by Gamma Back-Scattering. *Holz als Roh- und Werkstoff* **54**(4), 279-281, 1996.

Donn, B. D., The Formation and Structure of Fluffy Cometary Nuclei from Random Accumulation of Grains. *Astron. Astrophys.* **235**(1-2), 441-446, 1990.

Donn, B., The Accumulation and Structure of Comets. In *Comets in the Post-Halley Era* Vol. 1 (eds. Newburn, R. L., Neugebauer, M. and Rahe, J.), 335-359, Kluwer, Dordrecht, 1991.

Donn, B. and Meakin, P., Collisions of Macroscopic Fluffy Aggregates in the Primordial Solar Nebula and the Formation of Planetesimals. *Proc. 19th Lunar and Planet. Sci. Conf.*, 577-580, 1989.

Dziruni, M. and Kömle, N. I., Development of a Method for Hardness and Cohesivity Measurements on Cometary Surface Layers Using a Harpoon Device: Progress Report I. *Technical Report OAW-IWF* **94**, 1-32, 1995.

Ellis, D. V., Gamma Ray Scattering Measurements for Density and Lithology Determination. *IEEE Trans. Nucl. Sci.* **35**(1), 806-811, 1988.

Ellis, D. V., *Well Logging for Earth Scientists.* Elsevier, New York, 1987.

Espinasse, S., Klinger, J., Ritz, C. and Schmitt, B., Modeling of the Thermal Behaviour and the Chemical Differentiation of Cometary Nuclei. *Icarus* **92**(2), 350-365, 1991.

European Space Agency, *European Space Science Horizon 2000.* ESA SP-1070, December 1984.

European Space Agency, *Comet Nucleus Sample Return.* Proceedings of an ESA Workshop held at the University of Kent at Canterbury, UK, 15-17 July, 1986. ESA SP-249, December 1986.

European Space Agency. *Rosetta Comet Nucleus Sample Return: Report of the Science Definition Team.* ESA SCI(87)3, December 1987.

European Space Agency, *Proc. Int. Workshop on Phys. and Mech. of Cometary Materials*, Münster, Germany, 9-11 October 1989. ESA SP-302, December 1989.

European Space Agency, *Rosetta Comet-Nucleus Sample Return: Mission and System Definition Document.* ESA SP-1125, June 1991.

European Space Agency, Rosetta Comet Rendezvous Mission, ESA SCI(93)7, September 1993.

Fanale, F. P. and Salvail, J. R., An Idealized Short-Period Comet Model: Surface Insolation, H_2O-Flux, Dust Flux, and Mantle Evolution. *Icarus* **60**(3), 476-511, 1984.

Fanale, F. P. and Salvail, J. R., The influence of CO ice on the activity and near-surface differentiation of comet nuclei. *Icarus* **84**(2), 403-413, 1990.

Forrestal, M. J. and Luk, V. K., Penetration into Soil Targets. *Int. J. Impact Engng* **12**(3), 427-444, 1992.

Gayer, A., Bukshpan, S. and Kedem, D., In situ Density-Measurement in Aqueous Solutions by the Gamma-Ray Backscattering Method. *Nucl. Instrum. Meth. Phys. Res.* **192**(2-3), 619-621, 1982.

Giauque, W. F. and Stout, J. W., *J. Amer. Chem. Soc.* **58,** 1144, 1936.

Gorbachev, Y. I., *Well Logging.* Wiley, Chichester, 1995.

Gromov, V. V., Misckevich, A. V., Yudkin, E. N., Kochan, H., Coste, P. and Re, E., The Mobile Penetrometer, a "Mole" for Sub-surface Soil Investigation. *Proc. 7th European Space Mechanisms & Tribology Symposium,* ESTEC, Noordwijk, The Netherlands, 1-3 October 1997. ESA SP-410, 151-156, October 1997.

Grün, E. and Jessberger, E. K., Dust. In: *Physics and Chemistry of comets*. (ed. W. F. Huebner), 113-176. Springer, Berlin, 1990.

Grün, E., Kochan, H. and Seidensticker, K. J., Laboratory Simulation, a Tool for Comet Research. *Geophys. Res. Lett.* **18**(2), 245-248, 1991.

Gulin, Yu. A., *Gamma-Gamma Method of Investigation of Oil Wells.* Nedra, Moscow, 1975 (**Гулин, Ю. А.,** *Гамма-Гамма-Метод Исследования Нефтяных Скважин.* Недра, Москва) (in Russian).

Hagermann, A. and Spohn, T., Evaluation of MUPUS Data and the Inverse Heat Conduction Problem. Poster PS049 at the European Geophysical Society, Nice, 20-24 April 1998. Abstract in *Ann. Geophysicae* **16**(suppl. III), C1012, 1998.

Harding, G. and Kosanetzky, J., Scattered X-Ray Beam Nondestructive Testing. *Nucl. Instrum. Meth. In Phys. Res.* **A280**(2-3), 517-528, 1989.

Harvey, B., *The New Russian Space Programme.* Wiley-Praxis, Chichester, 1996.

Hearst, J. R. and Carlson, R. C., The RIDS: a Density Logger for Rough Holes. *Geophysics* **34**(2), 222-234, 1969.

Heiken, G., Vaniman, D. and Bevan, M., *Lunar Sourcebook: A User's Guide to the Moon.* Cambridge University Press, 1991.

Henderson, I. A. and McGhee, J., Modelling gamma-source backscatter density gauges. *IEE Proc.* **133**(A9), 611-617, 1986.

Hsiung, P. and Roessler, K., CO_2-Profiles in Cometary Analogs. In: *Solid State Astrophysics* (eds. E. Bussoletti and G. Strazzula), 267-277. North-Holland, Amsterdam, 1991.

Huebner, W. F., *Physics and Chemistry of Comets.* Springer, Berlin, 1990.

Hughes, D. W., The Interior of a Cometary Nucleus. *Planet. Space Sci.* **44**(7), 705-710, 1996.

IAEA, Commercial Portable Gauges for Radiometric Determination of the Density and Moisture Content of Building Materials. *IAEA Technical Reports Series* **130,** 1971.

James, L. H., On the Determination of the Effective Volume of a Gamma Ray Density Gauge in Backscatter Mode. *Nucl. Geophys.* **7**(2), 343-352, 1993.

Kaye, G. W. C. and Laby, T. H., *Tables of Physical and Chemical Constants.* 14th. ed., Longmans, London, 1973.

Keller, H. U., Surface Features and Activity of the Nucleus of Comet Halley. In *Comet Halley: Investigations, Results, Interpretations,* Vol. 2 (ed. J. Mason), Ellis Horwood, Chichester, 133-145, 1990.

Kemurdzhian, A. L., From the Moon Rover to the Mars Rover. *The Planetary Report* **X**(4), 4-11, 1990.

Kemurdzhian, A. L., Brodskii, P. N., Gromov, V. V., Grushin, V. P., Kiselev, I. E., Kozlov, G. V., Mitskevich, A. V., Perminov, V. G., Sologub, P. S., Stepanov, A. D., Turobinskii, A. V., Turchaninov, V. N. and Yudkin, E. N., Preliminary Results of Determining the Physical and Mechanical Properties of the Soil of Venus by the Soviet Automatic Stations Venera 13 and Venera 14. *Kosmich. Issled.* **21**(3), 323-330, 1983 (in Russian). Translation in *Cosmic Res.* **21,** 253-259, 1983.

Kemurdzhian, A. L., Brodskii, P. N., Gromov, V. V., Kiselev, I. E., Smirnova, L. I., Stepanov, A. D. and Yudkin, E. N., Instruments for Measuring the Physical and Mechanical Properties of Soil, Evaluating its Electroconductivity, and Determining the Inclination of Angles of the PROP Roving Vehicle in the Framework of the 'Phobos' Project. *Instrumentation and Methods for Space Exploration,* Moscow, Izdatel'stvo Nauka, 141-148, 1989 (**Кемурджиан, А. Л., Бродский, Н. П., Громов, В. В., Киселев, И. Е., Смирнова, Л. И., Степанов, А. Д., Юдкин., Е. Н.,** Приборы дла Проведения Экспериментов по Изучению Физико-Механических Свойств Грунта, Оценке его Электропроводности и Измерению Углов Наклона Подвижного Ашарата ПРОП в Проекте "Фобос") (in Russian).

Kemurdzhian, A. L., Gromov, V. V., Kazhukalo, I. F., Kozlov, G. V., Komissarov, V. I., Korepanov, G. N., Martinov, B. N., Malenkov, V. I., Mitskevich, A. V., Mishkinyuk, V. K., Rogovsky, G. N. and Sologub, P. S., Soviet Developments of Planet Rovers in Period of 1964-1990. *Proc. Int. Symp. on Missions, Technologies and Design of Planetary Mobile Vehicles,* Toulouse, September 1992, 25-43. CNES / Cépaduès-Éditions, Toulouse, France, 1993.

Klein, O. and Nishina, Y., Über die Streuung von Strahlung durch freie Elektronen nach der neuen relativistischen Quantendynamik von Dirac. *Z. Phys.* **52,** 853-868, 1929.

Klinger, J., Espinasse, S. and Schmitt, B., Some Considerations on Cohesive Forces in Sun-Grazing Comets. *Proc. Int. Workshop on Phys. and Mech. of Cometary Materials*, Münster, Germany, 9-11 October 1989. ESA SP-302, 197-200, 1989.

Klinger, J., Levasseur-Regourd, A.-C., Bouziani, N. and Enzian, A., Towards a Model of Cometary Nuclei for Engineering Studies for Future Space Missions to Comets. *Planet. Space Sci.* **44**(7), 637-653, 1996.

Knollenberg, J., Kührt, E. and Spohn, T., MUPUS-TM: IR-Measurement of Comet P/Wirtanen's Surface Temperature. Presented at the European Geophysical Society, Nice, 20-24 April 1998. Abstract in *Ann. Geophysicae* 16(suppl. III), C1012, 1998.

Kochan, H., Roessler, K., Ratke, L., Heyl, M., Hellman, H. and Schwehm, G., Crustal Strength of Different Model Comet Materials. *Proc. Int. Workshop on Phys. and Mech. of Cometary Materials*, Münster, Germany, 9-11 October 1989. ESA SP-302, 115-119, 1989.

Kohno, M., Tsukamoto, S., Kawaguchi, J., Mizutani, H. and Hinada, M., Dynamical Aspect of Lunar Penetrator. *Proc. Int. Symp. Space Tech. Sci.*, Tokyo, Japan, May 20-25, 1990, vol. 2 (A92-53451 23-12), 1865-1870, 1990.

Kömle, N. I., Kargl, G., Thiel, K. and Seiferlin, K., Thermal Properties of Cometary Ices and Sublimation Residua Including Organics. *Planet. Space Sci.* **44**(7), 675-689, 1996.

Kömle, N. I., Ball, A. J., Kargl, G., Stöcker, J., Thiel, M., Jolly, H. S., Dziruni, M. and Zarnecki, J. C., Using the Anchoring Device of a Comet Lander to Determine Surface Mechanical Properties. *Planet. Space Sci.* **45**(12), 1515-1538, 1997.

Kossacki, K. J., Kömle, N. I., Kargl, G. and Steiner, G., The Influence of Grain Sintering on the Thermoconductivity of Porous Ice. *Planet. Space Sci.* **42**(5), 383-389, 1994.

Kossacki, K. J., Kömle, N. I., Leliwa-Kopystynski, J. and Kargl, G., Laboratory Investigation of the Evolution of Cometary Analogs: Results and Interpretation. *Icarus* **128**(1), 127-144, 1997.

Kovtunenko, V., Kremnev, R., Rogovsky, G. and Ivshchenko, Y., Prospects for Using Mobile Vehicles in Missions to Mars and Other Planets. *Proc. Int. Symp. on Missions, Technologies and Design of Planetary Mobile Vehicles,* Toulouse, September 1992, 149-160. CNES / Cépaduès-Éditions, Toulouse, France, 1993.

Kührt, E. and Keller, H. U., The Formation of Cometary Surface Crusts. *Icarus* **109**(1), 121-132, 1994.

Kührt, E., Knollenberg, J. and Keller, H. U., Physical Risks of Landing on a Cometary Nucleus. *Planet. Space Sci.* **45**(6), 665-680, 1997.

Landau, L. D. and Lifshitz, E. M., *Electrodynamics of Continuous Media.* 2nd ed., Pergamon, Oxford, 1984.

Lang, K. R. and Whitney, C. A., *Wanderers in Space: Exploration and Discovery in the Solar System.* Cambridge University Press, 1991.

Leonovich, A. K., Gromov, V. V., Dmitriyev, A. D., Penetrigov, V. N., Semenov, P. S. and Shvarev, V. V., The Main Peculiarities of the Processes of the Deformation and Destruction of Lunar Soil. In the *Soviet American Conference on Cosmochemistry of the Moon and Planets,* 735-743, NASA SP-370, 1977. Also available in NASA Technical Translation F-16034, 1974.

Leonovich, A. K., Gromov, V. V., Semyonov, P. S., Penetrigov, V. N. and Shvartov, V. V., Luna 16 and 20 Investigations of the Physical and Mechanical Properties of Lunar Soil. In *COSPAR Space Research XV,* 607-616, Akademie Verlag, Berlin, 1975.

Lewis, J. S., *Physics and Chemistry of the Solar System.* Academic Press, London, 1995.

Lorenz, R. D., Bannister, M., Daniell, P. M., Krysinski, Z., Leese, M. R., Miller, R. J., Newton, G., Rabbetts, P., Willett, D. M. and Zarnecki, J. C., An Impact Penetrometer for a Landing Spacecraft. *Meas. Sci. Technol.* **5**(9), 1033-1041, 1994.

Love, S. G., Joswiak, D. J. and Brownlee, D. E., Densities of Stratospheric Micrometeorites. *Icarus* **111**(1), 227-236, 1994.

Lunne, T., Robertson, P. K. and Powell, J. J. M., *Cone Penetration Testing in Geotechnical Practice.* Chapman & Hall, 1997.

Markov, Yu., *Course to Mars.* Mashinostronie, 1989 (**Марков, Ю.,** *Курс на Марс.* Машиностроение) (in Russian).

Mason, J. (editor), *Comet Halley: Investigations, Results, Interpretations.* Ellis Horwood, Chichester, 1990.

Matese, J. J. and Whitman, P. G., Meteoroid Streams as Probes of the Subsurface Regions of Comets. *Icarus* **109**(2), 258-266, 1994.

McCarty, J. L. and Carden, H. D., *Impact Characteristics of Various Materials Obtained by an Acceleration-Time-History Technique Applicable to Evaluating Remote Targets.* NASA Technical Note TN D-1269**,** Langley Research Center, 1962.

McDonald, G. D., Whited, L. J., DeRuiter, C., Khare, B. N., Patnaik, A. and Sagan, C., Production and Chemical Analysis of Cometary Ice Tholins. *Icarus* **122**(1), 107-117, 1996.

Mendis, D. A., Hill, J. R., Houpis, H. L. F. and Whipple, Jr., E. C., On the Electrostatic Charging of the Cometary Nucleus. *Astrophys. J.* **249**(2), 787-797, 1981.

Mitchell, J. K., Houston, W. N., Scott, R. F., Costes, N. C., Carrier, W. D. III and Bromwell, L. G., Mechanical Properties of Lunar Soil: Density, Porosity, Cohesion, and Angle of Friction. *Proc. 3rd Lunar Sci. Conf.,* 3235-3253, 1972.

Mitchell, J. K., Houston, W. N., Carrier, W. D. III and Costes, N. C., Apollo Soil Mechanics Experiment S-200. Final Report, NASA contract NAS 9-11266, Space Sciences Laboratory Series 15, Issue 7, Univ. of California, Berkeley, 1974.

Mizutani, H., Lunar Interior Exploration by Japanese Lunar Penetrator Mission, LUNAR-A. *J. Phys. Earth* **43**(5), 657-670, 1995.

Möhlmann, D., Surface Regolith and Environment of Comets. *Planet. Space Sci.* **42**(11), 933-937, 1994.

Möhlmann, D., Cometary Activity and Nucleus Models. *Planet. Space Sci.* **43**(3-4), 327-332, 1995.

Möhlmann, D., *Comet 46 P/Wirtanen Nucleus Reference Model.* 1st ed., ROL-DLR/Möh-TN, DLR, Cologne, 1996.

Moore, H. J., Hutton, R. E., Scott, R. F., Spitzer, C. R. and Shorthill, R. W., Surface Materials of the Viking Landing Sites. *J. Geophys. Res.* **82**(28), 4497-4523, 1977.

MUPUS Proposal (Responsible Proposer: Prof. Tilman Spohn, Institut für Planetologie, Westfälische Wilhelms-Universität, Münster), June 1995.

National Aeronautics and Space Administration, *The Comet Rendezvous Asteroid Flyby Mission: A Search for Our Beginnings.* NASA, 1987.

NDT Abstracts- NDT Using Compton Scattering. *NDT & E International* **28**(3), 189-195, 1995.

Newburn, R. L., Neugebauer, M. and Rahe, J. (editors), *Comets in the Post-Halley Era.* Kluwer, Dordrecht, 1991.

Nicholson, P. D., Hamilton, D. P., Matthews, K. and Yoder, C. F., New Observations of Saturn's Coorbital Satellites. *Icarus* **100**(2), 464-484, 1992.

Oria, A. J. and Bowling, T. S., Orbit Perturbations in the Vicinity of an Active Cometary Nucleus. *Planet. Space Sci.* **43**(12), 1579-1585, 1995.

Peale, S. J., On the Density of Halley's Comet. *Icarus* **82**(1), 36-49, 1989.

Petler, J. S., Modelling the Spatial Response of a Compensated Density Tool. *IEEE Trans. Nucl. Sci.* **37**(2), 954-958, 1990.

Pickell, J. J. and Heacock, J. G., Density Logging. *Geophysics* **25**(4), 891-904, 1960.

Picton, D. J., Harris, R. G., Randle, K. and Weaver, D. R., Depth of Investigation of Density Tools. *IEEE Trans. Nucl. Sci.* **39**(4), 1014-1018, 1992.

Picton, D. J., Harris, R. G., Randle, K. and Weaver, D. R., Application of an Efficient Materials Perturbation Technique to Monte-Carlo Photon Transport Calculations in Borehole Logging. *Nucl. Instrum. Meth. Phys. Res. A* **359**(3), 559-565, 1995.

Podolak, M. and Prialnik, D., Models of the Structure and Evolution of Comet P/Wirtanen. *Planet. Space Sci.* **44**(7), 655-664, 1996.

Press, W. H., Teukolsky, S. A., Vetterling, W. T. and Flannery, B. P., *Numerical Recipes in FORTRAN: the art of scientific computing.* 2nd. ed., Cambridge University Press, 1992.

Prialnik, D. and Bar-Nun, A., Gas Release in Comet Nuclei. *Astrophys. J.* **363**(1), 274-282, 1990.

Probstein, R. F., The Dusty Gas Dynamics of Comet Heads. In *Problems of Hydrodynamics and Continuum Mechanics*, 568-583, Philadelphia Society for Applied Mathematics, 1968.

Putman, J. L., Jefferson, S. and Cameron, J. F., Tube Wall Thickness Gauge with Selection of Backscattered Gamma Radiations. *Proc. 2nd Radioisotope Conf. Vol. 2* 147-155, 1954.

Raeside, D. E., Monte Carlo Principles and Applications. *Phys. Med. Biol.* **21**(2), 181-197, 1976.

Richter, K. and Keller, H. U., On the Stability of Dust Particle Orbits Around Cometary Nuclei. *Icarus* **114**(2), 355-371, 1995.

Rickman, H., The Mass of the Nucleus of Comet Halley as Estimated from Nongravitational Effects on the Orbital Motion. In *Comet Halley: Investigations, Results, Interpretations*, Vol. 2 (ed. J. Mason), Ellis Horwood, Chichester, 163-172, 1990.

Rickman, H., Kamél, L., Festou, M. C. and Froeschlé, C., Estimates of Masses, Volumes and Densities of Short-period Comet Nuclei. *Proc. Symp. on the Diversity and Similarity of Comets*, Brussels, 6-9 April 1987. ESA SP-278, September 1987.

Rickman, H., Fernández, J. A., Gustafson, B. Å. S., Formation of Stable Dust Mantles on Short-Period Comet Nuclei. *Astron. Astrophys.* **237**(2), 524-535, 1990.

RoLand Cometary Lander of the Rosetta Mission. Preliminary proposal to ESA. RoLand consortium, October 1994.

RoLand Cometary Lander for the Rosetta Mission. Proposal to ESA. RoLand consortium, November 1995.

Rosetta Lander ECDR – Data Package. Rosetta Lander Consortium, ROL-DLR/SU-TN-002-97, 1997.

Sagdeev, R. Z., Elyasberg, P. E., Moroz, V. I., Is the Nucleus of Comet Halley a Low Density Body? *Nature* **331,** 240-242, 1988.

Scaife, B. K. P., *Principles of Dielectrics.* Oxford, 1989.

Schwehm, G. and Hechler, M., 'Rosetta'- ESA's Planetary Cornerstone Mission. *ESA Bulletin* **77,** 7-18, 1994.

Scott, R. F. and Robertson, F. I., Soil Mechanics Surface Sampler. In *Surveyor Program Results,* 171-179, NASA SP-184, 1969.

Seiferlin, K., Spohn, T. and Benkhoff, J., Cometary Ice Texture and the Thermal Evolution of Comets. *Adv. Space Res.* **15**(10), 35-38, 1995.

Seiferlin, K., Kömle, N. I., Kargl, G. and Spohn, T., Line Heat-Source Measurements of the Thermal Conductivity of Porous H_2O Ice, CO_2 Ice and Mineral Powders under Space Conditions. *Planet. Space Sci.* **44**(7), 691-704, 1996.

Sherman, H. and Locke, S., Depth of Investigation of Neutron and Density Sondes for 35-Percent-Porosity Sand. *Trans. 16th Symp. SPWLA*, 1975.

Smith, D. E., Lemoine, F. G. and Zuber, M. T., Simultaneous Estimation of the Masses of Mars, Phobos and Deimos using Spacecraft Distant Encounters. *Geophys. Res. Lett.* **22**(16), 2171-2174, 1995.

Snyder, D. D. and Fleming, D. B., Well Logging- A 25-Year Perspective. *Geophysics* **50**(12), 2504-2529, 1985.

Spohn, T., Ball, A., Banaskiewicz, M., Benkhoff, J., Hlond, M., Ip, W.-H., Jaupart, C., Kargl, G., Knollenberg, J., Kömle, N., Kossacki, K. J., Kührt, E., Leese, M. R., Lell, P., Leliwa-Kopystynski, J., Morgan, T., McDonnell, J. A. M., Rott, M., Seiferlin, K., Smith, A., Trow, M., Wright, M., Zarnecki, J. C., Zarnowiecki, T., MUPUS - a suite of small instruments for the RoLand Comet Lander to study thermal and mechanical properties. Presented at COSPAR 1996, Birmingham, 14-21 July 1996. Abstract in COSPAR 1996 Abstracts Volume, p. 68, 1996.

Steiner, G. and Kömle, N. I., Thermal budget of Multicomponent Porous Ices. *J. Geophys. Res.* **96,** 18897-18902, 1991.

Steiner, G. and Kömle, N. I., Evolution of a Porous H_2O - CO_2 - Ice Sample in Response to Irradiation. *J. Geophys. Res.* **98**(E5), 9065-9073, 1993.

Storm, E. and Israel, H. I., Photon Cross Sections from 1 keV to 100 MeV for Elements Z=1 to Z=100. *Nucl. Data Tables* **A7,** 565-681, 1970.

Strazzula, G. and Johnson, R. E., Irradiation Effects on Comets and Cometary Debris. In *Comets in the Post-Halley Era, Vol.1* (eds. R. L. Newburn, M. Neugebauer and J. Rahe), 243-275, Kluwer, Dordrecht, 1991.

Surkov, Yu. A., Geochemical studies of Venus by Venera 9 and 10 automatic interplanetary stations. *Proc. Lunar Sci. Conf.* **8,** 2665-2689, 1977.

Surkov, Yu. A., *Exploration of Terrestrial Planets from Spacecraft: Instrumentation, Investigation, Interpretation.* 2nd. ed., Wiley-Praxis, Chichester, 1997.

Surkov, Yu. A., Kirnozov, F. F., Khristianov, V. K., Korchuganov, B. N., Glazov, V. N. and Ivanov, V. F., Density of Surface Rock on Venus from Data Obtained by the Venera 10 Automatic Interplanetary Station. *Kosmich. Issled.* **14(5),** 697-703, 1976 (in Russian). Translation in *Cosmic Res.* **14,** 612-618, 1976.

Surkov, Yu. A., Khristianov, V. K., Korchuganov, B. N., Kirnozov, F. F. and Glazov, V. N., Method, Equipment and Main Results of the Measurement of the Venusian Rock Density on "Venera-10". *Space Sci. Instrum.* **3,** 287-299, 1977a.

Surkov, Yu. A., Kirnozov, F. F., Khristianov, V. K., Korchuganov, B. N., Glazov, V. N. and Ivanov, V. F., Investigations of the Density of the Venusian Surface Rocks by Venera 10. *Space Res.* **17,** 651-657, 1977b.

Surkov, Yu. A., Barsukov, V. L., Moskalyeva, L. P., Kharyukova, V. P. and Kemurdzhian, A. L., New Data on the Composition, Structure, and Properties of Venus Rock Obtained by Venera 13 and Venera 14. *Proc. 14th Lunar and Planetary Sci. Conf. Part 2,* 1983. *J. Geophys. Res.* **89** suppl., B393-B402, 1984.

SuSI Proposal (Principal Investigator: Dr. Johannes Benkhoff, Southwest Research Institute, San Antonio). SwRI Proposal No. 15-17876, May 1995.

Swinzov, G. K., Terminal ballistics in ordinary snow. Cold Regions Research and Engineering Laboratory (Hanover, New Hampshire), Technical Report **238,** 1-21, 1972.

Taylor, D. and Kansara, M., A Theory of the Nuclear Densimeter. *Soil Sci.* **104**(1), 25-34, 1967.

Thoe, R. S., High Resolution Tomography of Objects with Access to a Single Side. In *Underground and Obscured Object Imaging and Detection, Proc. SPIE* **1942,** 218-235, 1993a.

Thoe, R. S., Single Sided Tomography of Extremely Large Dense Objects. In *Underground and Obscured Object Imaging and Detection, Proc. SPIE* **1942,** 289-300, 1993b.

Thoe, R. S., Recent Progress in Single Sided Gamma-Ray Tomography. In *Aerial Surveillance Sensing Including Obscured and Underground Object Detection, Proc. SPIE* **2217,** 127-143, 1994.

Thomas, H., *Untersuchung der Festigkeit Poröser Eis-Mineral-Körper Kometarer Zusammensetzung.* Diploma Thesis, University of Cologne, 1992.

Thomas, P. C., Belton, M. J. S., Carcich, B., Chapman, C. R., Davies, M. E., Sullivan, R. and Veverka, J., The Shape of Ida. *Icarus* **120**(1), 20-32, 1996.

Tittman, J., *Geophysical Well Logging.* Academic Press, London, 1986.

Tittman, J. and Wahl, J. S., The Physical Foundations of Formation Density Logging (Gamma-Gamma). *Geophysics* **30,** 284-294, 1965.

Trow, M. W., Ball, A. J., Zarnecki, J. C. and Smith, A., *Requirements of the MUPUS Densitometer*. Internal MUPUS report, October 1997a.

Trow, M. W., Ball, A. J., Zarnecki, J. C. and Smith, A., *Densitometer Instrument of MUPUS– Design Thoughts.* Internal MUPUS report, October 1997b.

Uemura, T., Observations of Backscattered Gamma-Rays in a Surface Density Gauge. *Jap. J. Appl. Phys.* **4**(9), 667-676, 1965.

Ulaby, F. T., Bengal, T. H., Dobson, M. C., East, J. R., Garvin, J. B. and Evans, D. L., Microwave Dielectric Properties of Dry Rocks. *IEEE Trans. Geosci. and Rem. Sensing* **28**(3), 325-336, 1990.

Umiastowski, K., Buniak, M., Gyurcsak, J. and Maloszewski, P., Gamma-Ray Absorption Coefficient for Non-Homogeneous Materials. *Nucl. Instrum. Meth.* **141,** 347-351, 1977.

Verdant, M. and Schwehm, G. H., The International Rosetta Mission. *ESA Bulletin* **93,** 38-50, 1998.

Veverka, J., Thomas, P., Harch, A., Clark, B., Bell, J. F., Carcich, B., Joseph, J., Chapman, C., Merline, W., Robinson, M., Malin, M., McFadden, L. A., Murchie, S., Hawkins, S. E., Farquhar, R., Izenberg, N. and Cheng, A., NEAR's Flyby of 253 Mathilde: Images of a C Asteroid. *Science* **278**(5346), 2109-2114, 1997.

Wang, W. L., Low Velocity Projectile Penetration. *J. Soil Mech. Found. Div. Proc. Am. Soc. Civ. Engrs.*, 1635-1655, 1971.

Watson, C. C., Numerical Simulation of the Litho-Density Tool Lithology Response. *Proc. Soc. Petr. Engnrs of AIME 58th Annual Tech. Conf.,* SPE-12051, 1983.

Whipple, F. L., A Comet Model I. The Acceleration of Comet Encke. *Astrophys. J.* **111,** 375-394, 1950.

Whipple, F. L., A Comet Model I. Physical Relations for Comets and Meteors. *Astrophys. J.* **113,** 464-474, 1951.

Wiener, O. *Abh. Sächs. Akad. Wiss. Lpz Math.-Naturwiss Kl.* **32,** 509, 1912.

Wilson, A., *Solar System Log.* Jane's, London, 1987.

Wood, J., *Computational Methods in Reactor Shielding,* 324-342. Pergamon, Oxford, 1982.

Yeomans, D. K., Barriot, J.-P., Dunham, D. W., Farquhar, R. W., Giorgini, J. D., Helfrich, C. E., Konopliv, A. S., McAdams, J. V., Miller, J. K., Owen, W. M., Scheeres, D. J., Synnott, S. P. and Williams, B. G., Estimating the Mass of Asteroid 253 Mathilde from Tracking Data During the NEAR Flyby. *Science* **278**(5346), 2106-2109, 1997.

Young, C. W., Depth Prediction for Earth-Penetrating Projectiles. *J. Soil Mech. Found. Div. Proc. Am. Soc. Civ. Engrs.,* 803-817, 1969.

Young, C. W. and Keck, L. J., *An Air Dropped Sea Ice Penetrometer*. SC-DR-71 0729 / AD-739991, Sandia Laboratories, 1971.